Graphene bioelectronics for long term neuronal interfacing in-vivo

Antoine Bourrier

▶ **To cite this version:**

Antoine Bourrier. Graphene bioelectronics for long term neuronal interfacing in-vivo. Biological Physics [physics.bio-ph]. Université Grenoble Alpes, 2017. English. NNT : 2017GREAY011 . tel-01597689v2

HAL Id: tel-01597689
https://theses.hal.science/tel-01597689v2

Submitted on 3 Nov 2017

HAL is a multi-disciplinary open access archive for the deposit and dissemination of scientific research documents, whether they are published or not. The documents may come from teaching and research institutions in France or abroad, or from public or private research centers.

L'archive ouverte pluridisciplinaire **HAL**, est destinée au dépôt et à la diffusion de documents scientifiques de niveau recherche, publiés ou non, émanant des établissements d'enseignement et de recherche français ou étrangers, des laboratoires publics ou privés.

Communauté
UNIVERSITÉ Grenoble Alpes

THÈSE

Pour obtenir le grade de

DOCTEUR DE LA COMMUNAUTE UNIVERSITE GRENOBLE ALPES

Spécialité: **Physique pour les Sciences du Vivant.**

Arrêté ministériel : 25 mai 2016

Présentée par

Antoine Bourrier

Dirigée par **Vincent Bouchiat**[1],
Et codirigée par **Cécile Delacour**[1] et **Grégoire Courtine**[2].

Préparée à l'**Institut Néel – CNRS**[1]
et à l'**Ecole Polytechnique Fédérale de Lausanne – EPFL**[2],
au sein de **l'École Doctorale de physique.**

Graphene bioelectronics for long term neuronal interfacing in-vivo

Bioélectronique graphène pour un interfaçage neuronal in-vivo durable

Thèse soutenue publiquement le **23 mars 2017**
Devant le jury composé de :

Pr. Catherine PICART Institut Polytechnique de Grenoble, INPG, Grenoble, France	Présidente
Pr. Guy OWEN Engineering Center for Nanohealth, Swansea University, Swansea, Wales, United Kingdom.	Rapporteur
Pr. José Antonio GARRIDO Catalan Institute of Nanoscience & Nanotechnology, ICN². Barcelona, Spain.	Rapporteur
Dr. Blaise YVERT BrainTech Laboratory, Inserm, Grenoble, France	Examinateur

Abstract

Graphene, an atomically thin layer of carbon, is investigated as a biosensing and coating material in order to address the long term durability issues of invasive intracortical implants. These devices are essential tools to record specific single motor neurons activity for medical applications aiming at healing neural injuries. Today's implants suffer from their high invasiveness. It is responsible for local inflammation that leads to the failure in unique neurons activity recordings in the motor cortex on a long term basis. By combining a monolayer graphene growth and transfer with an ultra-sensitive electronic integration and a biochemical functionalization, this thesis proposes a new multidisciplinary approach to build intracortical implants with an improved bioacceptance. By using innovative methods of graphene integration in implants, and in-vitro and in-vivo studies to assess the reactions of living tissues to graphene, we provide an overview of graphene's potential contribution to future brain machine interfaces for long term medical projects.

Résumé

Le graphène, une couche monoatomique de carbone, est étudié comme matériau pour construire ou encapsuler des biocapteurs afin d'adresser les problèmes de durabilité rencontrés avec les implants intra-corticaux. Ces derniers sont des outils essentiels pour les projets médicaux de neuro-réhabilitation afin d'enregistrer les signaux de motoneurones uniques dans le cerveau. Les implants actuels sont invasifs et leur efficacité est limitée dans le temps par la réaction de rejet des tissus. En combinant une synthèse de graphène optimisée à cet usage (monocouche continue sur plusieurs cm^2) et son intégration dans des capteurs électroniques ultra-sensibles, protégés par des polymères bioactifs, cette thèse propose une nouvelle approche pluridisciplinaire pour construire des implants offrant une meilleure bioacceptance. Au moyen de méthodes d'intégration innovantes et d'études du comportement du graphène in-vivo et in-vitro, nous évaluons expérimentalement la faisabilité d'intégration du graphène dans les futures interfaces cerveau machines pour des projets médicaux au long terme.

Remerciements

Cette thèse s'est déroulée de janvier 2014 à février 2017 au sein des équipes TPS et Hybride de l'Institut Néel à Grenoble et au sein du Courtine-Lab à l'Ecole Polytechnique de Lausanne. Par ces quelques lignes, je voudrais exprimer ma gratitude envers les personnes qui m'ont accompagné tout au long de ces années et m'ont permis de finaliser cette thèse.

En premier lieu, je souhaiterai remercier mes parents. Pour les valeurs qu'ils ont su me transmettre et notamment l'ouverture d'esprit, l'ambition et l'autonomie sans lesquelles je n'aurai jamais pu accomplir ce parcours universitaire. Pour leur soutien inconditionnel au cours de ces longues années d'études et leur disponibilité. Il est d'autant plus aisé de gravir des sommets que le refuge est haut et confortable.

Pour la garantie de moments de bonheur à venir qui m'a permis de tenir le rythme, je souhaite adresser mes remerciements à mes amis de toujours, compagnons de voyage, de rire et de sport, Antoine et Samson, et ceux avec qui j'ai partagé les bancs de la fac, Mathieu et Quentin.

A Caroline et François pour votre indéfectible amitié et tous les weekends passés en mer, au lac ou en montagne.

A Charlotte, pour ton sourire, l'intensité des moments passés ensemble et l'enivrante perspective de tous ceux à venir.

A ma sœur Sandrine pour ton soutien et ta bonne humeur, à mes cousins, qui m'ont fait découvrir Grenoble, à Guilhem et Romain pour votre perpétuelle joie de vivre et les moments de rigolade, ainsi qu'à toutes les rencontres qui ont enrichi ces trois années lors de voyages, conférences, soirées ou défis sportifs, je souhaite vous adresser ma plus profonde reconnaissance.

Je souhaite par ailleurs remercier ces amis et compagnons de thèse pour leur aide précieuse : Timothée Flenet pour les moments de travail efficaces, les rires et voyages, Timothée Moulin pour l'aide à la correction Anglo-Saxonne de ces pages et ta bonne humeur pendant les sessions de pow.

Ces lignes n'auraient de sens si je n'exprimais ma gratitude à Thibault pour notre amitié et tout ce que nous partageons, des discussions scientifiques aux aventures entrepreneuriales.

Cette thèse n'aurait pu s'achever sans l'immense contribution de Vincent Bouchiat tout au long de ces trois ans. Je te remercie pour la richesse de tes enseignements scientifiques, ta disponibilité et la confiance que tu m'as accordée.

Je voudrais adresser mes remerciements à Cécile Delacour, pour ta confiance durant ces trois années, et pour m'avoir proposé, avec Grégoire Courtine, un projet ambitieux dans un cadre propice à son bon déroulement avec le soutien de Joël Cibert et Xavier Thibault du LabeX Lanef.

Les innombrables qualités humaines d'Olivier Bourgeois et le dynamisme de son équipe m'ont fourni un cadre d'une rare perfection pour un travail efficace dans la bonne humeur. Par conséquent je souhaite remercier l'équipe TPS : Olivier, Jean-Luc, Jacques, Hervé, Dimitri, Gaël et Manu, sans oublier les doctorants toujours souriants Adib et Clothilde.

A Laetitia Marty pour la correction bienveillante de ces pages, à Valérie Reita pour son enseignement et sa disponibilité sans faille pour les analyses Raman et bien évidement à Farida Veliev pour notre collaboration sur les mesures d'effets de champs et les cultures cellulaires.

A Sébastien, Bruno, Gwenaëlle, Jeff et Thierry pour leur accompagnement moral et scientifique m'ayant permis de persévérer face aux difficultés du travail en salle blanche.

Et enfin à tous mes collaborateurs, qui ont favorisé au quotidien le bon déroulement de cette thèse à la frontière entre médecine, neurobiologie, biochimie, science des matériaux et microélectronique: Grégoire Courtine, Silvestro Micera et leurs équipes de l'EPFL: Marco Bonnizato, Quentin Barraud, Polina Shkorbatova, Elodie Rey et Léonie Asboth pour leurs enseignements et leur disponibilité lors des campagnes in-vivo.

A Anna Szarpak et Rachel Auzély du CermaV pour avoir cru en mon projet dès le jour où je suis venu les rencontrer. Aux scientifiques Grenoblois que j'ai pu côtoyer au comité NaMiSCeB et bien sûr aux enseignants de master qui ont su me transmettre leur passion.

Merci,

Table of contents

Introduction

Le Graphène, premier cristal bidimensionnel stable à l'air, est constitué d'une couche monoatomique d'atomes de carbone, a été isolé pour la première fois il y a douze ans [1] et est rapidement devenu un matériau d'intérêt pour la fabrication de dispositifs en microélectronique.

Le Graphène représente notamment une plateforme prometteuse pour la bioélectronique [2] étant donné qu'il rassemble dans un seul et même matériau, de nombreuses propriétés exceptionnelles comme sa haute conductivité électrique, sa neutralité chimique, sa transparence optique et sa flexibilité qui lui confère une rigidité proche de celle des membranes phospholipidiques des cellules [3]. A mesure que ce matériau devient de plus en plus facilement disponible et qu'il peut être produit à grande échelle avec une qualité contrôlée [4], [5], son intégration dans le domaine des capteurs biologiques devient envisageable et des dispositifs biomédicaux intégrants ces capteurs sont en cours d'étude [6]–[8].

D'autre part, les progrès récents en matière de neurorehabilitation pour les victimes de lésions de la moelle épinière [9] ou dans le domaine des neuroprothèses pour pallier aux handicaps moteurs [10] sont confrontés à de nombreux obstacles dans la transition du modèle animal aux patients humains car ils souffrent du manque de fiabilité des dispositifs médicaux utilisés pour détecter l'activité neuronale sur le long terme. En effet, ces projets médicaux nécessitent l'utilisation chronique d'enregistrement des signaux moteurs du cerveau avec une grande résolution, de l'ordre du neurone unique, pour lesquels les technologies actuelles standard demeurent instables dans le temps, invasives et complexes en termes d'électronique.

Le but du travail décrit dans ce manuscrit est d'évaluer l'intérêt prometteur du Graphène pour améliorer l'interfaçage avec les cellules et augmenter la sensibilité des capteurs afin d'enregistrer l'activité de neurones uniques, in-vivo, avec une grande fiabilité dans la durée.

J'ai donc, à cet effet, relevé de nombreux challenges de micro fabrication pour construire des biocapteurs Graphène sur différents substrats, incluant des matériaux flexibles. J'ai étudié comment le graphène pourrait bouleverser le domaine des implants intra-corticaux en combinant pour la première fois une amélioration en terme de bioacceptance et de sensibilité électronique des capteurs implantés.

Au fur et à mesure de ce manuscrit, après une étude sur les prérequis nécessaires à la compréhension des signaux neuronaux et à leur détection (Chapitre I), j'ai adressé les problématiques suivantes en trois chapitres:

Premièrement, concernant la synthèse et l'intégration du graphène (Chapitre II), quelle qualité de graphène et reproductibilité dans le procédé de fabrication sont nécessaires à l'interfaçage neuronal avec une bonne bioacceptance? Quels sont les principaux avantages et inconvénients de l'enregistrement de signaux in vivo avec du Graphène ? Comment utiliser le graphène pour concevoir et fabriquer des dispositifs biomédicaux en 3D à partir de couches de microélectroniques 2D superposées ? Dans ce but, j'ai développé et détaillé dans ce chapitre des méthodes efficaces pour une synthèse de graphène et son intégration dans des procédés de fabrication de qualité et reproductibles.

Par la suite je dresse une étude (Chapitre III) pour déterminer comment des biocapteurs graphène intégrés sur des implants peuvent être combinés avec les nouvelles technologies pour l'amélioration de la bioacceptance. En particulier, je détaille le développement et les tests in vivo d'un bio-polymère utilisé durant ma thèse pour enrober et fonctionnaliser le graphène. Ce bio-polymère a pour but la protection de la couche monoatomique et le futur attachement d'hydrogels permettant la diminution de la rigidité de surface de l'implant et la délivrance progressive et locale de médicaments pour améliorer la bioacceptance.

Afin de procéder à l'intégration de graphène sur des dispositifs implantables in-vivo, je développe ensuite (chapitre IV) les réponses aux interrogations suivantes: comment construire un implant intégrant des biocapteurs graphène tout en préservant l'intégralité de cette couche monoatomique ? Comment construire des dispositifs flexibles avec du graphène, tout en conservant une certaine rigidité nécessaire à l'implantation ? Comment intégrer le graphène comme matériau d'enrobage sur les dispositifs existants afin de tester son influence sur la bioacceptance in vivo ? Finalement, à la fin de ce chapitre (4.3), je détaille comment le graphène s'est comporté comme matériaux d'enrobage durant la chirurgie et après plusieurs semaines in-vivo à l'EPFL à Lausanne, et quelles améliorations il a apporté en termes de bioacceptance dans le cerveau.

Introduction

Graphene, an atomically thin layer of graphitic carbon, has been first isolated twelve years ago [1] and quickly became a material of interest to build microelectronic devices. In particular, graphene is a promising platform for bioelectronics [2] as it gathers in one material many unique properties such as high electrical conductivity, chemical inertness, optical transparency and flexibility with a bending rigidity comparable to the phospholipidic bilayer of cells membrane [3]. As this material becomes more and more easily available and can now be produced at large scale [4], [5], its promising integration in biosensing and biomedical devices is being investigated [6]–[8].

On the other hand, one of the biggest challenge in neurorehabilitation for spinal cord injury victims [9] and neuroprosthetic for motor diseases [10], is to perform the migration from the animal model to human. To this end, they need improvements regarding reliability of the biomedical devices they use to sense neurons activity on a long term basis. Indeed, these long term projects request a high spatial resolution recording of the brain activity, meaning unique neuron sensing, for which today's golden standard devices remain chronically instable, invasive and challenging for electronics.

The goal of this thesis work is to assess the promising use of graphene to improve the interface with cells and the sensitivity of the bioelectronic sensors based on that material in order to record unique neurons activity in-vivo with higher long term reliability. For that purpose, I have explored the microfabrication challenges of graphene biosensors on several substrates, including flexible materials.

I have thus investigated how graphene could be a game changer by combining for the first time improved bioacceptance and high sensitivity electronics. Along this manuscript, after an investigation on the requirements in sensing neurons activity (Chapter I), I have addressed several interrogations in four chapters:

First, regarding the synthesis and integration of graphene (Chapter II), what quality of graphene and process reproducibility do we need to interface neurons with a good bioacceptance? What are the main advantages and drawbacks of graphene for in-vivo recording? How to use graphene for 3D engineering of biomedical devices?

For this purpose, I have developed efficient methods for high quality and reproducible graphene synthesis and integration.

I then investigate (Chapter III) how can graphene sensors be combined with today's new technologies in bioacceptance improvement? In particular, I detail the developments and in-vivo tests of a soft biopolymer coating to protect, functionalize and confer graphene a drug delivery ability.

In order to perform the integration of graphene on in-vivo sensing devices, I then focused (Chapter IV) on the questions: how to build an implant with embedded graphene sensors while preserving the integrity of such a monoatomic thin layer? How to build flexible devices with graphene that are stiff enough to be implanted? How to integrate graphene as a coating material on existing devices to improve their bioacceptance?

Finally, thanks to an *in vivo* campaign at EPFL in Lausanne (Chapter IV) I detail how our graphene behaves during surgical procedure and after several weeks in the brain?

I. Brain interfaces

The quest for a long term reliable neural/electronics interface provides challenges that, if overcome, could boost future medical applications. Neurons communication is based on their ability to create and propagate electric currents called action potentials, along their membrane. Neural interfaces can detect those action potentials, or stimulate neurons to modify their activity: this thesis is focused on the ability for neural interfaces to sense electrical activity of single neurons in vivo.

To begin this chapter (1.1), we explain the motor control function to understand the concrete role and organization of the nervous system to perform a task; here locomotion. We then introduce basic concepts on how neurons communicate and how information propagates in organized networks and subsystems to achieve brain functions.

In a second part (1.2) we review brain machine interfaces, i.e. the devices used to sense (or eventually stimulate) neurons electrical activity. Brain interfaces are classified in terms of their detection scales and potential medical applications.

This thesis medical application project consists in neurorehabilitation for spinal cord injury victims: the last part of this chapter (1.3.2) is thus dedicated to the sensors requirements for this project and the limitations of current medical devices in this field. We finally describe how graphene could solve these limitations issues

Chapter I - Table of contents

1.1 Neuronal signals

Neurons are the basic units of the nervous system which is organized in two levels: (1) the Central Nervous System (CNS) including the Brain and the Spinal Cord and (2) the Peripheral Nervous System (PNS). Whereas CNS and PNS act in continuous coordination to control body functions, each of these systems has its own specific neuron population with well-defined functions.

We differentiate two different pathways of information called tracts in the Spinal Cord: ascending tracts transfer sensory information coming from peripheral members and intern organ sensors to the brain; descending tracts transmit, among others signals, the CNS motor commands to peripheral members and internal organs.

Neurons support this **bi-directional communication**, involved in both the signals transmission and their treatment. While the Brain communicates with intern organs through the Autonomic Nervous System (ANS), we will focus on its communication with the musculoskeletal system supported by the Somatic Nervous System (SNS).

One important medical application that is discussed in this manuscript is indeed related to the SNS by targeting recovery of locomotion after spinal cord injuries. One of the main roles of SNS is indeed the motor control, responsible for locomotion.

1.1.1 Neural architectures and motor control

The description of motor control is an excellent opportunity to enumerate the specific functions of neuronal systems. It is responsible for voluntary movements and **locomotion** and intervenes in reflexes and balance. Motor control system is thus in charge of the coordination between the muscles and the brain –i.e. the musculoskeletal system and the central nervous system.

Because our movements always take into account our **environment**, the motor control have to receive and integrate the sensory information emitted by multiple sensors of our body [11]. Motor control is responsible for our actions and evolution in space including voluntary redundant (ex: walk) and accurate (ex: catching a ball) movements, reflexes and balance.

In order to achieve this **coordination** between the environment, the muscles and the brain, four different neural subsystems work together in a so called neural architecture to achieve proper motor control which is described in Figure 1.

- The first motor control subsystem (Red color on Figure 1) is the center of decision, called the **motor cortex**, and its "executive arms": the **upper motor neurons** in the CNS. Those neurons are part of the descending tracks and convey voluntary movement orders and important spatiotemporal information from the motor cortex to local circuit neurons**.**
  Local circuit neurons are either situated in the **brainstem** (green)**,** involved in posture and basic movements coordination, or directly in the grey matter of our spinal cord in the so called **Central Pattern Generators** (CPGs) [12].

- The **CPGs** are part of the second subsystem (labeled in blue), from which emerges the **lower motor neurons** carrying reflexive and voluntary information to the **skeletal muscles**, to achieve movements and balance for instance (underlined with the blue arrows lines). It receives direct sensory inputs and sends projections toward higher centers of the CNS to achieve muscles coordination (yellow arrows lines). This second subsystem (CPGs) can generate self-sustaining patterns (without descending tracks from the cortex) for locomotion movements (walking for instance)[13].
  Among all the involved local circuit in locomotion, the CPGs have a key role for neurorehabilitation medical applications that I will further detail in 1.3.

- The **cerebellum** is the third subsystem (labeled in brown), supporting motor control efficiency. The cerebellum is responsible for the **errors feedback loop**, treating sensory information relative to movement adjustments, in order to influence the descending tracks activity patterns in the cerebellar cortex. It acts as a **corrector for movement** and is partly responsible for motor learning by storing error information.

- Finally, the fourth and last subsystem (labeled in purple) is the **basal ganglia**. It generates a subcortical motor loop which impacts the motor cortex and provides regulation of the upper motor neurons information to prime **movement's initiation** and **suppress parasitic movements**.

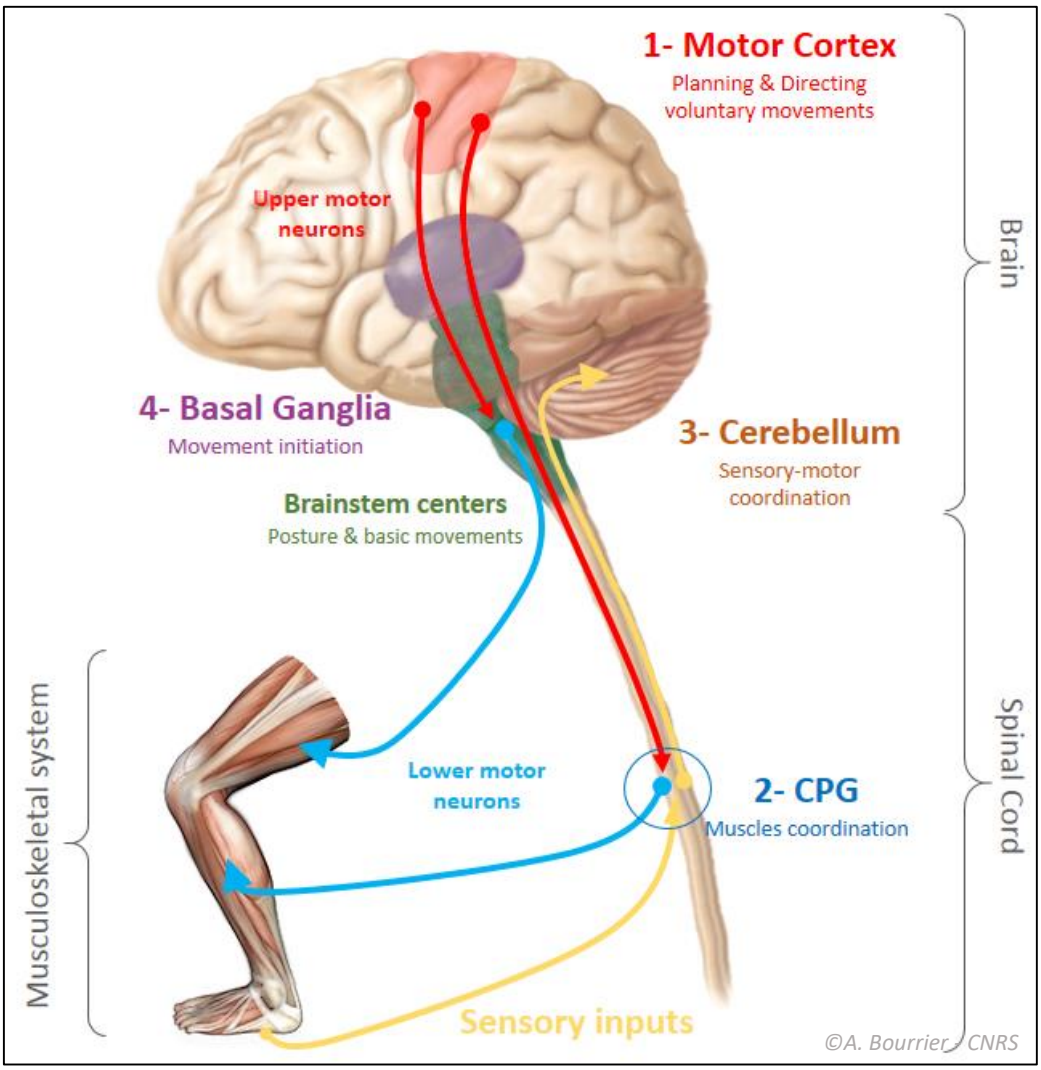

Figure 1 – The nervous system organizes itself in subsystems to perform motor control tasks: Motor control is processed by 4 entangled subsystems which allow the voluntary movement initiation in the basal ganglia, the movement processing and commands in the motor cortex which are then transmitted through upper motor neurons (red lines) to intermediate local centers called Brainstem and Central Pattern Generators (CPG). Brainstem allows posture and basic movements whereas CPG performs muscles coordination. They both command skeletal muscles through lower motor neurons (blue lines). Accurate locomotion movement maintenance and improvement are achieved properly thanks to sensory feedback (yellow lines) in the CPG and Cerebellum.

Motor control is a complex yet very organized function of our nervous system. It supports locomotion and is thus the target of neurorehabilitation projects for motor diseases or spinal cord injuries victims. We will describe, in the second part of this chapter, how the brain computer interfaces can help restore voluntary locomotion after a partial section of upper motor neurons in the spinal cord. Upper motor neuron regeneration and CPGs restoration trough electrical and chemical stimulation as much as sensory feedback are key factors to the neurorehabilitation project investigated during this thesis (1.3).

1.1.2 The Neurons electrical signals origins

Neurons are some of the electrically excitable cells of the human body, meaning that they can be stimulated to generate and carry ionic currents, supporting the information or commands to the next targeted cells. As seen before, neurons organize themselves in large architectures to perform functions like motor control.

Neuron cells own architecture is organized to fulfil that task (Figure 2) and is made of 3 main compartments: the body called the **soma**, the receiver and transmitting units respectively called **dendrites** and **axons**.

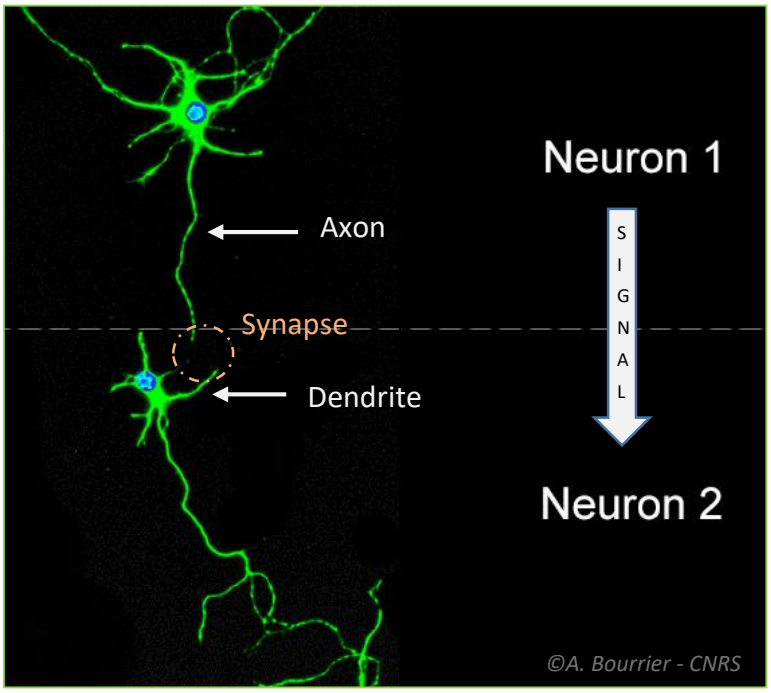

Figure 2 - Neurons are designed to receive and transmit complex information coded in electrical signals: This immuno-fluorescence micrograph aims to illustrate the expected oriented communication from the neuron-1-axon to the neuron-2-dentrite in order to transmit information using the chemical junction called synapse. Neurons have been extracted from mouse embryos hippocampus, cultured 5 days on poly L-Lysine coated glass. Green FITC fluorophore stains microtubules which are present in the whole neurons (body, dendrites and axon). Blue fluorophore marks nucleus position.

Dendrites and axons are “branches” shaped and made to establish a contact with other neurones through electrochemical transmitters. The soma share the complement of organelles found in all cells, including nucleus, mitochondria, endoplasmic reticulum, Golgi apparatus and a variety of vesicular structures that are respectively responsible for the cell

DNA preservation and replication, energy production, proteins transport and vesicular trafficking.

Neurons convey information to others cells by means of an electrical current impulse called **Action Potential (AP)**. It starts from the axon hillock[1] and propagates along its axon until it reaches another neuron's dendrite (Figure 2). The transmission of the AP between the axon and a dendrite is made through the extracellular matrix thanks to an electro-chemical transducer called a **synapse**.

1.1.3 From Ion channel activity to Action potentials

Cells in tissues are always surrounded by an Extra-Cellular Matrix (ECM), mainly composed of proteins, ions, nutriments, hormones, and vesicles. In the Central nervous System (CNS), ECM occupies 10–20 % of the volume [14] and is the guarantor of the stability of synaptic transmissions and the tissue structure [15]. In addition to this matrix, a specific ratio of glial cells supports the activity and coordination between the neurons.

Before discussing the impact of this environment on the electrical activity of neural networks (c -) and how the surgery during electronics implantation can disturb this fragile equilibrium and impacts the detection of network activity (chapter III part 1), we will describe the basic concepts of neurons signalling.

A cell is generally defined as an assembly of organelles: the nucleus, mitochondria, Golgi apparatus, vesicles and cytoskeleton proteins…. which are surrounded by the intracellular medium, all encapsulated in a bi-lipid membrane which delimits the cell body and complete the mechanical support role of the cytoskeleton.

The physico-chemical composition of that membrane is of paramount importance for the in-depth understanding of action potential propagation. Indeed, the specific trans membrane **ion channels** are responsible for a difference in ionic concentration between the intra and extracellular compartment – i.e. inner neuron and the ECM- resulting in a potential (voltage) difference.

As described in Figure 4, electrical potentials are generated across eukaryotic cell membranes, neurons included, because of the differences in ionic concentrations between ECM and intracellular cytoplasm. This difference is due to the membrane ion selective permeability

[1] The axon hillock is the junction between the soma and the axon and is the location where the definitive action potential starts to propagate.

through ion channels (Figure 4B) and **active ions transporters** (Figure 4A) which maintain concentration gradients between the two compartments.

At the neuron resting state (no action potential occurrence) the voltage gradient called the resting potential is around ΔV_r-70mV.

The action potential, explained Figure 6, results from the breakage of this difference thanks to ion channels fast opening and closing.

In a neuron, most concerned ions are Potassium K+, Sodium Na+, Chloride and Calcium found to the following concentrations:

	Concentration (in mM)	
	IntraCell	ExtraCell
Potassium (K^+)	**140**	5
Sodium (Na^+)	15	**145**
Chloride (Cl^-)	4 to 30	110
Calcium (Ca^{2+})	0.0001	1 to 2

Figure 3 - Ions concentration in extra and intracellular compartments: Potassium and Sodium ionic gradients are maintained by ion transporters and are responsible for Action Potentials occurrence thanks to ion channels. After [16].

Potassium have an overriding role in resting potential as it is the most concentrated ion inside the neurons and its diffusion through the membrane is the easiest. Negative charges contribute to intracellular electro-neutrality, creating the Donnan equilibrium [17] that prevents K^+ from total extracellular migration.

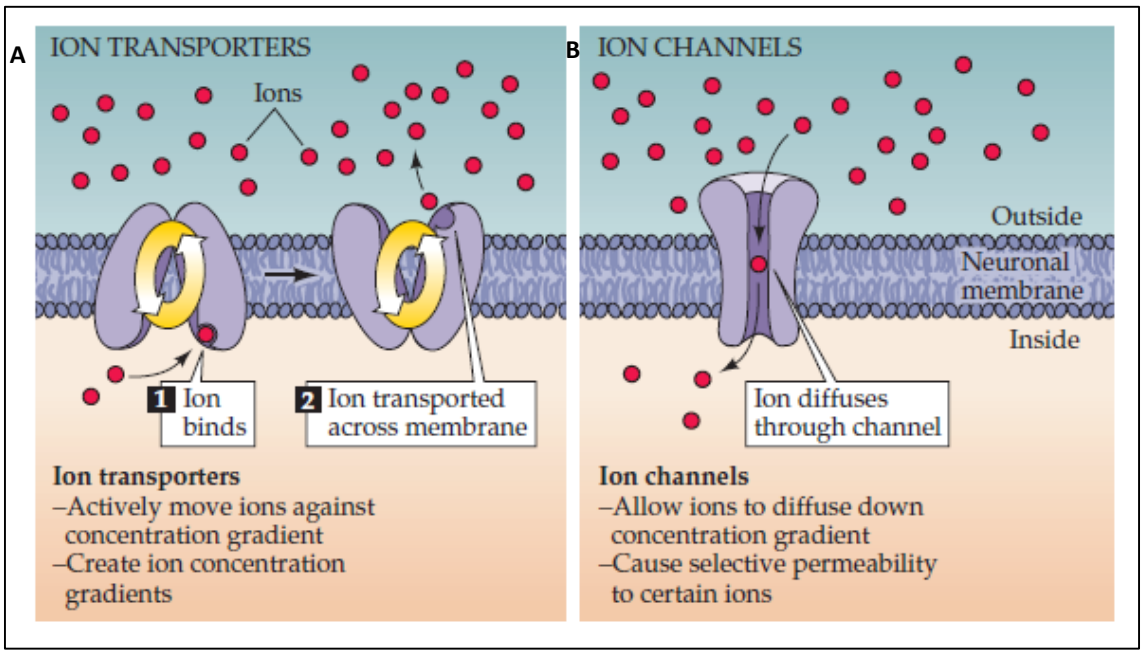

Figure 4 - Ion transporters and ion channels induce ionic movements across neurons membranes. Ion transporters actively create ionic concentration difference by carrying specific ions against their chemical gradients. Ion channels are passive transporters that use passive diffusion according to concentration gradients to select specify ions to diffuse through the membrane. From [18].

According to the Fick diffusion law, the spontaneous passive diffusion of ions across the membrane is a function of their concentration gradient. But because of the membrane selective permeability of ions, charges accumulate on both side of the membrane, generating an opposite electrical field which prevents ions diffusion. On the other hand, the Nerst equation expresses the equilibrium potential for each ion across the membrane E_x according to ion concentration $[X]_1$ and $[X]_2$ at each side of the membrane:

$$E_x = \frac{R.T}{z.F}\ ln\frac{[X]_2}{[X]_1}$$

With R the gas constant, T the absolute temperature, z the electrical charge of the concerned ion and F the Faraday constant. A law specific to membrane with permittivity consideration and all permeant ions has been written by Goldman[19]:

$$V_{membrane} = 58.log\frac{P_K[K]_2 + P_K[Na]_2 + P_K[Cl]_1}{P_K[K]_1 + P_K[Na]_1 + P_K[Cl]_2}$$

The neurons membrane resting potential is thus: $V_{membrane} \approx$ -70mV.

Among all the cells, the neurons distinguish themselves with their advanced intercellular communication skills. Thus, their membrane components, the ion channels, allow Action Potential (AP) initiation and transmission whereas the intracellular organization of the

cytoskeleton proteins favourits growth of neurites (axons and dendrites) as well as efficient vesicles trafficking. The neuron action potential is induced by the **depolarization** of its membrane following the opening of specific ion channels. A very important aspect to understand is the **spatio-temporal** dimension of this membrane depolarization.

a - Temporal representation

It is paramount to understand the role of ion channels and transporters role during the different phases of the AP: from the physiological excitation, to a fast depolarisation and repolarisation of the membrane which last less than 1ms. Physiological excitation can be electrical and chemical stimulus. Here we are interested in neurons response to electrical stimulation and how they generate AP. Neurons use these electrical signals to transmit information in neural systems, at a high speed ranging from 2 to 100m/s depending on neuron's type. This AP phenomenon is responsible for the nerve impulses.

Whereas Na^+, K^+, Cl^- and Ca^{2+} ions are all responsible for cells resting potentials, extracellular Na^+ and intracellular K^+ ions are specially involved in neurons action potentials as described with Figure 5. Neurons trigger a spontaneous electrical depolarization of their membrane by temporarily opening Na+ channels, and then opening K+ channels to set back the membrane resting potential, after an hyperpolarization preventing backward signal transmission [20].

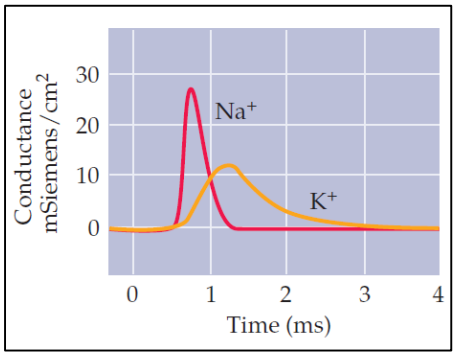

Figure 5 – Action potential decomposition in ionic flows: Time traces of the changes in Na^+ and K^+ membrane conductance (function of ion permeability and thus number of opened ion channels) during are responsible for a spontaneous change of membrane potential, here an action potential.

Action potentials are thus a brief variation of the membrane potential in response to an efficient stimulation that can be sensitive or motor coming from specific receptors. The neuron soma, which integrates all the incoming excitatory or inhibitory dendritic signals initiates the AP through the axon hillock. AP amplitude is around 100mV for a motor neuron and its duration is around 1ms. In Figure 6, from the resting potential of -70mV, physiological excitants will provide efficient stimulation to reach the -55mV threshold of membrane

depolarization, thus triggering the opening of Na+ channels. This will provoke massive Na^+ penetration in the cell and thus a depolarization of its membrane. Na^+ channels will then close and K^+ channels will slowly open simultaneously, causing repolarization. The depolarization/repolarization phase lasts 1ms and is called Absolute Refractive Period (ARP): during this time, no opening of Na^+ channels are possible. Just after repolarization, K^+ channels will close slowly, causing a small hyperpolarization: the negative late post-potential. During a 1 to 10ms (neuron dependent) period called Relative Refractive Period (RRP), Na+ channel "doors" status is not totally reset. Active ion transporters restore proper ion concentration gradients inside the cell. During RRP, only a stronger stimulation than the previous one will be able to trigger a new AP.

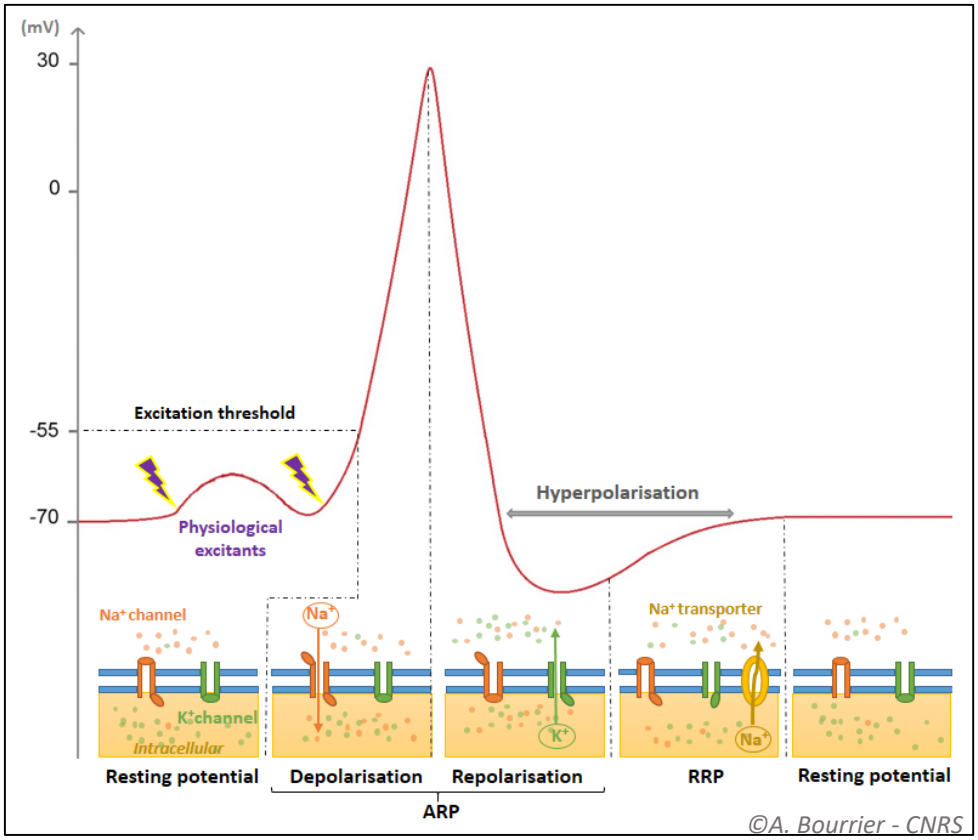

Figure 6 - Neurons communicate by transmitting action potentials: Time scale representation of an action potential (AP) and corresponding membrane channels schemes described in text.

b - The spatial scale

The action potential spatial aspect regards its propagation along the axon toward the targeted dendrites and from those dendrites toward the next neuron. Na^+ ion channels opens themselves one after the other along axon or dendrite membrane in a cascade reaction. This

particular “wave” of channels openings and closing gives birth to a macroscopic phenomenon called a nerve impulse in PNS and a **neuron spike** in CNS (Figure 7).

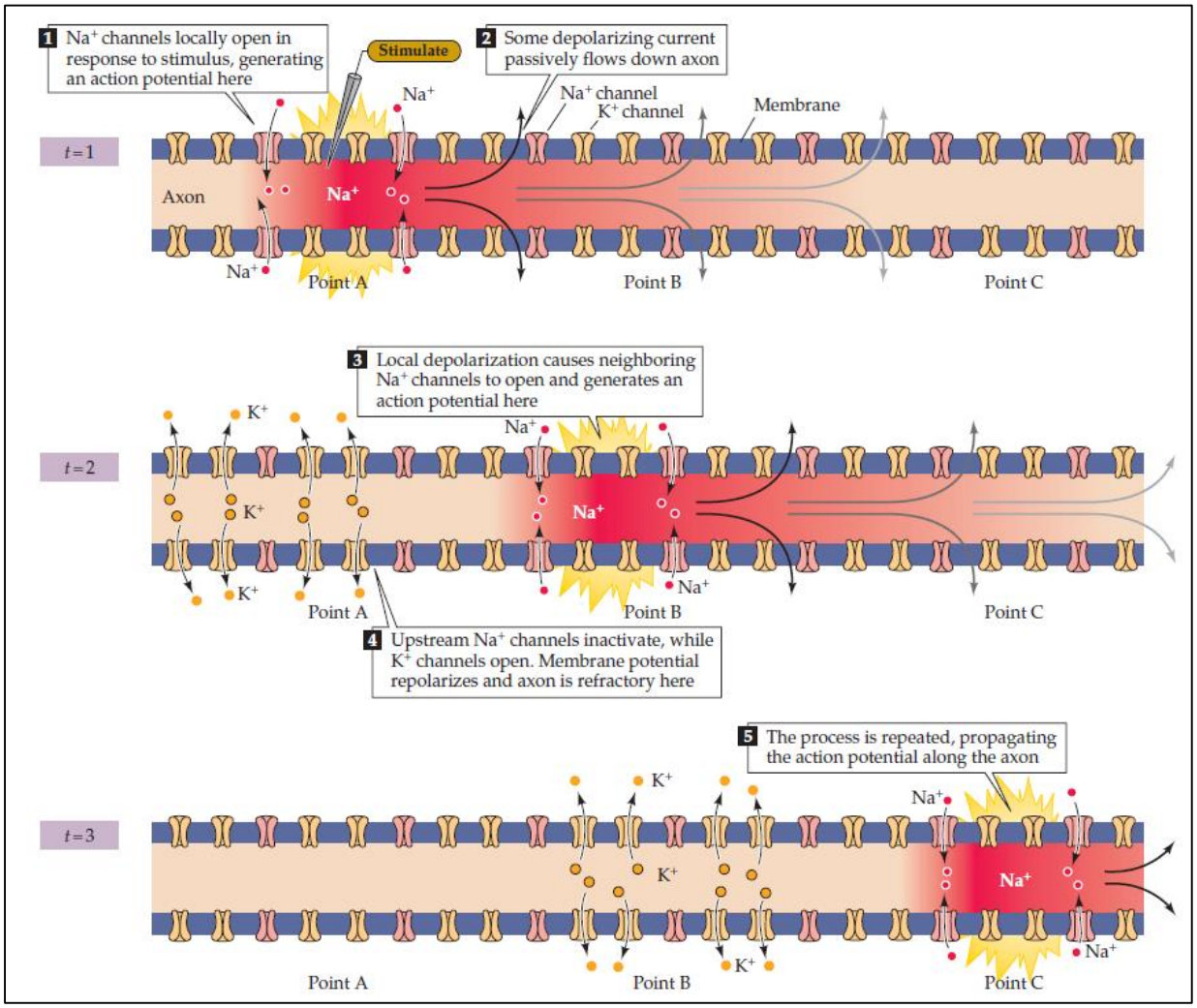

Figure 7 - "Wave" conduction along a neuron membrane, a dendrite or an axon for example. Active and passive flows are mobilized as local depolarization induce NA+ channels opening at a point A at t = 1. Then the current passively flows along the membrane, depolarizing an adjacent region, here point B, and thus initiating an action potential at this location inducing again inward current and so one until point C. When action potential has passed membrane potential is regain due to K+ channels openings and Na+ channels inactivation during a transitory period called refractory period. Figure from [18]

When organized in network, neurons spontaneously “fire” or “**spike**” and thus propagate depolarization trains in the network. When transmitting a motor order, motor neurons spike synchronously to stimulate different neural systems responsible for motor control. Action potentials transmit motor command or sensitive signals through spinal cord and PNS.

These signals exhibit the highest amplitude among neuronal cells signals, and can be characterized by their shape: duration and velocity. We will now describe how an extracellular activity sensor, of a size larger than an axon, will integrate several signals and how one can extract neurons spikes from a local brain activity.

c - Differences between local field potential and spikes

For further understanding of neural interfaces we will review here the difference between signals types regarding the scale of detection. To this end, we introduce a measurement technique called patch clamp.

From patch clamp to extracellular microelectrodes sensors

Patch clamp is the ultimate precision tool for thorough measurement of neurons electrical activity. It is used as the gold standard reference to evaluate the accuracy of every new neural interface technique. However, its invasiveness and range of use limit it to lab applications in-vitro. It consists of using a glass micropipette to contact a small area of a neuron membrane (few µm) and perform a local measurement (Figure 8A). Taking away a single channel from the membrane on the tip of the micropipette measures single ion channel electrical current [21], while piercing a hole in the membrane allows voltage measurement between the inner cell and the ECM and will thus sums the whole cell electrical activity. This whole cell summed activity corresponds to pure action potential or **spiking activity.**

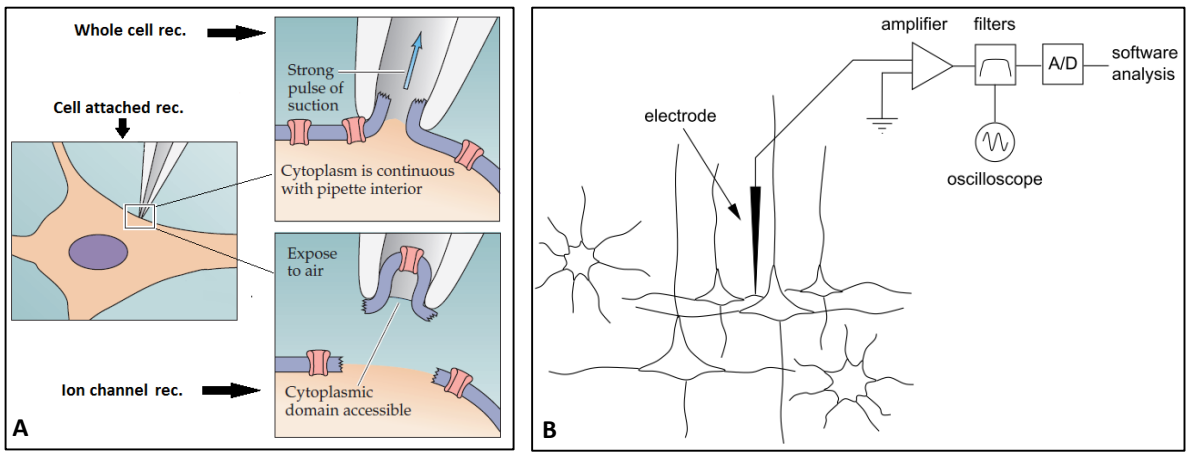

Figure 8 – Patch clamp intracellular recording is the most precise technique but, on the contrary extracellular recording, cannot be performed in vivo. ***A)*** *Patch clamp measurement methods depends on the pipette opening position and status of the membrane. Both methods are destructive for the cell, but allow whole cell depolarization recording or single/ few channels activity recording. After* [18] ***B)*** *Extracellular recordings with large electrode will record several cells activity (Local field potentials) and software analysis will allows single neuron activity isolation and recording after* [22].

For evident reasons, patch clamp technique - while being the most accurate methods todays- cannot be used for intra-cortical measurements regarding due to their invasiveness and single cell approach which is incompatible with activity patterns detection.

Local field potentials

In Vivo neural interfaces will generally read neuronal activity by measuring currents outside of the cell using cell sized electrodes (Figure 8B) : because their size remains larger than a single axon, the current microelectrodes measure a summation of APs, dendritic or post-synaptic signals, glial potentials and others Extra Cellular Matrix (ECM) proximity changes called Local Field Potential (LFP).

Neurons supportive **glial cells**, which play a role in nutrition, immune-protection and signal improvement are responsible for important exchange activity, provoking local current in the ECM. Other close neurons will also spike or induce subthreshold synaptic currents.

For this reason, extraction of single neurons spiking activity from the total **Local Field Potential** *LFP* (measured with the current extracellular microelectrode) is essential. Its complexity will be proximity and size dependant. The spatial resolution of neuronal probes is directly related to their size and their proximity with the targeted neurons (on which also depends the detection probability regarding the screening of the extracellular signals by the surrounding charges).

However, given the fact that LFP are generated by from supportive cells activity, they are directly related to neuron firing activity and have thus been shown to predict spiking activity [23].

When recording single neuron activity with intracortical implants one must process spike sorting. Computer assisted signal treatment allows filtering of pure neurons spikes from the LFP detected by the probe sensors. This spike sorting is based on a principal component analysis: a filtering algorithm based on amplitude of neurons spikes, their frequency and their velocity. [24] Spike sorting programs have been used during the two *in vivo* campaign of this thesis and are thus described in last parts of chapter III and chapter IV.

In order to understand the variety of neuronal activity detection tools, we will now review the neural interfaces available to read the Brain activity and describe this large family called Brain Machine Interfaces.

1.1 Neuronal signals - From Ion channel activity to Action potentials

1.2 Brain Machine Interfaces

Brain operation has fascinated men for centuries. Famous ancient Greeks writings testify of a great heritage: Herophilus or Erasistratus dissections already identified motor and sensory systems, whereas Hippocrates and Plato described the premises of the compartmentalization of physiological brain functions [25]. Along the centuries, studies were led by anatomical dissections together with physiological experimentation in order to understand the brain organization.

However, we had to wait until Hans Berger to develop, in 1924, a first Brain Interface technique: electroencephalography (EEG). Human brain electrical activity as oscillatory activity was then recorded [26]. In 1973, Jacques Vidal firstly used the expression “Brain Computer Interface” (BCI) to describe his project of EEG signals collection and computer processing [27]. During the last forty years, many brain signal recording techniques have been discovered and application for this new field are numerous and growing in number each year.

From now on, brain interfacing allows a very accurate detection and a better comprehension of brain related diseases. Research projects using BMI are focusing more and more on disease fighting. BMI’s applications are going toward improvement of sick and invalid patients life quality through, for example, ambitious researches on neurodegenerative diseases[28] and neurorehabilitation [9]. More and more challenges concern BMI performances and their daily use.

For those reasons, a growing domain of applications for BMI regards neuroprosthesis, a particular set of neuroprosthetic devices. Whereas BMIs are generally used to connect the brain to an electronic system, neuroprosthetic devices connect a neural system, spinal cord or peripheral member for example, to an electronic device. In this thesis field of applications, we replace a defective nervous system or peripheral member with a neuroprosthesis. A BMI will then be responsible for the control of this neuroprosthesis: for instance, to restore locomotion disorder through spinal cord neurorehabilitation orientated device [29] or even peripheral member substitution [30].

1.2.1 BMI's state of the art

Interfacing neurons is a key step for understanding the nervous system and its pathologies. We saw in the previous section that neurons act as communication units and use spatio-temporal defined action potential or spikes to communicate. Nowadays, many BMI tools are available to listen to these communications with a resolution's detection scale ranging from a single neuron to the whole brain subsystem activity depending on the technique used. Given the previously explained proximity dependence extraction of single neurons spiking activity from LFP, the detection scale will be related to the tool invasiveness.

In this part we sum up those BMI technologies as function of their **spatio-temporal resolution** from larger scales to single neurons recordings, describing their detection efficiency and their applications.

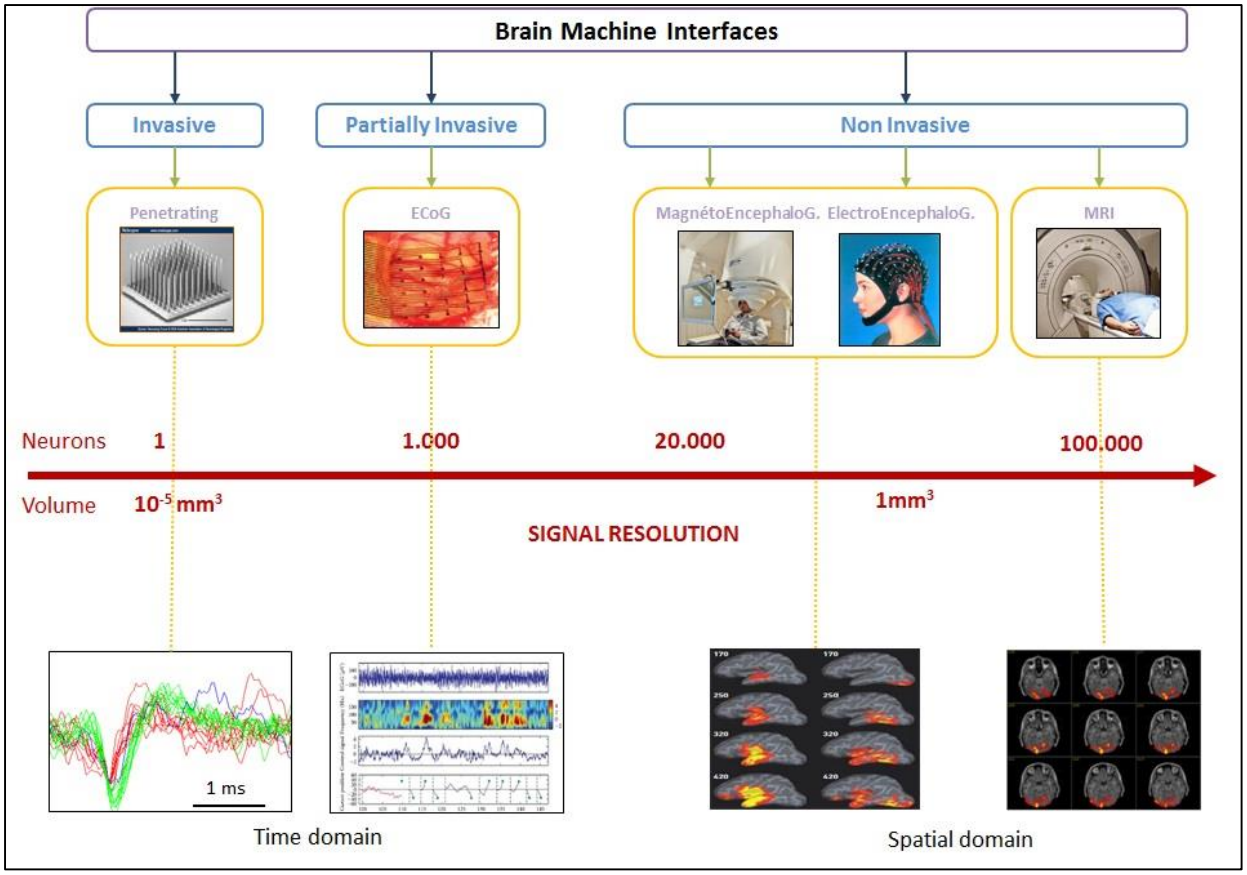

Figure 9 - BMI technologies sum up: Different available tools for interfacing neurons and their network. Classification is function of their spatial resolution in term of neurons number whom activity is recorded, and of assessed volume. The higher is the resolution, the more invasive is the technique.

1.2.2 Noninvasive extra-cranial interfaces

a - Large scale mapping with Functional Magnetic Resonance Imaging - fMRI

Large scale recording of brain activity is possible thanks to MRI imaging. MRI uses nuclear magnetic resonance to detect the hydrogen atoms density in successive 2D plans. MRI allows water detection in tissues and thus is used for structural defect detection. It is also a great surgical assistant tool for intracranial surgeries or implantations.[31]

In another hand, functional MRI (fMRI) focuses on behavioral studies and functional neurological diseases: fMRI uses blood oxygen level dependent contrast to characterize neuronal activity. MRI creates images with 1mm wide pixels. The resolution of $1mm^3$ is the equivalent in fMRI of a 100.000 neurons activity averaging. The important data treatment associated to this technique gives access to a temporal resolution of around 1s and consequently limits fMRI to more than 1s brain processes' studies [32].

b - Large scale high speed detection with Magnetoencephalography - MEG

The magnetoencephalography (MEG) is also a functional neuroimaging technique, recording very small magnetic fields (~0.01 to 1pT) linked to synchronized neuronal electric activity. MEG brain mapping is done by surrounding the head of the patient with an array of very performant magnetic field sensors called SQUIDs and must be performed in a magnetic shielded room to avoid ambient magnetic noise (~0.1µT).

The limit of detectability of such a technique is around 50.000 active neurons [33] preferentially with a uniform orientation of electric current. It is often used in cognitive science and to study fast occurring brain processes like epilepsy, to map brain area activity in real time. MEC is indeed able to record with a high temporal resolution of 1ms [34].

c - Cortex projections activity reading with ElectroEncephaloGraphy - EEG

ElectroEncephalography is an electrophysiological recording method: It measures previously described Local Field Potentials (LFP), to record activity from a non-invasive scalp electrodes array placed all over the head. The detection limit does not allow single neuron detection but it rather record a summation of synchronous activity of thousands of neurons. Electric fields being distorted by the skull on the contrary to magnetics fields, EEG will have a lower spatial resolution than MEG, and better EEG recordings will then need intracranial , invasive placement of electrode [35].

It is yet a lighter recording technology to implement than MRI or MEG but notwithstanding an affordable and good temporal resolved recording technique. It can be used with freely behaving subject on contrary to MRI and MEG who need head immobilization. Studies of patient's epilepsy is often using this tool.

1.2.3 Low invasive extra-cortical interface

a - LFP averaging with ElectroCorticoGraphy - ECoG

ElectroCorticoGraphy (ECoG) consists of recording surface cortex activity. The spatial detection scale provides a signal dominated by Local Field Potentials (LFP) at a better resolution than EEG, stripping out the skull distortion of electrical currents by placing an array of electrodes under the skull.

Thus, this technique requires an invasive intervention called a craniotomy. It consists in an implantation under the crane to place the ECoG device between meninges and Skull Bone (Figure 10).

The invasiveness degree depends on the targeted resolution and depth of detection. The location of the device thus changes within the meninges: Epidural devices preserves the superficial meninge, the dura-matter, whereas subdural devices are placed between pia-matter and dura-matter and thus must be flexible devices to preserve the pia matter integrity.

ECoG allows the LFP averaging of smaller populations of neurons: the spatial resolution being around 0.4 to 1cm wide [36]. However, the temporal resolution around 5ms allows very acute measurement of fast phenomena like epilepsy [37] and is also a very efficient technique for neural disorder rehabilitation [38].

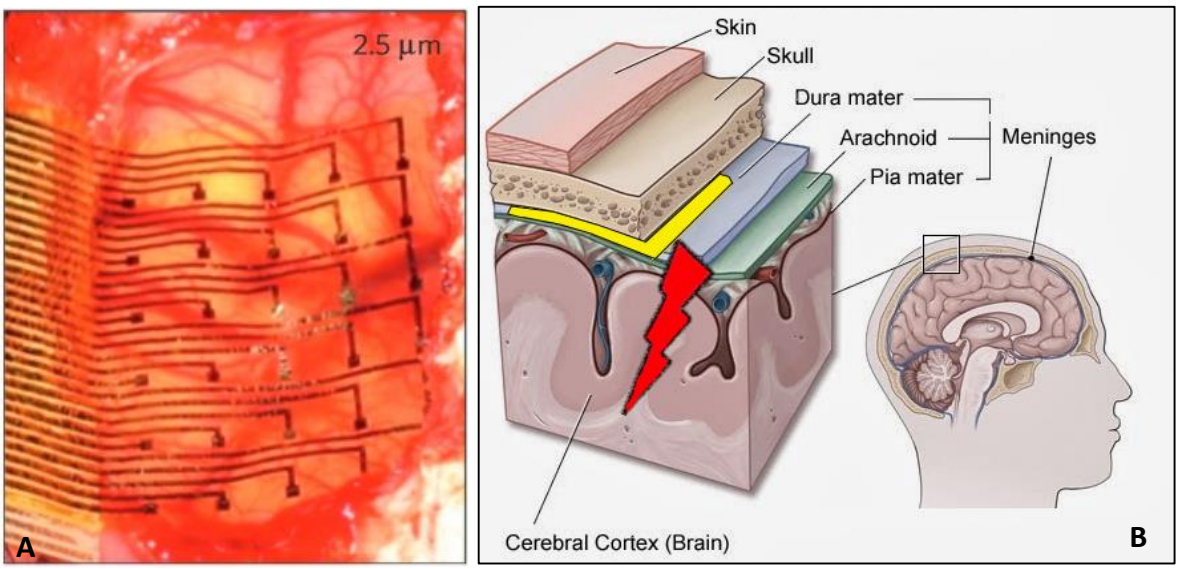

*Figure 10 – ECoGs need a craniotomy to place the electrodes as close as possible to the targeted area: **A** Biodegradable subdural ECoG placed on the pia matter of a cat to record multichannel LFP. From Kim et Al* [39] ***B** Meninges and skull layers representation showing the epidural ECoG (in yellow) and a penetrating intracortical implant in red.*

1.2.4 Invasive intracortical interfaces

a - Intracortical Calcium imaging.

Working in contact with neurons is not the only way to record single action potential activity. New optical technologies based on live calcium imaging and in situ two photons microscopy [40] seem to be a very promising approach. Calcium imaging technique uses the relationship between Ca^{2+} ions flows and the action potentials and ion channels activities [41]. Indeed, Ca^{2+} triggers release of neurotransmitters at synapses locations and supports the propagation of dendritic and somatic signals, this ion flow will then be related to information transmission activity by APs. Slow ions diffusion is a limitation to calcium imaging technique in term of maximum spiking frequency detectable. On the other hand, voltage-sensitive dye imaging provides higher time resolution by linking membrane potential variation with fluorescence signal strength. These two techniques rely on the fluctuations of low fluorescence signals which can be a limitation and also possible source of artefacts, being function of the camera sensitivity and the optics used.

These techniques can be combined with transgenic modification using viral **transfections** or mutant cells [42]. It allows the direct expression of optically sensitive ions channel and the optical stimulation of spikes. The optical detector, or a transmitting optical fibre array has to be surgically implanted into the brain to the desired recording area, as

illustrated on Figure 11. The invasiveness degree is consequently high. *In vivo* calcium imaging is nevertheless a promising multiple neurons activity recording technique as the optical answer might not be too much impacted by the inflammation reactive tissues. However it adds a degree of invasiveness, requiring viral transfection that excludes its use in human therapies for now [43].

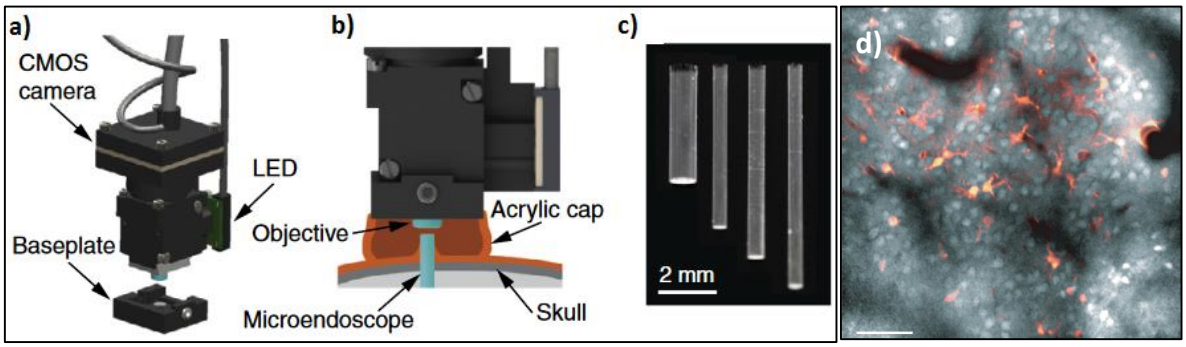

Figure 11 - In vivo setup for freely behaving animal recording of neuronal activity thanks to calcium imaging: ***a)*** *the CMOS camera and fluorescence stimulation LED are plugged when animal has to be recorded.* ***b)*** *The micro endoscope is implanted through pia matter and part of the cortex to the targeted area and allows directional light transmission from the targeted area to the CMOS camera as much as stimulating light transmission from the LED to the targeted area.* ***c)*** *Microendoscopes can be of different lengths for several targeted area or animal brain sizes. From Inscopix© and* [44]. ***d)*** *Two-photon image of a cell population stained with OGB-1 in L2/3 of mouse neocortex at 200µm depth below the pia. Image of astrocytes labeled with sulforhodamine 101 (red) is overlaid. Scale bar, 50µm. Picture From* [43].

b - Single neurons activity resolution with intracortical implants.

Intracortical[2] penetrating implants are the only BMIs to allow *in vivo* single neuron activity recording and spikes recording, and thus remain the gold-standard technique for high spatio-temporal resolution mapping of neuronal activity.

Those penetrating implants possess many capacitive sensors (1.3.4), mostly microelectrodes, in order to assess a large population of neurons and ensure a minimum number of sensors close enough to a cell (<10µm distance) to be able to record a signal dominated by a neuron spikes and not by local field potential. The signals will nevertheless be filtered in line with a **spike sorting software** in order to extract spiking activity from the recorded LFP. Intracranial implants are usually made of a rigid material in order to be able to penetrate the pia-matter and the cortex: most of the devices are based on silicon material, used to carry several microelectronics sensors called Micro Electrodes Arrays (MEA). The rigidity and volume of the implant is causing a lot of damages to surrounding tissues. Recent techniques investigate flexible electronic to lower the rigidity mismatch between neural tissue and implant but still have to be stiff enough to penetrate the tissues. Innovative designs propose solutions to the rigidity issue[45]–[47] but flexible sensors carried by these probes yet remains to be improved, and the occupied volume seems to give birth to a glial scar although reducing it [48] (description in chapter III).

These devices are described and their reliability issues developed in the **dedicated part 1.3.2**.

[2] Intracortical means inside the cerebral cortex, across skull, meninges and through the surface layer of the cortex to reach deepest regions of the brain.

1.2.5 **BMI applications sum up**

In order to sum up those interfacing techniques, it appears that brain functional studies, cognitive science, brain area interconnections and malfunctions related to neurodegenerative disease and epilepsy can be characterised and studied using MRI or MEG depending on the required time scale. EEG can also make accurate measurements for those applications, presenting a slightly lower spatial resolution but a way easier access and allowing freely behaving studies.

EEG and epidural ECoG can provide motor information by recording cortical projection on the surface layer of the cortex and associating those patterns of activity to motor control commands. Although ECoG have been successfully used to control robotics arms and basic neural interface systems such as mouse or keyboard control [49], average LFP recording of surface motor cortex does not provide enough precision for **accurate movements**: fine neuroprosthesis control like artificial hand [30] would need specific deep motor cortex neurons spiking information to reconstruct with precision the complexity of movements of our fingers, for instance by restoring an error feedback loop and precision mechanisms of motor control [50]. Neuroprosthesis would thus benefit from the intracranial recording but are facing the invasiveness of the current approaches resulting in signal degradation over time that limits the neuroprosthesis control lifetime (explained in chapter III).

1.3 Application to Neurorehabilitation

1.3.1 Project description

a - Neural interfaces considerations

Neurorehabilitation projects following spinal cord or peripheral nerves lesions need the higher precision degree of neuronal signals. Indeed, it needs to provide the injured area of PNS or spinal cord with the very same signal precision it used to get when uninjured [51]. Deep motor cortex single motor neuron spiking activity is required and this can only be performed using invasive intracortical implants which permit sensing of microscales areas of the deep motor cortex. In fact, the deeper the implant penetrates into the motor cortex, the closer it gets to the source of motor control. Thus, Layer IV and V of the motor cortex are targeted because they contain the upper motor neurons and pyramidal cells that transmit the cortical projections to the brainstem illustrated on Figure 12, which direct voluntary motor control (see part 1.1.1). This information is then processed through the lumbar spinal cord or through the medial medullary brainstem.

The **brainstem** receives inputs in an area called Midbrain Locomotors Region (MLR), consequently, rehabilitation projects also use penetrating implants to perform deep brain stimulation in the MLR [52].

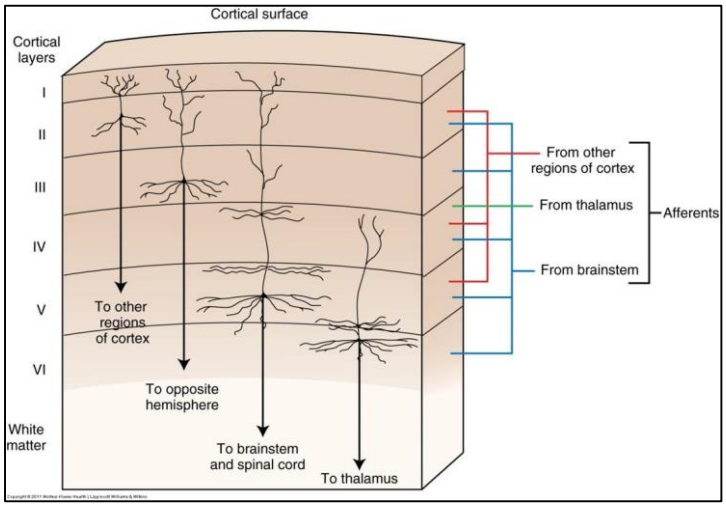

Figure 12 - Motor cortex layers contain specific descending pyramidal cells with respective functions and motor control subsystem targets. Source: Free-Stock-Illustration

b - Context of this thesis

This work aims to contribute to the implementation of a new generation of chronic intracortical sensors for **the recovery of motor functions after spinal cord injuries** (SCI). This thesis thus partly took place under the supervision of Gregoire Courtine, who holds the International Paraplegic Foundation (IRP) Chair in spinal cord repair in Lausanne, working on recovery of motor functions after spinal cord injuries (SCI). Combining serotonergic agonist injections with epidural electric stimulation, sensory inputs in the CPG and training, they achieved recovery of injured spinal cord circuits of rodents [53][54]. However, in order to restore voluntary control of those recovered circuits, **voluntary initiation of central pattern generators (CPGs) is necessary** (Figure 13). As a reminder from 1.1.1, CPGs have the ability to generate stepping-like activation patterns. CPGs integrate sensory feedback from visual, vestibular and proprioceptive sensors as a reflex pathway to organize locomotion muscles synergy. CPGs drive locomotion under supraspinal and long descending pathways initiation and control [55]. Following the recovery of damaged circuits, and to re-establish these long descending pathway between the motor cortex/brain stem and the CPGs, a reorganization of CNS neuronal pathway is necessary and might be possible thanks to neuroplasticity [56].

MLR and **cortex deep layers motor neurons signals** can be extracted and used for the stimulation of neural tissues below the lesion, improving this reorganization [52] It is by mixing sensory ascending feedback and descending motor pathways through CPGs that Courtine et Al. aim to achieve **recovery** of locomotion after SCI, based on voluntary control commands from motor cortex.

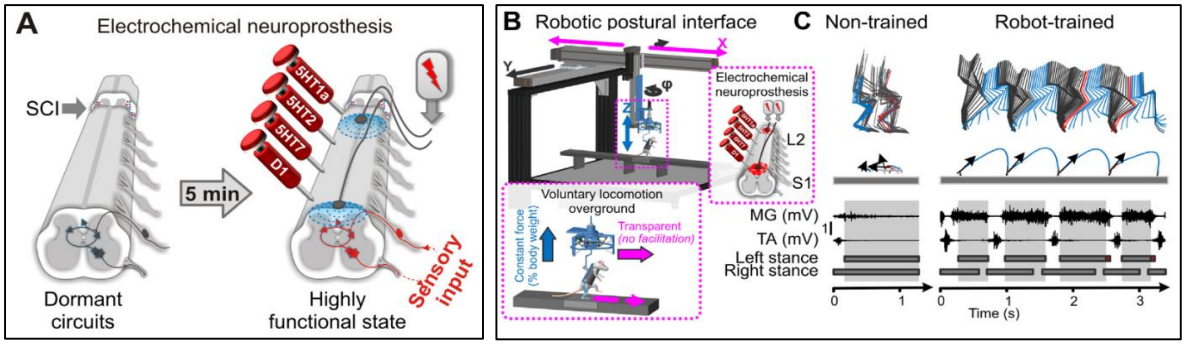

Figure 13 – Multimodal approach for locomotion recovery after spinal cord injuries uses motor cortex activity to stimulate the spinal cord ***A*** *Electrochemical neuroprosthesis to transform lumbar locomotors circuits from dormant to highly functional state.* ***B*** *Restoring supraspinal control and thus voluntary movement uses multisystem neuroprosthetic training with a robotic support* ***C*** *Kinematics and EMG activity of anterior muscles during walk shows rat training importance to gain locomotion control.*

c - State of the art of interfacing devices used in this project

The commonly used implants for motor cortex recordings are commercial Utah arrays purchased from Tucker Davis Technologies© and Blackrock Microsystems© while MLR stimulation and recording were performed using Neuronexus© Michigan probes.

Signal quality and bioacceptance issues are impacting the stimulation interfaces at a lower scale compared to the intracortical sensing interfaces. However, it remains tricky to stimulate properly the lower motor-neurons of the spinal cord without provoking inflammation that would aggravate the SCI.

S. Lacour et Al., at EPFL, designed and micro fabricated some high-performance and highly bio-accepted spinal cord flexible stimulation implants based on PDMS with stretchable gold microelectrodes [29] The stimulation of skeletal muscles is performed with intramuscular thin copper wires designed for electromyography (*EMG)*. This invasiveness degree is low and does not impact muscle stimulation on a long term basis.

Our approach:

During this thesis, I designed and tried to improve implants that could benefit this project. Main designs were made to interface the motor cortex or the MLR. The *in-vivo* tests performed were always comparing the commonly used commercial implants (control samples) with improved custom implants.

More precisely, this thesis goal was to investigate how **new materials such as highly biocompatible graphene monolayer** [2] can be used to build implantable electronics that would **lower inflammatory reaction** and provide a **more reliable signal**.

In the next Chapter II, we will see how high quality graphene monolayers can be obtained, how it could benefit long lasting intracortical probes and, by extention, be useful for many neuroprosthetic and neurorehabilitation researches around the world.

1.3.2 Intracortical implants description

Intracortical implants use **MEA** to transduce the ECM potentials changes, dominated by spiking activity, into electronic current (explained in 1.3.4). The working distance between neurons and MEA sensors is critical for the quality of recorded signal as previously explained proximity effect.

This category of BMI is the most suitable for neuro-rehabilitation and neuro-prosthetics projects as it allows the harvesting of specific motor neurons signals, which is necessary for fine movement orders decoding.

As illustrated on Figure 14 next page, three kinds of penetrating implants exist today on the market with different specific qualities.

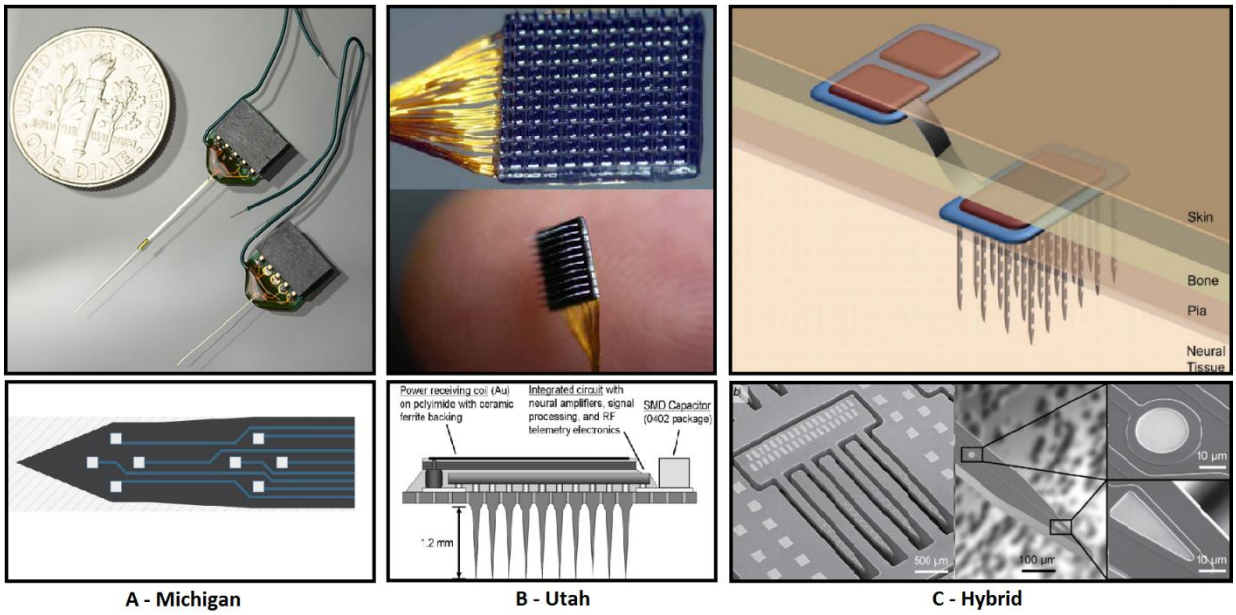

*Figure 14 - Penetrating implants technologies sum up showing the three main implant architectures, all based on silicon material. **A-** (Top) Neuronexus© commercial Michigan probes that resemble a long needle to penetrate the pia and the cortex. (Down)The 8 electrodes and recording sites at the end of the probe. **B-** Blackrock© commercial Utah Array which is an assembly of 100 insulated Silicon needles with uninsulated tip to record neuronal activity on the same level. **C-** Combination of the 2 architectures in a hybrid design from Wise et al., 2011* [57]

The Michigan probes: first penetrating array of sensors have been designed in the 70's in USA by Wise et Al. [58] and have been then improved to support several sensors and better insulation layer[59], [60]. They are qualified as Michigan probes and consists in a flat needle of SiO_2 covered silicon supporting an array of insulated electrodes paths terminated by uncovered round metallic microelectrodes which sense the surrounding neurons activity.

Their architecture is ideal to sense different layers of cortex or to follow descendant information between the cortex and the MLR.

Integration of graphene electronics in these devices is detailed on chapter IV.

Utah Array were designed in the 90's [61] to integrate more recording sites on a same penetrating depth. They consist in an array of insulated needles with uninsulated tip. This 3D design allows them to sense a lot of neurons at the same time on the same cortical layer, but makes them more invasive in comparison with Michigan probes. Horizontal CMOS integration make those electrodes array easier to process in large scale of around 100 recording sites[62].

Hybrid designed probes appeared recently [57], combining Michigan and Utah designs by 3D assembling many Michigan probes on a same implant and thus providing several depth and positions sensors. The high volume of this implant suggests a lower bioacceptance.

This category of BMI will be our tool of choice to test the opportunities offered by graphene in those devices improvements. Given their high invasiveness level, they suffer for a durability issue that is detailed in the next paragraph.

1.3.3 Limitations: invasiveness and long term failure

Nowadays, current electrodes array penetrating implants achieve motor cortex readings with high resolution but fail to perform chronic (stable in time) signal recordings [63]. The lifetime of these interfaces are both limited by their poor bio-acceptance and by the sensitivity of their electronics.

These drawbacks severely limit their use for SCI victims and thus prevent them benefiting from the recent progresses made in term of neurorehabilitation. Penetrating implants are among the most invasive techniques as they induce some destruction in the implanted tissue.

In particular, a traumatism in the central nervous system tissues, triggers an inflammatory reaction. The biological mechanisms behind this inflammatory reaction –i.e. the glial scar- and will be detailed later in this thesis (Chapter III - biocompatibility).

Briefly, the glial scar is a consequence of the implant invasiveness and consists in a strong inflammatory reaction called gliosis leading to a high concentration of reactive glial cells[3] around the implant site, creating a physical barrier (thicker than 50µm) between the motor cortex neurons and the micro-electrodes. The motor-neurons signals are thus moved away from implant sensors and recordings of their electric activity become flooded by surrounding noise (Figure 15A). The signal-to-noise ratio decreases as long as the glial scar is thickening, leading to a **detection failure** after a **few weeks** (Figure 15B).

In order to circumvent that issue, one must pursue ways to limit the development and establishment of the glial scar. Indeed, gliosis has the ability to stop when the implant is removed [64] but as long as an implant persists, it triggers perpetual immune system reaction and tissue inflammation because it is not well bio-accepted. It will thus provoke glial scar chronic establishment and thickening.

Prasad et Al. [63] have well described the evolution of the signal-to-noise ratio on a long term basis (Figure 15), highlighting the consequences of the gliosis on signal after several months. There is a total loss of signals and the implant cannot be used for rehabilitation, prosthesis control or other long term application anymore.

[3] Glial cells are part of neural tissues and provide nutrition and immune support to neurons. Whenever there is a lesion in the CNS, glial cells become reactive and have a defensive and healing activity, see chapter III for glial cells description

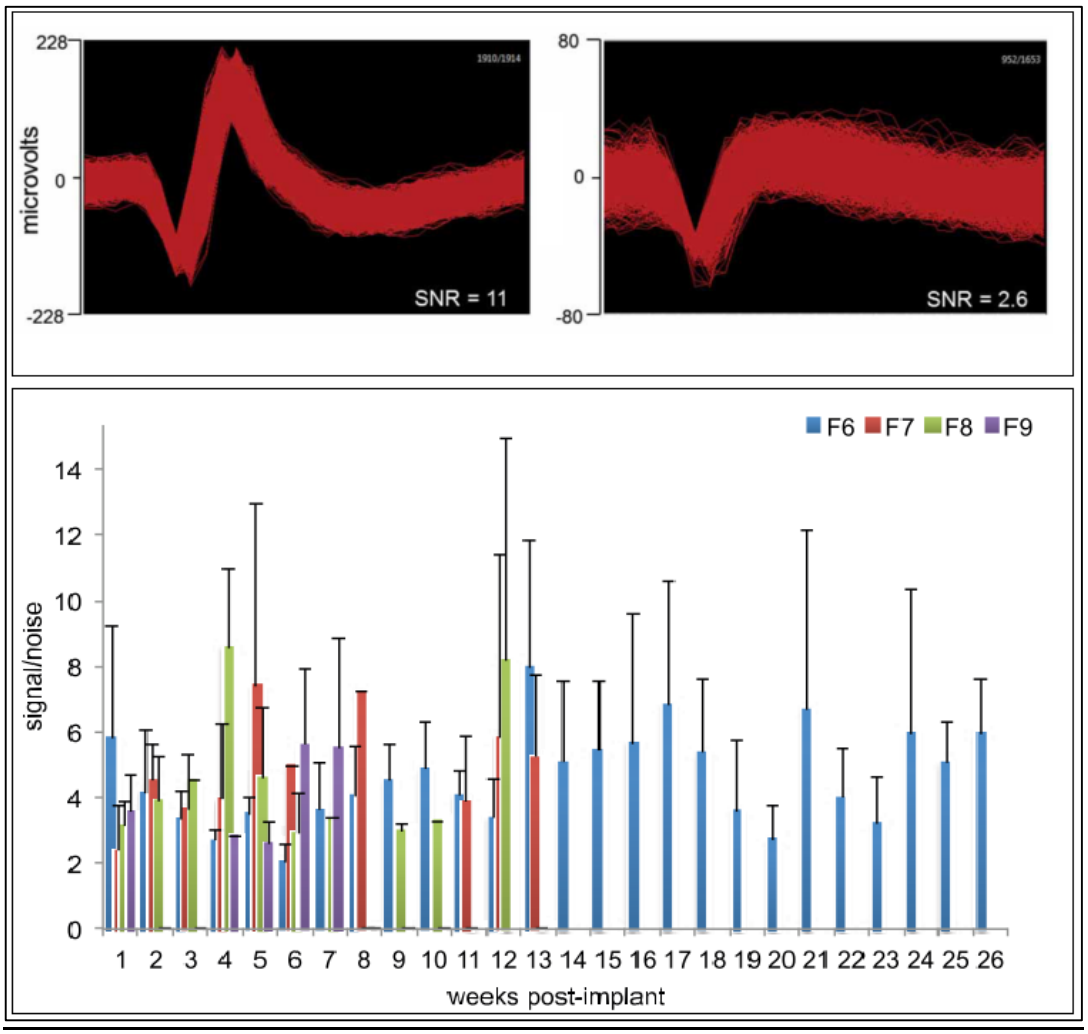

*Figure 15 – Penetrating implants invasiveness is responsible for their failure after few weeks: **A** Neurons spikes sorted and stacked on a 1.2ms period, recorded using an intracranial Utah array probe. The Left signal has a signal to noise ratio (SNR) of 11 whereas the right one exhibits SNR of 2.6 **B** SNR measurements were used to illustrate signal loss over time on a population of 4 rats F6,F7,F8 and F9; each color is a rat and we can clearly see that the probes in 3 over 4 animals do not provide any signal after 12 weeks. After Prasad et Al.*[63]

It is well known that the implant rigidity causes an even more important trauma in a tissue, resulting from the mechanical mismatch with the soft tissues in human body [65], [66]. Cells show the best affinity for their own rigidity similar substrates. The surface of the perfect implant should be soft and flexible as its surrounding tissue to be as invisible as it can get.

Connector's issues:

On a chronic timeline, flexibility of the connector is also an important point as it prevents perpetual damages due to **micro-movements** of the brain inside the crane and changes of blood pressure in the surrounding blood vessels[67]–[69].

Consequently, many new designs start to emerge using soft and flexible substrates instead of silicon to build the implants [70]–[73]. They yet need to be stiff enough to penetrate the tissues.

The last decade has shown the appearance of drug delivery to overcome the inflammatory reaction, using Neurons Growth Factors (NGF) and anti-inflammatory directly delivered on the implantation site with microfluidic [74], [75] or using bioactive coating [76] , that last option presents the advantage of improving the surface rigidity.

Our approach:

New materials: In order to address the poor lifetime of the today intracortical implants, this thesis has been focused on investigating the possible uses of graphene as a biomaterial that could benefits in the 4 following areas (Explained in Chapter II):

- Showing good electronic abilities,
- Allowing creation of flexible electronics,
- Being compatible with soft substrates,
- Allowing drug delivery functionalization.

1.3.4 Biosensors requirements

Penetrating intracortical implants are the only way to bring sensors in contact of active motor neurons and read the motor-cortex activity with unique neuron resolution in real time. For 40 years, microelectrodes (or MEAs) have been used, being now commercially available. Nevertheless, since few years, transistors sensors emerge allowing the reduction of the sensors size well below MEA at the micro or nanoscale.

a - Microelectrodes Arrays

In **MEA** biosensors (Figure 16) extracellular ionic currents supporting neurons activity are detected by differential voltage measurement between a micro-electrode and a **reference** electrode in the bath. A charge transfer occurs between the extracellular medium and the electrode surface, creating a **capacitive current** which is then amplified by the electronics setup. The ionic currents spread across a distance between cell and electrode -the **cleft** - which have a large influence on the extracellular voltage. We can define a cleft resistance R_c that will mostly depends on the distance and adhesion of the cell on the microelectrode sensor.

Microelectrodes arrays are alread investigated on flexibles substrates, using graphene as electroncis material to record extracranial activity by the mean of ECoG devices [77], [78].

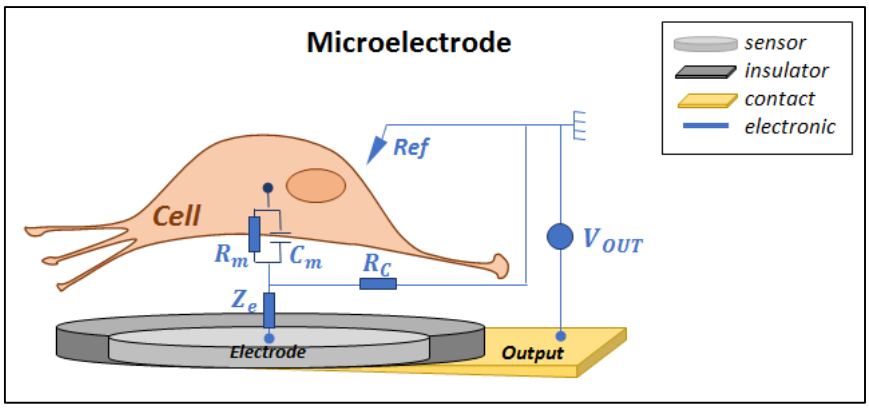

Figure 16 - Schematic of a microelectrode sensor coupled with a cell. Equivalent electrical circuit shows the capacitive and resistive compounds of the cell membrane potential (Rm, Cm), the impedance Z_e of the microelectrode interface and R_c the cleft resistance. Those parameters govern the extracellular voltage and the coupling to the sensor V_{out}.

b - Field Effect transistors (brief introduction)

Field Effect Transistors (FETs) bring in contact of the targeted medium the same way but with 2 contacting electrodes for the drain and source (Figure 17). A constant voltage needs to be maintained between the drain and source of the transistor. Extracellular electrical activity then **modulates the charge carrier's density** on the surface of the transistor and consequently modifies the current flowing in the sensor. Thus, by measuring current variations passing in a FET, we will be able to detect cellular activity around the transistor surface. The cleft resistance has also a large influence, because it lowers the amount of charges received by the transistor and thus the intensity of signal detected by the sensor.

The field effect transistors theoretical sensitivity, principle and operation modes are detailed in the next chapter II.

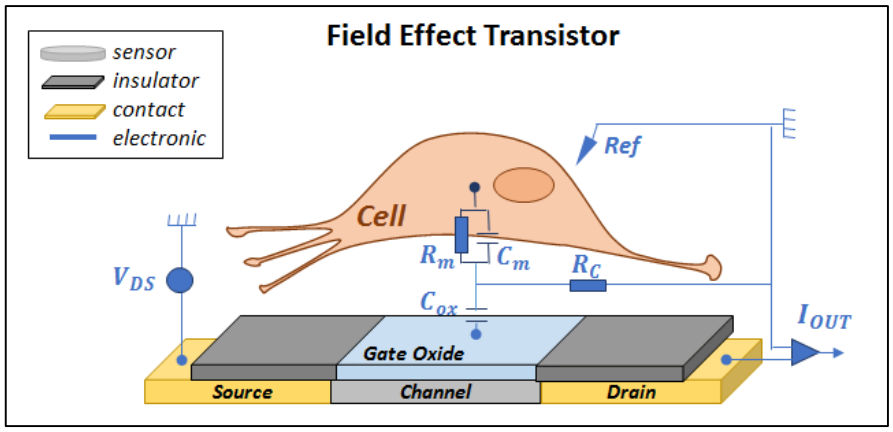

Figure 17 - Equivalent electrical circuit of a Field Effect Transistor biosensor as used to detect a neuron activity. Transistor is constantly polarized with a drain-source potential V_{DS} whereas extracellular activity will modulate the carrier density in the transistor channel through a gate oxide, and thus modifying FET channel, meaning Drain-Source current I_{OUT}, according to the extracellular activity. See next chapter II.

For the both MEA and FET sensors, a high R_c, through a strong cell – sensor adhesion, is important to obtain a good cellular activity recording. The sensors sensitivity and detection time are also paramount for good signal to noise ratio and sub millisecond recording. Microelectrode impedance Z_e will govern the sensitivity, whereas FET sensitivity will have a more complex expression detailed in the next chapter II about graphene.

1.4 Conclusion

Cortical neural systems are responsible for locomotion and adaptation to our environment through complex organization. Whereas neurons activity is governed by local microscopic events, most of their network activity can be red at the macroscale. Because of the subsystem organization of the brain, its activity can be detected by the mean of a large panel of Brain machine interfaces from the less binding to the most invasive.

Many medical applications depend on those brain-machine interfaces to improve patient's life quality, understand and treat diseases or injuries.

Locomotion is governed by multiple neuronal signals coordination. Consequently, most complete locomotion rehabilitation projects require the simultaneous sampling of multiple single neurons activities on a long term basis. Getting so close to microscopic phenomena implies high invasiveness and thus durability issues related to a chronic inflammatory reaction (Inflammation detailed in Chapter III).

This thesis investigates how graphene, a new material with promising properties, could improve the current implantable electronics and lower inflammatory reaction to provide a more reliable and long lasting signal at the single cell level.

In the next Chapter II, I detail graphene origins and properties and how I managed to produce large scale graphene for implants integration. I then detail how graphene could benefit to chronic use of intracortical implants thanks to its properties which make it a material which shows good detection abilities, allows creation of flexible electronics, is compatible with soft substrates and can undergo drug delivery hydrogel grafting.

II. Graphene for bioelectronics

Graphene is an atomically thin layer of carbon atoms which offers a promising platform for bioelectronics as it gathers for the first time in a single material many unique properties that we will detail in this chapter. It is a conductive, chemically inert 2D material that can be processed in many ways to build sensors on intracortical devices. Its integration in biosensing devices has already started and is raising many challenges that I contribute solving in this thesis.

This chapter will start with an introduction on graphene itself and the different existing graphene types with their specificities. Then, I will explain the properties that could benefit in biosensor fabrication and how I managed to test them.

In a second section devoted to the synthesis and integration of graphene, I will discuss quality of graphene and process reproducibility required to interface nervous tissues with a good bioacceptance.

Finally, aiming at an in vivo test of graphene bioelectronics interfacing, I will develop the characterisation of locally produced graphene and introduce the solutions developed in this thesis to integrate graphene in flexible devices and to coat 3D micro fabricated biomedical devices.

CHAPTER II - TABLE OF CONTENTS

2.1 Material description

Graphene is a 2D material, a flat crystal that has a honeycomb structure made of carbon atoms and that is highly conductive. Its periodic hexagon rings tiling can be seen as a polyaromatic compounds (technically a polymer of benzene).

Graphene is a monolayer of graphite and thus belongs to the family of pure carbon materials among which are also diamond and graphite. It is one of the few allotropes of carbon based on sp^2 hybridization, a characteristic shared with carbon nanotubes and fullerenes. Graphene is the precursor of all the graphitic forms (Figure 18): In a 3D graphite crystal, graphene layers are Van der Waals coupled together, stacking one on top of each other. For a 1D nanotube, a graphene sheet is rolled up as a tube whereas for a 0D fullerene, it has a sphere geometry thanks to the alternance of pentagons and hexagons. Each of these materials have a specific atomic organization. While diamond is a tetrahedral structure of carbon atoms, where each atom is linked to 4 other ones, in graphene, each carbon atom is linked to 3 neighboring atoms. Carbon atom having 4 valence electrons, graphene structure releases one valence electron per carbon atom which contribute to the formation of π stacks. Those π orbitals will then lead to a delocalized electron cloud within the sp^2 plane, providing very high electron mobility and conduction properties to the graphene structure.

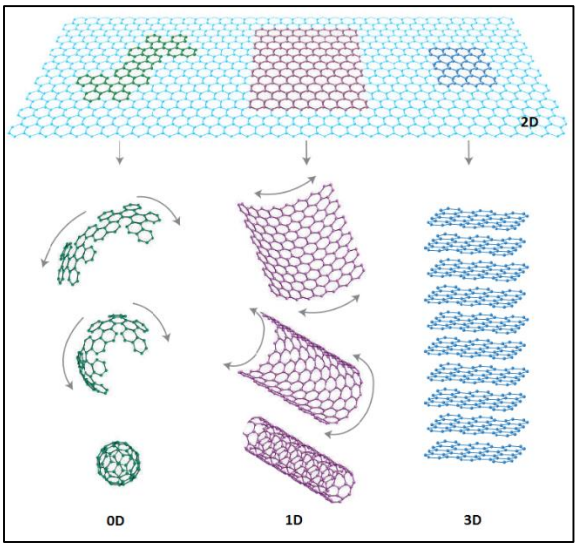

Figure 18 – Graphite materials are all based on different conformations of graphene foils: 2D Graphene is the elementary brick of following graphitic forms: 0D fullerenes, 1D nanotubes and 3D graphite, which is a stack of 10 or more graphene sheets. After [79].

Although graphene was theoretically described long ago (1947) [80], it was yet the last member of the nanocarbon family (Figure 18) to be isolated in 2004 by A. K. Geim, K.S. Novoselov and their co-workers at University of Manchester [1], [81]. By extrapolation of the

consideration that the melting temperature of thin films were proven to decrease with their thickness [82]–[84], 2D crystals were predicted to be thermodynamically unstable.

However, Geim and Novoselov proved that isolated continuous 2D crystals can be isolated at the crystal level because they are quenched in a metastable state. Strong carbon-carbon sigma bonds ensure robustness against thermal fluctuations and prevent crumpling in the third dimension [85], allowing a gain in elastic energy and suppression of thermal vibrations. Twelve years of active research have led to a tremendous number of publications and first industrial uses of graphene are now starting thanks to mass production techniques availability [86].

2.1.1 Electronic properties

a - The graphene exception in electronic transport

In order to understand the electronic properties of graphene, one has to consider that the honeycomb lattice structure is not by itself a Bravais lattice, meaning that every atom in the crystal are not equivalent. Indeed, there are two distinct environments for graphene carbon atoms.

In Figure 19, we present the **two Bravais lattices** respectively composed of the intertwined networks of respectively A and B atoms. Both create their own triangular Bravais lattice shifted to one another. These two distinct lattices are responsible for the very unique graphene's wave propagation properties: A and B sublattices energy bands for charge carrier intersect at zero energy near the edges of the Brillouin zone [87].

The **π electrons** in graphene form an ideal 2D system: a single atom thickness with π and π * non-interacting states. The π* form the positive energy conduction band whereas π states form the negative energy valence band, and those two bands intersect at six points called Dirac or neutrality points (Figure 19), that can be reduced to a pair of independent points K and K'. Graphene can thus be called a **zero gap semiconductor**, thanks to the orthogonal π and π* non- interacting states allowing the conduction and valence bands to touch. The dispersion relation of charge carriers is analogous to the dispersion of photons: $E = c\hbar k$ with c the light velocity and k the carrier wave vector.

In graphene, electrons interact with the periodic potential of the two Bravais sublattices A and B, allowing the Hamiltonian description of the structure to be written as a relativistic Dirac Hamiltonian as:

$$\boldsymbol{H} = v_F . \hbar . \boldsymbol{\sigma} . \boldsymbol{k}$$

v_F being the graphene Fermi velocity and σ the spinor-like wave function arising from the fact that there are two atoms in a unit cell. Defining a pseudospin that corresponds to the hopping of the electron between A and B leads to the description of electrons in graphene as relativistic particles of energy E with a mass m, velocity c and momentum p:

$$E = \sqrt{m^2.c^4 + p^2.c^2}$$

Electrons in graphene have a linear dispersion, giving birth to new low energies quasiparticles called massless **relativistic Dirac fermions** of energy. Graphene density of states increases linearly with energy. Electrons in graphene behave as massless Dirac particles. For all those reasons, graphene exhibits unique transport properties, the non-scattering nature of its surface allowing a very high carrier mobility, with carrier's velocity of $v_F = 10^6\, m.s^{-1}$ providing ballistic transport on tens of micron scale [88], [89].

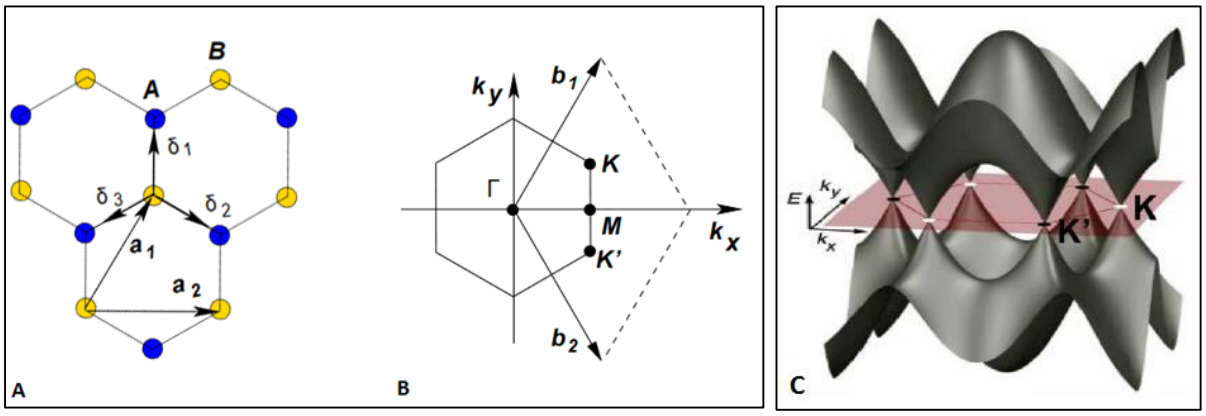

*Figure 19 – Its crystalline parameters provides peculiar band structure of graphene: A Graphene is a honeycomb carbon lattice that can be decomposed in two distinct Bravais lattices, one composed of similar environed A atoms in blue and the other composed of similar environed B atoms in yellow, of lattice unit vector a1 and a2. **B** Corresponding Brillouin zone showing the Dirac cones localization at K and K' points. After* [90]. ***C** the graphene 3D band structure. Graphene is a zero-gap semiconductor: valence and conduction bands are intersecting at zero energy in two points K and K' of the first Brillouin zone. After* [91].

Graphene is defined as **one or two layers of carbon atoms** organized in a honeycomb crystal lattice that has the electronic spectra of a zero gap semiconductor, with the valence band touching the conduction band.

Compared to commonly used materials in electronics, graphene can be classified as a semimetal when we pile up several graphene foils to delocalise conduction electrons, or a zero gap semiconductor when in its 2D crystal form.

b - Graphene as an active material for transistors

A **field Effect device** is a circuit in which a current flowing in a conductive channel can be modulated with an electrostatic field. A semiconductor-based Field Effect transistor (FET) is composed of a channel and two electrodes, a **drain** and a **source**. The channel conductance, will be modulated by the **gate**. The gate and the channel will be isolated with a barrier, generally an oxide (Figure 20A). The standard gating is made in back-gate mode through back oxide (Figure 20C). An alternative which consists in front liquid gating is explained in the next paragraph.

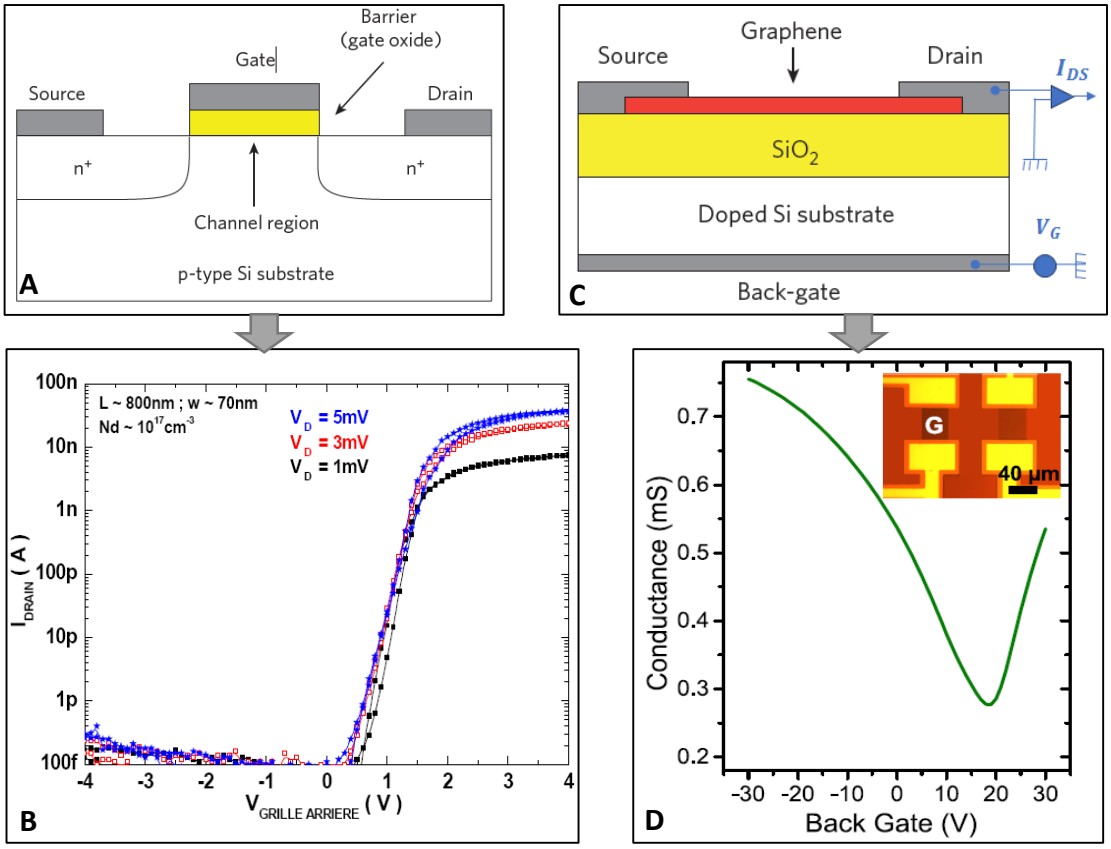

*Figure 20 – Comparing Si MOSFET with Graphene-FET with cross-sections and conductance curves:. **A)** When the voltage applied between source and gate electrodes exceeds a threshold voltage, a conducting channel is formed and a drain current I_{DS}, flows. The length of the channel is the gate electrode length; the thickness of the gate-controlled channel region is the depth to which the electronic properties of the semiconductor are influenced by the gate. After* [92]. ***B)** The transconductance is extracted from the curve $I_{DS}(V_G)$, for several back gate voltages on a 800x70nm² Si nanowire FET (From* [93] ***C)** Back gated G-FET with widely exposed graphene 2D channel in red. **D)** The GFET transconductance is ambipolar. Here measured for a 40x60µm GFET built on a 285nm silicon oxide on silicon, contacted with 5nm Ti and 45nm Au electrodes and measured in air at $V_{DS} = 75\ mV$. (F.Veliev, Institut Néel).*

The slope of the curve $I_{DS}(V_G)$ is the transconductance g. (Figure 20B&C).

The sensitivity of a transistor is given by

$$S = \frac{g}{V_{DS}} = \mu . C_{ox} . \frac{W}{L} \ ,$$

Where W the width and L the length of the channel. μ is the carrier mobility of the channel material and C_{ox} the gate capacitance per unit area.

The 2D dimension of graphene with no bulk avoid charges screening and thus favorites field effect detection. The electron cloud on its surface provide a very **high carrier mobility** and high **interfacial capacitance** to graphene and thus **promises great sensitivity**. The dimensionality dependence allows a better sensitivity with length reduction of the graphene channel. Graphene is a semi-metal –i.e. a zero gap semi-conductor- in which conductance can be modulated with an electrostatic field. The zero bandgap of graphene limits on-off current ratios I_{on}/I_{off} compared MOSFET. A comparison of these values with standard MOSFET is given in Figure 21 and shows GFET superior mobility, interfacial capacitance and transconductance, but limitations in term of cutoff current and a drawback in the transconductance shape: GFET are ambipolar and thus have a **neutrality point** (see Figure 20D).

	μ (cm^2/Vs)	$C_{interfacial}$ ($\mu F/cm^2$)	g (mS/V)	I_{on}/I_{off}	R_{square} (Ω/□)	Type
MOSFET	**450**	**0.35**	**0.2**	**1.00E+08**	**25**	**Unipolar**
GFET	**4000**	**2**	**5**	**<10**	**500**	**Ambipolar**

Figure 21 - Transistors properties shows GFET advantages and drawbacks: GFET are more overriding in term of mobility, interfacial capacitance and transconductance but shows limitations in term of cutoff current, sheet square resistance and their ambipolar transconductance with a neutrality point and a polarization change. Adapted from [94], [95]

In order to measure and trace the transconductance g, the charge Q is modulated applying a gate voltage Vg and gives a capacitive coupling as:

$$Q = V_g . C_{ox}$$

For a SiO_2 back gated transistor with an oxide capacitance C_{ox}, induced surface's charge carrier concentration per Volt is given by:

$$n_{carrier}/V_g = \frac{\in_{Ox} \in_0}{d.e} \sim 7{,}56.10^{10} cm^{-2}.V^{-1}$$

With d being the oxide gate thickness, e being the elementary charge and $\in_{Ox}$ the dielectric constant of SiO_2.

In order to extract mobility and charge density, one must take into account elastic and inelastic scattering mechanisms [96]. However, we use a fitting technique that approximate efficiently those parameters [97] and allows good evaluation of mobility.

Conductivity $\sigma_{conduct}$ is depending on charge carrier concentration $n_{carrier}$ and the residual carrier concentration n_0 as the following quadratic mean:

$$\sigma_{conduct} = \frac{1}{R-R_C} = \sigma_{sheetconduct.}\frac{W}{L} = n.e.\mu.\frac{W}{L} \; with \; n = \sqrt{n_0^2 + \left(n_{carrier}.\left(V_g - V_D\right)\right)^2}$$

The residual carrier density n_0 and the impurities related carrier density n_{imp} are related to the minimum conductivity according to the following expression [98]:

$$n_0 = \sigma_0 * \frac{h.n_{imp}}{20.e^2}$$

When integrated in a device, **charged impurities** adsorbed bellow or above the graphene surface generate charges fluctuations that can be seen as a random 2D potential that locally shift the chemical potential of graphene [99]. The typical amplitude and wavelength of these fluctuations have been assessed using scanning probe electrometers [100] and shown to be of around 10^{11}cm-2 with electron-hole puddles of about 1 micron diameter. (Illustrated on Figure 22).

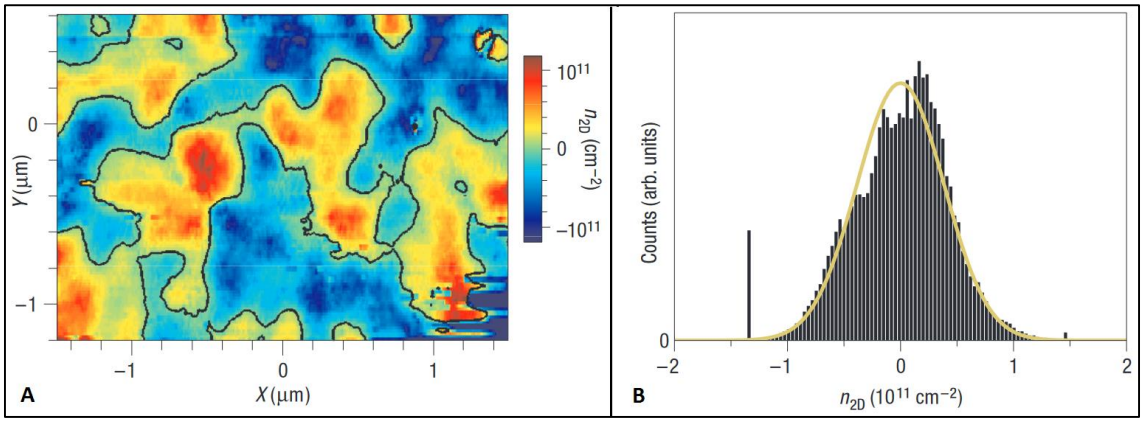

Figure 22 - Spatial density fluctuations of charge in graphene correspond to electron/hole puddles: ***A)*** *Color map of spatial carrier density variations in a graphene flake extracted from surface potential measurement with a scanning single electron transistor. Blue puddles correspond to holes and red puddles to electrons, whereas the zero density are the black contour.* ***B)*** *The histogram of the density distribution corresponds to a Gaussian distribution, which fit extraction gives a density fluctuation of the order of* $\Delta n_0 = \pm 3.9x10^{10}cm^{-2}$. *From*[100]

Graphene transistor resistance *R is then expressed as:*

$$R = \frac{L/W}{e.\mu.\sqrt{n_0^2 + \left(n_{carrier}.\left(V_g - V_D\right)\right)^2}} + R_C$$

With R_C the contact resistance of the graphene transistor ($R_C = 0$ with 4 points measurement) V_D corresponding to the charge neutrality point or Dirac point of the transistor, n_0 the residual carrier concentration and $\frac{W}{L}$ the aspect ratio of the transistor channel, with W its width and L its length.

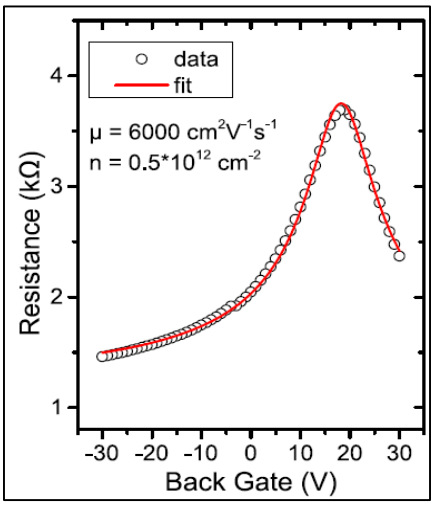

Figure 23 - Fitting channel resistance allows extraction of mobility μ and residual carrier concentration n_0 values A G-FET is built and its transconductance measured, plotted as resistance curve and fitted according to previous R expression, known values and incremental finding of μ and n_0 values that are of the same order than previously found (From [101]*)*

We can extract mobility and residual carrier density of our transistor by plotting, from the transconductance, the drain-source resistance as a function of the gate voltage.

We fit the obtained curve according to known parameters W, L, R_C and C_{ox} to find corresponding mobility μ and residual carrier concentration n_0 with an incremental research of best values using a fitting program on Igor© software. On Figure 23, the fit allowed us to find a mobility of 6000 cm^2 /V/s which is in good agreement with values typically found in CVD graphene devices [102] and n_0 equal to 5. 10^{11} cm^{-2}, a value consistent with electron-hole puddle amplitude (figure 22).

We will use and detail this fit technique in next Chapter III to assess a graphene coating influence on charge density and mobility.

c - Graphene transistor as a biosensing device

Graphene transistors can have surface-exposed channels that lead to very promising biosensors [2], [103]. Indeed, **charge carriers are readily on the surface** and therefore can be directly influenced by charged elements without any screening. This is in stark contrast compared to the previous generation of biochemical biosensors based on silicon nanowires that do have a "charged crust" of oxide that do impact their detection performance by partially screening the charge elements to be detected. Three types of devices can be made for biosensing (as a reminder from 1.3.4): MEA, G-FET for direct charge detection and G-FET coated with redox functionalized layers to make the transduction between a biochemical reaction and the associated charge modification. Ultrasensitive electrochemical affinity can be tuned for that purpose[104].

Graphene FETs have been previously used to detect cellular (cardiomyocyte cells) activity [6]. Several recent advances demonstrate graphene transferability on flexible materials like polyimide to perform reading of neuronal activity using Solution-gated Graphene Field-Effect transistors (SGFETs) [105], [106]. Such biosensors showed **robustness** when bending thanks to graphene flexibility (see 2.1.1e -) with a bending stiffness close to that of phospholipidic bilayer forming the membrane of a cell [3]. Graphene very high electron mobility compared to conventional semiconductors leads to SGFETs with a high transconductance and consequently a **high sensitivity**.

In a SGFET, the drain-source current will be modulated by the gate potential through an interfacial capacitance (see Chapter 1.2.4). The gate potential refers to the global charge on the device. This charge can be associated to a biologic element on the channel surface or to a biochemical redox reaction that will tune the transistor sensitivity to specifically react to a given compound in the solution. The transconductance of the transistor has to be known to deduce cell activity values with accuracy. Whereas previously described silicon based transistors use a gate oxide to create the interfacial capacitance, graphene transistors are either back gated trough the insulation oxide or front gated by liquid gating in solution gated FETs.

For Solution Gated FETs (SGFETs), the applied gate voltage drives ions to the surface of the graphene channel, forming a very thin Electrical Double Layer (EDL) that acts as a nanoscale interface capacitor which replace the gate oxide. The **Electrical double layer** is a thin diffusive layer that is directly in contact with graphene surface.

This thin layer will have a higher capacitance than a conventional gate oxide, it will increase the incidence of small ionic changes occurring in the liquid, conferring graphene transistor a very high gain [107].

Using front liquid gating instead of back gating will thus change the oxide capacitance C_{ox} in an electric double layer capacitance C_{EDL}. The relation between those two capacitance is given by the conductance ratio between Liquid Gate (LG) and Back Gate (BG) regimes.

Assuming a constant mobility μ of the transistor for both regimes, we can express:

$$C_{EDL} = \frac{\partial\sigma/\partial V_{LG}}{\partial\sigma/\partial V_{BG}} * C_{ox}$$

Previous measurement of this electric double layer capacitance were made by simultaneous back gating and front liquid gating a GFET device built on a 285nm silicon oxide in order to compare liquid gating influence on transconductance (Figure 24C). Due to the thinness of the EDL, around 1nm, the gate capacitance is higher than for back gate through 285nm SiO_2, and thus require lower gate voltage to induce the same charge carrier density. We then found a value of $C_{EDL} = 0.78\ \mu F/cm^2$. A literature comparison confirms the coherence of this value [107]

As illustrated on Figure 24B, the cellular activity acts as a gate and the EDL acts as a gate dielectric. Graphene being a 2D material, it has only 2 surfaces and no bulk, in consequence, the electron gas of graphene will be directly exposed to the biological medium and allows a very good coupling between sensor and cells, thus providing a better signal to noise ratio than with conventional oxide gated silicon transistor [6]. The EDL acts as a **layer of bio-recognition** composed of extracellular ions (Figure 24A) among which those resulting of cellular activity and a layer of ions migrated on top of graphene thanks to the applied potential V_{DS} [108].

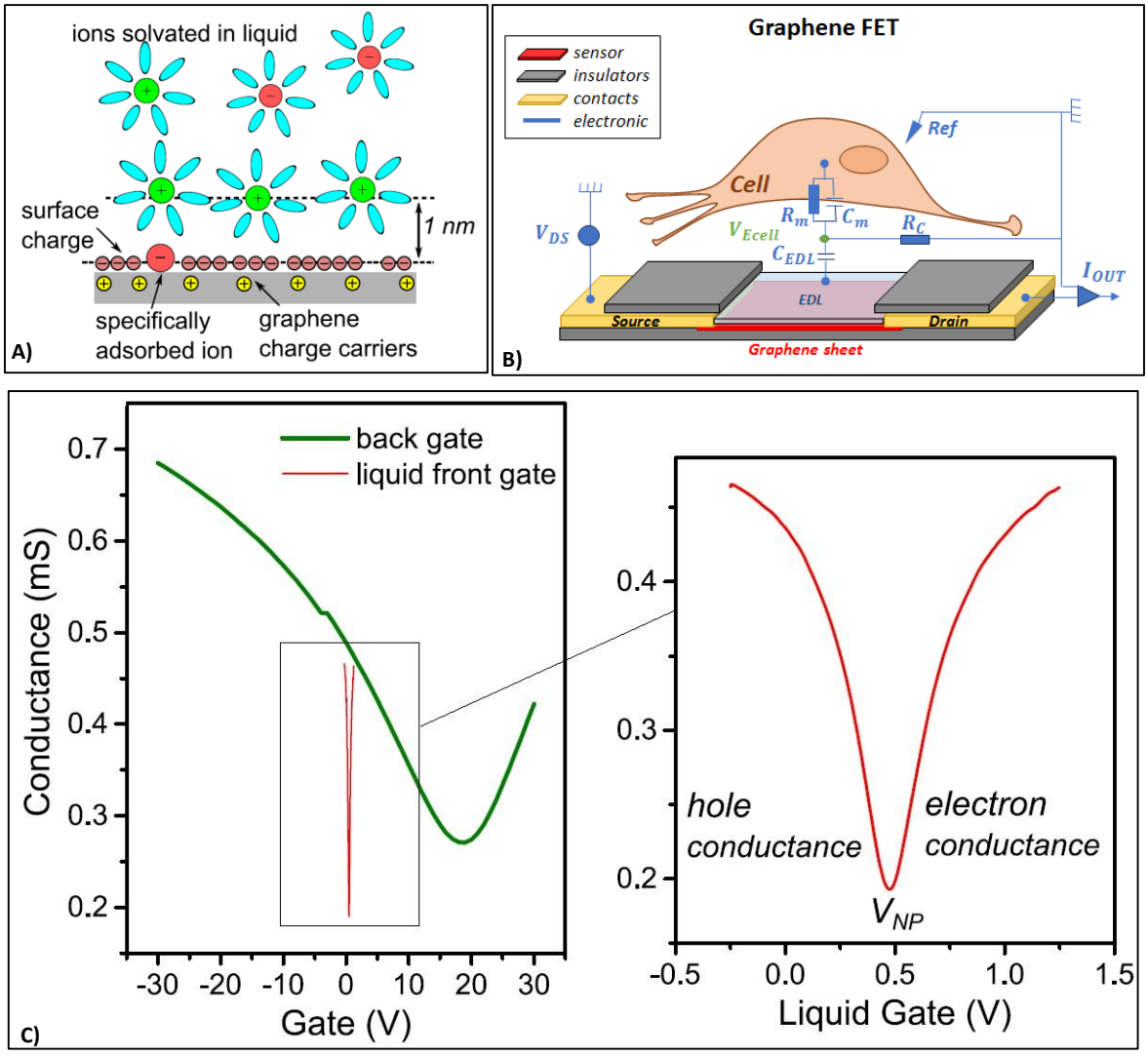

Figure 24 – Representation of the electrical double layer and our typical biosensor based on SGFET with equivalent electrical circuit: ***A)*** *Schematic of the 1nm thick electric double layer that forms at graphene-electrolyte interface* ***B)*** *A constant drain source potential V_{DC} is applied between drain and source contacts through the graphene sheet. The Electrical Double Layer (EDL) is formed at the graphene/ionic solution interface and act as a gate oxide. Extracellular activity V_{Ecell} depends on the neuron activity, its membrane resistance $_{Rm}$ and capacitance C_m and the cleft resistance R_c. V_{Ecell} modifies carrier density on top of the graphene sheet, in the EDL, and thus changes the drain source current I_{OUT}. C) Transconductance curves obtained by back gate and liquid front gate, with a close view on the liquid gate.*

This possibility to use graphene to build high sensitivity robust biosensors leads us to another very interesting graphene property: its cytocompatibility.

d - Graphene cytocompatibility

Graphene has been demonstrated in previous work [109] to be cytocompatible by favoring neurons adhesion and improving neuronal network development in vitro.

Cytocompatibility is defined as the affinity that cells have for a material by their tendency to attach, grow and differentiate when cultivated on its surface.

In vitro cytocompatibility studies can predict a tissue behavior when in contact with the tested material or surface. However, because in vitro is processed with neurons cells only (monoculture), the complexity of the tissue with its own immune and nutritive system (glial cells – see chapter III) might cause differences between in vitro cytocompatibility and in vivo bioacceptance.

In vitro cells culture are generally processed on glass slides coated by adsorption of adhesion polymer to favor neurons attachment (in the same manner we detail in 107). Bare graphene has been shown by our team to allow neurons adhesion without using these adhesive polymer[110].

We were able to verify this result with our locally produced graphene (Figure 25) thanks to in vitro tests by cultivating primary hippocampal neurons on the graphene monolayers.

Figure 25 shows that **bare graphene** -i.e. without surface functionalization- promotes adhesion, growth of neurons and further establishment of neural network, in comparison with bare glass on which neurons cannot survive (Figure 25).

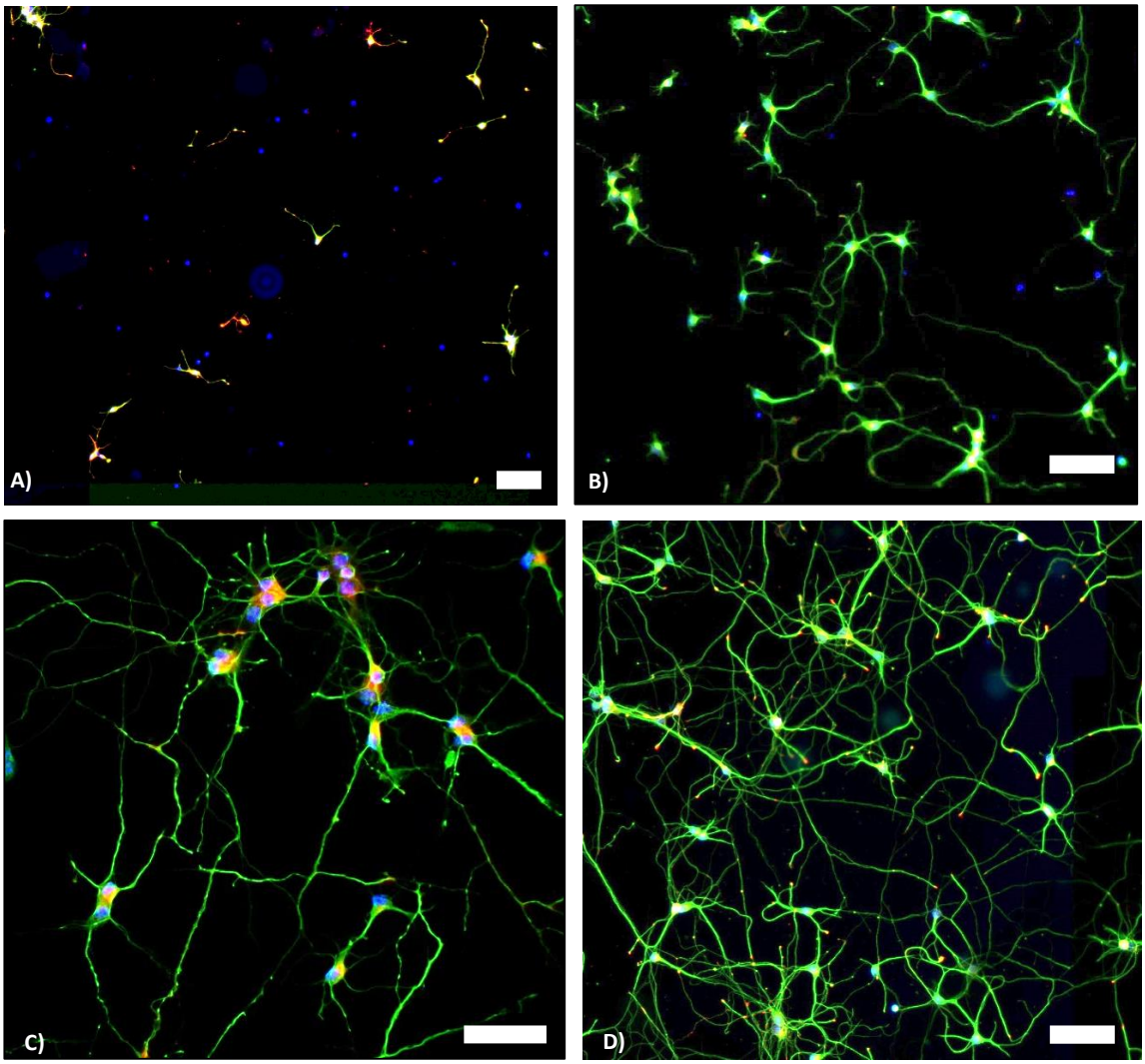

*Figure 25 – Graphene cytocompatibility proved by In vitro assessment: Primary hippocampal neurons (extracted from mouse embryos E16) were seeded on bare (uncoated) glass (A) and bare graphene (B), and **on** poly L-Lysine coated graphene transferred on glass (after 2 days in culture) (C) and graphene on PDMS films (D). Immuno-fluorescent staining labels the microtubules of the cytoskeleton (green) and the soma (blue). Red markers label the actins filaments. 4 days in culture. Pictures show the adhesion of fragile neurons on bare graphene and the positive impact of graphene on the adhesion and neuritogenesis. As PLL slightly improved adhesion, the use of a soft substrate enhance mechanical mismatch of the tissue and consequently provided a suitable surface for neurons growth. Scale bar are 100µm.*

Moreover, conventional poly-L-lysine coating of graphene on glass further enhances the adhesion and growth of neurons on the substrate (Figure 25C). These two results show that graphene does not exhibit cytotoxicity for primary hippocampal neurons in cultures, thus graphene can be considered as a **bio-accepted material**.

Our group previously demonstrated [110] the high affinity of neurons for our graphene. We showed that the high crystalline quality of graphene is a requirement for high

cytocompatibility and is preserved despite of the strong attachment of neurons. These results were obtained only with high crystalline quality of graphene, which was assessed by Raman spectroscopy.

Graphene can be used to offer a “matrix” platform -i.e. a scaffold to promote and guide the growth of neural cells. This result has been reproduced with several substrates such as soft, transparent and stretchable PDMS substrate.

Figure 25 shows our ability to transfer graphene on elastomer (PDMS) layer and culture neurons on top. We have extended this transfer on PDMS in order to further increase the neuronal affinity of the artificial interface.

Indeed, cytocompatibility is improved by **lowering surface Young modulus** and thus reducing mechanical mismatch between cells and interfacing material. A good mechanical compliance is indeed paramount to reduce adverse reaction of neural interfaces [111], [112].

e - Graphene mechanical robustness and flexible electronics:

The sigma carbon-carbon bond is one of the most stable in nature. It gives graphene exceptional mechanical properties: sufficiently robust to withstand strong capillary force in liquid and not break under its own weight, leading to exciting novel application in liquid [113].

It has an exceptional in-plane stiffness (in plane Young modulus of 1 TPa, comparable to diamond) and can undergo elastic deformation to an important extend of around 25% [114]. Graphene can in consequence be used on flexible and soft substrates as a conductive material, opening great perspectives for flexible devices and screens. Plastic bioelectronics is a rising research field as it could provide soft, stretchable and mechanically conformable devices to interact with biological systems using implantable or wearable devices[115].

Many graphene based devices on soft substrate have been reported so far [116], [117] as well as robust graphene 3D assemblies [118] and I also tested the ability to work with soft substrates in a perspective of **lowering our future implants stiffness** with different flexibles materials like PDMS, Parylene and polyimide. These studies will be detailed in chapter 4.

f - Graphene optical properties

Graphene is optically **transparent** with a white light transmittance of 97.7% for a single layer[119]. Even though sp^2 carbon strongly absorbs light, at the monolayer scale, this absorbance remains modest (2.3%) and is by far compensated by the exceptional electrical properties which give graphene interesting performance for transparent and flexible electrodes. This 2.3% absorption of light per graphene layer is a very important property that

allows the easy characterisation of the graphene state and number of layers after transfer on a silicon oxide substrate, as soon as the oxide thickness is well known and controlled (Figure 26). Indeed, 90 and 285nm silicon oxide thickness on silicon show the best contrast when observing graphene due to light interferences [120].

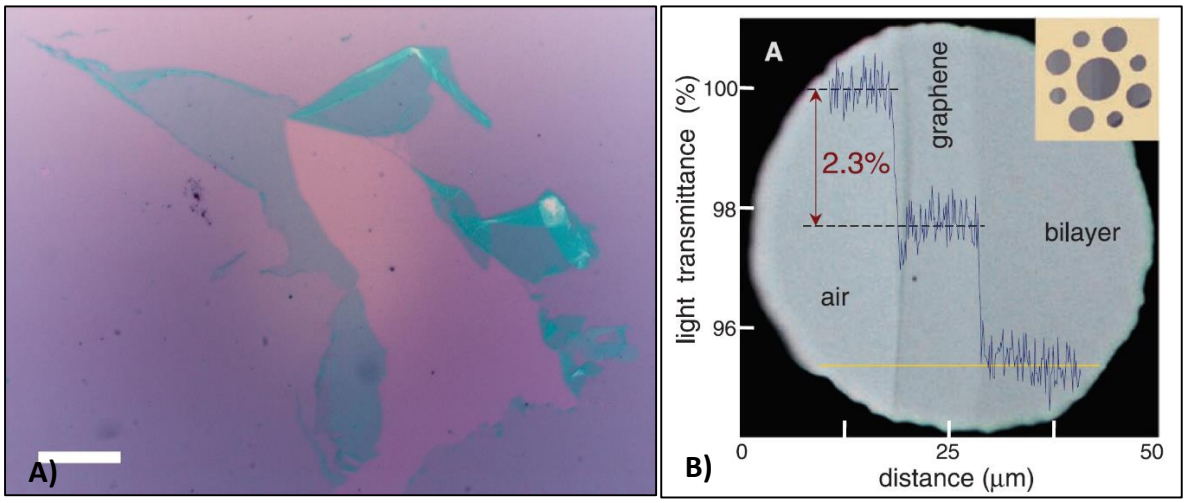

Figure 26 –Optical microscope photography shows graphene transparency relative to the number of layers: ***A)*** *here one of our graphene sheet shredded on a 285nm oxide thick SiO_2 substrate. The shredding in the monolayer shows the contrast difference with bilayer and 3- layers folded graphene parts. Scale bar: 40µm.* ***B)*** *Suspended graphene on a 9 holes matrix (on top right hand corner) (illustrates 2.3% absorbance per layer. After* [121]

Associated to the high graphene conductivity and flexibility tolerance, graphene optical properties open the way to flexible electrodes in displays, touch screens etc… with flat absorbance spectrum (perfectly "gray" material) it could replace commonly used ITO that has a 90% maximum transmittance only and is rigid, expensive and brittle.

In terms of biological applications, transparent device are welcome in vitro as they are compatible with **inverted microscope**, allowing see-through cell growth monitoring. In vivo, more and more researches are using optogenetics to control biological behaviour of a tissue in situ during the experiments. **Optogenetics** (more details in chapter IV) use a stimulation light to trigger activation of special light sensitive proteins in the targeted cells. In the brain those proteins will modify the cell membrane ion channels permeability, triggering action potentials in the stimulated area. The quest for implants coupled with optogenetic systems rises an interest in transparent materials such as graphene to further enrich neural bioelectronics interface [122], [123]. For example, one could think of a graphene-covered optical fiber to couple both functionalities on a single needle probe.

2.1.2 Graphene types

a - Monolayer or multilayer graphene

Graphene is defined as one or two layers of carbon atoms. Multilayers reduce electron mobility and induce local doping [124]. The electronic structure become the graphite's 3D one above 10 layers of stacked graphene [125] as field effect loose little by little its efficiency due to graphene self-screening upon thickening of the layer.

Figure 27 shows monolayer (1L), bilayer (2L) and trilayer (3L) of graphene obtained with layer by layer successive transfers, performed in liquid phase, on SiO_2. Interesting gain in electrical conductance of the film can be obtained by such stacking as defect in one layer can be shunted by the others. A resistance of about 100 Ohm/square (without doping) is obtained with 4 stacked layers that retain 90% optical transparency.

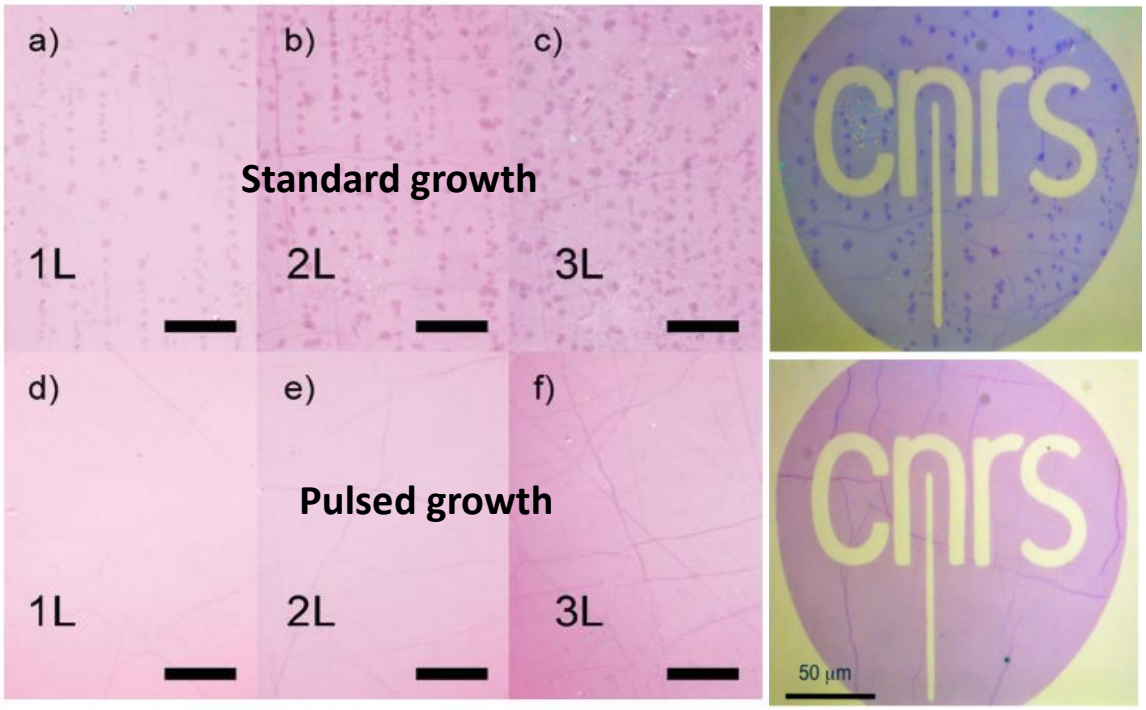

Figure 27 – Comparison between stacks made of piles of continuous CVD and pulsed CVD graphene: Optical microscope photography shows monolayer (a&d) transferred graphene on oxidized silicon. And multilayers obtained by successive transfers (b, c e and f). Top pictures (a,b&c) show standard CVD growth whereas bottom ones show pulsed growth graphene. Pulse growth allows removal of multilayer patches and is detailed in next paragraph. Right pictures show corresponding graphene patterned with CNRS logo. Z. Han, Institut Néel-[126].

The main goal of this thesis being the fabrication of graphene biosensors with a preserved high crystalline quality, a good mobility and a low impedance, I need to use high quality

graphene. It is then important to choose a fabrication process that leads to continuous monolayer graphene on size exceeding the neuron size.

b - Overview of graphene production techniques

The graphene forms a peculiar nanostructure because it is **macroscopic** along two directions and **sub-nanometric** along the third one. Transferring it in a routine fashion from its growth substrate to a host substrate while keeping its structural integrity and cleanliness remains a challenge. Indeed reproducibility of the process is very hard to achieve depending on the techniques. Nowadays, several methods are available to produce graphene. One must choose the production method to adopt in order to optimize, cost, crystalline quality and throughput (Figure 28).

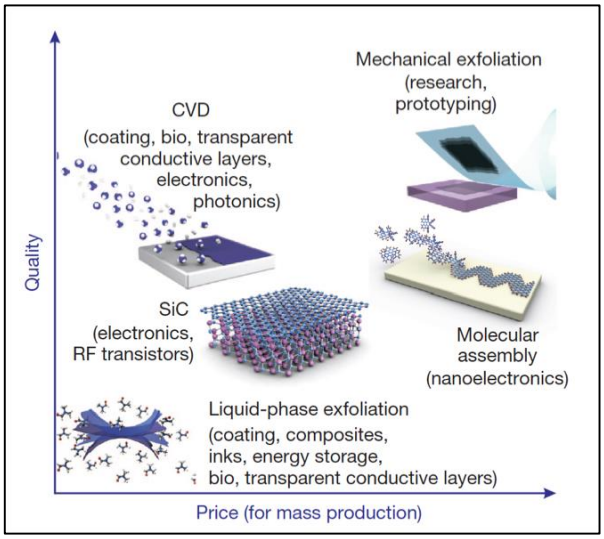

Figure 28 - Method of graphene synthesis are classified in function of their production cost and the quality produced; Depending on the application targeted, one must choose the preferred method in term of surface and quality as much as cost. Note that there is a sweet spot occupied by the CVD techniques which enable mass production of polycrystalline graphene with rather good yield. From [127].

First graphene sheets ever characterized were mechanically exfoliated from graphite crystal [1]. **Exfoliation** consists in peeling off a graphene sheet starting from a graphite crystal on a substrate, generally SiO_2. The experimentalist uses a scotch tape to compete with the weak Van der Waals forces that rule the adhesion between graphite sheets, and break these bonds. Mechanical exfoliation remains the easiest and most low cost technique but can only produce small graphene flakes of around 10 µm [128] in an unrepeatable way. Once the graphite crystal is mainly peeled off from the SiO_2 surface, the single layer flakes are easily identified using contrast difference with an optical microscope. They can then be isolated and contacted for electrical characterization or another purpose.

Some other techniques use liquid phase and chemical exfoliation, using ultrasounds to exfoliate from graphite oxide, followed by a hydrazine reduction. However, this method does not completely remove oxygen from the structure [129].

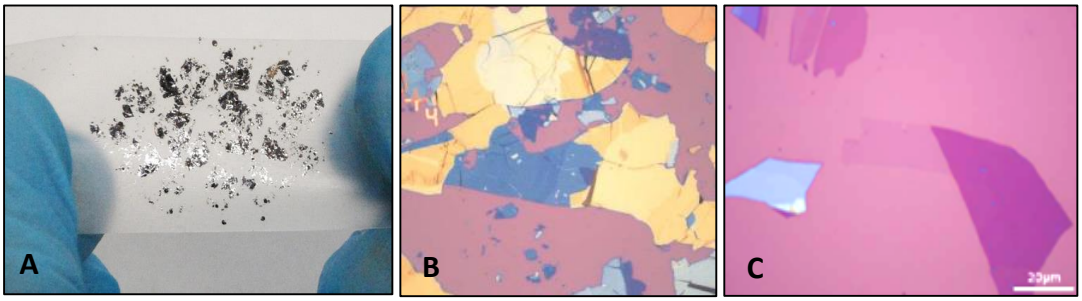

Figure 29 - Step by step exfoliation of graphite crystal provide small flakes of variable size en number of layers. A Scotch tape shows graphite layer removed from B the silicon oxide substrate on which graphite has been spread show final resulting graphene layers.

Graphitization from SiC: A second graphene synthesis method is the graphitization from a silicon carbide (SiC) substrate. SiC is easily available in great quality as it is used as a semiconductor in microelectronics. SiC has two sides, one Si terminated and one C terminated. By placing a SiC substrate or wafer in an oven under vacuum and heating up to 1300°C, silicon atoms are sublimated, releasing carbon atoms and allowing them to reorganize themselves with sp^2 hybridizations. Silicon side thus allows graphene domains growth in a repeatable way [130] but with a strong coupling with Si substrate and difficulties to control the number of graphene layers.

Chemical Vapor Deposition growth: Third main graphene synthesis method is the most promising method for high quality large scale graphene sheets: Chemical Vapour Deposition (CVD).

CVD has been used for years to grow graphite on nickel and copper [131], [132]. CVD basically consists in the chemisorption of carbon atoms from a hydrocarbon gas precursor on a catalytic surface. It takes place under high temperature and a flow of reactive gas in order to dissociate precursor gas and leave carbon atoms covalently bonded to the substrate. The accumulation and relative mobility of those carbon atoms will then trigger nucleation until they unbound from metal and form the graphene sp^2 lattice and honeycomb structure. CVD growth conditions have to be very well controlled in order to lower the number of graphene layers grown on the metallic surface. Working under controlled atmosphere and vacuum helps managing the amount of carbon injected in the CVD chamber and thus the number of graphene layers resulting on the surface after growth.

Substrate:

The metal choice is important as it must not sequestrate carbon atoms during the growth process. Copper and nickel are often used as substrates for growth [133] because they present the advantages of being low cost and easily dissolvable after growth to release the graphene produced. Copper presents a lower carbon solubility than nickel at high temperature [134] and consequently will easily allow mono and bilayer graphene growth.

Note on Variability:

There is a strong variability in graphene produced due to non-controllable parameters like local gases concentration on the substrate zone and also to differences in copper sources, their preparation process, the CVD recipe, the oven ramping speed, the eventual leaks in the machine, the contamination by accumulation of previous growth materials in the chamber and the storage and transfer process before graphene can be used as a biomaterial. We proved the variability in our graphene crystals quality to have direct biological consequences in term of cytocompatibility [110].

A large part of this thesis has been dedicated to the study and improvement of the graphene CVD growth on copper to obtain repeatable graphene source for biological experiments. Consequently, the fabrication process and improvements will be described in the following dedicated part.

2.2 Graphene CVD growth for biosensing

During this thesis I performed CVD growth graphene in order to optimize it to be suitable for bioelectronics.

As we previously described, in order to create sensors from graphene, the best way is CVD growth because it gives large area (~600 cm^2) of controlled quality graphene and it is the only way to have these large area of pure 2D crystal carbon monolayer. The great opportunities given by CVD graphene properties led us to investigate how it can be brought to brain computer interface fields, as an electronic conductor, a sensor and a coating for bioacceptance improvement.

However, poor graphene **quality repeatatibility is an obstacle** to proper cytocompatibility studies and also to microelectronic fabrication of implants. Graphene CVD growth was the first brick of our future implants design and consequently had to be mastered and **improved** to have a good repeatatibility degree.

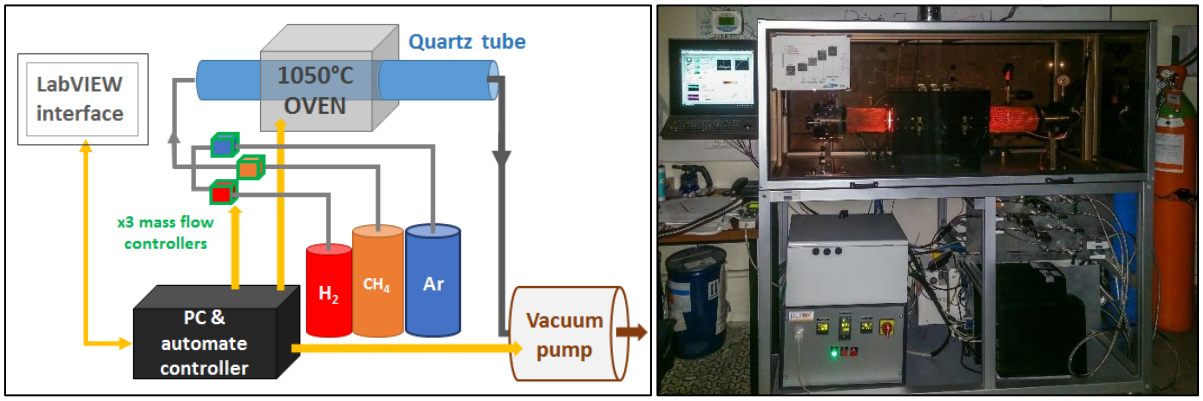

Figure 30 - CVD growth machine setup I used to grow graphene. This picture shows our CVD machine principle: mass flow controlled gases injection in an oven quartz chamber under vacuum back pumping. Recipe are semi- automated thanks to a LabVIEW program and many sensors (pression, temperature, cooling and venting systems). Photography shows our setup illustrated on left.

2.2.1 Monolayer graphene growth

a - Substrates selection

First step of graphene growth is the substrate preparation. As discussed before, copper substrates have been chosen to provide a sacrificial layer with a minimum amount of defects to avoid carbon diffusion inside the copper, limiting the graphene nucleation process to strict methane injection [135].

Copper foils were purchased from several industrial furnishers: Alfa Aesar, Lux Foil, Neyco….and were generally sell covered with an anti-oxidative coating (Figure 37) that needs to be removed before graphene growth. Several Cu surface cleaning methods have been reported so far, mostly by wet etching with nitric acid [136]. During this thesis I developed a novel cleaning methods to obtain the purest copper before starting growth. This will be developed in the next paragraph.

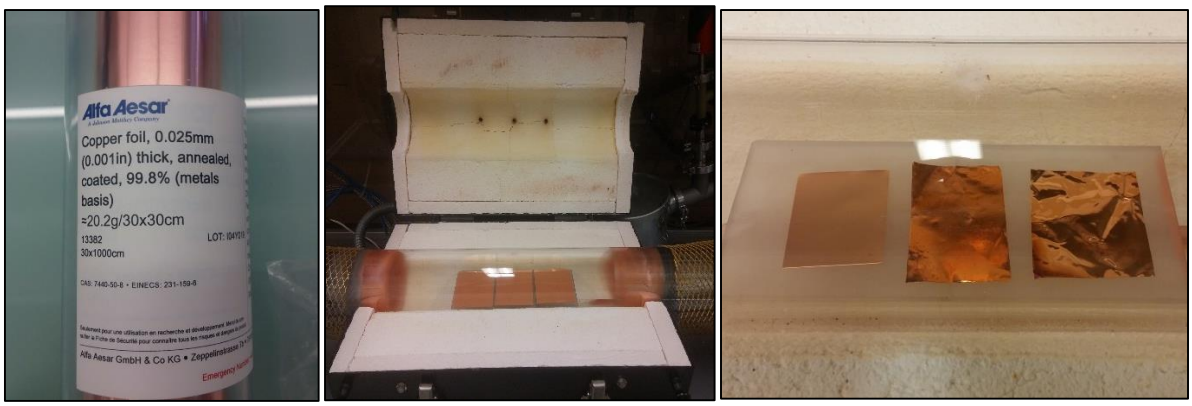

Figure 31 - Copper source is presented the same way as an aluminum consumer foil and cut as growth substrates of few centimeters squares: The copper is rolled and sold as 25µm thick and 99.8% purity/ Future copper substrate for growth are then cut and charged on a quartz sample holder in the CVD quartz tube (right picture)

Next Figure 32 illustrates the growing process steps. After substrate surface cleaning to remove copper coating and contaminants, the copper foil is charged in the oven quartz tube of our home built setup [126] under ambient air , creating a thin layer of dark copper oxide on the surface of our copper. The chamber is pumped until we reach a pressure lower than 1mbar to ensure the lowest possible concentration of oxygen in our chamber before starting heating. Once pumped bellow 1mbar, temperature ramp up is started until the desired temperature, generally between 950 and 1050°C.

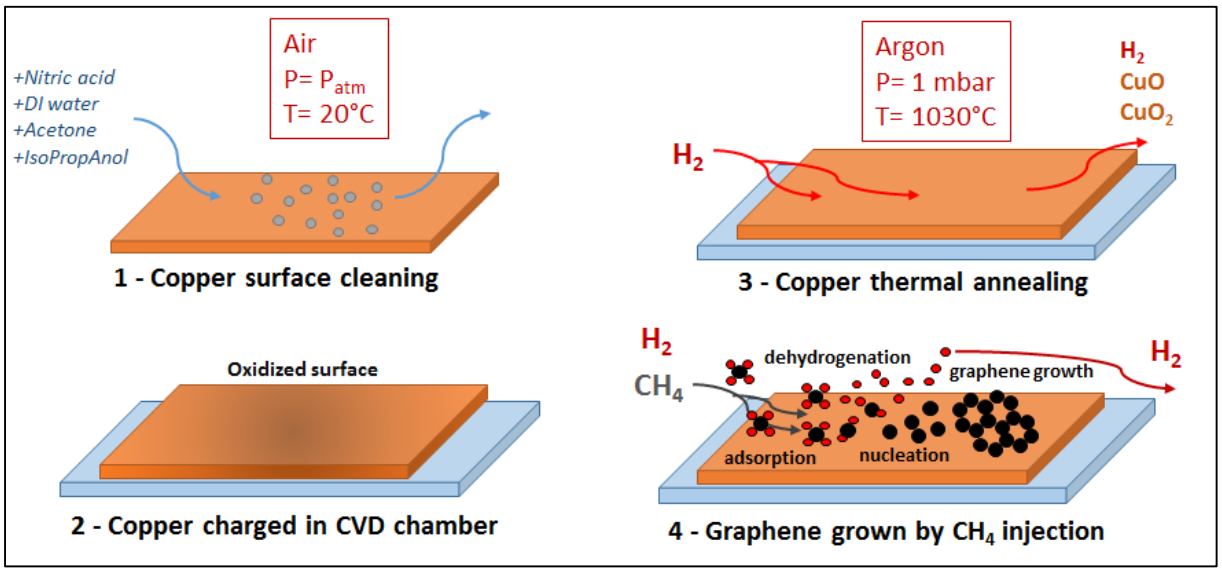

Figure 32 - Main steps of graphene growth on copper from hydrocarbon precursor: 1 – Copper surface is cleaned according to our recipe detailed in next paragraph "substrate preparation". 2- Copper foil is charged in the CVD quartz tube on a quartz holder (see photo on Figure 9). 3 – After vacuum pumping and heating up to 1030°, copper is thermal annealed during 30 to 60 min to remove surface and bulk oxide and eventually clean bulk contaminants that should leave the surface during this step. 4- Graphene growth is launched by CH_4 injection in a H_2 and Argon atmosphere that will trigger physisorption of CH_4 and chemisorption of H_2 on the surface then dehydrogenation of CH_4 and nucleation of carbon atoms on the surface to form honeycomb lattice of graphene. Bulk in and out diffusion of carbon atoms happens also but is not represented here, they will be detailed after.

b - Role of thermal Annealing

Next step is thermal annealing of copper foil and consists in injecting a high throughput of hydrogen in the chamber for 20 to 60 minutes at 1030°C. Hydrogen at this temperature will remove copper oxides present on the surface and **etch away the surface copper** that could be contaminated by previous steps or by bulk contaminants lighter than copper like silicon particles, that would consequently ascent to the surface under high temperature.

Hydrogen is also able to enlarge the grains size of Cu, **lowering the roughness** of the surface and the defective sites of the copper substrate. Indeed a low defect substrate topology has been shown to be warrant of low stress on graphene [137] and consequently a more successful graphene transfer afterwards.

c - Role of forming gas

Final step is growth by injection of a graphene hydrocarbon precursor: methane. The reactive gas used to dissociate methane is called forming gas and is composed of 10% dihydrogen diluted in argon.

In most reported recipes of CVD graphene, the reacting gases injected consist not only of a carbon precursor, but also hydrogen, sometimes mixed with another inert gas, such as argon for dilution purpose. Inert gases are used as they can reduce the partial pressure while keeping a reasonable global pressure (at least compatible with the system which is only design to withstand primary vacuum).

Forming gas is used to clean the chamber before growth and maintain control atmosphere inside the furnace. The 10% dilution has also a safety purpose by lowering hydrogen concentration closer to its lower expositive limit of 4.1%.

d - Standard growth of graphene

At high temperature, methane dissociation occurs by dehydrogenation during physisorption of CH_4 and chemisorption of H_2 molecules [138]. Carbon atoms then bond to our copper foil surface and also diffuse to the copper bulk. After few minutes injecting methane, those carbon atoms accumulate and start nucleation: they unbound from metal to create sp^2 bounding with each other's and form the graphene honeycomb lattice. This is the kinetically limiting step.

The whole substrate is covered after 20 to 30 minutes of methane injection. Oven heating, hydrogen and methane injection are immediately turned off and the chamber is pumped and flushed with pure Argon to remove eventual methane excess as much as hydrogen that could etch away the freshly grown graphene. Once cooled down, our graphene can be characterized either directly on copper with SEM, or after transfer on silicon substrate for AFM, Raman spectroscopy and electrical measurements (see 0).

On Figure 33, standard CVD grown monolayer graphene shows many multilayers patches under its surface on copper then once transferred on silicon. Hall devices (GFETs, see 2.4.5) were fabricated using electron beam lithography and plasma etching. One Hall bar included a multilayer patch while the other device was used as a control. Our team showed that the device including multilayer patches are in-homogeneously doped, thus electron mobility is lowered by a factor five and the patches are inducing an increase in device resistance due to patches edges resistance [102]. The sensitivity of such devices in strongly lowered and multi-layered graphene are consequently not the best ones to use to build our biosensors.

We observed that multilayers patches were preferentially present at the defect sites on Cu surface. As explain just before, during physisorption of carbon atom to the surface some carbon atoms diffuse into the bulk. Multilayer formation is due to this segregation of carbon at the Cu foil defect sites such as grains boundaries and releasing after nucleation of the first layer is complete.

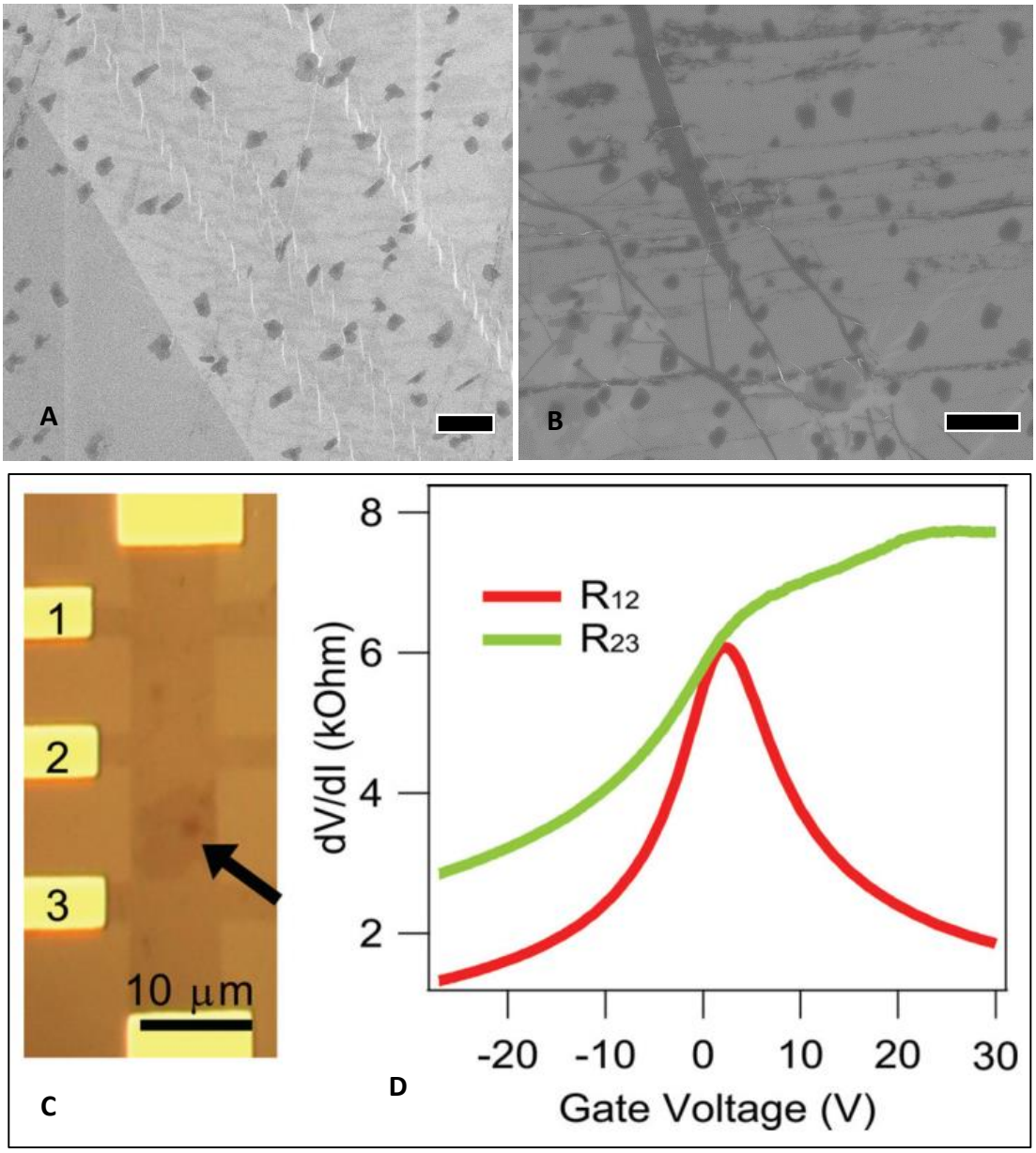

Figure 33 – Multilayer patches graphene on copper and transferred on SiO_2 show patches incidence on future devices. A – SEM picture of graphene on copper shows copper atomic step on the first third of the bottom left hand corner and multilayer patches all over the surface. B - Same graphene SEM picture once transferred on a SiO_2 substrate: big dark lines represent wrinkles in graphene that folded after transfer and created an additionnal multilayer zone. Scale bars are 2µm. C-Optical image of Hall-bar device made using standard-CVD, with two adjacent regions: zone probed between electrodes 1 and 2 is fully monolayered while zone probed between electrodes 2 and 3 shows a multilayer patch as indicated by the arrow. D- Differential four probe resistance of the two adjacent regions 2–3 (green curve) and 1–2 (red curve) respectively with and without a multi-layer patch. C&D are from our team article [102]

e - Pulsed growth for perfect monolayer

Our team developed a patented recipe [139] using alternate injection of methane by short periods interspersed by simple forming gas injection during several hours to prevent these multilayer patches to form and thus produce a **very high quality monolayer** graphene [140].

This pulsed growth process has been used and improved to produce the biology study purpose graphene. The pulsed growth is based on a 2 steps alternate standard nucleation and etching of the non-graphene carbon atoms on copper surface and defects. We illustrated these two phases on Figure 35.

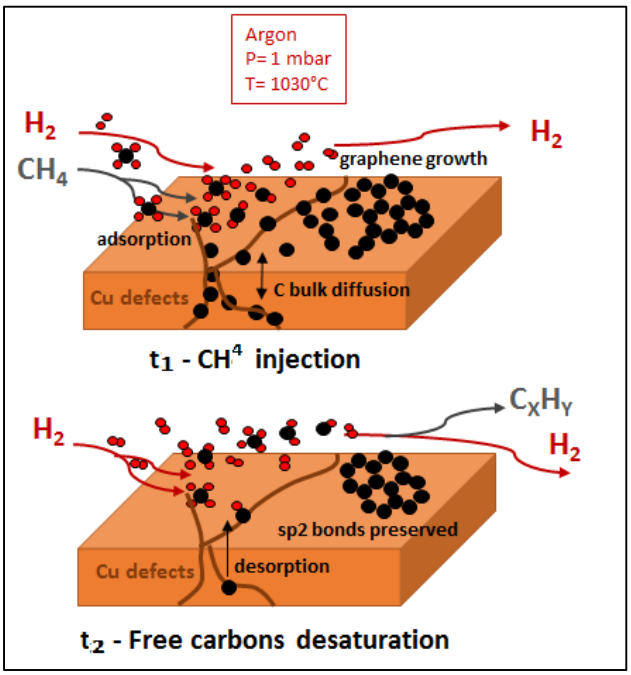

Figure 34 - Pulsed growth principle in 2 steps: CH_4 injection and H_2 alone alternance allow desorption of diffused carbon atoms in bulk through Copper defect. sp^2 bonds are strong enough to overcome the H_2 "etching of non-sp^2 bonded carbon atoms. This alternance allows monolayer growth favoring only sp^2 surface segregation of carbon atoms.

The resulting unpatched graphene is due to the fact that high temperature hydrogen dissociates the carbon atoms from the methane precursor and also dissociates non-robust carbon links. During etching t2 pulses, only sp^2 bonding will be preserved thanks to their robustness. All others nucleation types like second layer of graphene giving birth to patches will be etched away. The etching phase is also used to discharge the copper from defects segregated carbon atoms. One inconvenient of this alternance of phases is the important slow-down of growing process. The standard recipe that does not warranty a monolayer of graphene takes one cycle of 20 to 40 minutes whereas the pulsed growth takes approximately 350 cycles for a total of 6h.

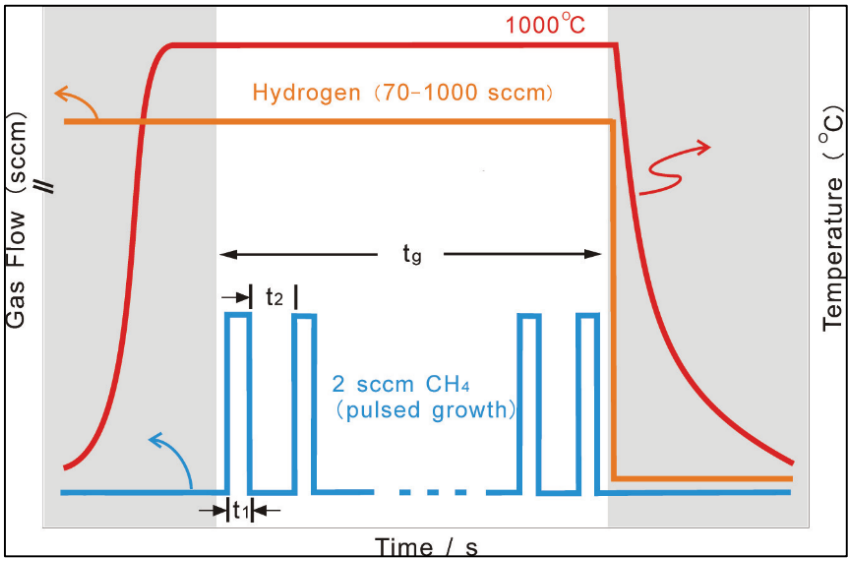

Figure 35 - Pulsed growth recipe diagram shows temperature ramp up and plateau together with injected gases: forming gas is continuously injected whereas pulses of methane injection allow the slow nucleation of carbon atoms in their sp^2 honeycomb conformation.

A very important property of the graphene I wanted to obtain to create biosensors was its purity, I wanted to lower the contaminations of graphene surface in order to make sure they were not the sources of any future positive or negative cytocompatibility results and that I was really investigating pure graphene behaviour in vitro and in vivo [110].

Another negative aspect of having contaminations on graphene is that it makes it fragile, modifying pure sp^2 conformation and making it harder to handle during our microelectronics process. Contamination will also alter the electronic conductivity of graphene making sensor not sensitives enough.

The next paragraphs are then dedicated to this thesis work on lowering theses contaminations to build pure monolayer graphene devices.

2.2.2 Substrate preparation

During this thesis, I have made many improvements in copper preparation prior to growth. Copper is usually bought from some companies selling it for PCB processing purposes. The copper is sold pure at around 99.9% and is generally coated with a very particular anti-oxidative layer in order to protect the foil from oxidation. At the beginning of this thesis; copper source was Alfa Aesar #13382 but recipe just seemed to have been changed without notice by this furnisher, which was one of the main copper provider for CVD graphene growth on copper. The copper had still the same purity degree but usual thermal annealing under hydrogen was unable to remove the coating from the surface, resulting in very contaminated graphene (Figure 38A).

I investigated the origin of the strong contamination by performing SEM EDX on particles and identified chromium and silicon peaks as shown on Figure 36.

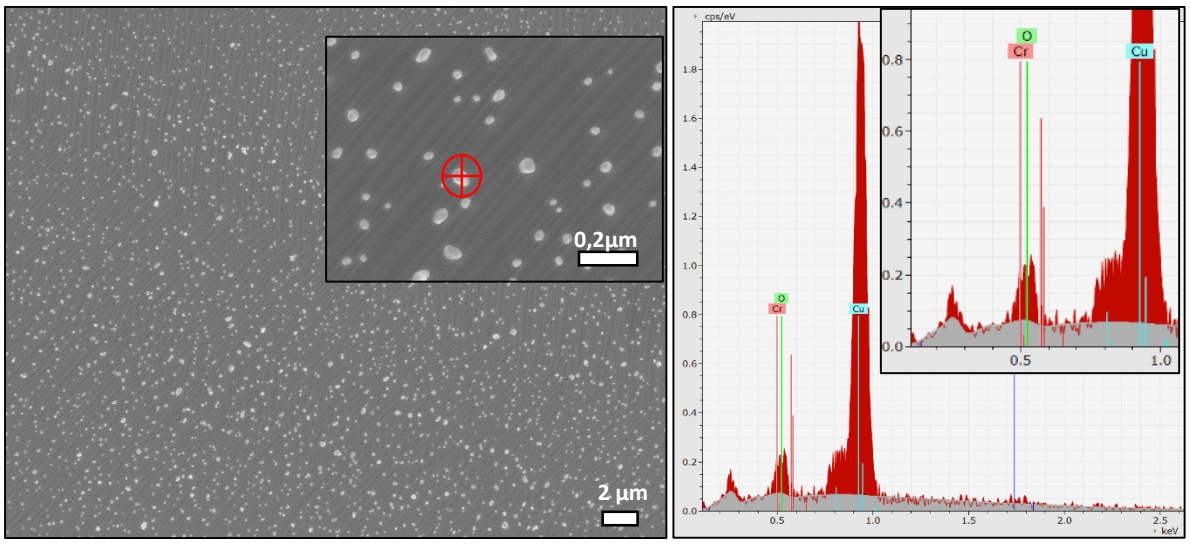

Figure 36 - SEM picture shows very dense contamination after #13382 copper thermal annealing. Contaminants are around 100nm diameters and EDX shows strong copper peak as much as chromium and oxygen peaks, suggesting a related contamination. The higher peak corresponds to copper.

In order to find the thickness and verify the composition of this coating, I performed Ion Beam Etching, a process known to etch at a constant speed any layer, in order to track the material detected by the integrated EDX. Figure 37 shows that the coating is made of an alloy of chromium and copper without eliminating the possible presence of another untracked compound.

I measured the etching speed with an integrated laser interferometer and obtained a mean etching speed of 0,9 µm/min along the process. I can then conclude from the EDX tracking

curves that the ion flow really initiates etching after 60 seconds of heating and etching of chromium lasts until 110 second. The chromium being etched during 50 seconds, I deduced chromium/copper alloy was around 750 nm thick.

Figure 37 - EDX shows a chromium alloy on standard copper surface. Chromium and Copper tracking when physically etching a copper foil with Ion Beam Etching. In red, copper is more and more present when chromium in blue decrease along the etching of the Alfa Aesar #13382 copper foil surface

I consequently tried chromium etchant but it has let a lot of residues on the copper surface despite multiples rinsing.

a - Annealing incidence

During the CVD growth it is important to remember that we use a temperature of around 1000°C during which copper atomic planes reorganize themselves. This reorganisation induces impurities inside the foil to come out on the surface, a clean surface before growth is then not a warranty of a clean surface after growth; a paramount step is then what we call annealing, which consists of a 30 to 60 min period during which the temperature is at 1030°C and the atmosphere in the furnace is mainly composed of hydrogen. Hydrogen at this temperature has a corrosive property that allows to clean surface residues and remove oxide from the copper. We have shown that even with annealing, the coating layer on the copper let some residues on it. (Figure 38).

Many other copper sources with different degree of purity were then tested to assess the differences in graphene contamination.

The role of annealing on **copper impurities reductions** has been previously shown by coupling a SEM with a CVD chamber and directly imaging the impurities delocalisation on the surface and removal during H_2 injection [141].

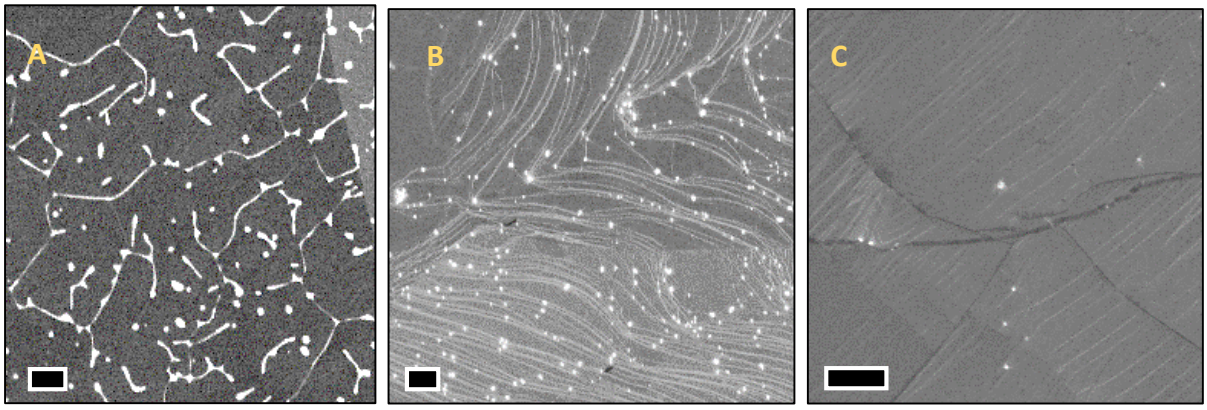

Figure 38 - SEM pictures of different growths done during this thesis show the improvement of graphene surface achieved with proper preparation of copper substrate; Graphene surface, from left to right: ***A*** *#13382 copper without surface preparation besides annealing,* ***B*** *New copper source after annealing only and* ***C*** *after nitric acid cleaning recipe and annealing. Scale bars: 2µm*

b - Chemical preparation of copper substrate

Nitric acid was previously shown to successfully allow the reduction of contaminants [136] by direct etching of the surface as much as a chemical reaction that happen during thermal annealing of such a prepared copper. Indeed, nitric acid reacts with copper according to this formula:

$$Cu(s) + 4HNO_3(aq) \rightarrow Cu(NO_3)_2(aq) + 2NO_2(g) + 2H_2O$$

However, remaining Copper nitrate $Cu(NO_3)_2$ on our surface cannot be properly removed with a simple DI water rinsing and copper nitrate is known is chemistry to be a precursor of copper oxide as much as a producer of nitric oxide and dioxygen gases [142] according to the following formula, when exposed to temperature above 170°C:

$$2\ Cu(NO_3)_2 \rightarrow 2\ CuO + 4\ NO_2 + O_2$$

Although previous SEM pictures showed a quite clean surface using nitric acid, we found out that nitric acid were lowering the graphene quality, making it very hard to transfer with a success rate down to 10% of proper transfers. $CuNo_3$ presence in the copper bulk and its possible migration on the surface during growth may induce interactions with graphene, changing sp^2 conformation, doping and changing adhesion properties of graphene. Those changes in adhesion properties might be responsible for transfer failures.

Several studies showed efficiency of acetic acid [143] to etch copper oxides. Copper nitrates and acetic compounds are well known to react together and are often used as reagent for nitration of aromatic compounds [144]. This affinity has then been used to improve our copper surface preparation.

I developed **a recipe to prepare the surface** and the bulk material by cleaning it with this combination of nitric acid and acetic acid. Several etchant have been tested and compared by performing a standard graphene growth with 60 min thermal annealing on 5 separated copper foils that underwent different pre-treatments, the results are illustrated on Figure 39. Without pretreatment, the high amount of contaminants on the surface led to a bad bonding between graphene and SiO_2 substrate, graphene is thus teared of. Ammonium persulfate has been tested to etch the copper as we already use it in our transfer process (see 2.3) but shown many contaminants and weak adhesion of graphene; nitric acid only is improving a bit the adhesion but not enough to have repeatable large scale transfer graphene. Acetic acid alone provides a good solution although SEM imaging showed 200 nm contaminants remaining on graphene surface.

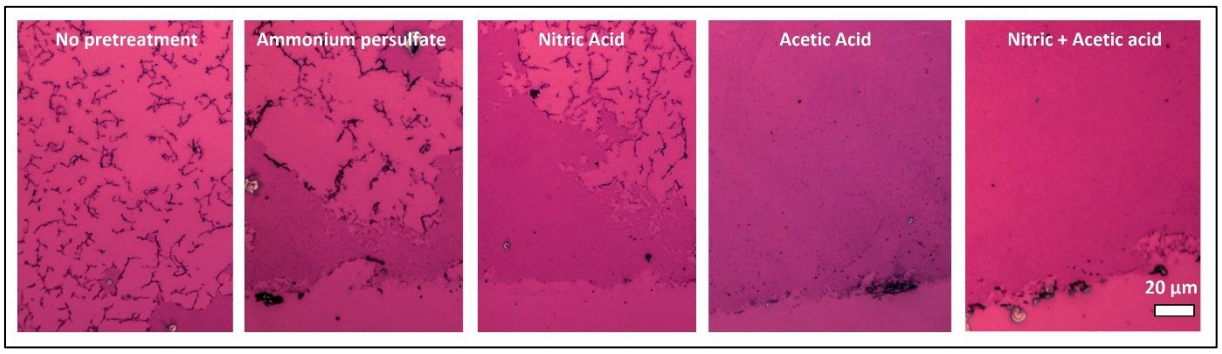

Figure 39 - Optical microscope pictures of different graphene sources transferred on SiO_2 substrates. Each transfer shown was done using a differently prepared copper before standard graphene growth with 1h thermal annealing were performed. Graphene damages are very important without surface preparation of copper, ammonium persulfate and nitric acid make graphene fragile and almost half damaged. Acetic acid alone shows graphene everywhere but with high granularity suggesting dirty surface. Finally nitric acid followed by acetic acid shows a perfect transfer ability.

The best recipe found, and used for most of the devices fabricated during this thesis, was dipping the copper foil in 10% diluted Nitric acid in order to remove the contaminants layer and, after a DI water rinsing, cleaning the Copper nitrates using acetic acid. Acetic acid post cleaning led to a better graphene quality and a 60% proper transfer rate. After each treatment, cleaning with acetone and IPA was done primary to the graphene growth in the oven.

This recipe has given a near zero contamination of graphene after growth, characterized by SEM on Figure 40. Graphene presence is assessed thanks to **wrinkles**, produced during after growth cooling down of the graphene on copper because of the difference of copper and graphene thermal expansion coefficients.

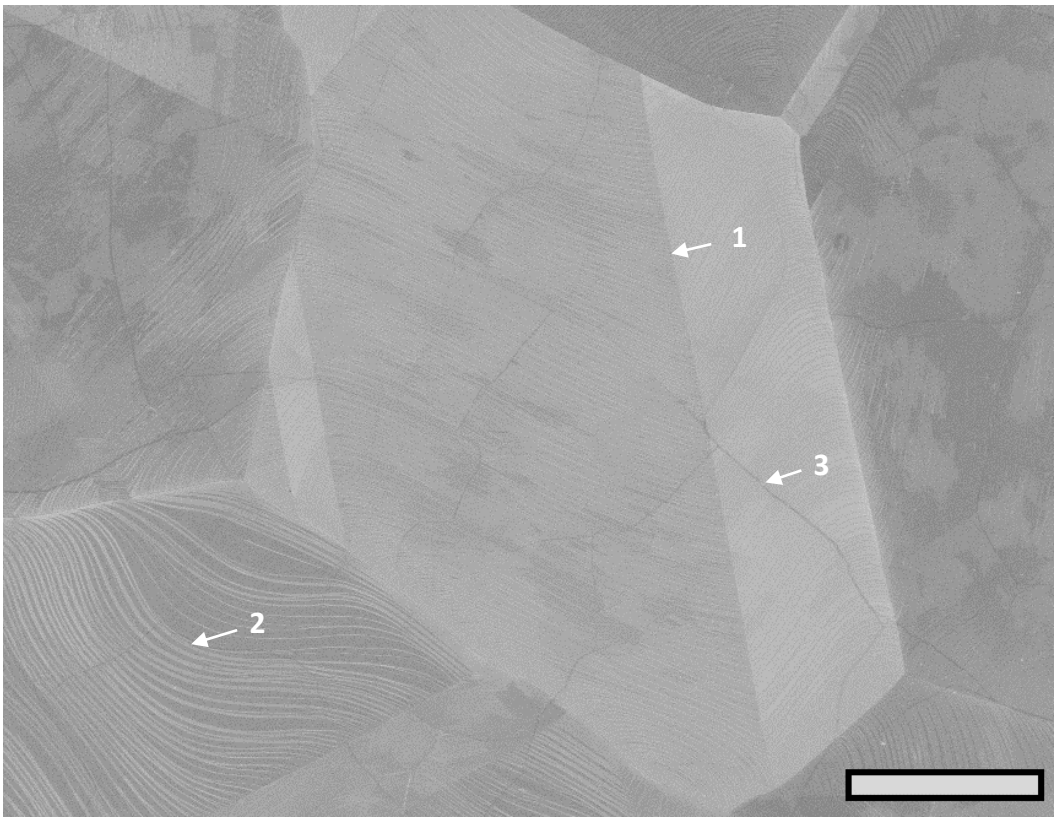

Figure 40 - SEM picture of clean monolayer graphene is after our bi-acid preparation: Graphene grown on bi-acid pre-treated copper foil shows zero contaminants on large area. There are 3 types of linear defects visible on that picture, (1) copper grain boundaries, (2) copper step edges between terraces and (3) graphene wrinkles due to differences in thermal expansion coefficient between graphene and copper during cool down. Scale bar is 20µm wide.

2.3 Graphene transfer process

Graphene being a two-dimensional material, it has essentially two exposed surfaces highly sensitive to the environment and no bulk. Therefore great care has to be taken to remove the material from its growth substrate, here a copper foil on which synthesis was processed by CVD as shown before, and transfer it onto host substrates without contaminating nor damaging the atomically thin basal plane.

First step after growing graphene is generally storage, which is done under a vacuum chamber to limit graphene surface and copper bulk oxidation and prevent any graphene contamination. Once we want to use this graphene, the following transfer technique has to be processed in cleanroom, as illustrated on Figure 41.

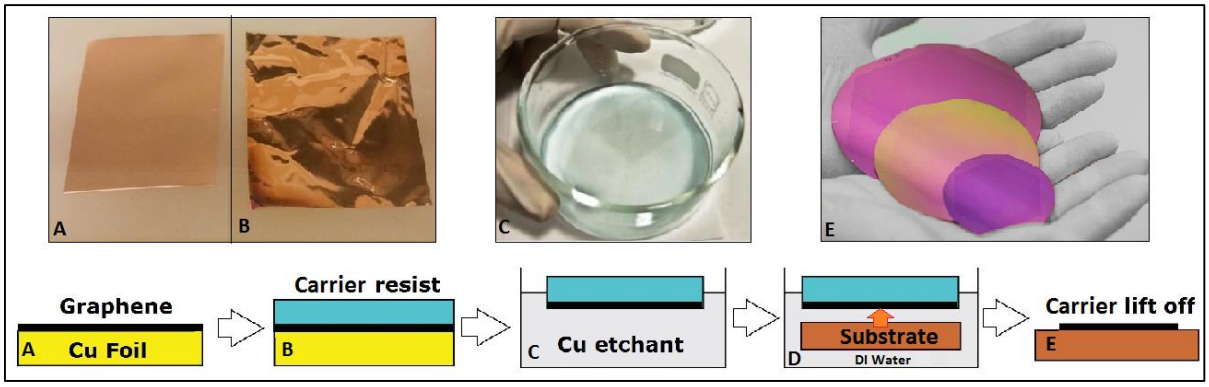

Figure 41 - I improved cleanroom methods to transfer graphene from copper growth substrate to a target substrate: After the Graphene growth on a copper foil A) It has to be Transferred on a substrate using a resist carrier B) as a vector in order to support the graphene layer during wet etch of the copper C). Graphene with its carrier are then transferred in DI water and fished onto a substrate (D). In the case of flexible substrate, flexible material like PDMS, polyimide or, Parylene is used directly as the carrier and the device is dried after rinsing it with DI water E) The carrier can then be removed by acetone lift-off: here graphene has been transferred on 2 to 4 inches silicon wafers.

Graphene being nearly invisible and in order to preserve its integrity, we use a transfer vector to carry graphene from the copper to the future substrate we want graphene on.

The carrier used is AllResist© PMMA ARP 679-04 which is a commonly used e-beam resist. The thickness of this resist is around 270 µm when spin coated at 4000rpm on our graphene on copper foil, its compliance with graphene makes it the most used carrier for transfer.

In order the evacuate the solvent from this resist we bake it during 1min at 180°C

Next step is to prepare the copper to be etched. For that purpose, we back etch the copper foil. Graphene in the CVD chamber is deposited on both sides of the copper foil and graphene

acts as a barrier for many chemical elements like copper etchants. Consequently, prior to the copper chemical etching, we process to a back etch with a Reactive Ion Etching (RIE) O_2 plasma for 10 seconds to remove graphene on the back. During this process top graphene is protected by the PMMA and by the relative vertical directionality of the O_2 plasma created in the chamber.

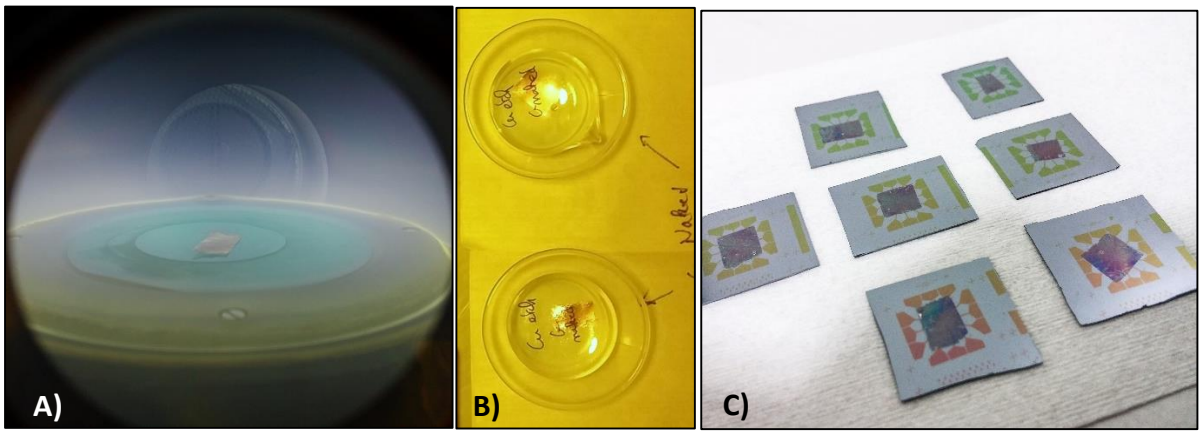

Figure 42 - Graphene transfer process from substrate RIE back etching to transfer on devices: ***A)*** *Plasma RIE copper foil graphene back etch* ***B)*** *wet copper etching by putting sample pieces on top of a solution of ammonium persulfate to expose copper and release graphene-PMMA stack* ***C)*** *Graphene-PMMA stacks are then rinsed in several beakers her before being transferred on samples and dried, here some future silicon probes.*

The next step is to take the Copper – Graphene-PMMA stack and drop it on the surface of a copper etchant medium. The graphene will thus float on the surface. Several medium can be used and we chose ammonium persulfate $(NH_4)_2S_2O_8$ for the low defect it will induce on graphene compared to others acids compounds. Ammonium persulfate has also the advantage of being a salt with high water solubility of 80 g/100 mL at 25 °C consequently providing a relative uniform etching rate of the whole surface.

We use a 1g/10mL dilution in water and are thus way under this solubility limit. Ammonium persulfate and copper reaction products are highly soluble in water, after 60-90 minutes, we have many compounds in the solution in contact with graphene, resulting from the following reaction:

$$Cu + (NH_4)_2S_2O_8 \rightarrow CuSO_4 + (NH_4)_2SO_4$$

Copper is dissolved and graphene-PMMA stack is floating on the surface of the wet etchant. Products of this reaction, $CuSo_4$ and SO_4 are highly soluble in water.

2.3 Graphene transfer process - Substrate preparation

In order to remove the wet etchant and copper residues from the graphene surface we will "fish" this stack and put it in 5 different clean DI water baths, one after the other, by taking the stack and a very few amount of solution under it (4mL in a watch glass). After those 5 rinsing in a 500 mL beaker, the estimated dilution of the water soluble contaminants is around $1{:}10^{13}$ which is estimated sufficient to have a very good graphene quality.

However, it is important to note here that this dilution does not concern eventual amphiphilic floating compounds that would be preserved with our process during transfer. It is consequently very important to avoid any lipidic contaminants during the whole fabrication and transfer process.

Finally we will proceed to the deposition of graphene-PMMA Stack by fishing it with the target substrate. This process being done in a water solution and graphene being quite hydrophobic, it is really important to try to reduce the amount of water which we will keep between the stack and the substrate. In this purpose, we need to prepare the substrate to make it hydrophilic. The higher the surface tension will be, the more constraints will be applied to graphene and higher is the risk to disintegrate the graphene layer.

Silicon based substrate like glass slides, SiO_2 or Si_3N_4 are naturally hydrophilic. However, when exposed to air, there are quickly covered with hydrocarbons contaminants that make them hydrophobic. Reactive Ion Etching O_2 plasma activation of the surface during 2 to 10 minutes –i.e. O_2 plasma ashing- allows removal of theses contaminants.

Once the graphene is deposited on the substrate and the remaining thin water layer evaporated, we will help the bonding of graphene on substrate process by improving the adhesion forces (Van der Walls and hydrostatic forces) heating the sample to 150°C during 5 minutes. Final step of the transfer process is the removal of PMMA carrier layer with acetone during 60 to 90 minutes.

2.3.1 **Recipe improvements**

Several improvements of this recipe have been made during my thesis to obtain a better quality of graphene and facilitate the transfer on different substrates like glass slides or soft materials.

First improvement in this process flow is regarding the carrier used, choosing to use 2 layers of PMMA instead of 1 layer. A first 80nm PMMA layer will be deposited and baked, then a second 400nm layer is spread. This help acetone lift- off by reducing the amount of PMMA to be dissolved before releasing the whole PMMA layer from graphene.

Second improvement has been done regarding the baking temperature and process and preferring the slow cooking at low temperature than the opposite: instead of a bonding bake of 5 min at 150°C I decided to go through an overnight self-bonding under vacuum chamber followed by a 5 min 80°C bonding bake. This allows a good bonding without hardening too much the PMMA layer on top; making the acetone lift-off better with a cleaner surface afterward (less PMMA residues).

As a solution for strictly hydrophobic substrates transfer or substrates that cannot go through RIE chamber, I tested a recipe, lowering the surface tension of the last DI water rinsing medium. IPA can be dissolved in water if a few minerals or salts are added to the water, consequently, ammonium persulfate residues can help dissolving water to IPA and lower the rinsing solution tension surface. This process allows transfer on non RIE prepared substrate but shows less clean graphene in the end due to the ammonium persulfate residues between graphene and substrate.

2.3.2 Transfers on soft materials:

Graphene can be transferred directly on soft substrates whenever those material can be spin coated on top of the graphene on copper foil instead of the traditional supportive PMMA layer. However, the adhesion forces of graphene on this polymer must be good enough in order to preserve graphene integrity when etching the copper.

I successfully used Dow Corning© Polydimethylsiloxane (PDMS) to create a simple device in order to test graphene elastic deformation resistance, protecting two sides of the copper support with Kapton© tape in order to have contacts of our graphene layer as illustrated on Figure 43.

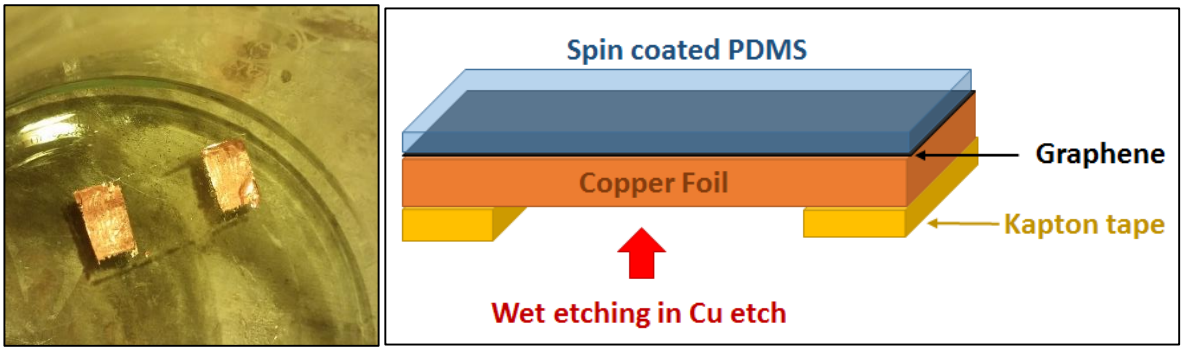

Figure 43 – PDMS simple device made by replacing PMMA with PDMS during transfer process Native copper contacts are kept by protecting extremities from wet etch with Kapton tape.

This device showed a low resistivity of 2kΩ but elastic deformation immediately made it unusable. I was however still able to read the 2kΩ resistivity value by contacting an Ohmmeter directly on the PDMS. We deduced that the thick 25µm copper on thin 2µm PDMS had created a cantilevered mechanisms that broke graphene along the interface during the first elastic deformation. This process is yet useful to create soft devices easily by spreading polymer directly on graphene. A thinner copper foil or thicker PDMS layer could be a solution to measure properly elastic deformation.

I also did some graphene on PDMS cytocompatibility test, detailed in the next chapter. In order to respect biological standard and ease of manipulation, I glued PDMS to some glass slide on PDMS spread on graphene (Figure 44). The resulting stacks were successfully used for cell culture and PDMS with graphene gave promising results in terms of cell development.

2.3 Graphene transfer process - Transfers on soft materials:

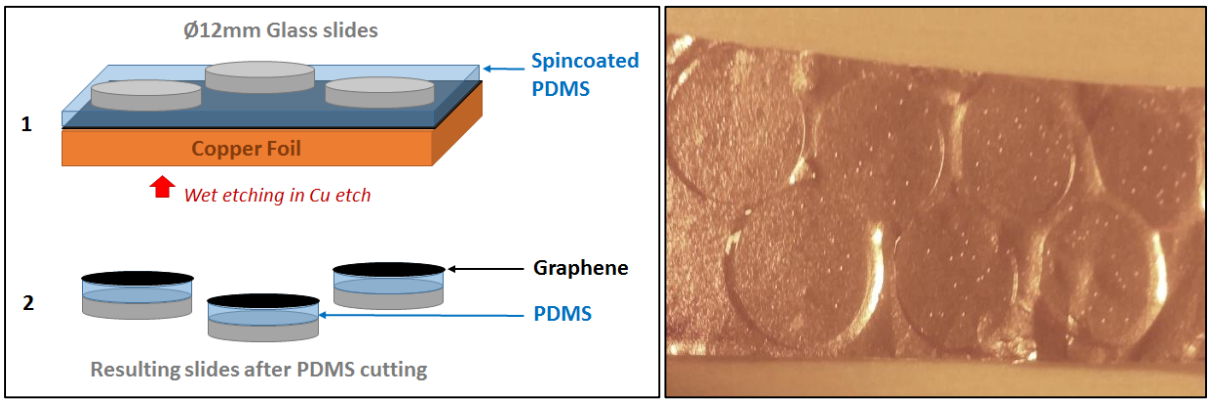

Figure 44 – Fabrication of Graphene on PDMS glass slides for in vitro studies: Glass slides with PDMS and graphene devices fabrication illustration for in vitro graphene cytocompatibility studies; After stack is cured, slides are released by cutting PDMS around glass round sides with a blade.

I did a similar process with polyimide Fujifilm© LTC 9505 and was able to create small transparent and soft conducting devices but unfortunately, devices where self-rolling immediately after drying from copper etch, making them impossible to measure properly.

This was explained by what happens when polyimide is cured at 250°C during 90 minutes in an oven: the interaction with copper on one side and air on the other side created thermal induced strain, related to a Poisson's ratio gradient [145] along polyimide thickness. This gradient then induce film self-rolling.

2.3.3 Direct transfer on 3D probes

Another strategy that I have investigated in parallel was to encapsulate commercially available 3D active probes (integrated sensors) with graphene (Chapter IV -Figure 98). Graphene is expected to enhance the neuronal regrowth on the surface of the probe and thus improve the neuron-sensor coupling and finally the detection efficiency.

It is also expected to provide an **efficient diffusion barrier** for both metal atoms or ions, preventing the release of metals in the body and corrosion of the electrodes, thus increasing the lifetime of the implants [146], [147]. The **anticorrosion** properties of graphene remains disputable because it has been contradicted on long term basis for metal oxidation protection [148]. Graphene defects and substrates nature might play a role on oxygen diffusion that would explain results variation in literature. However, biological medium behave in a different manner than gases and the corrosion protection might here be provided by graphene acting as a barrier for enzymatic activity.

Graphene coating of already commercialized implants might be a very good transition solution to **improve implants bioacceptance** without changing the whole implants design. In order to investigate graphene coating of already 3D shaped commercial implants, I developed very specific techniques of transfer.

I detail these transfer techniques in chapter IV about implants neuroengineering.

2.4 Graphene characterization methods

2.4.1 From optical to Electron Microscopy

The simplest way to differentiate between different thicknesses of graphene is, as we already saw in the previous paragraphs by using contrast spectra on an optical microscopy on Si substrate with a 285 nm SiO_2 capping layer. Graphene is visible thanks to its 2.3% light absorption per layer that inevitably leads to light interferences when on a silicon reflective surface.

The best way to understand the structure of graphene, -ie by directly looking at the honeycomb structure, defects and graphene grain boundaries is however using Transmission Electron microscopy (TEM). Although it is a destructive analytical tool that damage graphene, and that needs graphene to be suspended.

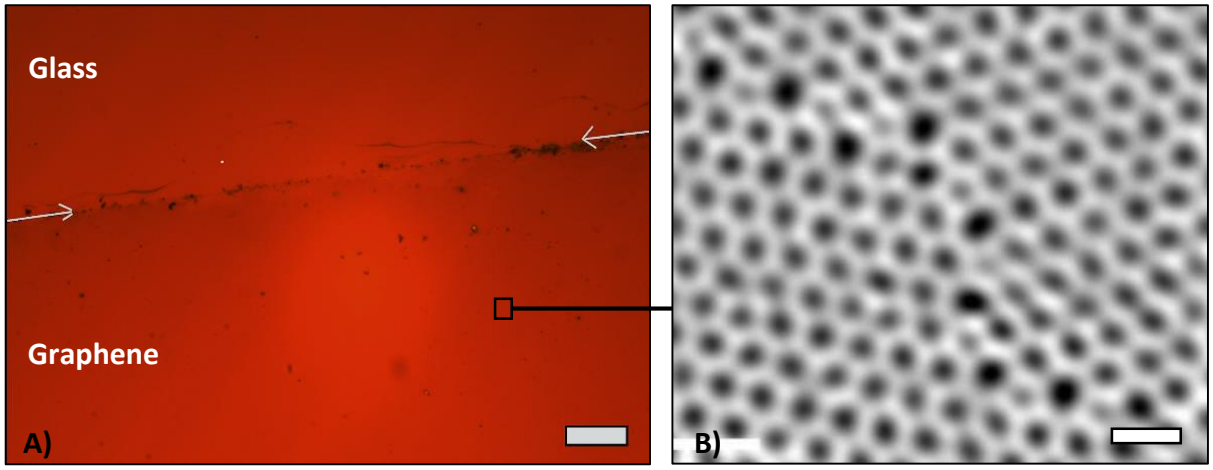

Figure 45 – Optical microscopy is a good tool to evaluate graphene film integrity and number of layers, on the other hand, TEM provides information about atomic structure. ***A)*** *Optical microscopy allows easy macroscopic characterization of a pulsed grown graphene foil transferred on silicon substrate, thanks to graphene light absorption. Scale bar is 20µm* ***B)*** *TEM picture shows graphene honeycomb structure and defects in the center which is here the grain boundary that corresponds to the link between two grains of graphene, issued from 2 nucleation sites that merged during CVD growth. ADF -STEM was performed at 80keV and scale bar is 5A. After* [149].

2.4.2 Scanning electron microscopy

As we saw in previous paragraphs, Scanning Electron Microscopy (SEM) is a very good way to see graphene contaminations and structural defects as much as multilayer patches or important structural defects. Indeed, SEM is displaying contrast in relation with electrical conductivity, the most graphene will conduct electrons, the better will the contrast be between it and an insulated area. Graphene is however fragile to high current and we generally never go above 5 kV of e-gun voltage to image it. Copper is also highly conductive and it can be hard to distinguish graphene on top of copper especially when visualizing monolayers, it is then very useful to identify the graphene wrinkles (Figure 46). Indeed, during growth at more than 1000°C, copper undergoes thermal expansion. When cooling down, it retracts and induce “waves” called wrinkles on graphene surface which are easily observed on SEM pictures. During this thesis, I mainly used a Carl Zeiss FESEM with an ESD-X analyzer to characterize copper defects. Images were generally done using In-Lens detector and for some specific copper topography characterization, I used SE_2 detector. Maximum resolutions obtained on graphene on copper were generally around 10nm.

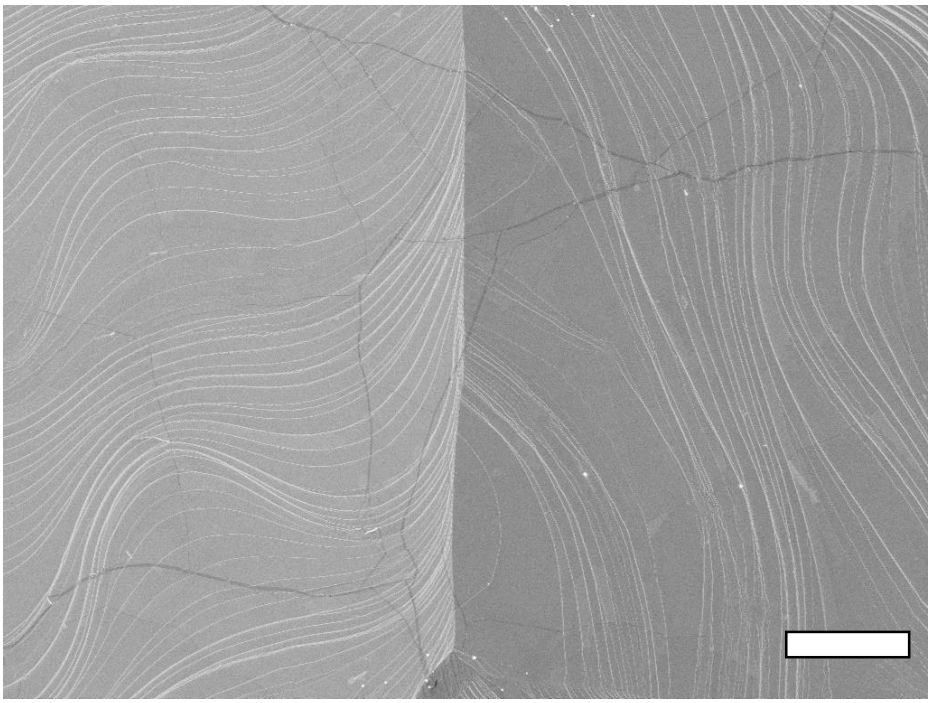

Figure 46 - SEM imaging allows graphene and atomic planes conformation observation SEM picture shows apparent monolayer graphene covering the surface. The grey lines represent graphene wrinkles and are resulting from copper thermal expansion during growth. Graphene foil is consequently larger than copper once cold. Scale bar is 10µm.

2.4.3 Raman spectroscopy

Raman spectroscopy is a fast and non-destructive characterization tool that transduces vibrational modes of atoms into radiation wavelength shifts. The atomic configuration in molecules and crystal have specific vibrational mode. Raman spectroscopy uses a monochromatic laser source with a frequency ω to interact with matter by polarizing the electron cloud. It will then place electrons in a transitory unstable state during which they will interact with phonons. When relaxing, an **in-elastically scattered photon** will be detected at a frequency which is one vibrational mode $\omega 0$ different from the incident photon: $\omega - \omega 0$ (Stokes) and $\omega + \omega 0$ (anti-Stokes). Using that excitation – emission frequency shift, Raman spectroscopy allows to detect local matter vibration modes and thus identify a crystal structure locally and fast.

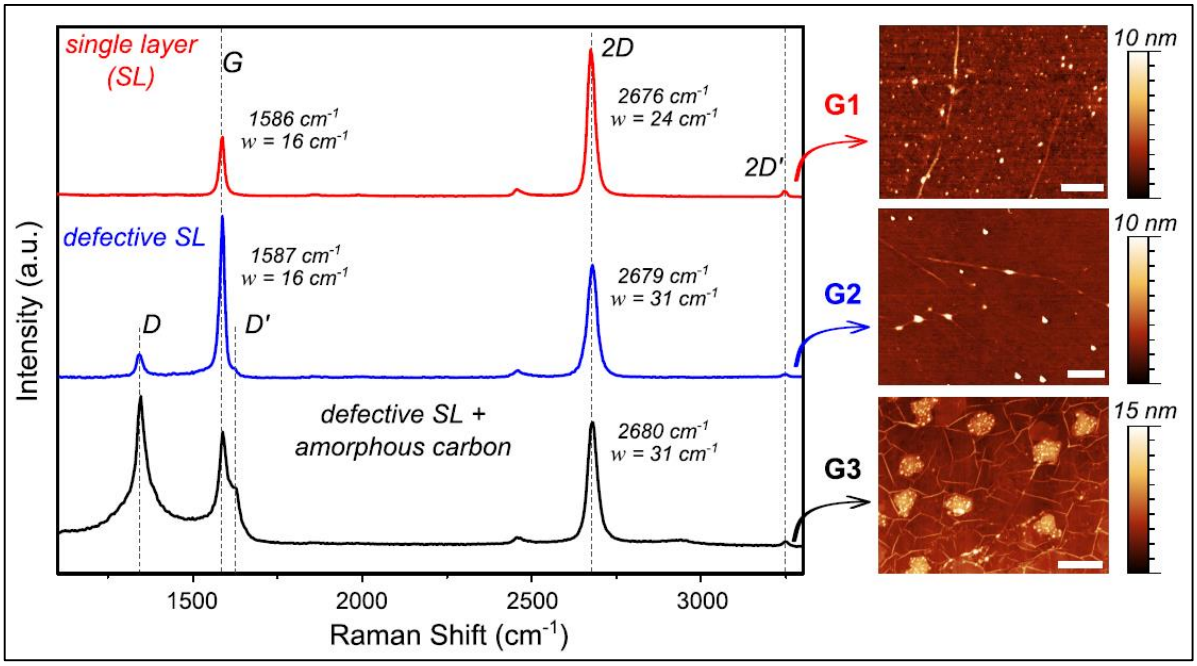

Figure 47 - Raman spectrooscopy on several graphene qualities and corresponding AFM analysis of graphene layers.: Raman spectras show the graphene structural quality decreasing from top to bottom, from a single layer of very good graphene, a low defect multilayer graphene and an amorphous carbon contaminated graphene. The AFM scale bar is 500 nm.Institut Néel – F.Veliev.

Spectra obtained from different portions of graphene can thus give information about the graphene thickness, number of layers or structural defect in the crystal. These information can be estimated from the intensity and position of the specific graphene Raman emission peaks called G and 2D bands and representing following hybridizations [150]:

- **D band**, around 1350 cm^{-1} reflects disorder is present as much as there are defects in the carbon lattice: like grain boundaries, edges, vacancies sites…
- **G band**, around 1580 cm^{-1} is the main first order band corresponds to sp^2 C-C stretching mode, present in all carbon derivate materials. Its intensity rises when increasing number of graphene layers [151].
- **D' band**, around 1621 cm^{-1} is sometimes mixed with G band and seen as enlargement but is consequence of defects.
- **2D band**, around 2700 cm^{-1} is specific to graphene, and corresponds to the in-plane breathing mode of the carbon lattice. It undergoes shape and position changes when increasing the number of graphene layers [152].

Graphene number of layer is determined by evaluation of the ratio between G and 2D peaks. During this thesis I often used Raman spectroscopy to assess graphene quality and improve CVD growth and transfer recipes according to Raman spectroscopy results.

2.4.4 Atomic Force Microscopy

Atomic Force Microscopy on graphene allows **topography** studies by scanning the surface **roughness** with an AFM cantilever, generally in tapping mode to avoid graphene damaging. Topography gives information about defects, wrinkles and contaminants (Figure 48). AFM can scan up to 100 µm wide square and can also use contact mode to modify surface structure, perform lithography or contaminants removal.

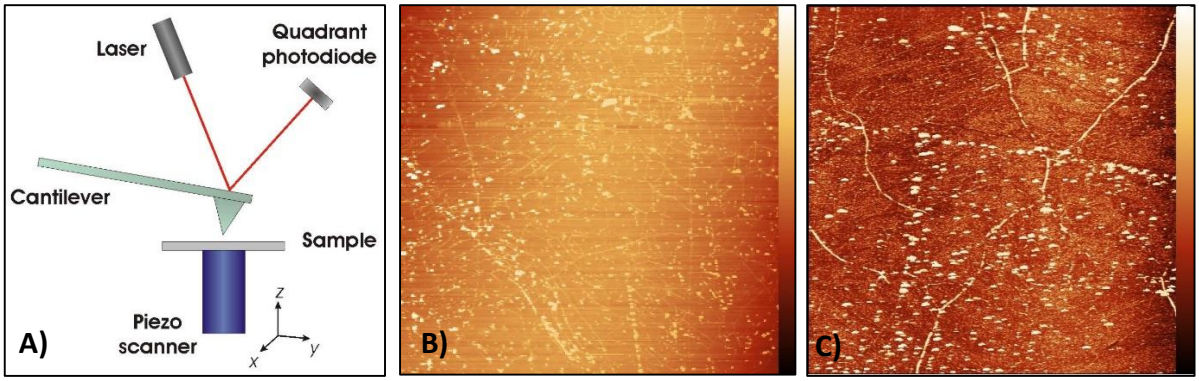

Figure 48 – AFM provide a very good surface contaminants observation tool for graphene ***A)*** *AFM principle illustration , after* [153]. ***B)*** *AFM graphene characterization shows wrinkles high density at 30x30 µm scale with 20 nm thickness scale* ***C)*** *Many spherical like contaminants of 20 nm diameter or more are visible at a 10x10 µm² scale with 20 nm vertical scale from black to white look up table.*

2.4.5 Electrical characterization

As explained in 2.1.1b -, graphene can be used as a 2D material for transistors, using the silicon substrate as a back gate and its covering oxide as a dielectric, when transferred on 280 nm thick silicon oxide or replacing the back gate by liquid front gate. This is made possible on graphene thanks to an interface called electrical double layer that allows field effect detection (see 2.1.1c -).

This process will be detailed in next part when using this transistor detection properties to assess influence of our coating on graphene ability to sense field effect modification despite the thin polymer layer that is covering the sensor.

Graphene is often contacted using **Hall bar** microfabrication (Figure 49) in order to evaluate its electronic properties providing field effect measurement on several points of the devices and for more precision on evaluation of charge carrier mobility, sheet resistance etc… 4 points measurements are used to get rid of contacts influence on the measurements. Those measurement are generally processed under vacuum to avoid graphene contamination and air moisture to deposit as a water thin layer on graphene surface and thus change its properties. One might isolate hall mobility by applying a magnetic field on a hall device. We were not able to conduct this measurement during this thesis but used other methods to measure carrier mobilities.

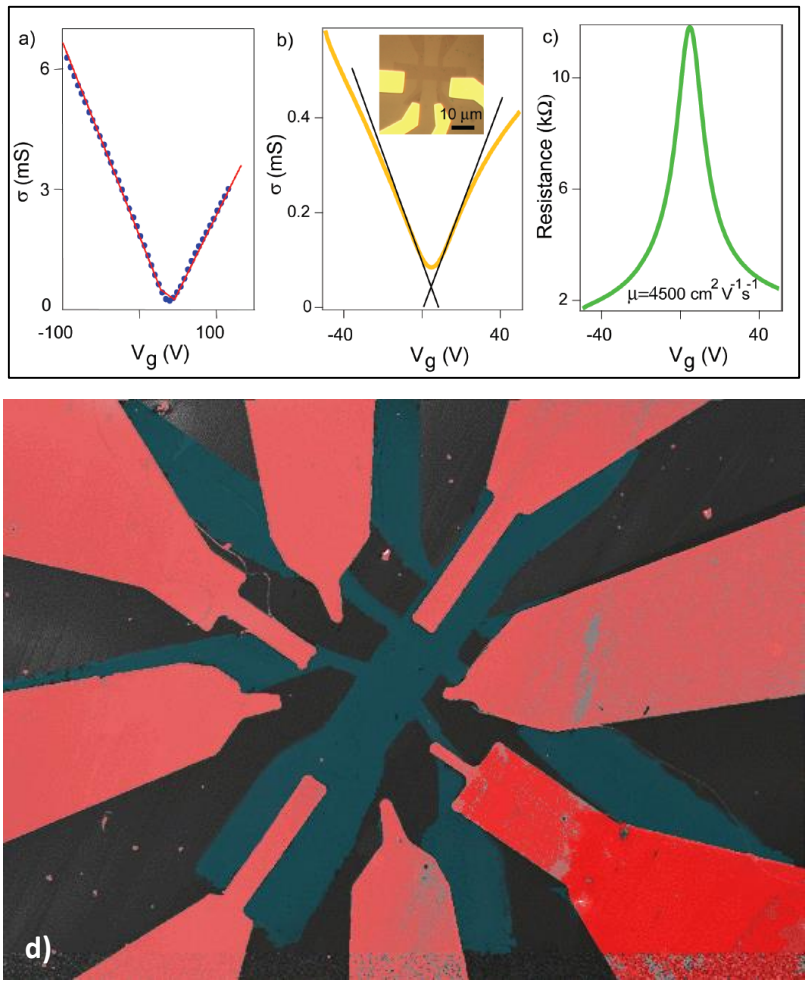

Figure 49 – Hall bars for evaluation of graphene electrical properties: ***A)*** *Reference field effect curve at 70K, shows conductivity as a function of gate voltage. From* [1]. ***B)*** *One of ourteam sample measured at 300 K, from CVD grown graphene. Graphene is plasma etched and contacted with metal electrodes (Au/Ti) to build a Hall bar C****)*** *Resistivity plotted in function of gate voltage. Institut Néel V. Z.Han.* ***D)*** *A Hall bar built during my thesis is imaged with SEM and colored to distinguish in red contacts and in blue graphene sheet transferred and patterned onto a silicon oxide substrate.*

2.5 Conclusion

During this thesis, I investigated how graphene could be a game changer by combining improved bioacceptance and high sensitivity electronics for the first time. For this purpose, I have developed new methods for producing high quality and reproducible graphene by optimizing synthesis and integration.

An important part of this work has been dedicated to graphene growth on copper with our CVD machine. Quality improvement has been brought after modification of the growth recipe according to our patented method. In order to lower contaminants density, I successfully developed a chemical preparation method for copper foil used as growth substrate.

Many transfers of graphene have been done with each growth batch in order to perform Raman spectroscopy, AFM or Hall bar measurements and thus assess my obtained graphene's quality.

The graphene I've optimized during this thesis has been used in our team to evaluate influence of graphene quality on neurons grown in vitro [110]. *I also successfully verified our graphene cytocompatibility by performing cell cultures on graphene coated glass and graphene coated PDMS.*

I have demonstrated the feasibility of transferring graphene on both flexible substrates and silicon oxide surfaces. Transfers techniques on commercial probes I will detail in chapter IV could allow a progressive technological introduction of graphene into the field of in-vivo implants.

III. Bioacceptance Improvements

Improving bioacceptance of an implant or a transplant is often achieved by drug deliverance to the patient. Drugs reduce the inflammation and the immune response in order to minimize the rejection reaction of the body against the implant. However, most of the drugs based on global deliverance do not reach the CNS, since our brain tissues are isolated from the general blood circulation thanks to the blood brain barrier. Consequently, a drug must be delivered locally to chemically reduce the brain reaction to the implant. Current research projects relative to the next generation of neural interfaces are indeed focusing on this approach by providing microfluidic functions to their devices [154] *or hydrogels coating for in situ drug delivery* [155].

Given that my aim is to improve bioacceptance of the devices, I had to anticipate this need. In the same time, the apparent graphene fragility during manipulation of 3D micro machined assemblies led me to think about a protective layer which should keep the integrity of the graphene based devices and prevent delamination during insertion. Moreover, physiological activity in the brain being stronger than in vitro, biodegradation of our graphene could occurs. Since hydrogels could provide drug delivery functions as well as protect the graphene layers from delamination, I investigate in this chapter the possibility of attaching it to graphene based implant and develop a uniform biopolymer graphene coating method that could be of interest for further hydrogels grafting.

CHAPTER III - TABLE OF CONTENTS

3.1 Glial Scar

One over two cells composing the brain is a neuron, whereas the other one is a glial cell [156]. Glial cells provide mechanical, nutritive and immune support to neurons. Among glial cells, we can distinguish Astrocytes, Oligodendrocytes and Microglia. **Astrocytes** provide homeostatic functions as well as energy and nutrition supports. **Oligodendrocytes** insulate axons providing myelin[4] sheath to increase signal propagation efficiency and **Microglia** are the macrophages of the nervous tissue, getting rid of dead cells, cellular debris and pathogens through a mechanisms called phagocytosis, and responsible for recruiting immune cells when necessary.

The glial cells over neurons ratio varies a lot depending on the zone considered. Neocortex, in particular, has a 3,8 ratio with a specific distribution of 75% oligodendrocytes, 18% astrocytes and 6% microglia [157]. This high amount of glial cells in the cortex is important to take into account when trying to explain the inflammatory reaction following the penetrating implant neurosurgery, well known as glial scar formation or gliosis. Inserting an implant trough the motor cortex constitute a local trauma (Figure 50) and consequently triggers a strong reaction of the brain tissue, mainly characterized by a strong mobilization of reactive astrocytes [158].Along this paragraph I will explain the mechanisms involved in the **Gliosis** and the methods available to lower this reaction when penetrating the cortex to sense its activity.

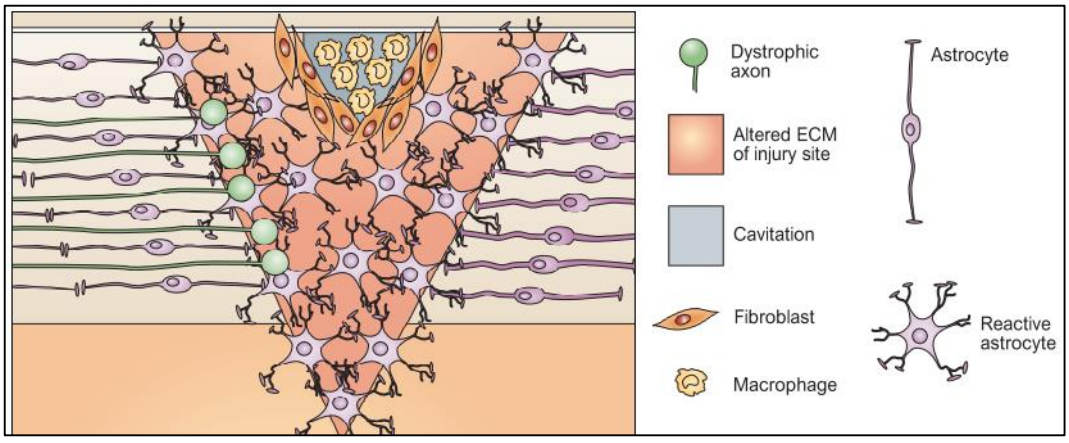

Figure 50 - CNS lesion by meninges penetration of an implant triggers tissue reaction; this representation shows the gliosis reaction process around the lesion, witch reactive astrocyte mobilization, BBB fibroblast penetrating the cerebellum and macrophages brought by blood and by microglia cells differentiation. Dystrophic astrocytes will be a cause for oligodendrocytes migration. Modified from [64]

[4] Myelin is a substance produced by oligodendrocytes which surrounds axons to form an electrical insulation layer. Myelin role is to increase signal propagation speed by a mechanism called saltatory conduction

3.1.1 Blood Brain Barrier (BBB) & Bleeding

The Brain is an indirectly irrigated tissue. The homeostasis of the Central Nervous System (CNS) corresponds to the regulation of its osmolality, ionic concentration, glycaemia, acidity… This homeostasis is carried out through the Blood Brain Barrier (BBB) which isolates CNS neurons from blood circulation[159]. The BBB has an immunologic protection and a highly selective nutrition functions [160] To this end, it is partly formed by endothelial cells, connected in tight junctions that provide a strong restrictiveness. Consequently the BBB has a high electrical resistance around 1,5-2kΩ·cm² in rats [161].

Many astrocytes surround the blood brain barrier and some of their endfeet form a lacework on the outer surface of the endothelial cells: they're called perivascular endfeet (Figure 51). Those endfeet can modulate BBB permeability by influencing many specific transport and enzyme systems which regulate molecular traffic across the endothelial cells [162].

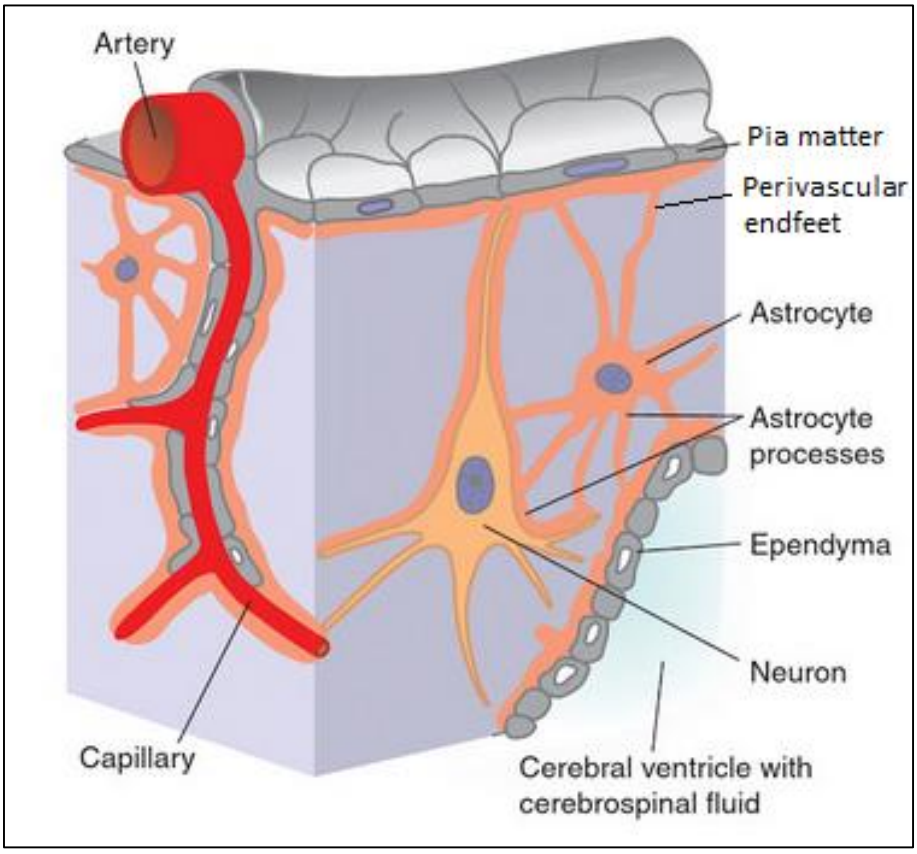

Figure 51 - Brain slice schematics showing the blood vessels, astrocytes perivascular endfeet as intermediates between BBB and neurons. Astrocytes are directly in contact with BBB to perform energy and nutrition support for neurons and other glial cells. Figure modified from [163]

The high concentration of mitochondria and glucose transporters in these endothelial cells testifies to the role of BBB in energy transmission from blood to neurons through BBB covering astrocytes [164]. Astrocytes have a nutritive role to neurons, and are responsible for the maintenance of the Brain Extra Cellular Matrix (ECM) homeostasis. They do so by controlling the endothelium permeability as well as exchanging nutriments and ions between blood plasma and neurons.

As explained in Chapter I, neurons communication ability is based on their electrical potential compared to the ECM's. Ionic concentration differences between neurons and ECM are required to stabilize the resting potential: extracellular K+ control is thus particularly important to that matter. Astrocytes are the main responsible for K+ concentration regulation [165]. Consequently, neurons function stability is linked to proper astrocytes activity.

a - Impact of a penetrating implant on the BBB

Intracortical implants insertion is necessarily inducing a **local breaking** of the BBB as much as an upheaval of ECM homeostasis. ECM stability is paramount to communication between neurons as it allows the electrical potential to be stable along time. Such a traumatism induces the gliosis by migration of reactive glial cells to the **injury location**, in order to preserve damaged tissue[64], repair the blood-brain barrier and restore the lost homeostasis[166].

First, BBB vascular damage induces microglial macrophages recruitment. Then, local communication disruption between neurons provoke migration of oligodendrocytes. Finally, astrocytes, after they have proliferated, will recreate an astrocytic boundary around the implant area by becoming hypertrophic. They undergo cell division and assemble in tight junctions, in a process called "**reactive astrogliosis**". Any axons regeneration attempt will then fail to penetrate this astrocytic glial scar. [167]

Glial fibrillary acidic protein (GFAP), similar to collagen fibres, and important in regeneration process, is synthetized by astrocytes. GFAP can thus be stained with a fluorophore attached to a specific GFAP antibody to locate and count the astrocytes and quantify the glial scar formation with post mortem labelling, as processed during the biocompatibilities studies detailed in 3.3.2 and 4.3.3b -

Figure 52 shows one of this GFAP staining made on a coronal brain slice with a high GFAP concentration in yellow, around the implant insertion site to the deepest cortex layers, testifying of a strong gliosis on both side of the implant ex-location. The high density of

astrocytes around the high blood vessel concentration at the brain surface and around the lateral ventricles is also remarkable (green arrow shows right ventricle).

This process of brain slice staining is called immunohistochemistry and will be detailed later in this chapter.

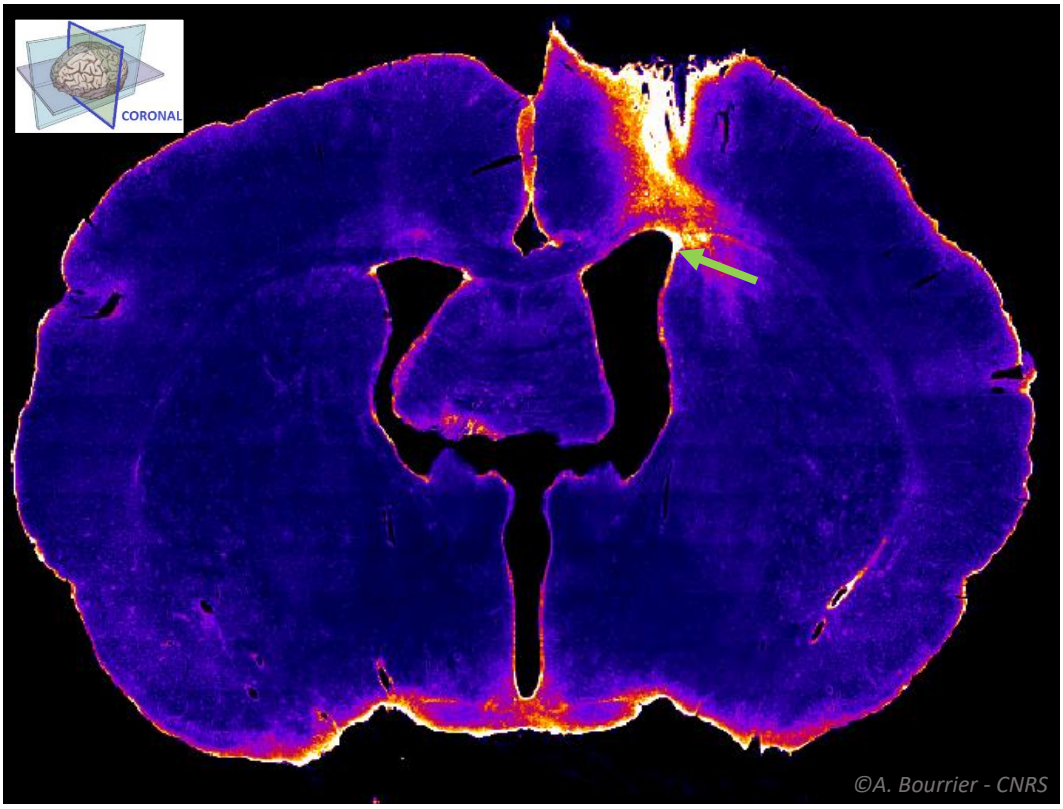

Figure 52 – One of our implanted rat shows strong gliosis around the implant site after 7 weeks. Rat brain Coronal section at bregma -0,9mm three months after implantation of a TDT multi-electrodes Array implant in the left motor cortex M1. GFAP immunostaining shows strong astrocytes migration around the implant location.

b - Impact of a penetrating implant on meningeal cells

The brain is surrounded by 3 layers of meninges: the dura matter, made of fibro-elastic cells, is removed during the surgery we perform. Penetration of the implant is made through thin flat cells membranes called Arachnoid and Pia Matter. The implant carry in some parts of those membrane inside the CNS during penetration. This transplantation of meningeal cells into the CNS leads to a more important astrocytic reaction [168]. This phenomena of general migration around the implant will provoke, after few weeks the formation of a glial scar which will then limit the life time of the implant and its capacity to record surrounding neuronal activity.

3.1.2 Influencing factors on glial scar

There are many reasons explaining the obstructive environment of CNS implants induced injury. Regeneration-associated genes are expressed at low level in the CNS [169]

Following the CNS injury, glial scar is formed and inhibitory molecules are released at the site of injury. Moreover, astrocytes proliferate at the site of injury and form a glial capsule around the implant that physically isolates local neurons from electrode recording sites after several weeks.

Direct measurements suggest that the maximum distance between electrode site and a neuron is somewhere between 50 and 100µm [170]. Thus, the distance required to maintain a recording between an electrode site and a targeted cell body is of the order of cell dimensions.

BBB mechanical breach result in **chronic inflammatory reaction and neurodegeneration**, irremediably leading to electrode **recording failure**[171]. There is therefore a very big interest in reducing the impact of the surgery on the CNS environment to reduce astrocytic proliferation and preserve implant recording functionalities over time.

The gliosis has a transitory nature after the trauma. Electrodes tracks could not be found after several months when electrode was inserted and quickly removed [70]. The **implant occupied volume** and persistent presence increases the tissue response. Many studies have reported the benefits of small implant size [172], sharp design [173] and implant flexibility [70][174][175] to reduce this response.

However, the Szarowski et al. [176] study of the effect of shape, size, and texture (of the intracortical implant) on the immune response suggests that a non-biological approach to electrode design may not be sufficient to overcome the biological hurdles of chronic electrode implantation. Thus, the use of **anti-inflammatory bioactive coatings** [177][178][179] might be necessary to overcome the reactive gliosis.

These techniques and bioactive coating have to be taken into account when designing new chronic brain computer interface implantation strategies.

3.1.3 How can graphene bioelectronics be a solution?

Graphene might be used as a replacement material for actual metal electrodes used on MEA. GFETs could also **improve biosensors sensitivity** and therefore provide a better lifetime expectancy. There are many advantages of developing graphene as an interfacing material on implants.

Its mechanical stability offers the possibility to use it **on flexible substrate** like parylene [123] or polyimide [116], and its inert nature provides a very good biocompatibility [180] although some recent studies reported a strong inconsistency in cytocompatibility depending on the type of graphene used [110]. We investigated this inconsistency and detailed it in the previous graphene chapter. **Cytocompatibility** is defined here as the ability of an in vitro monotype cell culture to survive, adhere and grow on a material.

Graphene can be **functionalized** [181][2] but grafting molecules to this atomic thing monolayer has to be done carefully in order to avoid damages to its structure and its changes in electronic properties, for instance with a too strong doping of the material.

During this thesis, I developed an appropriate graphene synthesis recipe to have stable quality graphene. We did characterize this graphene cytocompatibility in vitro and compared it to other potential surface materials we currently use regarding the actual well spread technologies: silicon[182], parylene[72], polyimide[183] and graphene (Figure 53), Graphene surface shows a way better bioacceptance than silicon, parylene or polyimide. Consequently, graphene transfer is planned to cover the whole implant surface and thus improve general biocompatibility of the implant when in contact with neurons in vivo. Our graphene bioacceptance is also developed in the previous Chapter II.

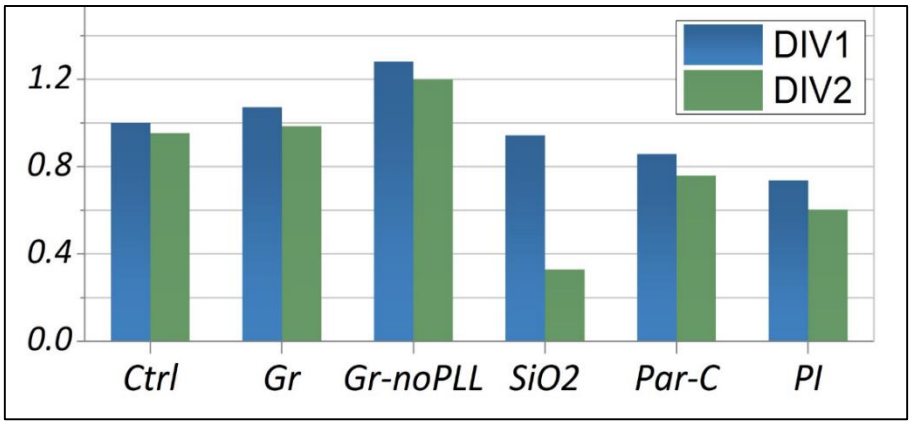

Figure 53 – Cell cultures on our panel of material revealed high graphene cytocompatibility: Statistical in-vitro neurons counting after hippocampal cells spreading on different substrate material has shown graphene to be a better supportive material for neurons development than SiO2. Institut Néel – F.Veliev [101].

Nevertheless, **the fragility of graphene to friction** forces and consequently to a possible tearing off during insertion in the cortex might be a problem that has been identified at early stage of this thesis. I will detail the fabrication process of the implant illustrated on Figure 54 in the Chapter IV on microfabrication.

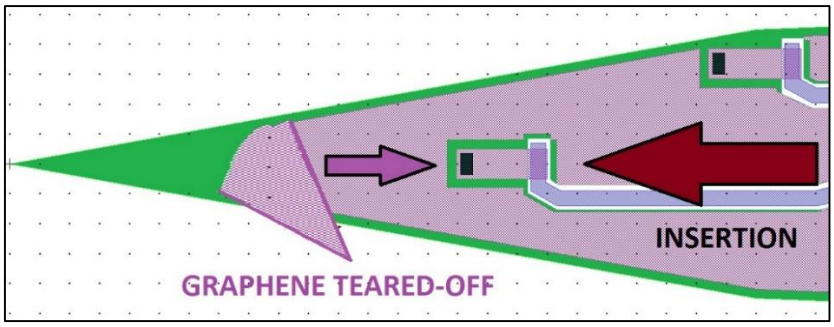

Figure 54 - Implant tip representation shows potential graphene tearing-off during insertion: Insertion through Pia-Matter and CNS tissue, revealing the need for a protective layer to be developed. The electrodes in blue are contacting two rectangular sensors that will be detailed in chapter 4.

I addressed this need by merging it with the pre-developed neuro-engineering field need to develop bioactive coating to reduce gliosis [76], [179]. Developing a bio-polymer coating for preserving the graphene monolayers integrity during implantation was thus a first challenging step for this thesis.

3.2 An active Biopolymer for protection

The first step of this thesis has been to develop a **protective biopolymer** that can be grafted to graphene without altering its properties and integrity. In collaboration with expert biochemists in this field, we investigated Hyaluronic Acid (HA), a natural biocompatible polymer, and customized it to coat our graphene monolayers. The customization purpose was to enhance the HA adhesion on the highly hydrophobic graphene.

A multilayer polymer deposition is also investigated as a premise for **future drug delivery hydrogel grafting** as illustrated on Figure 55. It would allow progressive drug delivery as much as provide a soft and chemically favorable surface for CNS injury healing.

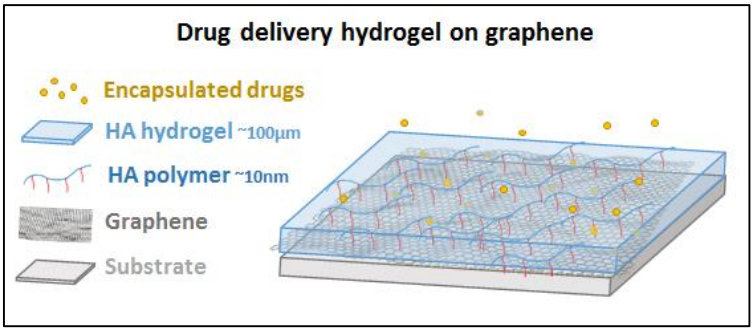

Figure 55 - Covering graphene surface with a degradable drug delivery hydrogel could allow reduction of inflammation during the few weeks following implantation, thanks to its soft surface and drug activity. It could also provide a robust protective layer for graphene. HA hydrogels must be grafted on a uniform layer of HA polymer. We thus investigated how to cover graphene with a uniform layer of HA polymer.

3.2.1 Polymer selection

We investigated a bio-polymer well known as adhesion basis layer for hydrogels and drug delivery multilayer assemblies: HA (Hyaluronic Acid) [184].

Hyaluronan or hyaluronic acid (HA) is an **omnipresent glycosaminoglycan found in the extracellular matrix** in many connective tissues including the brain (Figure 56). It is an interstitial protein that insures the coherence of the tissue and interacts with proteoglycans to form a mesh-like structure in the perineuronal network [185].

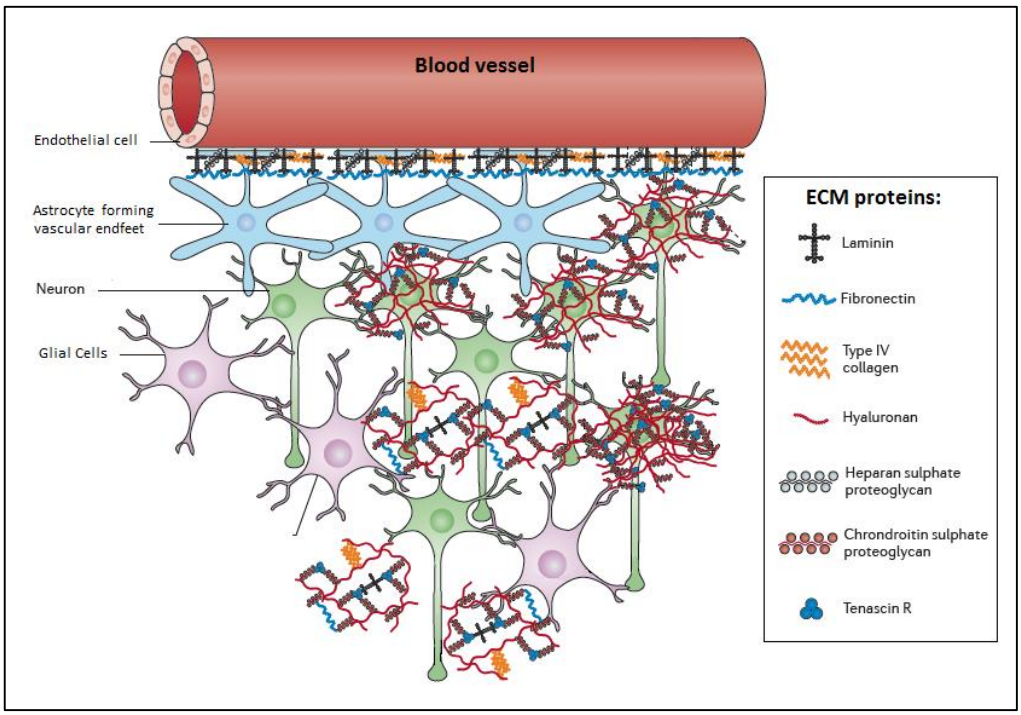

Figure 56 - Representation of CNS Extracellular Matrix components illustrates Hyaluronan role: we can see the neurons nutrition mechanism through the Blood Brain Barrier basement membrane and the complex protein net that constitute the neural interstitial matrix. Hyaluronic Acid (Hyaluronan) is one of the most present protein of the ECM. Adapted from [15]

In the CNS, hyaluronic acid is naturally and slowly biodegraded by a specific category of enzymes, the hyaluronidases [186]. Numerous research have previously focused on HA for tissue engineering and drug delivery [187]–[189].

Encouraging previous studies also showed potential gliosis inhibition by HA [166] and HA implication in wound repair[190]. Hyaluronic acid and its derivatives are thus some very good biopolymers to be use as our graphene sensor coating, in order to increase our implants bioacceptance and lower gliosis.

First, we tested HA absorption on bare graphene using different molecular weights of HA, between 600.000g/mol and 200.000g/mol. Observations where made with a microscope direct control of graphene integrity after functionalization.

a - Fluorescence characterization of integrity issues

A fluorophore FITC (Fluorescein isothiocyanate) was grafted to our polymer layer in order to track the uniformity of adsorption on the graphene coated glass slide. HA is hard to graft directly to FITC. However, PAH (Polyallylamine hydrochloride) is also a good candidate for multilayers assemblies [191]. PAH is indeed a biocompatible precursor to encapsulate drugs in hydrogels[192] and can be grafted with FITC and HA. We have consequently chosen PAH to characterize HA adhesion on our graphene. PAH-FITC and bilayer HA-PAH-FITC were adsorbed on 12mm diameter monolayer graphene pre-covered glass slides and observed under fluorescence microscope with excitation wavelength filter at 495 nm and emission filter at 519nm. Graphene layer was often showed damaged like shown on Figure 57 when using PAH. Fluorescence microscopy picture suggested that PAH-FITC and HA-PAH-FITC were not present on graphene.

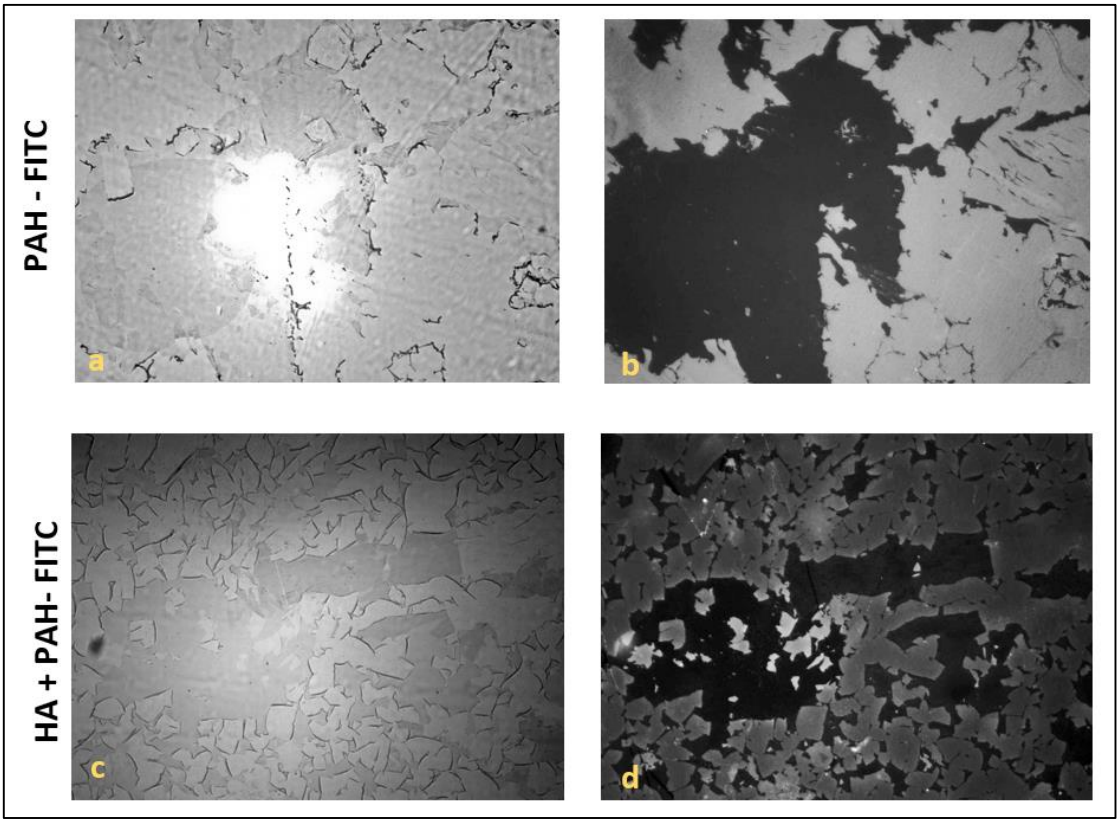

Figure 57 - Optical Microscopy on left and FITC fluorescence microscopy reveals graphene tearing off by saline solution drying: on right micrography reveals damages caused to graphene layer in black) after PAH-FITC layer adsorption; the graphene shows FITC emission, suggesting no PAH adhesion.

b - Fluorescence quenching assessment on HA/PLL bilayers

PAH was identified as an incompatible polymer to preserve graphene surface as shown on Figure 57. However, we were used in our team to coat graphene with Poly L-Lysine without issues. Next experiments of multilayer assemblies were thus made using PLL of PLL-FITC instead of PAH.

Despite the damages provoked to graphene, those previous results suggest HA and PAH absence on graphene because of the absence of fluorescence expression on microscopy imaging. However, it was shown that a proximity phenomenon called Förster Resonance Energy Transfer (FRET) might occurs as it seems to happens with many fluorescence markers on graphene [193]. FRET is a non-radiative energy transfer between two close molecules that interact as dipoles: one donor and one acceptor. Graphene has been shown to be a good energy acceptor in energy transfer due to its peculiar electronic properties. It is an efficient quencher for electronic excited states of dyes and dots. When fluorescence imaging is made on graphene, FRET occurs from the fluorophore to graphene and fluorescence is cut. This phenomena is known **as fluorescence quenching** [194]

In order to verify if this phenomena occur on our samples, we functionalized two glass slides half covered with graphene with two different thickness of polymer. Thickness of polymer is tuned by changing the amount of layers adsorbed on our graphene. To create multilayer assembly, one must alternate adsorption process with two polymers that have good affinity one for each other, like HA and PLL.

We thus proceeded to the coating of our samples with 2 and 4 bilayers of HA-PLL before a PLL-FITC layer. By increasing the number of layers, we increased the distance between the fluorophore and graphene, one layer being around 5nm thick (assessed by AFM). According to the scheme on Figure 58, only half of the glass slide have been covered by graphene to be able to compare the intensities of fluorophore emission between glass and graphene covered by the same layer of polymers.

The presence of 1 HA/PLL-FITC layer revealed a 2.4 Ratio of Intensity (ROI) between graphene and glass whereas 4 layers assembly 4x (HA-PLL) + HA-PLL-FITC revealed a ratio of 1.24. The 50nm distance increasing between graphene and fluorophores induced a 48% reduction of the ROI, proving that quenching phenomena depends on the distance from graphene and can explain the previously seen absence of uniform polymer coating on graphene when imaging HA-PAH-FITC layers. A distance between fluorophore and graphene superior to 100nm should be sufficient to avoid FRET occurrence.

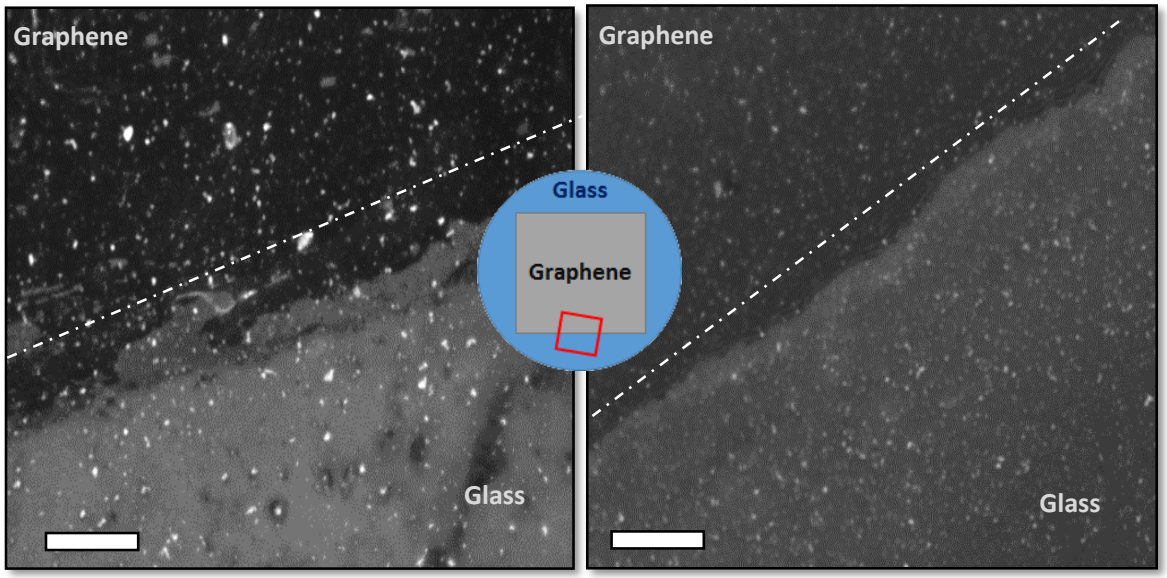

Figure 58 - Fluorescence quenching intensity is tuned by the number of HA/PLL bilayers under HA/PLL-FITC. The location of the pictures on the sample is illustrated. On left 1 bilayer HA/PLL-FITC shows a 2,4 Ratio of Intensity (ROI) between graphene surface on glass and naked glass surface. On right, the use of 4 bilayers of HA/PLL before HA/PLL-FITC decreased this ratio by 48% to 1,24. 1 Layer thickness=5nm. Scale bar is 10µm.

c - Raman spectroscopy analysis of HA on Graphene

In order to assess the presence of polymer and preservation of our graphene underneath, I then proceeded to Raman spectrum analysis with a Jobin Yvon T64000 Raman spectroscope, a 488nm laser source and x50 optic. Previous samples with PLL-FITC inducing too much noise on Raman spectrum, thus, I tested HA alone on some graphene coated glass slides.

I performed three measurements per graphene sample with an approximate 1µm wide spot (size of the laser spot) after coverage by one layer of HA only. Raman spectrum of those spots showed very good **graphene integrity** as much as the **undeniable presence of Hyaluronic Acid** main peaks (Figure 59).

The Graphene Raman resonance peaks:

As a reminder from Chapter II, graphene integrity is determined by evaluation of the ratio between specific graphene peaks, this peaks are the indicator of atomic bonds in graphene, and thus shows crystalline structure of graphene:

- G band, around 1580 cm^{-1} the main first order band and correspond to sp^2 C-C stretching mode, present in all carbon derivate materials.
- D band, around 1350 cm^{-1} Disorder, is present as much as there are defects in the carbon lattice.
- 2D band, around 2700 cm^{-1} is specific to graphene, and correspond to the in-plane breathing mode of the carbon lattice.

HA Raman resonance peaks:

Hyaluronic acid specific peaks have been previously determined[195], [196] as followed in Figure 59 and are underlined (red curves) in the Raman spectrum (Figure 60).

Raman Shift	Band assignment	Raman Shift	Band assignment
899	β-linkages, C_1-H deformation,	1210	CH_2 twist
945	Skeletal C-O-C linkage stretch	1330	Amide 3, C-H bend
1045	C-O, C-C links	1370	COO^- stretch, CH_3 deformation
1090	acetyl group, C-OH bend	1410	COO^- stretch, CH_3 bend
1130	C_4-H and C_4-OH bends	1460	CH_2 bend
1150	C-O, C-C, Oxygen bridge		

Figure 59 - Raman bands for Hyaluronic Acid observed for solid HA. Assignments are based on previous Raman studies of HA [195], [196]

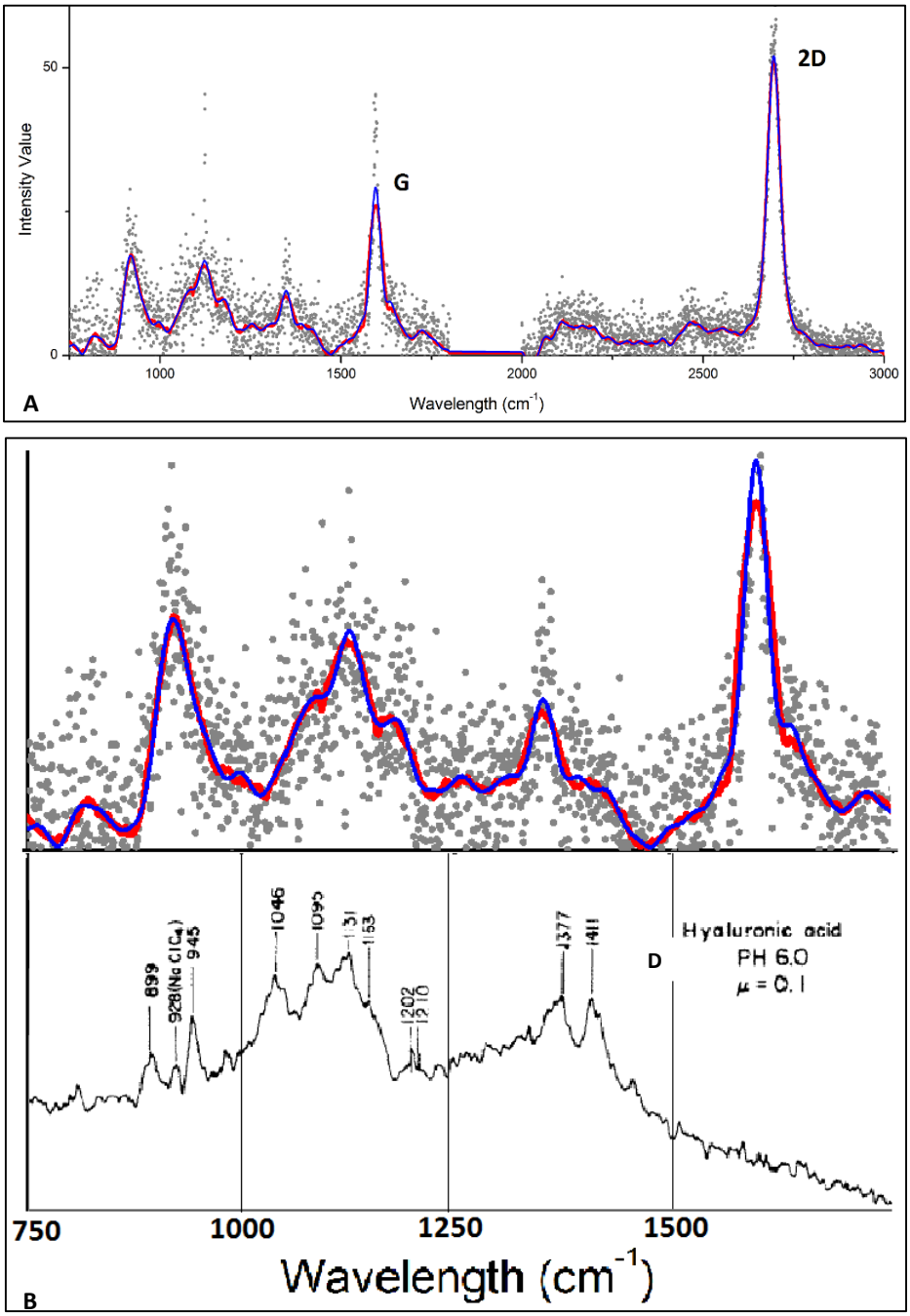

Figure 60 – HA coating of graphene monolayer is confirmed by Raman spectroscopy: ***A*** *Raman spectrum good integrity graphene specific peaks at 1352, 1560, 2699 cm^{-1}, purple graphene only spectrum is superposed to the graphene on HA orange peak.* ***C*** *A close-up view on our Raman measured peaks for HAa compared with literature reference peaks for HA* [196] *shows typical HA polymer peaks at 899, 950, 1090, 1180 and 1450 cm^{-1} confirming HA presence on top of good quality graphene.*

This last experiment confirms the distinction of Hyaluronic acid as a uniform covering polymer that seems to preserve typical graphene Raman peaks intensities (as shown in chapter II). Raman study suggests graphene crystal integrity after HA adsorption and thus opens the way to layer by layer assemblies on graphene, providing for instance drug delivery hydrogel adhesion possibilities.

3.2.2 Adhesion optimisation

a - Homogeneity of the functionalization

Hyaluronic acid film should be uniform and the coating process reliable on the graphene monolayer. Because the first layer is crucial for the next sur-imposed layers (HA multilayers or hydrogel film) on the future implant, a characterization strategy have been set up to determine the ultimate parameters of coating process and molecular weight used to functionalize graphene. First, drop angle contact measurements have been processed systematically to assess the polymer **incidence on the graphene hydrophobicity**. This study has shown the ability to tune graphene monolayers hydrophobicity as function of the HA molecular weight (Figure 61).

Increasing Hyaluronan molecular weight lowers the final (coated) surface tension, confirming the graphene functionalization, and the homogeneity of the HA coverage.

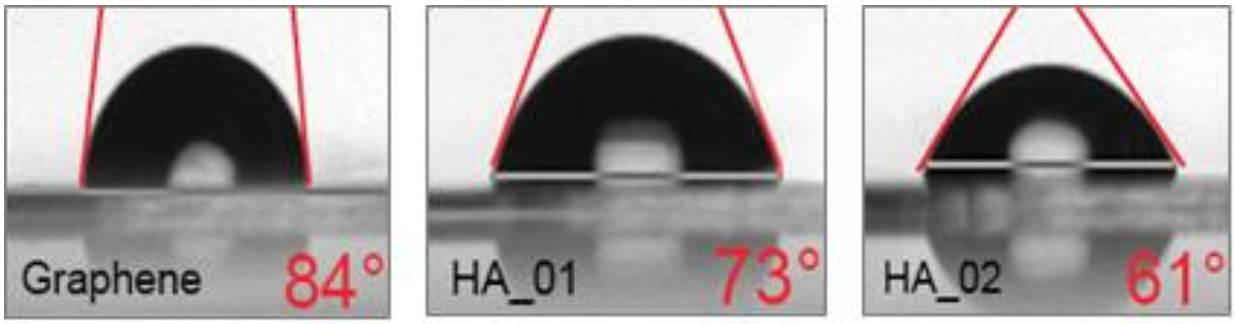

Figure 61 – Drop angle contact measurements as function of the HA molecular weight which tuned the hydrophobicity of the coated graphene. From left to right, pristine graphene (without coating), HA_01 is a 100000g/mol dilution of polymer and HA_02 is 200000g/mol diluted.

Poor repeatability of adhesion was encountered during the hydrophobicity tests. Nearly all samples showed rough HA agglomerates on the surface (Figure 62). For this reason, we have investigated new ways to reinforce the adhesion between HA and graphene.

HA backbone is known to adhere with a better **uniformity** to hydrophilic surfaces. Nevertheless, naked graphene on glass is very hydrophobic, with an average drop angle of 84°. This mismatching between surface tension affinities could induce HA agglomerates as often observed on our graphene monolayers.

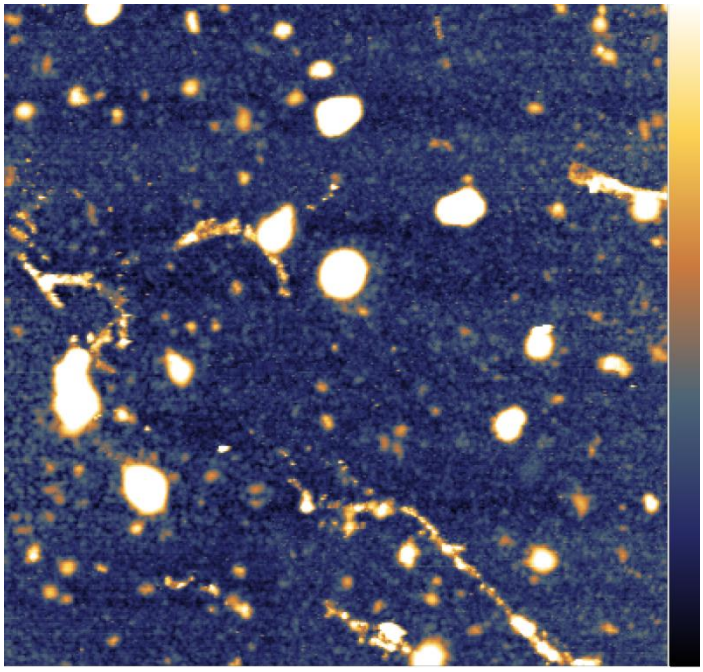

Figure 62 – Atomic force micrograph (non-contact mode) performed on HA coated graphene (10 x 10 µm size) showing agglomerates of HA (brightness areas).Color z-scale is 10 nm.

b - HA Alkyl-amino hydrazide derivatives

The solution found to improve adhesion on hydrophobic substrate is a biodegradable alkylated HA polymer [197] presenting many alkyl hydrophobic chains all around Hyaluronan backbone (Figure 63), which should provide a better adhesion to graphene. The alkylated Hyaluronic acid is also capable of releasing hydrophobic drugs in a controlled manner by changind the amout of layers and their molecular weight[198], [199]. Alkylated HA (HAa) has been, from here, systematically used as the first layer to put on top of graphene.

As proven by previous studies by Kadi et Al. [197] HA derivatives have a tendency to aggregate on themselves, and therfore it is paramount to use **short alkyl chains** and use a step by step multilayer assembly **with alternance of HAa and PLL**.

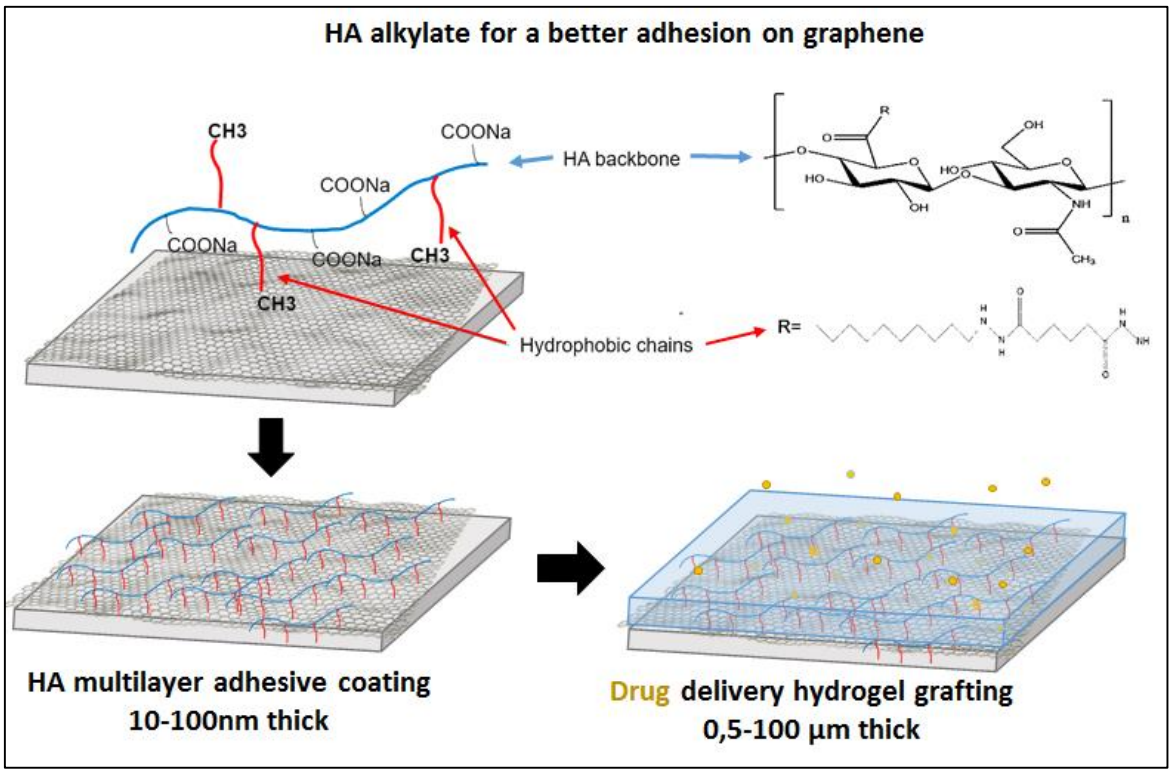

Figure 63 - Alkylated HA structure and adhesion principal for future drug delivery hydrogel grafting. Alkylated HA is made of a HA backbone and a given density of alkyl lateral chains to provide adhesion on graphene hydrophobic surface [197]. *Once the graphene surface uniformly coated with HAa, HA backbones are exposed on the surface and allow drug delivery HA hydrogel grafting for progressive encapsulated drugs delivery* [199].

Uniformity of the covering has first been investigated with AFM, showing a “spider web” like network (Figure 64) when dried before AFM characterization. This spider web phenomena was amplified on too quick dried processed samples as much as low number of bilayers coating (<2 bilayers) and the ideal functionalization process has been found using AFM systematic characterization after drying the samples.

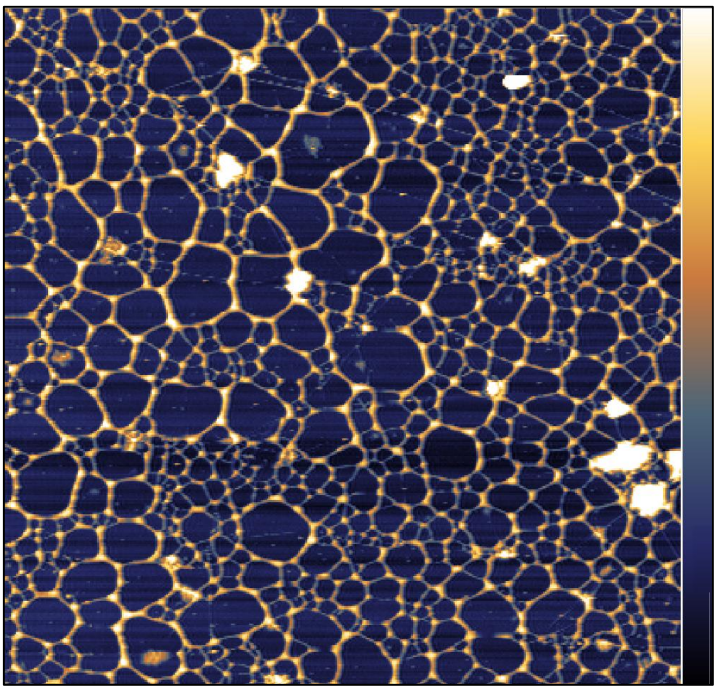

Figure 64 – Spider web aspect of the surface polymer suggest lack of matter provoking resorption during dry process: AFM 10x10 µm picture of HAa monolayer coated graphene showing "spider web" partial covering of the surface. Color z-scale ranges from 0 to 10nm thickness. The brighter yellow is the thicker, the darker blue is the lower areas (z=0nm).

The coupling of AFM and SEM imaging allows precise graphene integrity evaluation as much as roughness and coverage ratio of the HA Coating. SEM imaging on HA coated graphene require a lowering of the gun tension to avoid surface burning testified the presence of an organic polymer on the surface.

Nevertheless, using very low (1.5kV) gun tension, a slight increasing of contrast on graphene wrinkles also testified of the presence of the layer on the surface, and is confirmed by AFM imaging (Figure 65, the white arrow underline low contrasted wrinkles before the coating). AFM allows surface topographic characterization giving a roughness indication of the given sample.

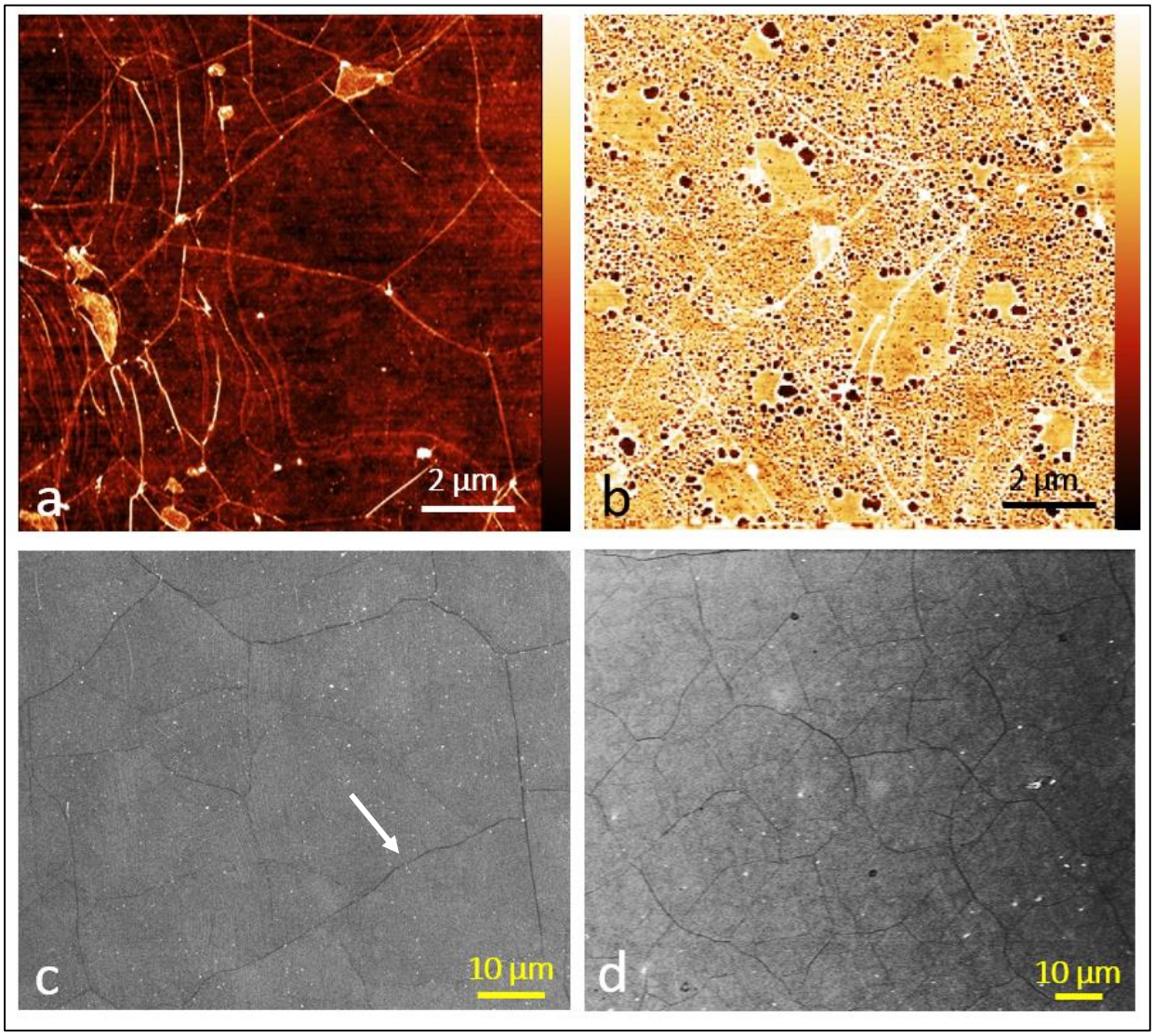

Figure 65 – Graphene surface before and after HA alkylate adsorption testify of the uniformity of coverage by the biopolymer: a) and b) 10x10µm AFM characterization of graphene surface respectively before and after 5 HA/PLL bilayers adsorption. Color scale goes from 0 to 10nm thickness. We can see a uniform coating of the whole surface minus some regular holes that could be covered using a larger amount of bilayers; Nevertheless the obtain roughness is known to present a better bioacceptance [200] *c) SEM picture shows graphene naked using 5kV E-gun tension. Little white dots are some graphene contaminants d) after adsorption of HA on graphene, 1kV e-gun SEM shows wrinkles integrity and suggest quasi-uniformity of the surface coverage by HA polymers, despite few agglomerates.*

c - Impact of HA on graphene electronic properties

Given the fact that the graphene field effect transistors (GFETs) or MEA should still allow the detection of ultra-low extracellular signals associated to the neuronal spikes despite the presence of the protective top layer, we have assessed the impact of HAa on the GFETs sensitivity by fabricating GFETs on silicon (Figure 66A) and measuring the transconductance of many devices before and after functionalization. In particular, the charge carrier mobility measurement of the GFETs allowed us to estimate the doping induced by our functionalization. GFETs have been micro fabricated with cleanroom processing (detailed in chapter IV) by contacting a monolayer graphene sheet, previously transferred on a oxidized Si wafer, with gold electrodes (Figure 66).

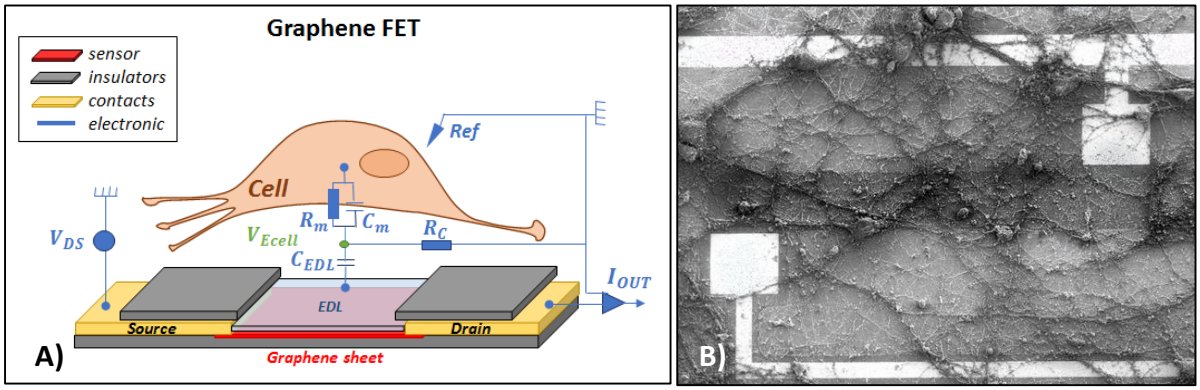

Figure 66 - Neurons in situ grown onto graphene Field Effect Transistors. ***A)*** *Principle of extracellular detection of neurons spikes and the GFET electronics showing liquid gating measurement process.* V_{DS} *Corresponds to drain source polarization tension and* C_{EDL} *to the Electrical Double Layer Capacitance responsible for the gating insulation.* ***B)*** *SEM picture of neurons grown on a FET showing multiples neuritis and soma covering the G-FET. They will act as a front gate for the transistor and the two electrodes will allow detection of activity by Drain Source current measurement. From F. Veliev* [101] *Scale bar is 50µm.*

According to the measurement and fitting process explained in chapter II – part 1, we extracted from the measurements the capacitance of the graphene transistors related to the applied liquid gate voltage, before and after functionalization (Figure 67).

Here, we performed a liquid gating in PBS instead of back gating to be closer to biosensing application of our functionalized GFET. The oxide capacitance $C_{ox}$is no longer the same and we should instead use Electric double layer capacitance C_{EDL}= 0. 78 µF/cm².

We were interested on extracting charge mobility μ in order to evaluate the changes on interfacial capacitance bring by functionalization.

I used Igor software (WaveMetrics, USA) in order to perform the fitting technique (see chapter II part 1) by incremental approach to find the right parameters and thus I have been able to

deduce the doping induced and detect the number of added charges on the graphene after functionalization shown on Figure 67. We can see that HAa adsorption on GFETS **shifted the neutrality point by negative doping** and slightly lowered the conductance probably given the covalent bounding of HAa onto graphene. The contact resistance is unknown and thus justify the use of a constant mobility fitting model. A variable mobility model, based on the formula $\mu = \frac{\sigma}{C_g V_g}$ could give a more precise illustration of the mobility in function of the carrier density if the contact resistance were known.

The fit results show a **29% loss in hole mobility** and **25% loss in electron mobility**. Two phenomenon occur: a change of interfacial capacitance, characterized by both h+/e-mobility decreasing, and a change of quantic capacitance, a very small doping in holes, characterized by the difference of charge density change between holes and electrons: the charge density brought by the functionalization is expressed by Δn_d as:

$$\mathbf{\Delta n_d} = \frac{C_{gD} \Delta V_d}{e}$$

- C_{gD} is the gate capacitance of the device extracted from the Liquid ionic capacitance C_g = 0,78 µF/cm² and the Device area S_{GFET} = 200 µm². We obtain: $\mathbf{C_{gD} = 1{,}6x10^{-12}\ F}$.
- ΔV_d is the shift induced by HA coating is $\mathbf{\Delta V_d = 0{,}46\ V}$.

Consequently: $\mathbf{\Delta n_d = 4.10^6\ e^-}$

With this amount of charges brought on top of the device, we can estimate an average surface covering ratio from the internal charge of hyaluronic acid. The Mulliken charge $\mathbf{M_k}$ for absorbed molecule gives the amount of charges, in elementary charge ratio, that a molecule can exchange with a surface. The polar surface coverage $\mathbf{P_{SC}}$ gives the projected surface of a molecule on a surface. For an accurate estimation, one may take into account the availability of charge in dipoles, that we can approximate to 4% to 11% according to previous work of grafting molecules on nanotubes [201].

Thus, the charge density brought by a full covering of the device would be:

$$\mathbf{\Delta n_{full} = [0{,}04\text{-}0{,}11].\ M_k.N}$$

The hyaluronic acid is made of D-Glucuronic acid and N-Acetyl-D-Glucosamine chains for which $\mathbf{M_k = 0.65\ e^-}$ [202] and $\mathbf{P_{SC}}$ = **1.25 nm²** [203], we can thus calculate the theoretical amount of molecules on a fully covered FET: $\boldsymbol{N = \frac{S_{GFET}}{P_{Sc}}} = 1{,}7.10^8$ **.**

We obtain $\mathbf{\Delta n_{full} \approx 4{,}4.10^6}$ **to** $\mathbf{1{,}2.10^7 e^-}$

Thus, we can estimate our device surface covering ratio $\mathbf{\Delta n_d / \Delta n_{full}}$ to be between 35 and 90%.

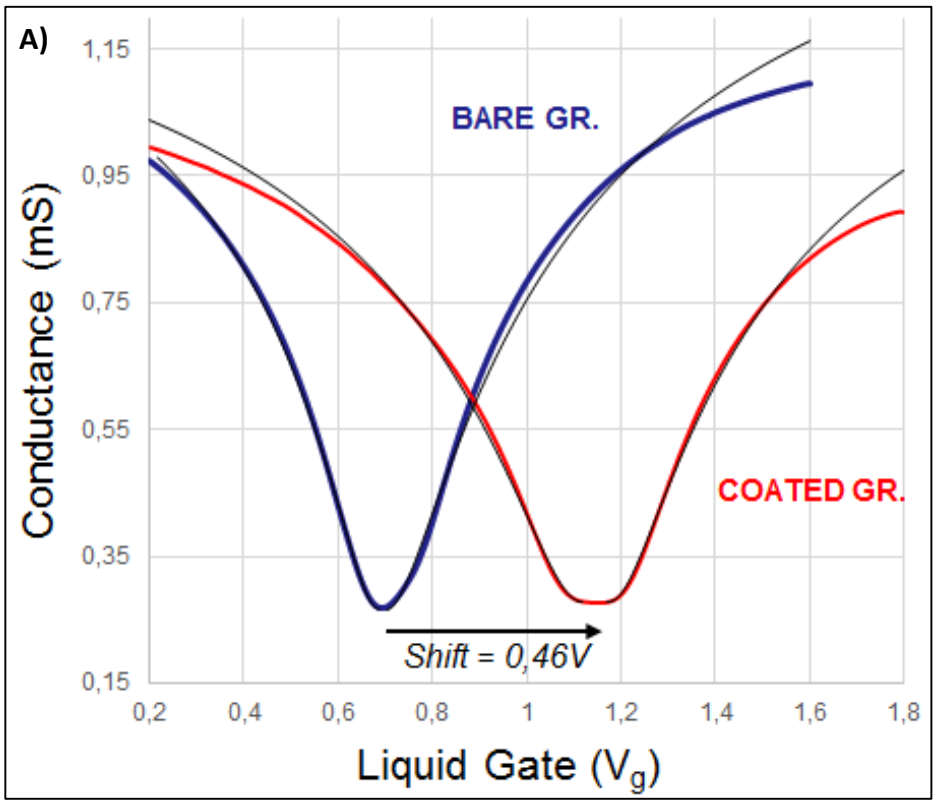

B)

	Mobility µ ($cm^2.V^{-1}.s^{-1}$)			Charge Density n (nbr/cm^2)		
	Naked	**Funct**	**%Var**	**Naked**	**Funct**	**Δnbr of charges**
Holes	2855.0	2024.0	-29.11	7.10E+11	1.057E+12	3.466E+11
Electrons	2725.9	2038.5	-25.22	7.26E+11	1.056E+12	3.303E+11
%Var h+/e-	4.52	0.72		2.26	0.03	

Figure 67 – Resistance of the GFET channel (10x20µm) as a function of the applied voltage in the liquid gate before (yellow curve, on the left) and after (red curve on the right) HAa coating. The charge carrier mobility and density are extracted from numerical simulations (black curve, equation details in the corresponding chapter of the thesis). Adsorption of HA on the graphene monolayers shifts the neutrality point revealing a negative doping of our transistors. ***B)*** *Table showing charge carrier mobility and charge density before and after functionalization. Both electrons and holes regimes are evaluated to compared which carrier is the more impacted by the functionalization.*

Hyaluronic acid functionalization of our device has not damaged the sensor (Figure 60) nor suppressed its sensitivity (Figure 67) and thus should still enable GFETs to sense neurons spiking. Graphene field effect transistors are one of **the most sensitive tools** to assess for the surface state modification of the graphene monolayers by the presence of HA and also for the potential alteration of detection of neuronal signals. However, GMEA have also been successfully used for sensing neuronal activity [106] and the impact of HA on the capacitive interfacial layer should also be considered for their future integration on the implants made during this PhD (chapter IV).

3.3 Biocompatibility assessment

The adhesion of neurons to the sensors is a key feature for extracellular recording as it defines the seal resistance and thus the amplitude of the extracellular voltage sensed by the GFETs (Figure 66). Because the neurons growth depends on their adhesion to the substrates, we can estimate the impact of the new HA layer on the **Neuron-GFET coupling** by assessing the neuritogenesis on bare (control) and HA-coated samples. Thus, the last step developed in this chapter is the study of the graphene - polymer assembly cytocompatibility in vitro and its bioacceptance in vivo.

3.3.1 In vitro cell cultures

Firstly, in the same way we have assessed graphene cytocompatibility (chapter II), we have used glass slides coated with standard adhesive polymer Poly-L-Lysine (PLL) and compared them with HAa coated glass slides. The results of this study are detailed in the Figure 68. Although AFM imaging of dried samples previously showed uniform coverage (Figure 65), the **HAa monolayer does not provide a good uniformity** in cellular culture medium.

a - HAa Monolayer cytocompatibility

Three IF staining were used, to mark for the synapses, microtubules the axon and the soma. Imaging was processed on the whole surface of the sample, using an automated step by step merging mode on a Carl Zeiss Axio M1 fluorescence microscope to reconstruct very large pictures of the samples.

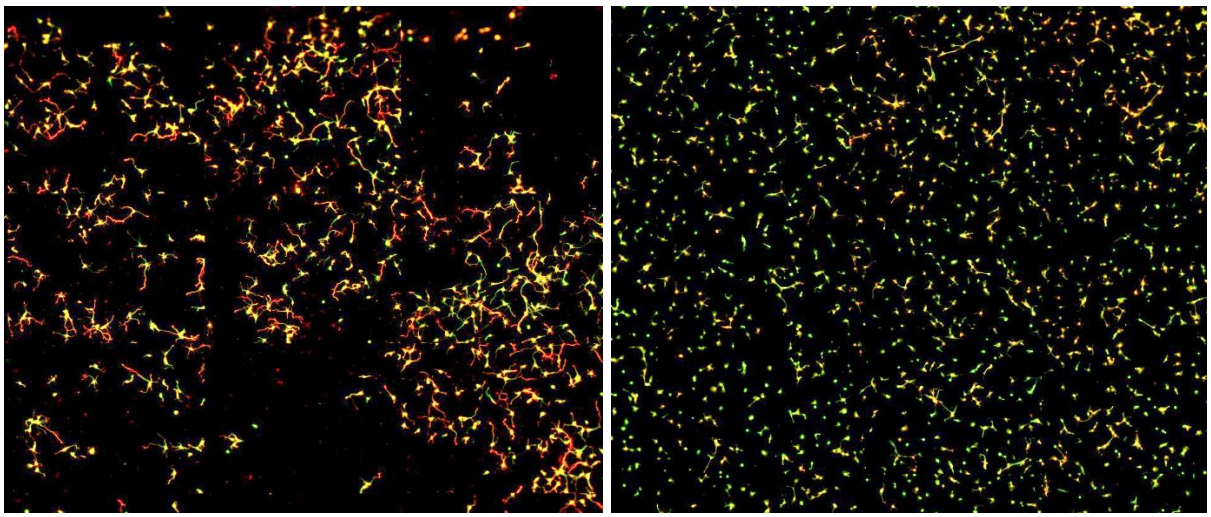

Figure 68 - In vitro study showed one layer of alkylate HA was not providing sufficient uniformity. Primary hippocampal neurons grown on 5 (HA/PLL)-bilayers shows a better coverage of the surface after 5 days in culture, proving an improvement of neurons network development than on the (control) PLL-coated glass sample (left). It suggests an enhanced cytocompatibility thanks to the biopolymer. Soma, neurite and synapses are labeled in blue, green and red respectively. The axon stained in infrared is not shown on this immune-fluorescent micrograph.

In order **to improve the coverage uniformity** of our samples and thus the cell seeding uniformity, we have thickened this polymer layer by assembling **5 bilayers of our biopolymer** and then seeded neurons on their surface to observe the neuron network development (Figure 69). Four 12 mm diameter glass slides where prepared and HA have been adsorbed in several layers separated by PLL polymer. In the end PLL and HA terminated 4 bilayers coated glass slides were obtained. In vitro assessment was made by spreading mouse embryo hippocampi neurons on the surface of the different investigated coated slides (see materials and methods3.5.3). Control samples only use one layer of PLL. Once neurons spread, Immuno-Fluorescence (IF) staining were made 5 days after cells were spread on the surfaces and neuronal network formation started on the substrates.

I compared the cell's growth behavior by comparing the surface covered by the neurons, calculated using a brightness threshold on ImageJ software (method detailed in chapter III - methods). The expression of each of the markers is displayed in Figure 71. The soma (blue) indicated the % of attached cells with respect to the seeding density, and the microtubule give

insight on the neurite's growth while the expression of the tau proteins gives an insight of the axonal polarization which should be reached after 3-4 days in cultures. Neurons have been fixed and stained at DIV5[5]. As shown on the histograms, all proteins are significantly more expressed on the HA/PLL coated samples whereas the control PLL coated samples demonstrate that our coating successfully improves neuronal development by increasing all coverages from 15 to 30% after 5 days of cell growth.

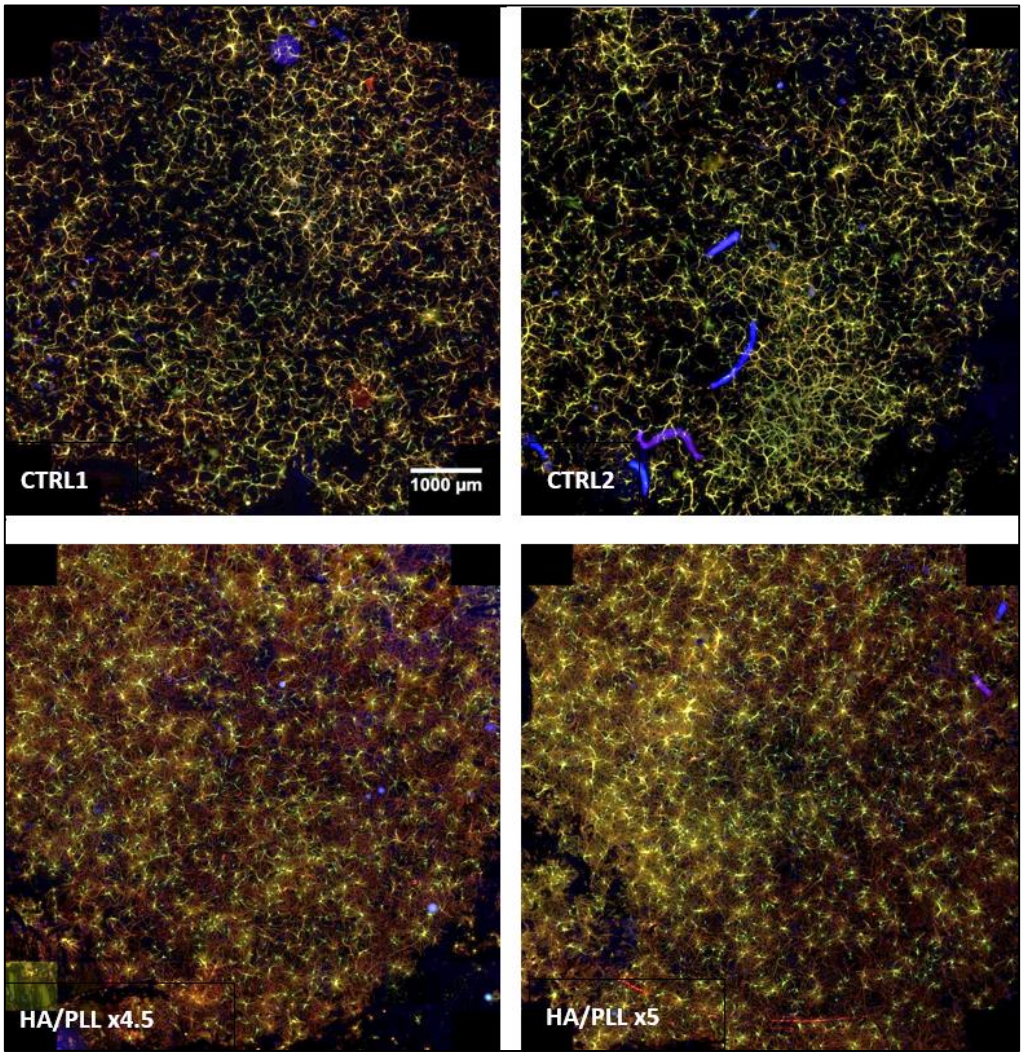

Figure 69 - In vitro study showed great improvement in neurite growth on our custom polymer: Those pictures are reconstructed by step by step merging. Primary hippocampal neurons grown on 5 (HA/PLL)-bilayers shows a better coverage of the surface after 5 days in culture, proving an improvement of neurons network development in comparison to (control) PLL-coated glass sample (left). It suggests an enhanced cytocompatibility thanks to the biopolymer. Soma, neurite and synapses are labeled in blue, green and red respectively. The axon stained in infrared is not shown on this immune-fluorescent micrograph

[5] DIV is used for Days In Vivo and indicates the number of days since cells were seeded on the surface

b - Surface coverage analysis

Image analysis was process using image J for nucleus counting and neurons surface occupying rate measurement. (See materials and methods 3.5.3)

I obtained a synthesis of results (Figure 70) in which we can see that the nucleus number is stable between samples, remaining between 3250 and 4200 and its variations are more coming from the initial spreading variations than from cells death. There are more important amount of clumped nucleus on bilayers but it can be related to the surface coating irregularities.

We clearly see the very good improvement brought by the coating in term of surface coverage at Div5, showing a better neurons network development on bilayers coated samples: the covering rate is doubled, going from 15% of the surface to 30% in average for all the proteins marked with fluorophores. This testify of an improved cytocompatibility of the surface (Figure 71).

	CTRL 1		CTRL 2		HA/PLLx4,5		HA/PLLx5	
	ISOLATED	CLUMPED	ISOLATED	CLUMPED	ISOLATED	CLUMPED	ISOLATED	CLUMPED
Nucleis Number	3008	777	3133	574	2427	826	3245	959
Ratio in %	79,5	20,5	84,5	15,5	74,6	25,4	77,2	22,8
Average nuclei surface (µm²)	191,7	1003,3	154,3	1049,7	222,9	1063,7	220,5	1090,3
Nucleis Total Number	**3785**		**3707**		**3253**		**4204**	
FITC Covering	14,70%		16,80%		28,20%		34,40%	
Cy5 Covering	15,60%		18,20%		29,70%		31,70%	
TRITC Covering	10,40%		10,06%		25,80%		27,70%	
Average covering	**13,57%**		**15,02%**		**27,90%**		**31,27%**	
Rationnalized to Nucleis nbr.	13,57%		15,34%		32,47%		28,15%	

Figure 70 - Cell culture neurons counting of coverage prove improvement of affinity by multilayers of HA/PLL: fluorescence imaging neurons development analysis synthesis.

3.3 Biocompatibility assessment - In vitro cell cultures

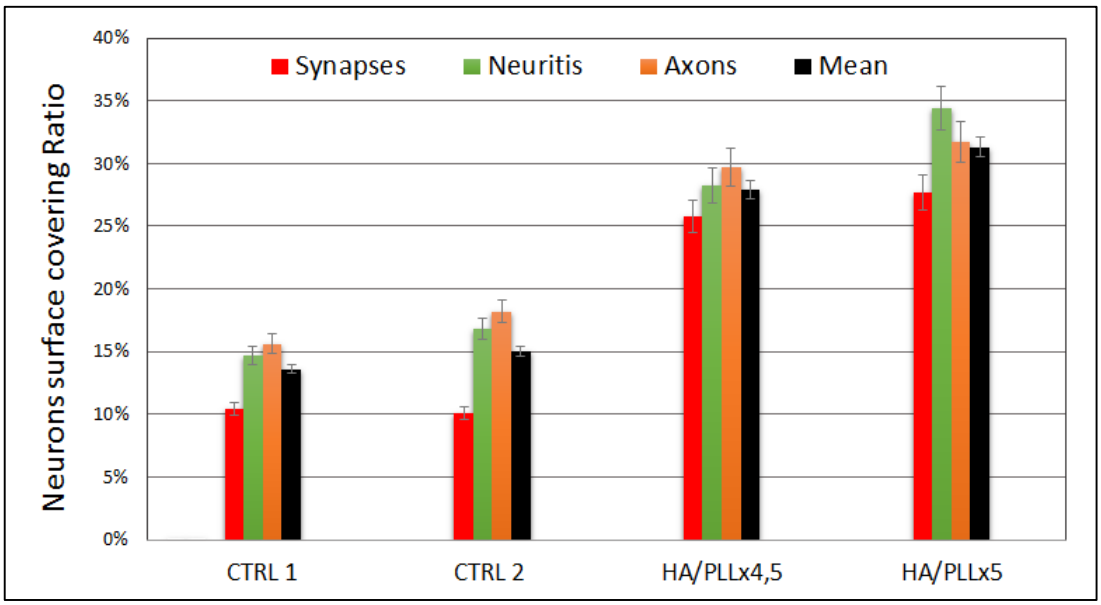

Figure 71 - Statistical graph analysis shows coverage improvement on our functionalized surfaces: surface coverage in percentage by proteins stained and coating applied to the substrate.

Other materials and coating were tested in - vitro and I obtained the following synthesis for cells adhesion and network development statistics (Figure 24).

	Div	1	2	3	4	5	7
Controls	PLL-Neel	Good spreading 3/4 samples	Good spreading/start of axonal growth	Very good	Very good	Nice Network	Network ok
	PLL-Anna	Good spreading 4/4 samples	x	x	x	x	x
Monolayers	Gr-PLL	Very good spreading	Good adhesion	Good dev	Nice network	Very nice Network G edge +++	Nice Network
	HA	No adherence	x	x	x	x	x
	HA on Gr	Irregular but good spreading	x	x	Mainly dead cells	Dead cells only	x
	Haa	Irregular but very adhesive	Good adhesion and VG dev	x	x	x	x
	Gr-Naked	Few spreding /Repulsive	Good spreading and adhesion	x	x	x	x
	Gr-PDMS	Good Spreading	x	x	Nice network	x	x
	PDMS	Very good spreading	x	x	Nice Network	Nice Network	x

Figure 72 – Table showing coating evaluation of a 7 days cell culture on glass substrate functionalized with several materials and polymers. Affinity have been evaluated a large number of time for implants functionalization and design purpose. Empiric evaluations are based on a comparison with control samples. Cross represent the sample which were not tested at these days, mainly for some limitation on the number of samples reasons, given the fact that each sample were doubled for statistic reliability.

Two sources of PLL worked very well as control sample all over the 7 days of the study (12 samples).PLL coated Graphene (6 samples) also showed a very clean development of the neuronal network despite an apparent irregular development, particularly along the graphene foil edges. As a reminder, a 5x5mm graphene is transferred on a 12mm diameter glass slide, exposing, for this sample, one part off PLL on glass, and on part of PLL on Graphene on glass (see illustration on Figure 73). This can be explained by the very good neuronal affinity for nanoscale rough surface [200] offered by the edges of the graphene layer, which are often rolled and full of carbon impurities.

The irregularities of spreading and even the numerous dead cells illustrated by nucleus alone (blue dots) seems to testify a bad adhesion of PLL on graphene surface who led to an instable coating for neurons , and thus to these irregularities on the PLL side of this sample.

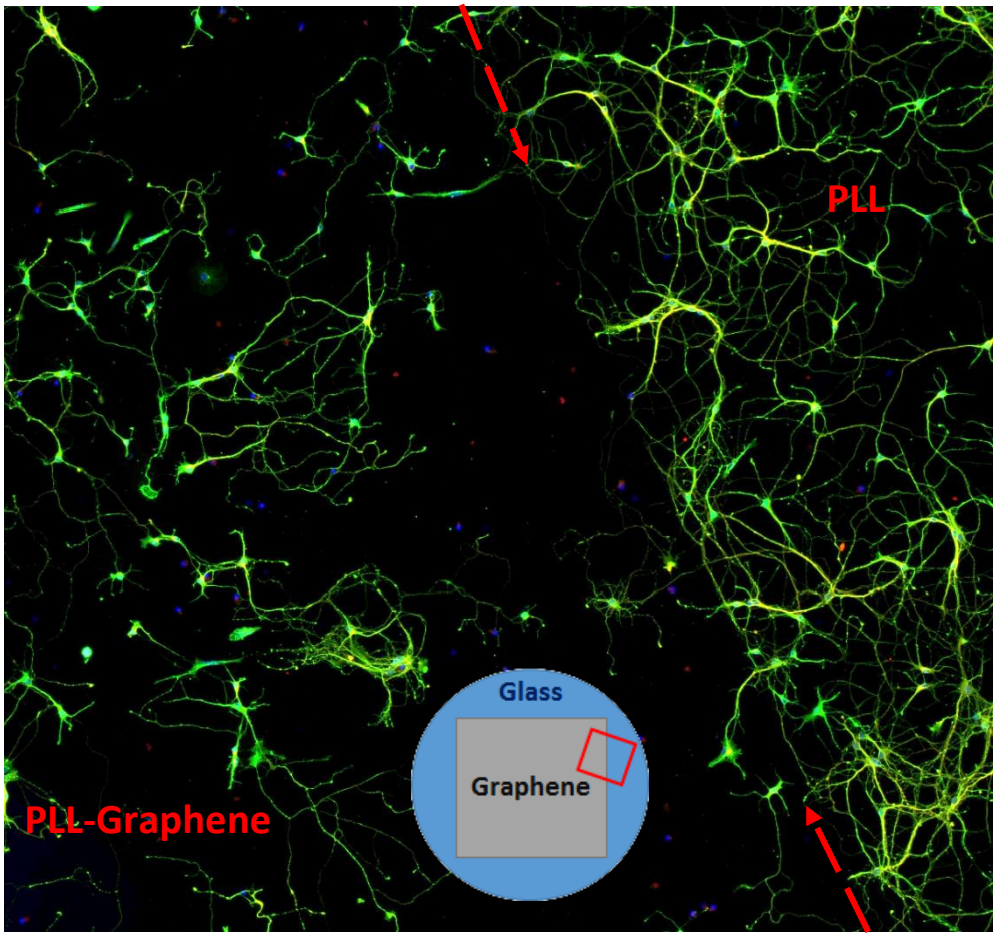

Figure 73 – We demonstrated that graphene edges provide confinement for neurons to grow. However, on this sample, graphene surface was slightly repellant. Div5 PLL coated Graphene on glass immunofluorescence optical microscopy picture show DAPI stained Nucleus and FITC stained microtubules. We can clearly see the edge of the graphene foil and the neurons developing axons along this edge with strong affinity, despite the PLL coated graphene seems irregularly covered by neurons, even showing a dead cells zone. This can be explained by a bad adhesion of PLL on top of graphene, creating an irregular coating or by this batch of graphene repulsive nature for cell.

The analysis of alkylated Hyaluronic Acid HAa and of naked graphene shows proper adhesion of neurons on the surfaces (Figure 74). PolyDiMethylSiloxane (PDMS) and Graphene on PDMS show the best behaviors of network development, with or without graphene on top of it, certainly due to PDMS softness which mimic neural tissue softness and thus provide a very suitable surface for neurons development (Figure 75), in agreement with recent studies of in-vitro neurons growth on PDMS [204]. However, HA alone or on top of graphene was deadly to cells by showing no adhesion during the whole study.

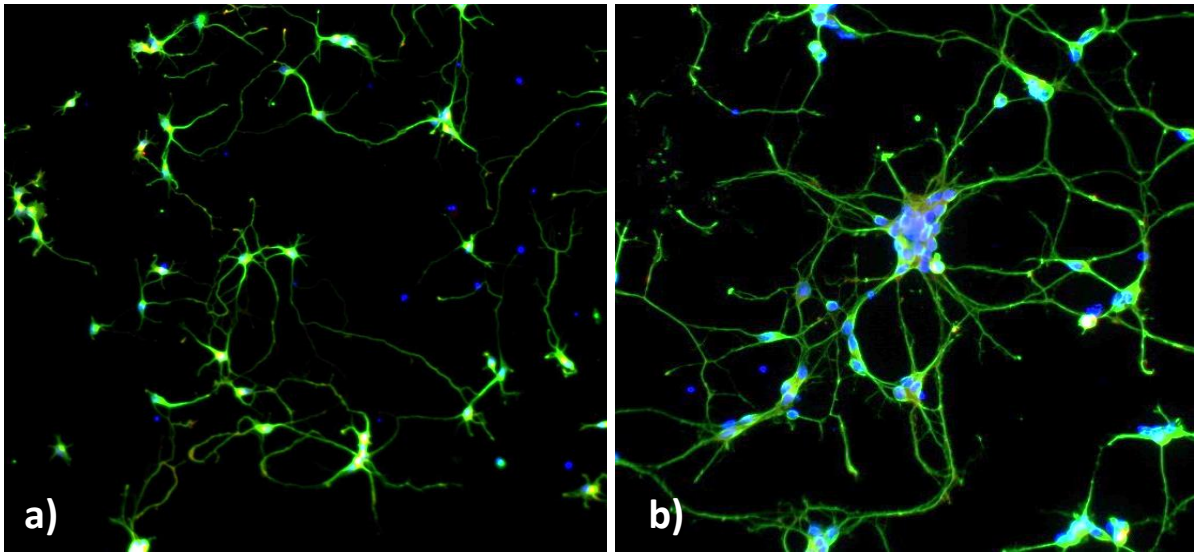

*Figure 74 – Some specific bare graphene batch provided affinity for cells after 2 days. Div2 immunofluorescence optical microscopy pictures show DAPI stained Nucleus and FITC stained microtubules **A)** proper adhesion and network beginning on naked graphene without any PLL coating **B)** very good adhesion and network on HAa alone despite big neuron heap on this picture.*

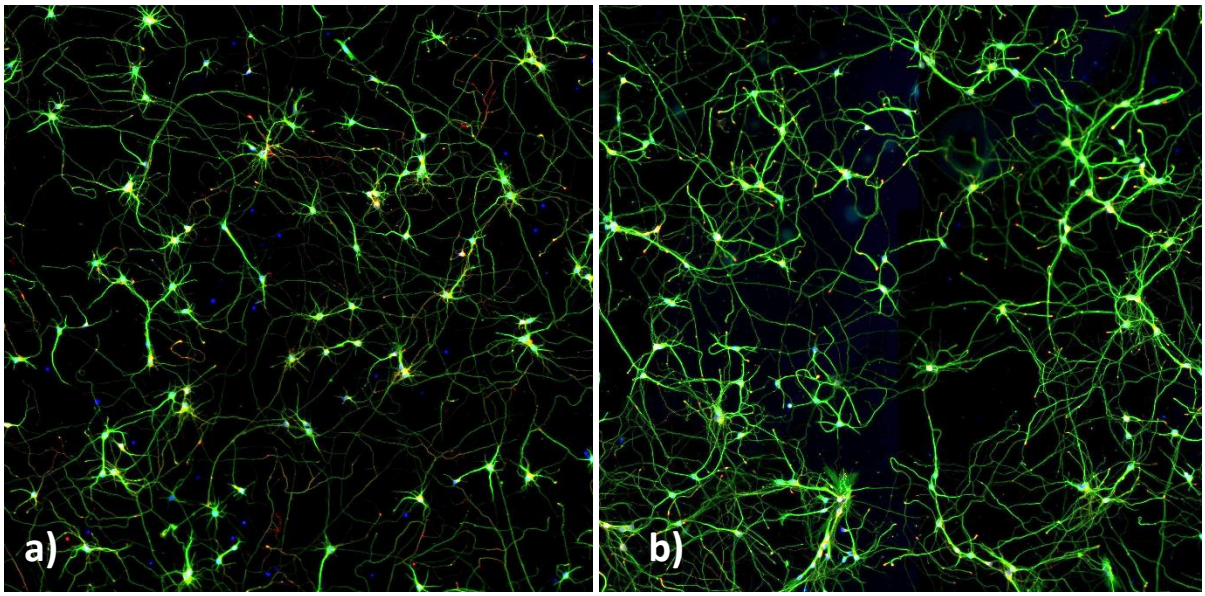

Figure 75- During this thesis, we studied that PDMS improve the affinity by reducing mechanical mismatch between surfaces: Div5 IF microscopy pictures show a) Ctrl sample standard good adhesion b) Graphene on PDMS covered glass slide adhesion and very expanded network suggesting a strong bioacceptance improvement

3.3.2 Intracortical bioacceptance study

The final achievement in our functionalization development for graphene bioelectronics has been its bioacceptance study in the motor cortex. For that purpose, we have separately considered the impacts of biopolymers and the impact of graphene (chapter IV) along this thesis. Here we detail the biopolymers functionalization test.

a - Implants:

Our strategy was to coat commercial implants (Tucker Davis© Utah Array) with our polymer multilayer assemblies. Each implant contain 32 independent sensing electrodes made of tungsten wires encapsulated in polyimide. I proceeded to the coating of a batch of 3 probes (Figure 76) with the same 5 (HA-PLL)-bilayers assembly. Regarding the previous results obtained in-vitro, the coating is expected to improve the detection by enhancing the coupling to the cells and might lower the gliosis. 3 others uncoated implants were used as control samples.

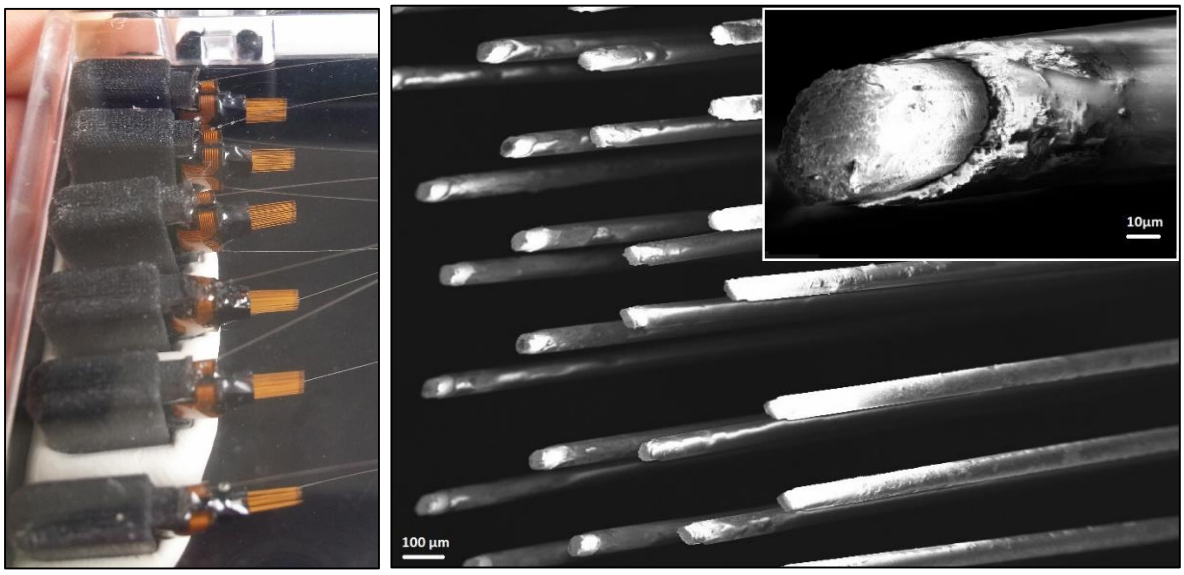

Figure 76 - Commercial implants (Tucker Davis© Utah Array) that were coated with our polymer multilayer assemblies: SEM imaging of the TdT implants needles tips. White part is the Iridium Oxide electrode recording site, whereas grey part shows the polyimide isolated electrode.

b - Surgery procedure:

All surgical procedures were performed in accordance with Swiss federal legislation and under the guidelines established at EPFL. Local Swiss Veterinary Offices i.e. the Swiss "Service de la consummation et des affaires vétérinaires du Canton de Vaud", Switzerland, approved all the procedures.

Six Adult female Lewis rats (200-225 grams, N.23, Charles River, UK) were housed individually on 12-h light/dark cycle with access to food and water *ad libitum*. Before surgery, animals were first habituated to human presence and manipulations during 2 weeks. Stereotaxic fixation was performed after administration of 0.1ml of Dorbene anaesthesia and surgeries were performed under inhalant anaesthesia of 2% diluted isofluorane in 2 L/min oxygen.

The targeted cortical area of implantation is the layer IV of their motor cortex (see chapter I). As described previously, the recording traces aim to map the electrical activity of motor neurons identified as involved in the locomotion in order to command the appropriate stimulation of the spinal cord below the injury (see chapter I) with dedicated stimulation electronics to bypass the lesion [29].

An incision was made on the crane and a windows was opened in the skull above the motor cortex, taking the bregma[6] as a reference. Four screws were screwed into the skull for future implant sealing. Once the windows opened, Dura matter was carefully removed and the implant was positioned above the target zone (Figure 77). Reference position was measured in order to have a depth control during the implant insertion. Once the implant have been inserted, a refrigerated chlorine solution have been used to stop the eventual haemorrhage bleeding around the insertion site, then a dental cement have been used to seal the implant body to the rat skull and avoid any parasitic movement of the probe.

[6] The Bregma is an anatomical point located on the intersection between two sutures of the skull bones: the sagittal and the coronal suture. It is used as a reference to position our implant above the motor cortex with the same parameters (coordinates to Bregma).

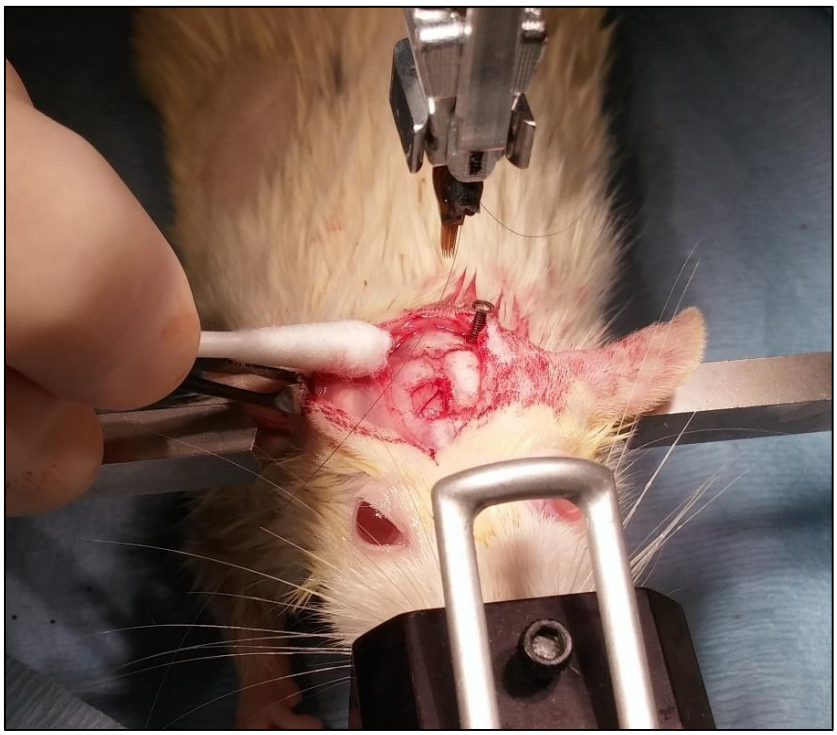

Figure 77 - Photography of the surgery procedure and alignment above M1 cortex: the rat is in the stereotaxic frame breathing isofluorane anesthetics, a windows have been opened in the skull and Dura matter above the motor cortex and TDT implant is aligned on top of it for coming insertion.

During the surgery, an **important biological variability has been highlighted** regarding vascularisation schemes on animals' cortex surface. Figure 77, for instance, represents rat #480 that presented a big blood vessel in the middle of the insertion target. The large dimensions of the implant chosen impeded avoidance of blood vessel damages. The inevitable breaking of this blood vessel increased glial scar formation because of the large amount of blood macrophages and endothelial cells carried inside by the implant (as explain in 3.1.1b -).

c - Signal measurements

We investigated the quality of the cortical signal during 7 weeks after surgery, once a week with a freely moving recording of the 6 animals. A walking recording was done after 1 month in order to verify kinetic signals and thus associate motor cortex reading with locomotion behaviour. Signal amplification and recording were made with the Tucker Davis Technologies PZ2 preamp and RZ2 amplifier at the sampling frequency of 25 kHz.

We have been able to **isolate the signal of a few motor neurons** involved in **locomotion** by tracking specific spikes sorted neurons activity in real time during a rat walk on a treadmill (Figure 79). Spike sorting is processed in real-time by using TdT© OpenEx© commercial software and spikes of interest were stored when spike occurrence was matching with the walking status. We then labelled the corresponding sensors among the 32 sensing sites of each implant. The experience was repeated once a week by in-cage free-movement recordings for all sensors and compared to previous results. The **number of operational sensors** (successfully measuring one motor neuron or more) have been tracked along 7 weeks.

The biological variability discovered during surgery have had a critical influence on our signal quality like it can be seen on the sum up table (Figure 78).

	Functionnalized - HA/PLL 5 Bilayers coated TDT electrodes arrays		
	#478	**#479**	**#480**
Surgery	Brain Vessel size = 2/5 . **Bleeding = 1/5**	Brain Vessel size = 3/5 . **Bleeding = 2/5**	Brain Vessel size = 5/5 . **Bleeding = 5/5**
W+1	Weak signal	Good signals/best channels: 23,29, 24XL	Weak signal
W+2	Good signals	Good signals	Almost silent except ch16
W+3	Good signals/best channels: 11,14XL,27	Good signals/best channels: 20 , 31XL	Good signals
W+4	Walk OK kinetics on ch 13XL, 11, 6, 15	WALK OK kinetics on ch 15,20	WALK OK kinetics on ch 16
W+6	Good signals	Good signals/best channels: 15,24XL, 27XL	Good signals/best channels 1, 16
W+7	Good signals	Good signals/best channels: 14,15,24	Almost silent except ch16
	Control - out of the box TDT electrodes arrays		
	#481	**#482**	**#483**
Surgery	Brain Vessel size = 4/5 . **Bleeding = 4/5**	Brain Vessel size = 1/5 . **Bleeding = 1/5**	Brain Vessel size = 4/5 . **Bleeding = 5/5**
W+1	Weak signal	Good signals/best channels:6XL,8XL,31XL	Silent
W+2	Almost silent except ch 24	Good signals	Silent
W+3	Ch 22XL	Good signals/best channel: 27 XL	Silent
W+4	Almost silent exept ch 24	WALK OK kinetics on ch 24	Silent
W+6	Silent	Good signals/best channel: 7,27,25,6,7	Silent
W+7	Silent	Good signals/best channel: 7,11,12,14,27	Silent

Figure 78 - Surgery and recordings sum up for the 2 groups of rats. We can see clearly the influence of surgery bleeding on the signal long term quality. Color code shows signal global quality: green when several channels allow neurons recordings, yellow for only 1 working channel and red when implant is silent.

Very good quality spiking neurons signals have been obtains on many channels of 2 rats 479 and 482 (Figure 79). Spikes were regulars and clearly **associated with trunk and legs** movements.

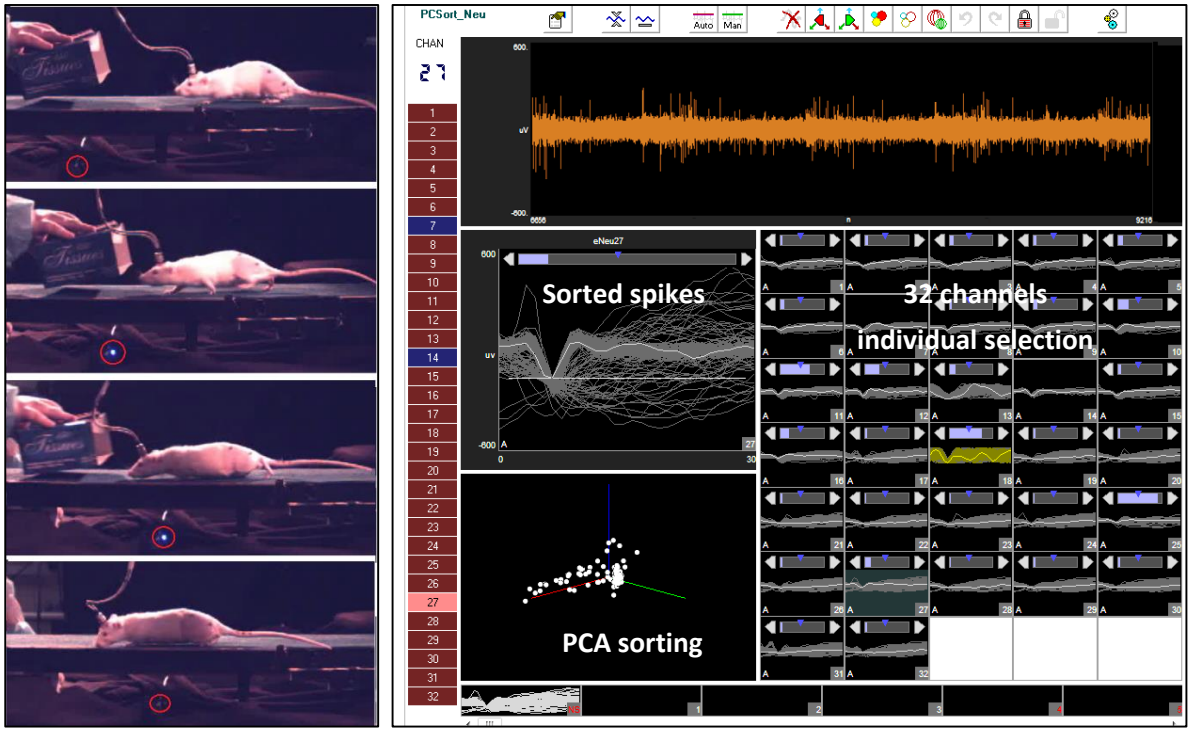

Figure 79 – Real time recordings of motor cortex neurons spiking activity during walk: ***A*** *implanted rats were trained to walk and were recorded doing so. Blue light activates whenever motor neuron activity is detected by in line spike sorting software.* ***B*** *In line spike sorting is processed with the TdT OpenEx© software. Filtered live signal in orange is sorted using Principal Components Analysis based on spikes amplitudes, periods and velocity. Spikes are then associated with a walking motion and blue light activates whenever a spike is validated.*

d - Immunohistochemistry analysis

Post-mortem Immuno-histo-chemistry of the extracted cortical tissues (Figure 81C&D) was performed in order to evaluate the importance of glial scars by labeling the astrocytes and microglial cells generally involved in post lesion reactive gliosis.

The post campaign biopsies were performed doing -1mm bregma coronal sections (Figure 80). Astrocytes and microglia reactivity were revealed respectively by-staining Glial Fibrillary Acidic Protein (GFAP) and Ionized Calcium Binding Adapter molecule 1 (Iba1). Brain coronal sections were incubated overnight in serum containing anti-Iba1 (1:1000, Abcam, USA) or anti-GFAP (1:1000, Dako, USA) antibodies.

Immunoreactions were visualized with secondary antibodies labelled with Alexa Fluor 488 or 555. Fluorescence counterstaining of Nissl substance was done using neurotrace 640/660 solution (1:50, Invitrogen, USA). Tissue sections were observed with a laser confocal fluorescence microscope (Leica, Germany).

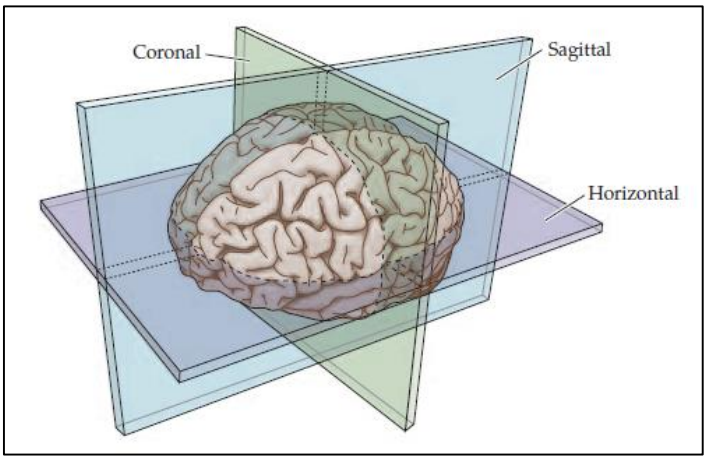

Figure 80 - Major planes of section used in cutting and imaging the brain. From D. Purves et Al. - Neuroscience 3rd ed.

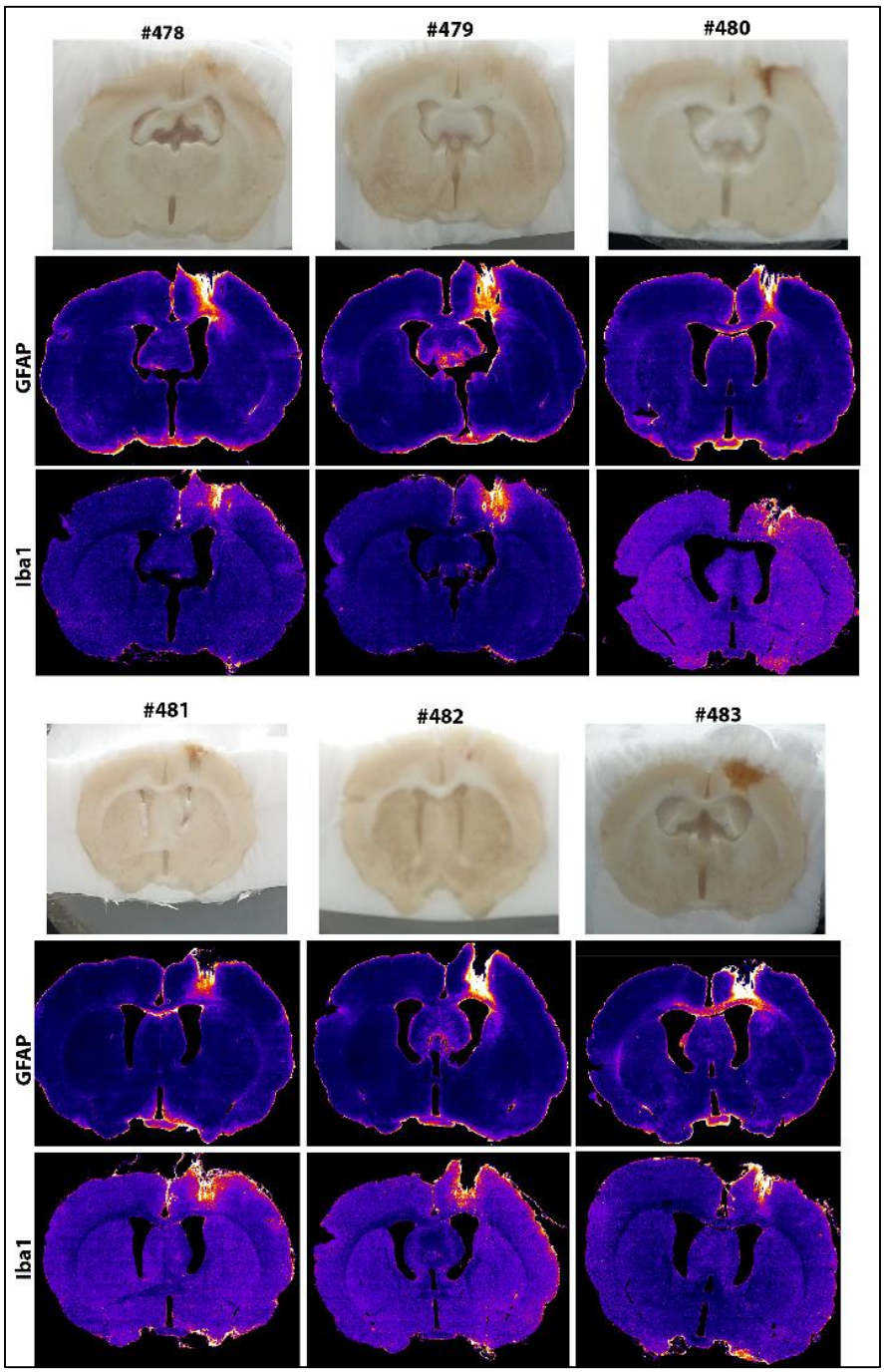

Figure 81 - Coronal Slices of rat brain 3 months after the surgery and 48h after implants removal. There was a strong variability in bleeding during surgery that we can find back on the slices pictures particularly on #480 #481 and #483. GFAP staining represents astrocytes and Iba1 represent microglia immune-staining, showing a strong localized chronic inflammatory reaction at the implant location. We also see an important biological variability between subjects brain shapes and the corresponding variation of gliosis intensity.

Those biopsies showed us the bleeding phenomena that occurred 7 weeks sooner when implanting rats' n°480,481 and 483. The intensity of the inflammatory reaction (Figure 81) was linked to this bleeding.

Unfortunately we considered that this bleeding overwhelmed to much the influence of the functionalization layer to see a significant difference between functionalized and control implants. We thus performed a **comparison between the best animals of each group** in term of signals, being n°479 and n°482, by performing a pixel counting (Figure 82) to evaluate the amount of microglial and astrocytes cells stained for each brain.

The result showed that **functionalized implant induced a slightly lower gliosis after 7 weeks than the control implant**, particularly in term of Microglial reaction (Iba1).

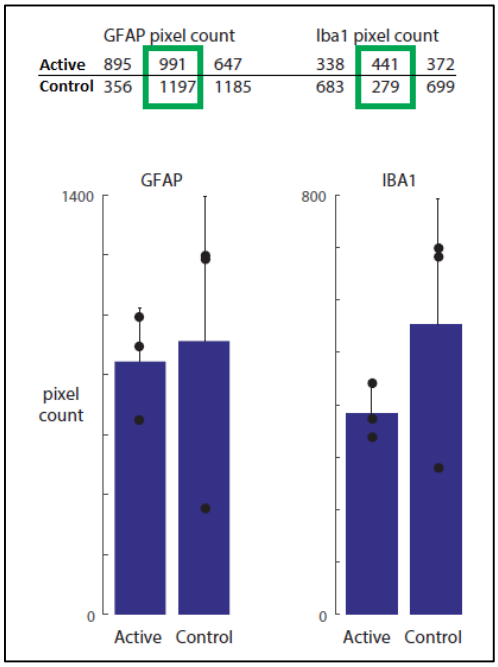

Figure 82 - Pixel counting allow evaluation of the relative populations of GFAP stained astrocytes and Iba1 stained microglia present at the site of insertion of the 6 rats. Histogram show mean pixel number with variance among the population. "Active" represent functionalized implants and "Control" represent standard TdT probes.

Immunohistochemistry suggests a better bioacceptance of our functionalized implants and thus an improvement in term of gliosis reduction after 7 weeks. The improvement seems to have had a bigger influence on astrocytic reaction after 7 weeks, suggesting a better healing process despite the high number of microglia remaining. However, the high variability induced by bleeding and the low number of animals provide an insufficient amount of data to conclude with a strong statistic. Indeed, bleeding is known to bring a lot of macrophages to the implant site, triggering microglia migrations (3.1.1b -), which we can confirm by reading the pixel counted values for bleeding animals Iba1: 683 and 699 compared to non-bleeding animals between 279 and 441.

3.4 Conclusion

An important part of this thesis has been dedicated to the development of this uniform polymer layer on graphene. Many progress have been made until we found a method to cover graphene with a thin (<100nm) layer of biodegradable polymer.

We thus provide to graphene the possibility to graft hydrogels without modifying its properties and efficiency as a biosensor.

After the surgery campaign, we can, despite the disputable strength of this statistics, come to the conclusion that functionalization did not lower signal quality and chronic recording and even suggested a lower gliosis on an un-bleeding animal, to be confirmed in further experimentations. Further experimentations should be conducted with a bigger populations to create good statistics, and also be performed on animals like mice, showing lower biological variability. The in vivo study was however substantial to consider moving on to the next brick of our graphene based bio electronic assembly.

We have been able to prove the feasibility of a combined approach to use graphene bioelectronics on intracortical implants together with drug delivery polymers grafting to lower the gliosis after invasive surgical intervention and improve lifetime of such devices.

In the next chapter, we will detail how graphene should be integrated in intracortical implants and, thanks to innovative integration method, we will assess graphene behaviour and bioacceptance in vivo.

3.5 Materials and methods:

3.5.1 Polymers coating preparation

Square 4x4 mm graphene sheets have been wet transferred on the center of 12mm circular glass slides. Poly(allylamine hydrochloride) (Mw ~ 70 000 g/mol) was purchased from Sigma-Aldrich. Poly(L-lysine hydrobromide)-FITC (Mw ~ (15-30 000 g/mol) was purchased from Sigma-Aldrich. Poly(L-lysine hydrobromide) (Mw ~ (21 000 g/mol) was purchased from Alamanda Polymers. Hyaluronic acid under the sodium salt form, having a molar mass of Mw of 200000 g mol−1, was purchased from MEDIPOL Distribution. The decylamino hydrazide derivative of hyaluronic acid (HA200C10) was synthesized in CERMAV as previously described [197]. HA200 means that the weight average molecular weight of the parent HA used for synthesis HA200C10 was 200 000g/mol and C10 indicates number of carbon atoms on the grafted alkyl chain. We used two different degree of substitution DS=0.1 and 0.2 (number of substituent per repeating disaccharide unit of HA).For simplicity, the term “alkylated” is used instead of “alkylamino hydrazide” to refer to the modified HA samples. HA, PAH and PLL were dissolved at 2 mg.mL^{-1} in a 0.15M NaCl solution adjusted at pH 6.5. During film build-up, all the rinsing steps were performed with 0.01M NaCL solution (pH 6.5). The water used in all experiments was purified by a Millipore Milli-Q Plus purification system, with a resistivity of 18.2 MΩ.cm^{-1}.

Every layer was deposited by sample drop deposition during 10min, followed by rinsing with 0.01M NaCl x2. At the end samples were kept in 0.01M NaCl.

Figure 83 - Line of becher for layer by layer deposition and rinsing between each layer.

3.5.2 In vitro neurons culture method

For in vitro neuronal cultures I used E16 mouse embryos hippocampus neuronal stem cells. Embryos were isolated from the mouse and kept in cooled dissection medium (10:1 HBSS:HEPES, Invitrogen).

Hippocampus is in the temporal lobe of embryos brains, we isolate it by separating the two cerebral hemisphere and then remove non-cortical tissues and meningeal tissues using surgical tweezers and scissors under binocular. Chemical dissociation of the hippocampi is then processed at 37°C in a 10% trypsin and 2% EDTA solution (Life Technologies) during 15minuts. Finally, we help dissociation by washing the hippocampi in dissection medium and creating turbulences with a pipette. Cell suspension so obtained is diluted to the desired concentration in plating medium (10% FBS, 1% Glutamine, 0.05% Penicillin, Gibco)

Once diluted, we can use this cell suspension to plate it on prepared substrates, control and functionalized graphene for example. 3 hours in an incubator (5% CO2 @37°C and 95% humidity) allows a first cell attachment and is then followed by excess cells removal and medium replacement with final pre conditioned cell culture medium (1 mM AraC diluted in Neurobasal B27, Invitrogen).

Control sample we used in our studies were functionalized with a single layer of Poly-L-Lysine (PLL) adhesive polymer in order to improve neuron attachment which would be bad on naked glass. To perform that, PLL was diluted as 1mg/ml and ph was stabilized by filtering PLL solution in borate buffer at pH 8.5. Finally, PLL coating was made by putting a drop of solution on each substrate overnight, then before spreading cells on the substrate, excess PLL was washed in sterile DI water baths.

3.5.3 Image analysis protocol

Nucleus detection is made by particle analysis Image J plugin after Picture conversion in 8Bits and threshold definition in order to insulate nucleus from the background noise and to separate neurons nucleus from glial cells less brightening nucleus (Figure 84). Nucleus size has first been measured manually on a dozen of nucleus per picture in order to define the average nucleus area to detect. Detection range is set to be large because of defocus that sometimes appeared on some pictures and thus increased the apparent size of nucleus. This can occurs when the glass slide is not perfectly flat.

Next step was taking into account nucleus circularity to select nucleus that have a ratio Vertical width/horizontal width superior to ½ in order to select good circular nucleus.

Excel post sorting allows to select a restraint population of nucleus, defining a minimum and maximum area. Thus I obtain a number of isolated neurons and an average nucleus area for each picture.

Parameters Detection		
	Nucleus	Heap
Area ImaJ (µm²)	0-655	655-18720
Circularity ImaJ	0,5-1	0-1
Area Mini ? (µm²)	**28**	**655**
Area Maxi ? (µm²)	**655**	**3276**

“Heaps” of nucleus cannot be counted as separated nucleus by the particle analysis plugin. For this reason, I process to a “heap” detection by surface, without taking into account their bad circularity, then I estimate the number of nucleus by heap from the pre calculated average nucleus area. Obtained results after automatic treatment of heap have been verified with manual counting. (Figure 84)

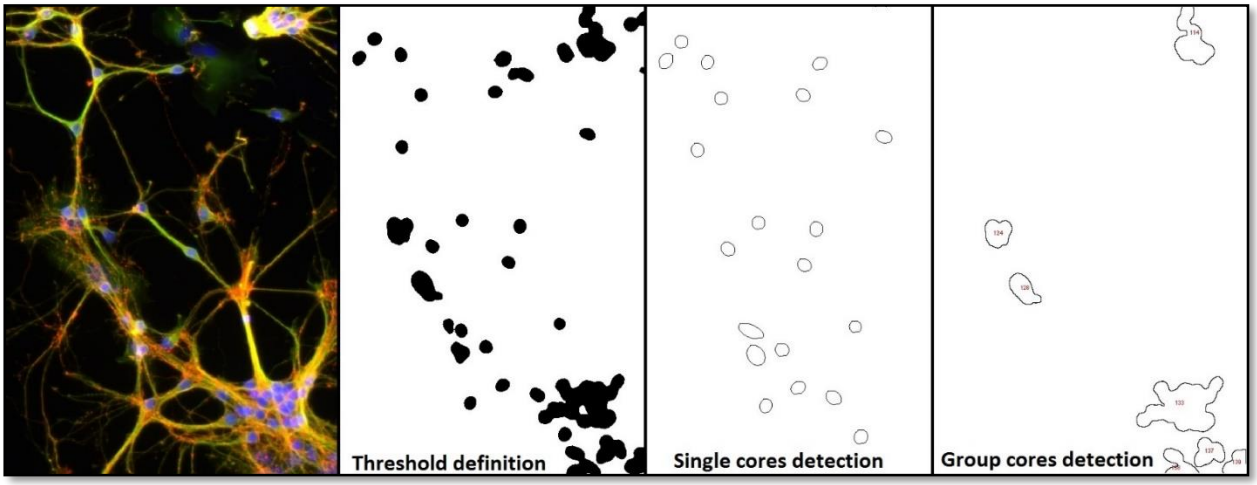

Figure 84 – Protocol example on the CTRL 1 sample. On left: a heap of nucleus on right hand corner. Manual counting reveal 19 nucleus aggregated. After threshold definition, I detect isolated nucleus then groups. My heap of interest, here labelled number 133, represents an area of 3200µm² according to the software, that to say, with our analysis method, an estimated number of 17 nucleus. A 10% error.

Neurons surface covering rates have been extracted thanks to the threshold tool in Image-J, preserving a constant brightness level for each fluorophore. Defocus images will generate less brightness and the increasing of appearing surface will be compensate by the fact that the threshold level of brightness between all pictures remains the same.

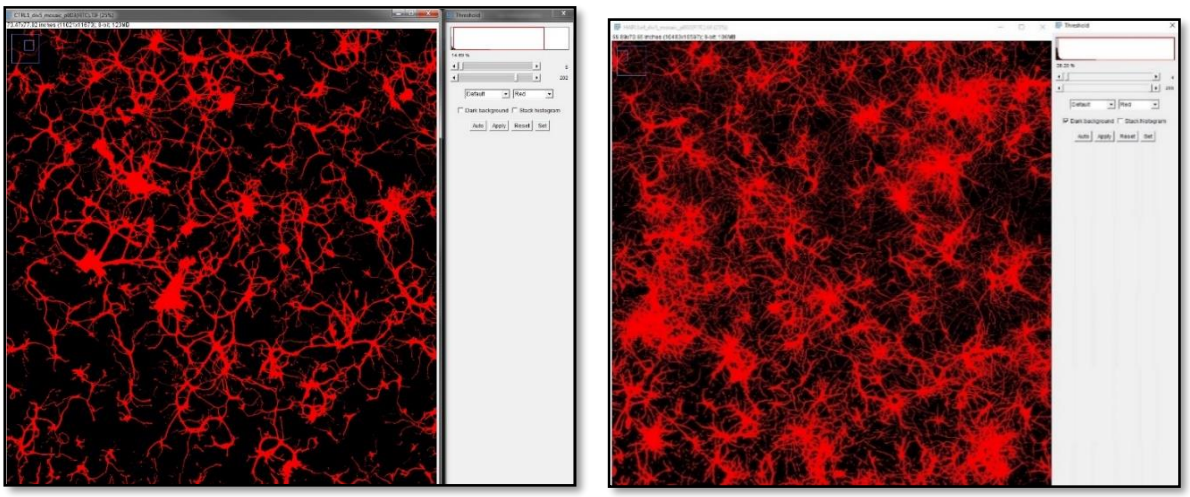

Figure 85 – FITC pictures threshold neuron surface covering analysis. On left: CTRL1 14.7% surface covering, On right: HA/PLLx4.5 28.2% surface covering

IV. Neuro-engineering & graphene integration

In the last neuro-engineering part of this thesis I will detail the design and cleanroom fabrication processes I implemented and how I overcame integration issues to test graphene bioacceptance in vivo during the last months of this thesis.

I will start with a quick overview of implant computer design technique and then explain, through process flow charts, how I turned from a 2D computer drawing to a 3D multilayer microelectronic assembly.

Each layer building is detailed and final fabrication of devices is demonstrated on silicon with the use of silicon deep etching process. At the end of this part, I develop these issues and the solutions found to assess graphene bioacceptance in vivo.

Last part of this chapter is the overview of the last in vivo campaign that took place at the end of year 2016 to assess graphene bioacceptance and durability in ten mice motorcortex.

CHAPTER IV - TABLE OF CONTENTS

4.1 Design and fabrication of implants

4.1.1 Computer design

a - Semi-automatic electrodes routing

The first step of an implant creation is its design. A microelectronic design consists in the preparation of microelectronic stacks which are piled up to create the devices.

Each stack is firstly designed in 2D to create a mask. For that purpose, I used Tanner L-Edit© software to draw each layer of the future implant in a mask file.

The software is an intuitive application that allows C++ array programming to draw patterns point by point according to predefined parameters. I was able to set an **automatic electrodes routing** (Figure 86) to follow every change made in the design without re-drawing each wire. Each similar block of electrodes has been coded with array parameters in order to manipulate inflexion point's coordinates, thus linking external contacts pads to the interest zone: the sensor.

```
LCoord x;
LCoord y;                                   In green: uses of predifined grids parameters
LCoord xcount;
LCoord ycount;
pLayer = LLayer_Find( pFile, "Electrodes bas" );          First electrode coordinates
LPoint ptArray[60][5];
   ptArray[0][0].x = 0-6*trap; ptArray[0][0].y = 0;
   ptArray[0][1].x = 0-6*trap; ptArray[0][1].y = -76850;
   ptArray[0][2].x = -1000000; ptArray[0][2].y = -1634450;
   ptArray[0][3].x = -1000000; ptArray[0][3].y = -1634450;
   ptArray[0][4].x = -1000000; ptArray[0][4].y = -1634450-electrodlength+deltabloc;

for(i=0;i<nstart4;i=i+1){

                                            Matrix coordinates automatic generation
   if(i>1 && i<nstart2)
   {
   ptArray[i][0].x = ptArray[i-1][0].x-trap;     ptArray[i][0].y = ptArray[i-1][0].y;
   ptArray[i][1].x = ptArray[i-1][1].x-trap;     ptArray[i][1].y = ptArray[i-1][1].y;
   ptArray[i][2].x = ptArray[i-nparbloc1][2].x-deltabloc;          ptArray[i][2].y = ptArray[i-1][2].y;
   ptArray[i][3].x = ptArray[i-nparbloc1][3].x-deltabloc;          ptArray[i][3].y = ptArray[i-1][3].y;
   ptArray[i][4].x = ptArray[i-nparbloc1][4].x-deltabloc;       ptArray[i][4].y = ptArray[i-1][4].y;
   }
   }

   LObject pObj = LWire_New( LC_CurrentCell, pLayer, NULL, 0, ptArray[i], 5 );
   LWire_SetWidth( LC_CurrentCell, pObj, wirewidth1 );
         }
```

Figure 86 – Custom electrodes routing block array programing to perform semi automatic routing according to changes in design: I programmed this in order to simplify design modifications when testing integration of GFETs on implants.

I finally obtained the linkage of all connectors available to the interest zone on G-FET in a symmetric manner and with a minimum electrode length to **reduce impedance** of our electrodes pathways and thus improve future sensor reading values.

On Figure 87, I designed four layers and virtually piled them up to check alignment of the layers together. Dark green represents graphene etching to obtain graphene channels for our transistors, then, the blue layer represents metallic contacts for these transistors. Next layer (red) is paramount for SGFETs and consists in insulation of metallic contacts and non-channel graphene parts. Finally, the clear green layer represents future deep etching of probes in order to create thin 3D implants supporting GFETs.

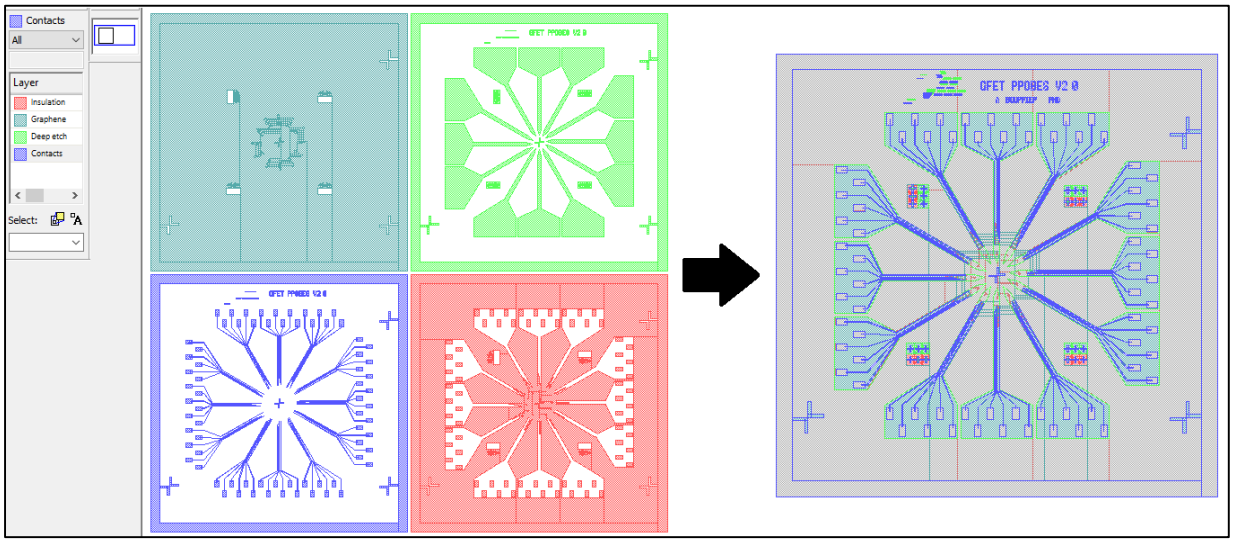

Figure 87 - Device design is made through 2D stacks representing layers that will be piled up during step by step microfabrication: here one of my first design to test Graphene FETs fabrication on 3D probes. The process will be detailed along this chapter from this first computer design step to microelectronic layer assembly.

b - Sizing and variations of the device designs

Implants sizing was set up according to the neurorehabilitation project to target our interest zones: at the beginning of this PhD I designed large MLR sized probes (Figure 87) because they are bigger and thus easier to process. When microfabrication steps were mastered, I started building implants to target rats motor cortex layer V (Figure 88).

Indeed, as a reminder from chapter I, **motor cortex layers IV and V** are dense in term of **pyramidal** cells that transmit motor orders to subsystems 2, 3 and 4 via upper moto neurons.

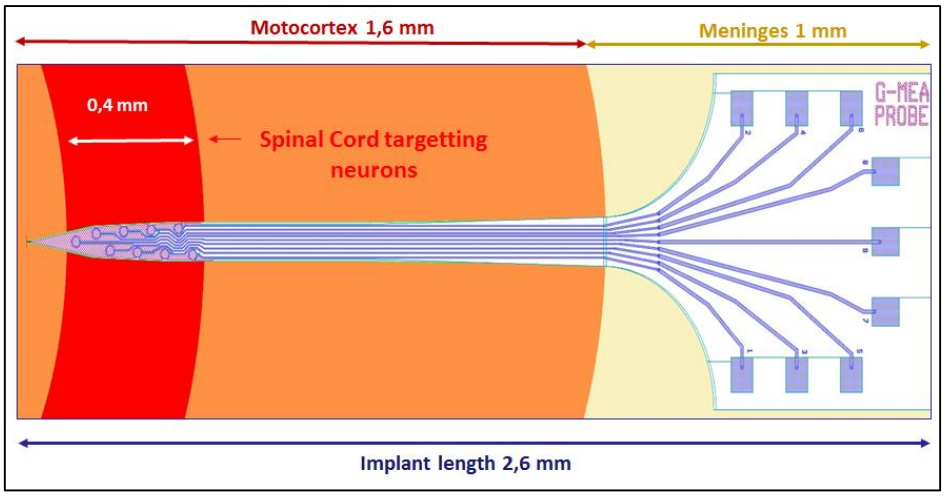

Figure 88 - Rat layer V motorcortex targeting implant is designed with my computer program with L-edit software

Once the sizing were made according to the physiological parameters, I prepared two designs of implants with corresponding process flow in order to build either polyimide flexible or silicon probes carrying different kinds of sensing electronics on top of them: both MEA and FETs (Figure 89) were designed and built on silicon probes, in order to perform a benchmark of their performance as Neural activity sensors. These devices fabrication will be detailed in next paragraphs.

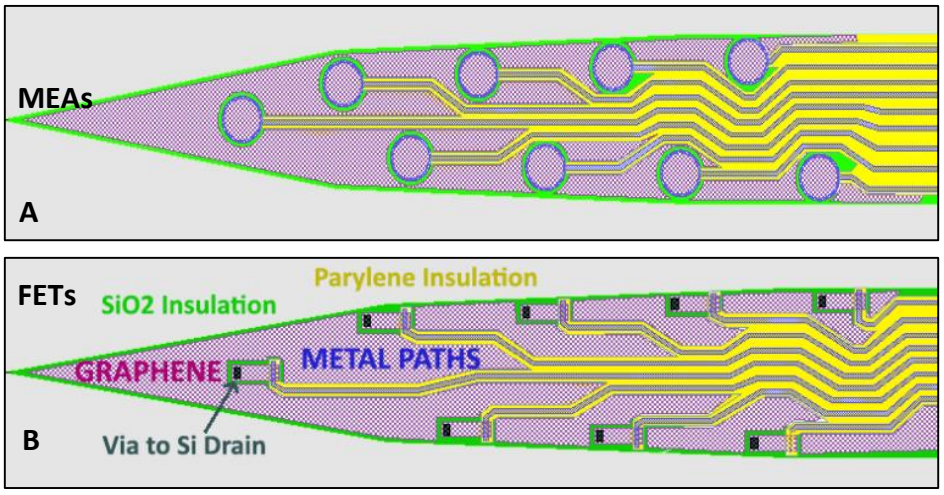

*Figure 89 - Both MEA and GFETs sensors were designed to fit on intracortical probe: **A** Nine microelectrodes are placed all over the tip of the probe to cover the targeted length of 400 µm. Graphene is designed to cover the whole non-active surface in accordance with or bioacceptance improvement hypothesis. **B** Eight transistors are created all over the surface. As transistors need drain and source contacts to operate and the size of the implant being limited, I found a way to contact drains by creating vias into silicon oxide for the graphene to be in direct contact with underlying conductive silicon.*

4.1.2 Photolithography and bottom up fabrication

Once the design of the future devices is made, photolithography is used to transform this 2D virtual design in a 2D hard mask. To do so, I used a laser lithography to build a dedicated chromium mask on an achromatic soda lime glass (Figure 90A).

The mask aims at allowing selective transmission of UV light to perform patterned polymerization of a photosensitive resist, mostly Microposit© S1805 during this thesis, and thus build the microelectronic assembly layer by layer in an approach defined as bottom-up..

The resist is previously spin-coated on the desired substrate, here an oxidized silicon substrate. The mask is then used with a mask aligner to superimpose new layers on top of each other. The mask aligner integrates a UV source (MicroSuss© MJB3). Once polymerized, the resist is developed with a chemical reagent (developer) in order to pattern it.

Such developed resist will selectively expose underlying substrate and thus allows modification of its surface according to resist pattern. On Figure 90B, a 2 inches surface oxidized silicon wafer was patterned through a resist to remove its oxide layer (500 nm thick oxide) using Reactive Ion Etching (RIE). Same photolithography process also allows silicon etching, graphene etching and metal deposition to contact sensors (Figure 90D). In order to perform easier measurement of sensors or in vitro cell growth on those devices, we cleaved the silicon wafer to reduce the size of the devices (Figure 90C & D)

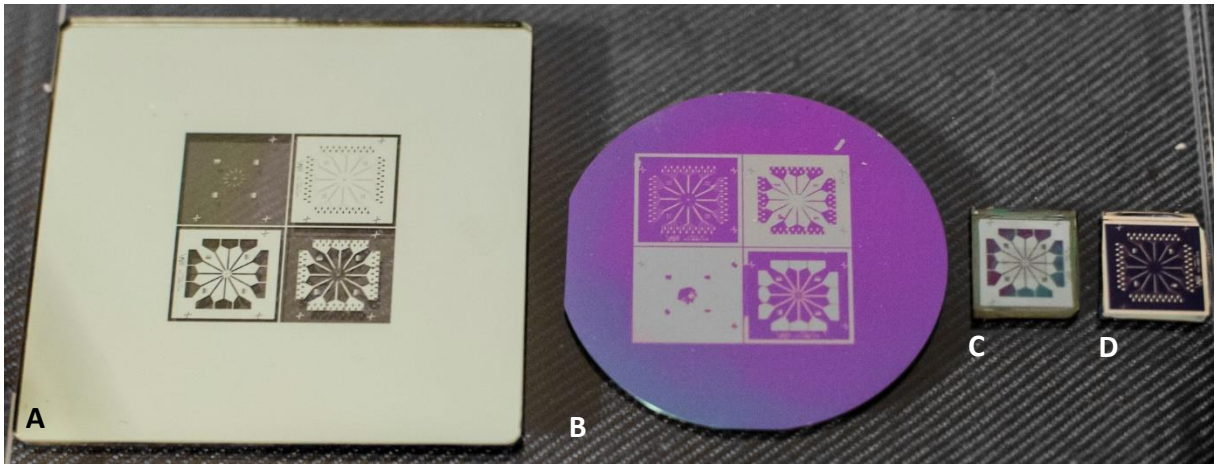

Figure 90 – Main microfabrication steps from 2D mask to multilayers samples: ***A*** *Chromium on glass mask allows selective transmission of UV light on a substrate to pattern a photosensitive resist.* ***B*** *The photosensitive resist is then used to modify an oxidized silicon wafer: here by patterning silicon oxide for future deep etch phase.* ***C*** *The sample is cleaved for easier manipulation and the layers are assembled until graphene is contacted with metal electrodes (on* ***D)***

4.1 Design and fabrication of implants - Photolithography and bottom up fabrication

The fabrication flow of my devices is illustrated in Figure 91 and steps are described below:

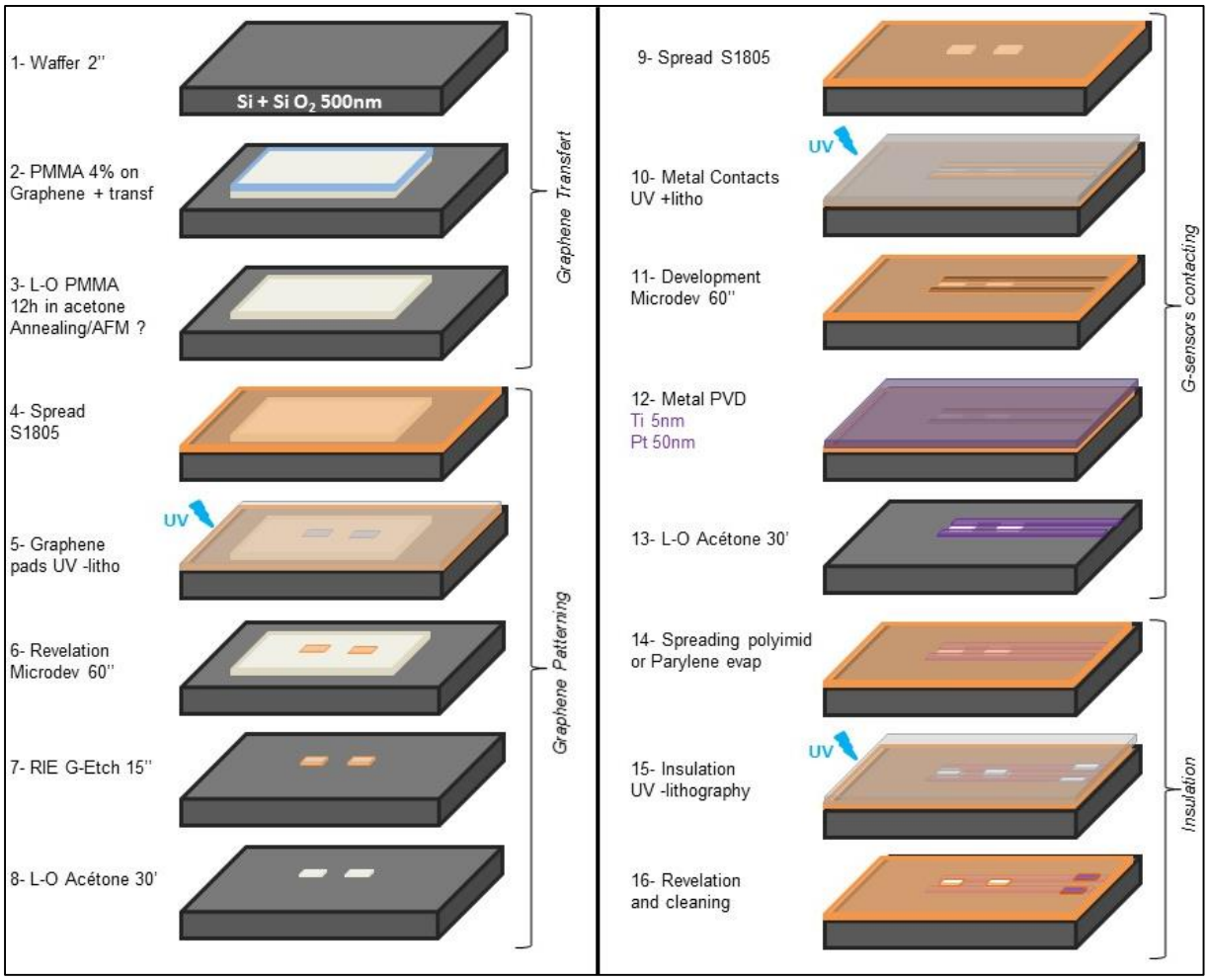

Figure 91 -Fabrication flow of G-FETs on silicon oxide: The steps are described in the text of the thesis to explain the tools used to perform devices fabrication.

1 - 3 Graphene transfer First step is the integration of graphene using standard previously described wet transfer method on a Silicon wafer (Chapter II). The alignment of the graphene sheet on the wafer is performed by manually positioning the sheet on the desired area pushing it with a tweezer.

4 – 8 Graphene patterning: Second step is the photolithography patterning of graphene to create GFET channels. Photolithography is performed with a graphene compatible resist: Microposit S1805.

Indeed, resist choice when working with graphene is important as many resists use either a solvent or a developer that is damaging graphene. After the S1805 polymerization under UV for 30 seconds, it is developed with a specific basic solution called Microposit developer.

Graphene is then etched with oxygen plasma in a Reactive Ion Etching machine (RIE) and the protective resist is removed from the graphene channels with acetone Lift Off (LO).

9 –13 Contacting Graphene sensors: another photolithography step is performed to create contacts for graphene. Once the resist is spread and developed we perform metal evaporation on the sample. During this thesis, we used 5nm titanium known to provide a good adhesion layer [205] and 50 or 100 nm platinum for electrodes fabrication. After the metal evaporation, the protective underlying resist is removed with another acetone lift off.

14-16 Insulation: A final insulation layer is then deposited and patterned on top of the contacted devices in order to insulate metal contacts from our future measuring electrolyte or living tissue. To this end, I either used a 5 µm thick photosensitive polyimide Fujifilm PI 9505 or a parylene evaporation in a specific reactor, followed by a photolithography to pattern the insulation layer. Parylene advantage was not only its biocompatibility and FDA approval for biomedical devices use [206], but also its thinness, providing a sufficient insulation with 100nm and thus allowing a better coupling between our sensors and neurons.

4.1.3 Deep etching for 3D shaped implants

The previous fabrication flow (Figure 91) allowed to work with FETs on flat substrate, to perform in vitro neuronal activity reading and GFETs tests. However, in order to fabricate 3D probes sharp enough to penetrate the pia matter and thin enough to have a low invasiveness (see Chapter III) I had to perform deep etching of the supportive silicon on both sides with a process detailed in Figure 92.

Deep etching of silicon is performed using a Deep Reactive Ion Etching machine. I used the patented Bosch process [207], [208] well known in MEMS microfabrication as it provides **high etching rate and uniformity** [209]. The Bosch process consists in alternating 2 etching phases, an isotropic SF_6 plasma etching is interrupted by a passivation layer deposition with C_4F_8 injection in an oxygen plasma. The etching rate of such process for silicon is around 10 µm/min.

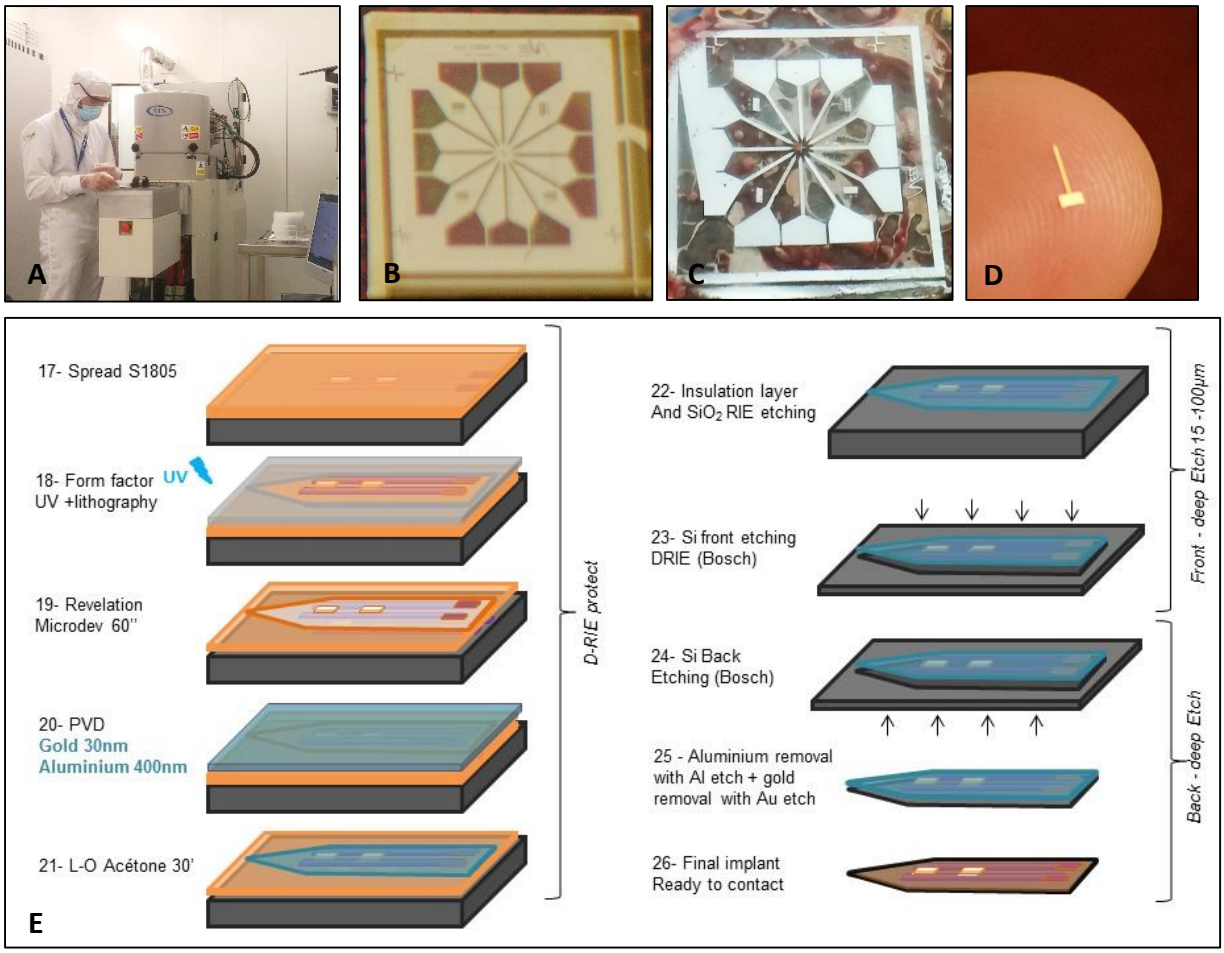

*Figure 92 - From flat substrate devices to a 3D micro machined probe using Deep Reactive Ion Etching: **A** Shows DRIE machine, **B** a flat device (previously introduced) and **C** the same device after DRIE etching. **D** shows the size of an implant I built to be used as a dummy probe to test 3D graphene transfer. **E** Process flow: I start with a photolithography to pattern a protective metal hard mask, then use PVD deposition of metal to create a layer of gold and aluminum and finally, after resist liftoff, I perform etching of the different layers until probe of the desired thickness is released.*

17-21 Protection of future devices before DRIE: First step for DRIE process is masking the area not to be etched. The standard process to this end is photolithography, however, here, the strength of the DRIE technique and the presence of O_2 plasma would induce resist etching. One must either use a special resist that is thick enough to overcome DRIE (but hard to remove) or use a metal protective layer to this end.

I used a 400nm aluminum hard mask to perform DRIE during this thesis. However, this mask wet etching removal being damageable to graphene sensors, I first evaporated a thin layer of gold on top of graphene. Indeed, gold remover is potassium Iodate KI/I_2 does not damage graphene.

2 -26 Front and back etching of silicon wafer:

Previously deposited insulation layer (Figure 91 step 14) and silicon oxide are first removed with standard RIE process. The targeted implant thickness was based on commercially available implants that are of a minimum of 15 µm thick. Two inches wafers are generally 280±30 µm thick and I consequently have to etch back side of the sample to reduce this thickness before patterning the future implants by front etching.

4.1.4 Flexible devices fabrication

The fabrication of flexible polyimide implants was first investigated in this thesis because it allows a decrease of implant rigidity and thus is one of the **way to counteract gliosis** strength during implant insertion [70], [72], [210]. I set up and used the Figure 93A process flow to build polyimide devices supporting graphene bioelectronics.

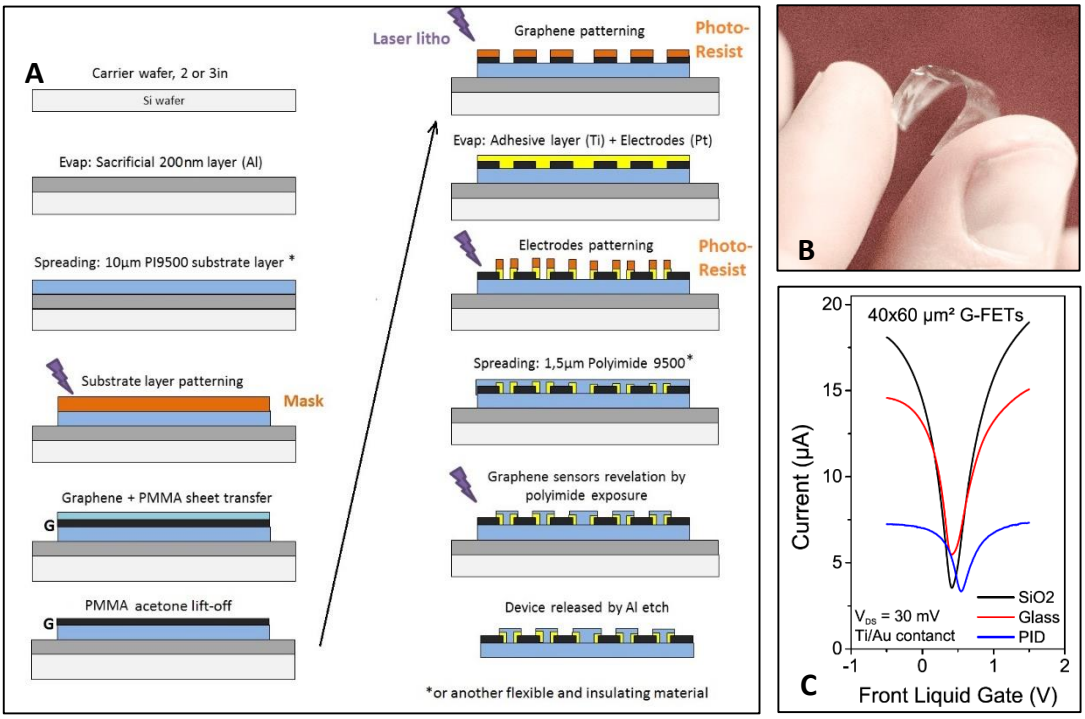

Figure 93 – Process flow to build a polyimide flexible device supporting GFETs and transconductance measurement of our GFETs devices built on different substrates: ***A)*** *Pprocess flow to build a flexible device on polyimide (PID) or another flexible and insulating substrate uses the same steps than standard silicon devices except that we previously prepare a 200 nm sacrificial Al layer between the silicon wafer and the flexible material, here a 10 µm thick polyimide, in order to release the device from silicon after all the lithography and metallization steps.* ***B)*** *A flexible device released from silicon wafer* ***C)*** *Field effect in 40x60 µm G-FETs fabricated on different substrates in collaboration with F.Veliev, Institut Neel. The measurements were made in liquid gate condition in PBS solution at Vsd=30mV. GFETs on polyimide exhibit the higher contact resistance and a shifted Dirac point, however performance in terms of transconductance are not changing compared to SiO_2 based GFETs.*

The flexible device is built **with same bottom up** approach than previously described (Figure 91) but with few notable differences. Here we use polyimide as a 10µm flexible carrier and the insulating material. In order to release the polyimide device in the end of the fabrication process, a sacrificial thick layer of aluminum (<200nm) is first evaporated on our wafer surface.

In a second time, our chosen polyimide is spin coated onto the surface to create the basis layer of our device.

I chose a **photosensitive polyimide** to build our devices easily and avoid too much steps of resist development when graphene is integrated. The polyimide choice was made in function of its developer as graphene is sensitive to aggressive solvent often composing developers. I first tested several developers and their incidence on graphene integrity and quality (assessed by Raman spectroscopy) and came to the conclusion that Polyimide Fujifilm© LTC PI 9505 for which developer is cyclopentanone, was a perfect material to integrate graphene in polyimide devices.

Polyimide generally needs a high temperature (350°C) baking to be hardened and to remove any contained solvent. LTC PI 9505 allows a lower temperature baking of 250°C that would be less dangerous for graphene integrity.

Once the first polyimide layer spread and cooked, graphene is transferred, patterned and contacted according to previously described photolithography and metal evaporation steps.

The last step of the device fabrication, insulation, is here made using a thin polyimide layer: LTC9505 is diluted in its Gamma-butyrolactone solvent in order to make it 1µm thin and thus to reduce the future distance between our devices and the neurons.

At this point of the fabrication, the series of previously described DRIE steps allows devices patterning as 3D probes. In the end, device is released when removing the deep etch aluminum protective layer (Figure 93B), thus also removing sacrificial aluminum layer underneath the polyimide basis.

The development of these flexible implants allowed to create and characterize graphene transistors on polyimide as shown on Figure 93C. Comparison with our others G-FETs built on silicon oxide and glass shows a much higher contact resistance, a decrease in I_{on}/I_{off} and a slight shift in Dirac point, but the transconductance of the flexible GFET is preserved. Fabrication of such devices was not pursued during this thesis to create in vivo devices. Indeed flexible implants need very specific manipulation tools and surgery skills to be inserted through the pia matter. Still we demonstrate here the **feasibility of such flexible implants with graphene**.

The first goal was to try graphene sensors for intracortical neurons activity recording. I thus developed a silicon based probe with a similar design it would take to create a flexible device.

During this thesis I only fabricated GFETs on polyimide and SiO_2, however, others flexible material could be used the same way, provided that this material would be resistant to PMMA acetone lift-off which is mandatory in the previous process flow.

4.1 Design and fabrication of implants - Flexible devices fabrication

For the fabrication of flexible device with acetone sensitive materials, I developed a process to transfer graphene without PMMA during this thesis, this process is detailed in the part 2 of this chapter (4.2)

4.1.5 Silicon probes carrying GFETs an GMEA

After all the microelectronic steps previously detailed in this thesis, I achieved the fabrication of implant probes and was finally able to integrate high quality graphene as illustrated in Figure 94.

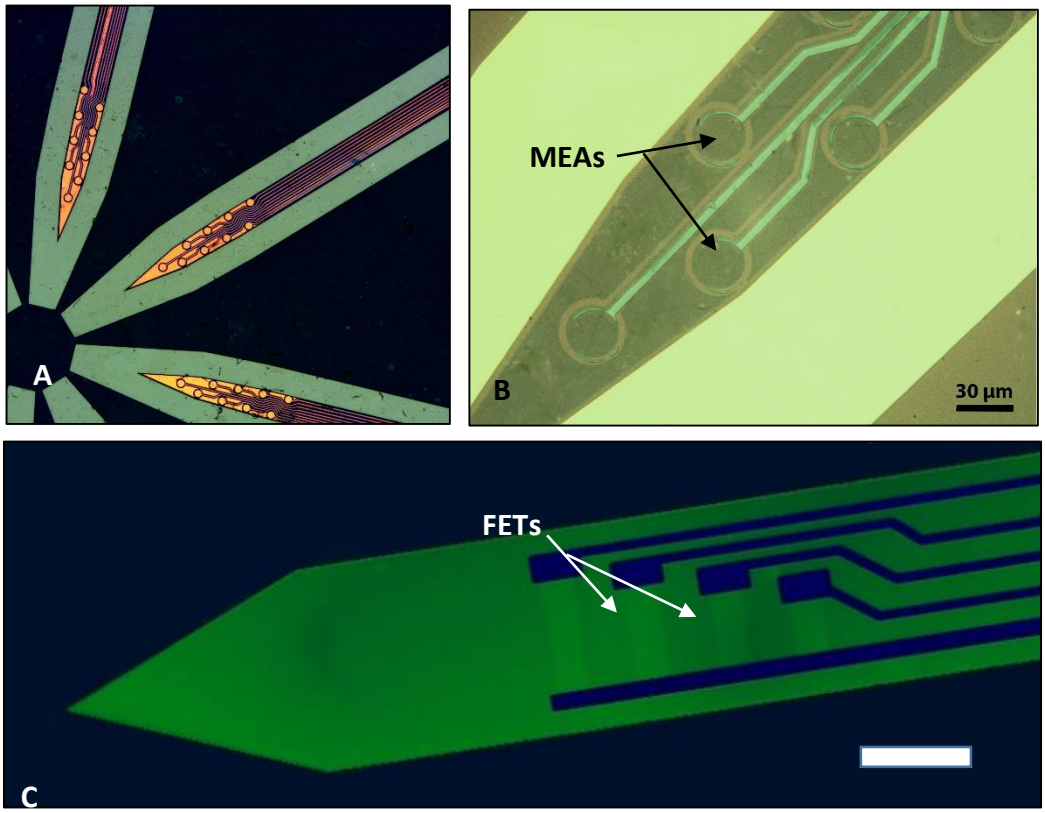

Figure 94 – Fabrication of graphene biosensors on 3D micro machined devices ***A*** *Optical microscope imagery shows micro fabricated MEA probes* ***B*** *Close up view shows GMEA with graphene before the 3D DRIE etching and implant releasing. Graphene is not only used for detection but also coating the whole surface of the probe to improve bioacceptance. SiO_2 is the back insulating layer for the probe..* ***C*** *Optical microscope colored picture of micro fabricated probe supporting 4 different sized graphene transistors after DRIE and probe releasing. Scale bar is 40 µm*

a - Connection of implant to extra cranial connector

Linking microelectronic stage to proper macro-electronic output connector compatible with EPFL setup (TdT Zif-clip or Omnetics connectors) requires self-alignment and specific capillary bonding machine we do not possess in our lab (Figure 95).

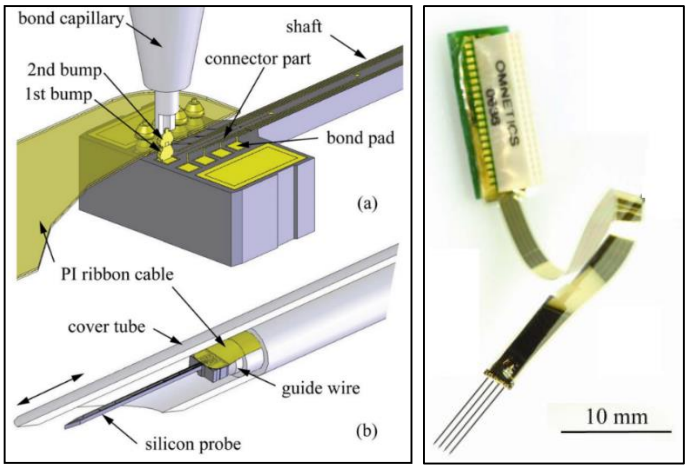

Figure 95 - Capillary bonding process commonly used to solder silicon probe contact to a connector: The macro electronic connector can be connected directly on a PCB or here via a polyimide ribbon cable. after [47]

However, I investigated a custom way to connect my silicon probes to a homemade flexible polyimide ribbon. For that purpose I created a ribbon design that would allow micro soldering with our standard wire micro-soldering machine. As illustrated on Figure 96, through vias on polyimide and shifted pads, we can contact underlying probe with a gold wire and link it to the corresponding polyimide electrode.

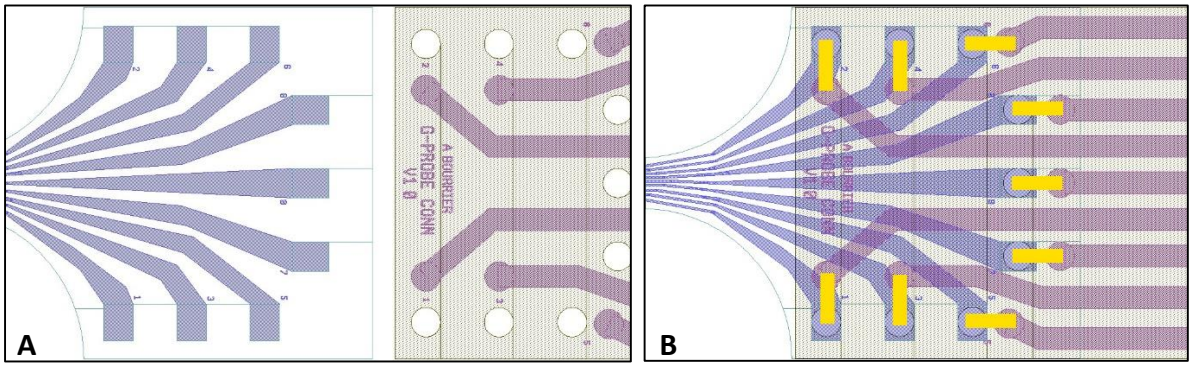

Figure 96 - Polyimide ribbon connector custom design which allows wire soldering through polyimide vias: ***A*** *On left the connector pads of the implant, and on right the polyimide ribbon I designed.* ***B*** *When aligning polyimide ribbon extremity on top of the pad area of the implant, holes in polyimide are facing implant pads and thus allow wiring (in yellow) with gold wire to connect implant and polyimide electronics paths.*

After fabrication of this polyimide connector I tested it by measuring its electrical conductivity as a function of deformation rate to assess the proper behavior for future in vivo experiments. For this purpose, I measured the resistance between 2 points of the ribbon connector while folding it slowly. The folding angle variation between flat 180° and 90 ° folded was associated to a deformation rate in percentage and traced on Figure 97. Polyimide ribbon's platinum wire

resistance remains stable until 30% of deformation and then starts to increase until 80% of deformation. The bending stability up to 30 % is then taken into account to choose the length of the future ribbon that will come out of the brain and be slightly folded to be connected on the top of the skull.

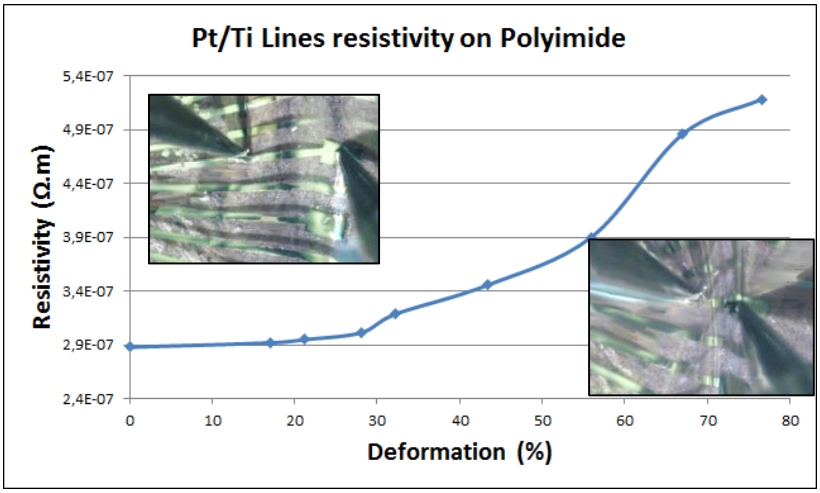

Figure 97 - Polyimide ribbon's platinum electrodes resistivity variation during deformation: The deformation rate was calculated from the distance measurement between the two probes while folding the ribbon progressively as illustrated on the two pictures.

Such polyimide ribbons were thus micro fabricated and measured during this thesis but I had to overcome self-rolling of the polyimide ribbon when released from the silicon supportive wafer, as much as many difficulties coming from alignment of a 1 mm probe with a 1 cm self-rolling polyimide ribbon. Due to the extensive time spent on graphene optimization, and the developments needed on the polyimide ribbon cable design to make it easily usable compatible with our bonding machine, I was not able to create the output connector during the remaining time of this thesis. In order to investigate graphene bioacceptance, I focused on coating an available implant and thus developed processes to coat commercial implants with graphene. The advantages of commercial probes for this thesis were that connectors were adapted to EPFL setup and already bonded to silicon probes. The drawbacks were that I was not able to test our full GFET or GMEA graphene electronics. However, the **coating of a commercial device** offers potential improvement on **electronics and bioacceptance** I will develop in the next part of this chapter.

4.2 Coating implants with graphene

In vivo **metal degradation** in vivo was demonstrated to be a source with signal degradation of time thanks to abiotic characterization of devices after few weeks [211]. On the other hand, and as explained in chapter II part 3, graphene could provide a way to protect electrodes metal degradation thanks to its **anti-corrosion properties** [147] and the uniformity of our transferred layer on the probes.

4.2.1 Strains induce cracks with standard transfer

We firstly bought a probe from Neuronexus©, an US intracranial implants manufacturer, in order to test direct transfer on a commercial probe. Figure 98 illustrates first tests, by standard fishing of PMMA-graphene stack. Important deformation of the stack was seen with optical microscope (Figure 98B) suggesting connector leverage is responsible for deformation of the PMMA stack, avoiding good contact between graphene and probe surface. Several tries were made using thinner PMMA layer on graphene, and finally resulting in a very low graphene piece on the probe as illustrated on the SEM picture on Figure 98C.

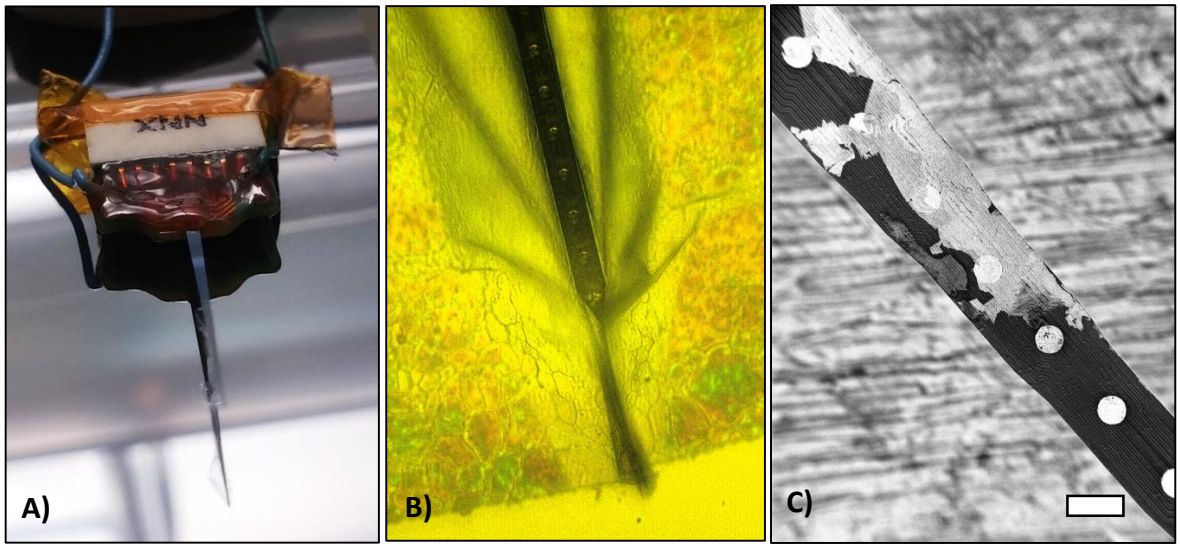

Figure 98 – Standard graphene transfer on 3D thin device does not provide good graphene coverage because of carrier strains ***A)*** *Neuronexus implant with its connector placed on top of a silicon wafer for direct transfer.* ***B)*** *Optical microscopy shows important strain on PMMA layer once covering the probe, suggesting graphene strain linked to connector leverage.* ***C)*** *SEM picture after acetone PMMA removal shows very few and in bad shape graphene one some parts of the implant. Scale bar: 40 µm*

The issue faced here was the connector **cantilevering** the probe and avoiding good contact between the probe and the underlying silicon wafer, thus limiting graphene adhesion on

probes. I then contacted another intracranial implants manufacturer, Atlas microsystem©, that were ready to provide me some of their commercial probes without connector as illustrated on Figure 99A. I was then able to lay down these probes on a silicon wafer, bond them with Kapton tape to insure stability and perfectly flat surface for graphene transfer (Figure 99B).

However, despite the apparent good environment for transfer, graphene appeared burst on SEM picture. It suggests that not only the connector cantilevering the probe can provoke strains, but, at a lower scale, the step between the implant surface and the wafer surface is sufficient to induce graphene breaking all around the implant, despite being of good integrity on underlying silicon wafer.

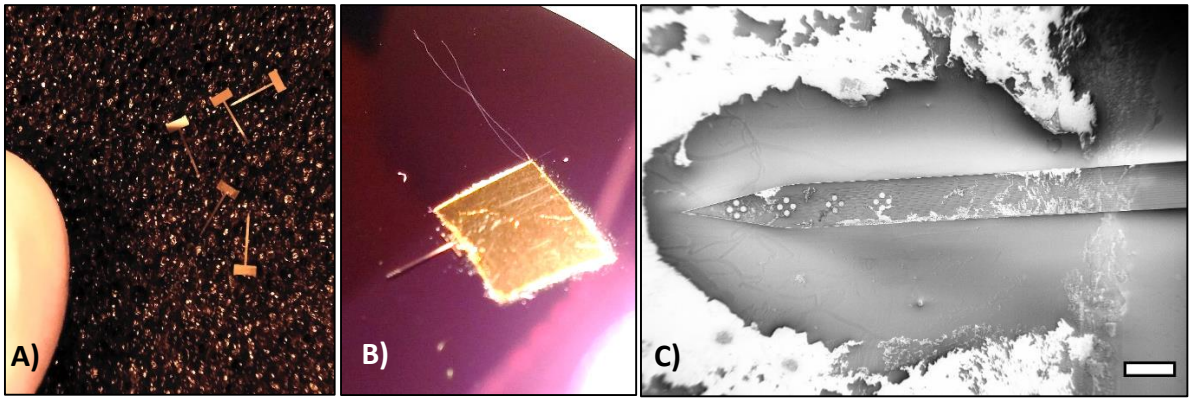

Figure 99 – Unconnected implants are easier to coat with graphene but too thick to avoid film breaking during acetone lift off A) Unconnected micro machined probes used for graphene transfer on 3D tests. B) Despite perfect lying on a silicon oxide wafer, C) SEM imaging shows that strain were yet too strong to avoid graphene blowing out all around the probe. Scale bar is 200µm.

I consequently developed several graphene coating methods in order to transfer graphene on micro machined implants. I will detail these methods to coat implants first without and then with a connector bonded.

4.2.2 Solution for unconnected implants

Next level of improvement I brought to coat previous unconnected implants was creating a **negative mold** for the probes to provide a perfectly **flat surface to the graphene** sheet, putting the top surface of the probe at the same level than its carrying wafer.

For that purpose, I designed a negative lithography mask and performed several microelectronics steps like photolithography, metal evaporation and deep etching, in order to create proper probes shaped holes inside a supportive wafer for future transfers. Figure 100 details this fabrication process: after a positive photoresist spreading I position implants on the surface to serve as hard masks (masking light), then UV exposure polymerize resist making it removable by a specific chemical developer solution. Implants are then removed and resist is used to deposit aluminum everywhere except on the desired etching area (implant shaped). Finally, Deep Reactive Ion Etching is applied to etch 100 µm thick implant shaped molds in the silicon wafer. The process used and the Deep RIE techniques are detailed in part 1 of this chapter.

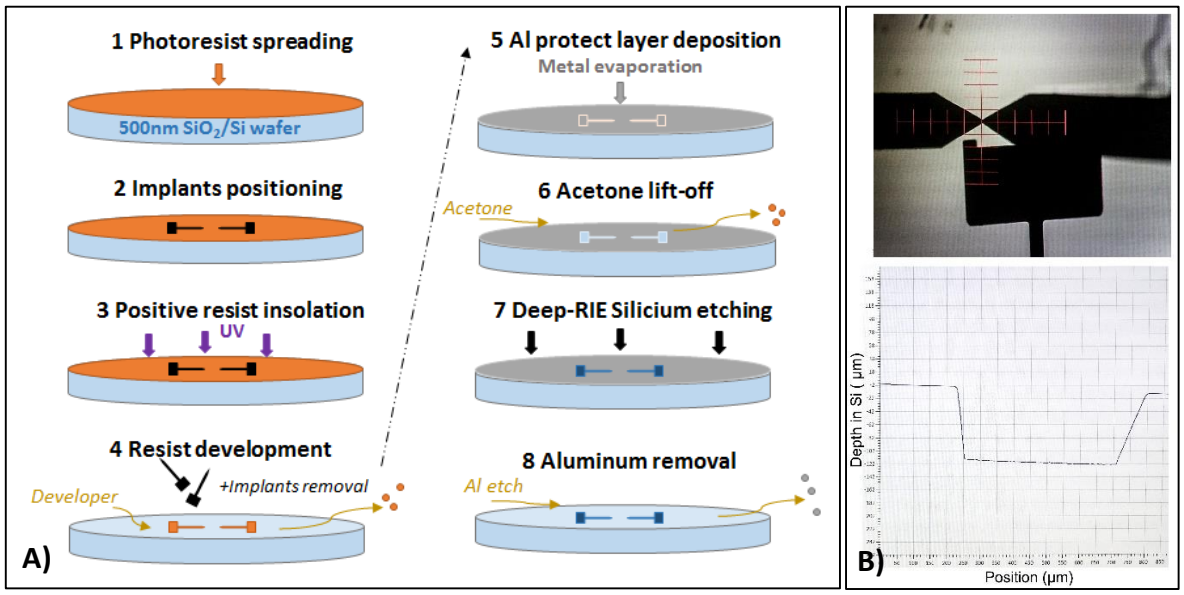

Figure 100 –Deep RIE etching of a mold to transfer graphene on a drowned probe in silicon wafer avoids graphene breaking during PMMA carrier lift off ***A)*** *Process flow to etch negative commercial unconnected implant mold into silicon without creating a mask, by using implants as hard masks.* ***B)*** *This process then allows Deep Reactive Ion Etching of silicon on the desired depth corresponding to the thickness of our implant, here around 100 µm thick. The depth is here controlled with a Bruker profilometer.*

Figure 101 shows the obtained uniform graphene coverage of the commercial unconnected probes thanks to the drowning in silicon method that allowed important lowering of strains on graphene sheet during transfer process. However, few cracks on graphene still appear on this picture. The thickness of the probes being always few

micrometers above 100 µm, burying it in 100µm mold was still creating a little step that was inducing strains on graphene. Height of probes and depth of mold have to match perfectly to totally reduce the strains and the cracks. This method was perfect for post processing unconnected implant but was irrelevant to coat already connected implant given the bulky connector impossible to burry in a silicon mold.

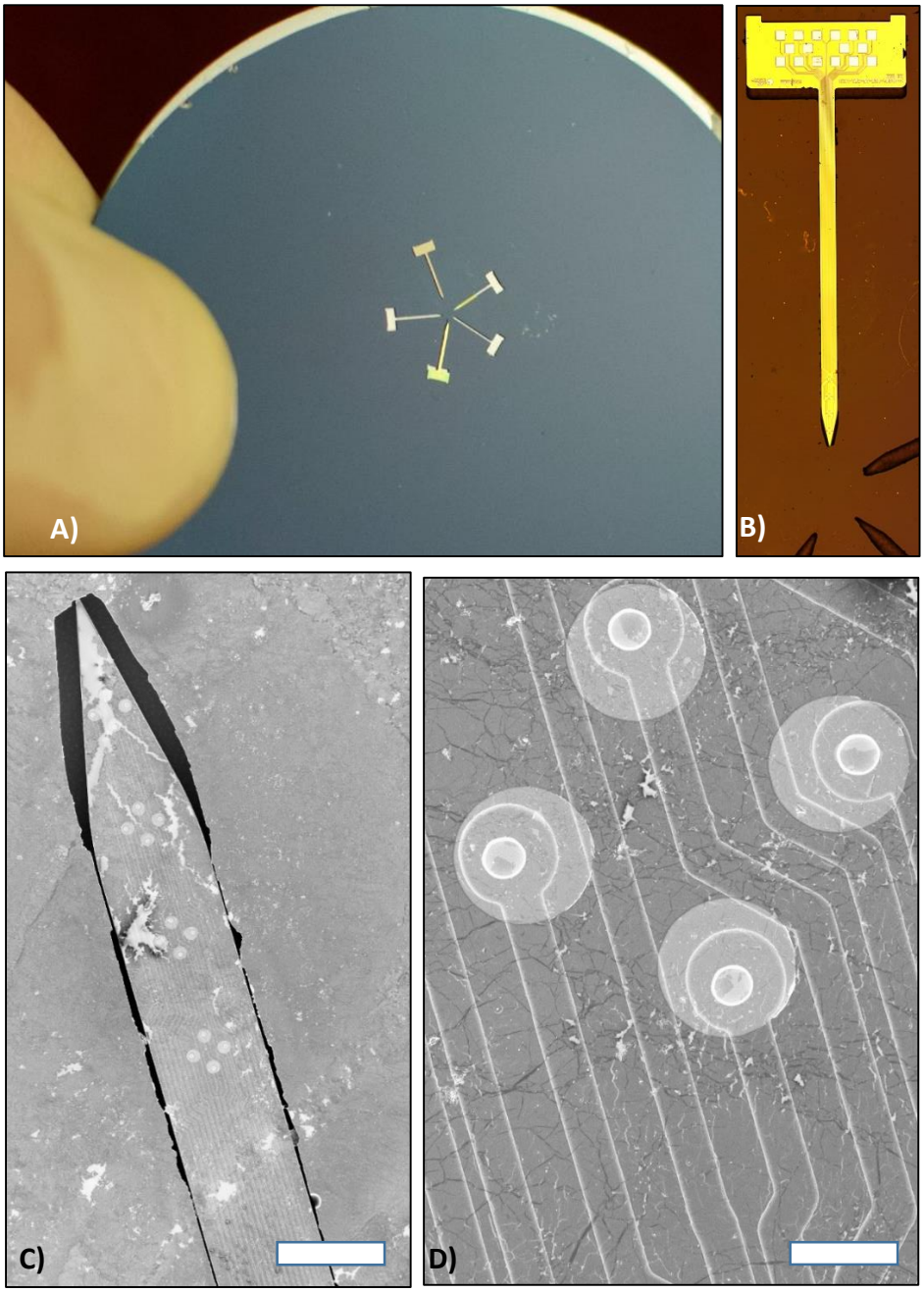

Figure 101 – Buried probe in a wafer is properly covered with graphene except few sites with graphene cracks: ***A*** *wafer is used a mold to burry probes and have them on the same surface than silicon oxide to reduce strains on graphene during transfer* ***B*** *The probes are placed inside the molds (Micrography)* ***C*** *SEM picture of commercial intracranial probe drowned into its silicon mold and uniformly covered with graphene in grey. Scale bar is 100µm* ***D*** *Close up view of graphene coated electrodes on the implant shows few graphene cracks and graphene wrinkles on the surface. Scale bar is 10µm*

4.2.3 Direct transfer on ready to use implants

For commercially available implants with connectors (Figure 103A&B) I then developed a recipe for direct naked graphene transfer (Figure 102) without the resist carrier.

Transferring naked graphene and still preserving the integrity of our graphene monolayer and preventing cracks was tricky. Cracks can weaken the monolayer and thus lead to release of graphene pieces in the body during the insertion and must be avoided.

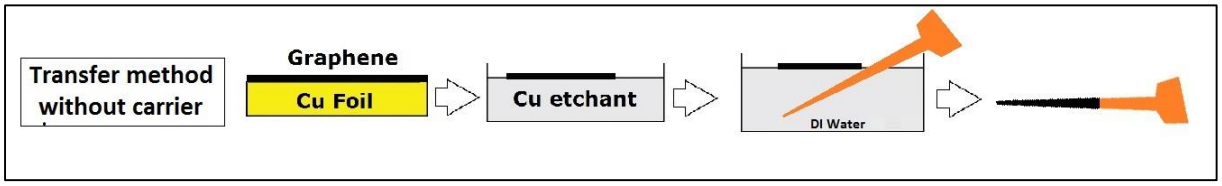

Figure 102 – Transfer without PMMA carrier is tricky but allow coating of delicate 3D objects with graphene: We demonstrated in this thesis the possibilities to get rid of the carrier resist to perform a direct continuous graphene layer transfer on 3D devices.

Not using the capping layer (generally PMMA) that allows coherence of the graphene film, visibility and ease of manipulation during transfer make the process very delicate to set up. Changes of copper etchant bath was made to obtain more uniform etching of the copper and thus reduce strains on graphene during wet etching. The basic principle is to increase the etching speed using stronger acids in order to reduce the time graphene is partly exposed to the solution. This recipe will be published later and cannot be detailed in this thesis.

Manipulation tools in cleanroom were adapted as much as RIE processing, to avoid connector burning while allowing good activation of the implant surface. RIE activation was indeed paramount to obtain a very high surface hydrophilicity and thus reduce the thickness of the water film between graphene and probe during transfer.

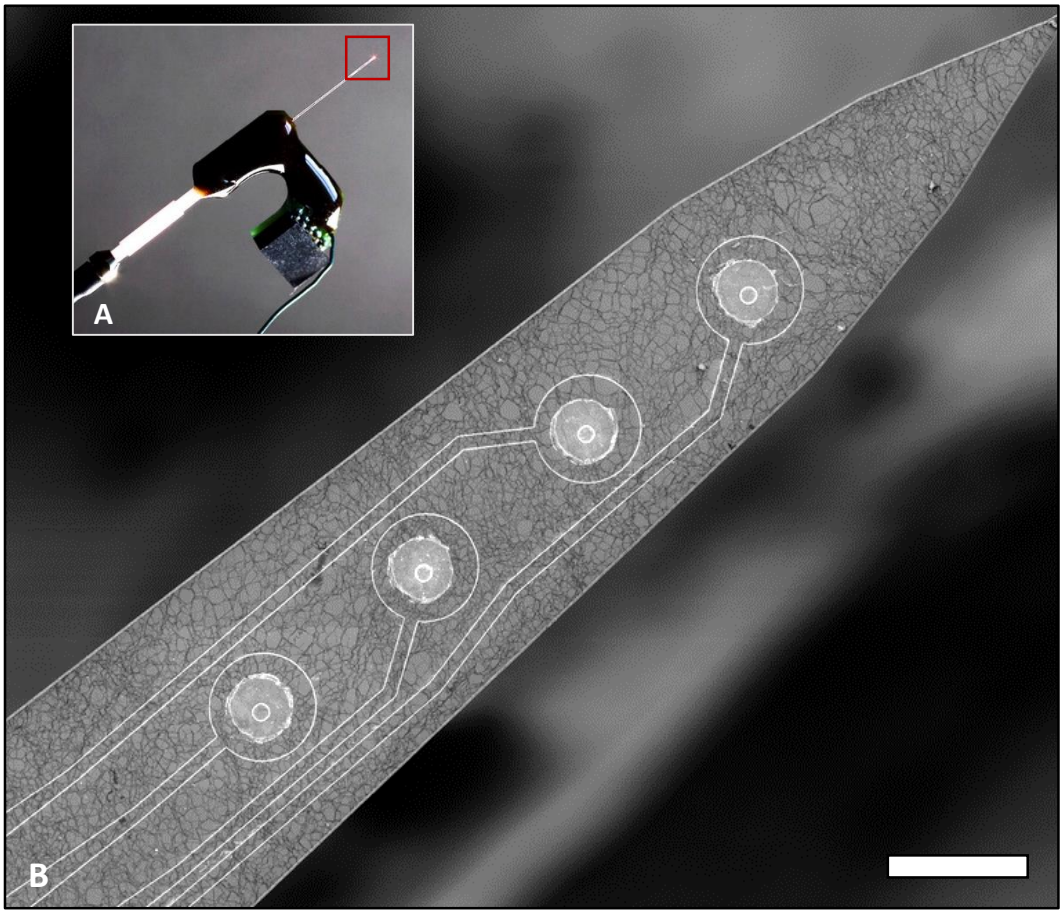

Figure 103 - Monolayer graphene conformal coating into commercial available silicon probes: ***A)*** *A Neuronexus Q-trodes probe with an optical fiber integrated to the device and its connector attached* ***B)*** *A Neuronexus© Qtrode implant with its connector underwent direct no-carrier graphene transfer (as shown in Figure 102) to successfully achieve uniform coating of its whole surface with a preserved continuous monolayer of graphene. We distinguish the wrinkles on the graphene surface corresponding to graphene local folding. Scale bars are 50 µm.*

After carrying out series of development and tests on homemade probe dummies, I was able to put forward a **unique recipe** to avoid graphene to tear apart during copper etching and rinsing. I managed to coat 5 test implants from Neuronexus (Q-trodes) with **perfect continuous graphene layers** showing good electronic conductivity: graphene connection between Electrodes was measured after transfer to verify the continuity of our graphene (Figure 104B). Raman spectrum allowed verification of graphene integrity and number of layer measurement (Figure 104A). According to the Raman's peaks evaluation of graphene type and integrity explained in chapter II, graphene is her **slightly multilayer**, most likely because of wrinkles that we see on the close up view (Figure 104C).

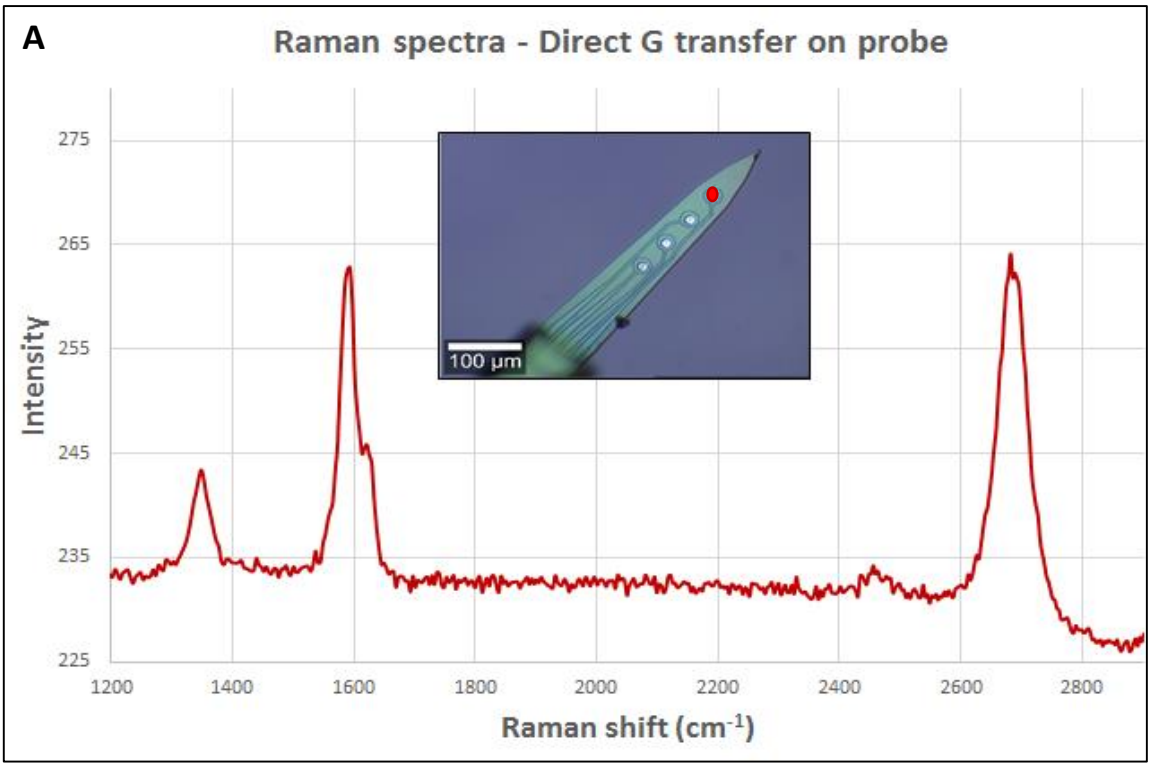

B

	Resistance Values (kΩ) 21/09/2016				
	89C	86C	86D	86E	86F
R21	17,6	15,2	∞	179	∞
R24	21,8	15,7	∞	190	∞
R23	26,1	20,7	∞	196	∞
R14	21,3	16,2	33,7	55,7	39,4
R13	25,8	20	39,1	57,1	48,2
R34	20,2	19,9	20,3	24	28

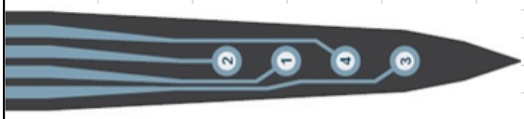

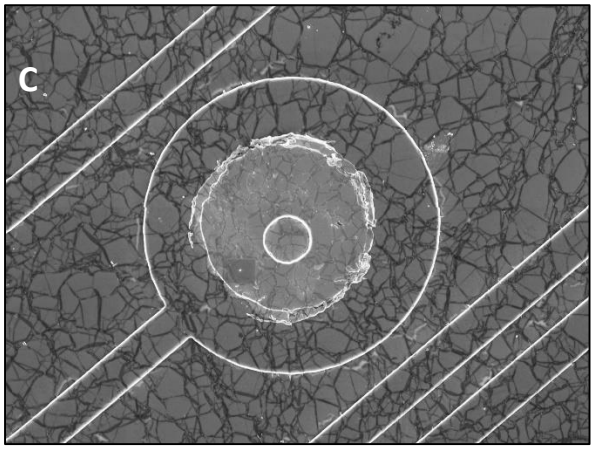

Figure 104 - Graphene coating is continuous as verified by conduction measurement and Raman spectroscopy: ***A)*** *Raman spectra shows specific graphene peaks as explain in chapter II, G peaks is almost as high as 2D peak, suggesting multilayer graphene, probably linked to wrinkles seen on SEM picture. D peak however reveals few defects in graphene structure, most likely due to the strains induced on graphene by transfer without carrier* ***B)*** *A majority of sensors are connected to each other. The resistance between 2 well connected sites was evaluated to around 4kΩ by extrapolating the different values in function of distance between sensors. The main resistance value of around 20 kΩ might be coming either from graphene coupling to metallic sensors, or to the length of contact electrodes to the connector.* ***C)*** *Close up view of a covered sensor shows wrinkles that resemble multilayers area which could explain previous Raman state.*

Defect peaks D at 1350 cm^{-1} and D' at 1620 cm^{-1} are suggesting defects in the carbon lattice: grain boundaries, edges, vacancies sites and could also be linked to the numerous wrinkles of graphene on the surface as seen on (Figure 104C).

Those implants were used to assess graphene bioacceptance in vivo, its influence on glial scar formation and its durability in the cortex after weeks. This work is detailed in next part 4.3.

4.2.4 Electron-beam lithography on 3D devices

Once covered with graphene, such 3D devices might face shortcut between electrodes sites as we see on Figure 104B. In order to address this issue, I developed a method to perform Electron Beam (e-beam) lithography on 3D devices using a FESEM LEO 1530.

E-beam lithography uses specific resists to be polymerized by electron beam, such as PMMA that need to be spin-coated, or QSR-5 that can be evaporated on any device [212].

I thus evaporated QSR5 resist on a graphene coated silicon based implant to perform graphene lithography. QSR5 resist developer is MEK (Methyl-Ethyl Ketone) and its lift-off solution is TMAH (Tetramethylammonium Hydroxide), both known to damage graphene.

I consequently developed a process illustrated in Figure 105, using a gold interlayer hard mask to isolate graphene from the QSR5 resist. Once graphene covered with 30nm gold (2) and QSR5 (3), the resist is lithographed with e-beam (4) and developed in MEK (5). The probe is then dipped into gold etchant (KI/I2) to uncover underlying graphene that needs to be etched (6). This uncovered graphene is then etched away under O_2 plasma in Reactive Ion Etching chamber (7). The final steps consist is the QSR5 removal in a TMAH solution (8) and another gold etch step to remove protective gold from patterned graphene (9).

This process allows for example, the **insulation of GMEA electrodes** one from the other as illustrated in the Figure 105 design, mask and microfabrication pictures.

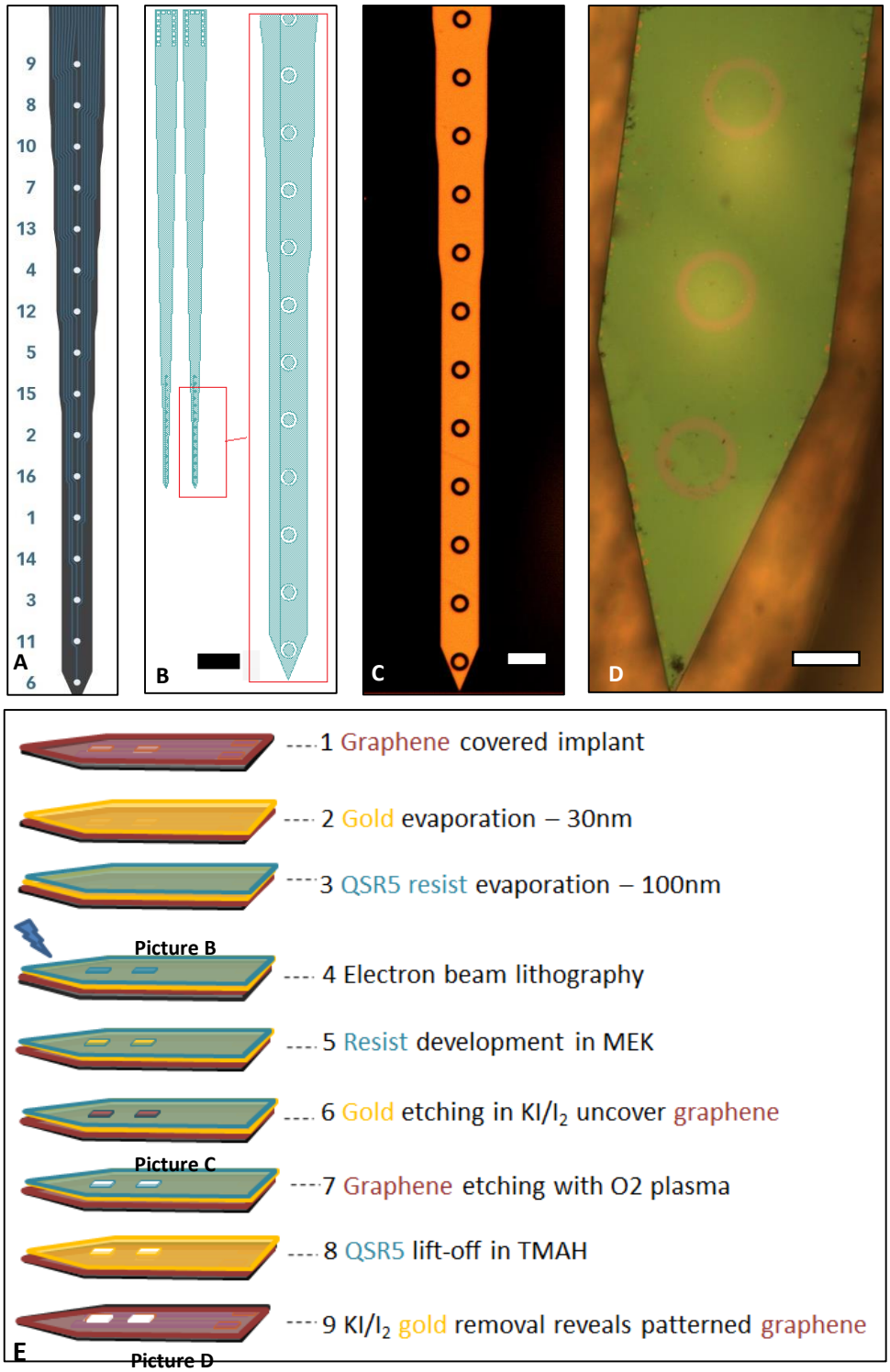

Figure 105 - 3D lithography custom process for graphene patterning on an implant using electron beam lithography: ***A)*** *A Neuronexus 16MEA probe was taken as the reference design to develop this process* ***B)*** *I created a lithography mask by reverse engineering to prepare graphene e-beam lithography on the implant* ***C)*** *An optical microscopy picture of the so lithographed probe at step 6 shows etched gold to uncover graphene on desired zone to isolate underlying electrodes. A, B and C scale bars are 50µm* ***D)*** *This photography shows very well the graphene etched on desired zone at step 9. This picture have been made on a dummy probe I built to find the perfect recipe and the good electron beam energy dose to polymerize QSR5 on gold. Scale bar: 40µm* ***E)*** *Process flow of the QSR5 e-beam lithography process and graphene patterning through gold hard mask. Process is explained in text.*

4.3 Graphene bioacceptance In-vivo study

4.3.1 Experimental conditions

As explained in previous part 4.2 of this chapter, in order to test graphene coating behavior in vivo, in terms of bioacceptance and durability of graphene in the cortex, I coated a batch of 5 commercial implants from Neuronexus. Regarding the size of the commercial connectors shown in Figure 106A, transfers were not processable with the previously developed wafer probe burring technique but with the naked graphene direct transfer. After carrying out series of development and tests on homemade probe dummies (Figure 92D), we were able to put forward a unique recipe to avoid graphene to tear apart during copper etching and rinsing. I was able to coat 5 test implants with perfect continuous graphene layers showing good electronic conductivity (measured between each MEA sensor) and great Raman spectrum (see part 4.2 of this chapter).

I did not process the previously described e-beam lithography (4.2.4) on these coated probes to isolate the 4 sites one from each other: indeed, having the possibility to measure the graphene resistance between sites weeks after weeks could provide information on graphene monolayer durability in vivo.

Ten similar Neuronexus© optrodes were bought: 5 were coated and 5 kept as control.

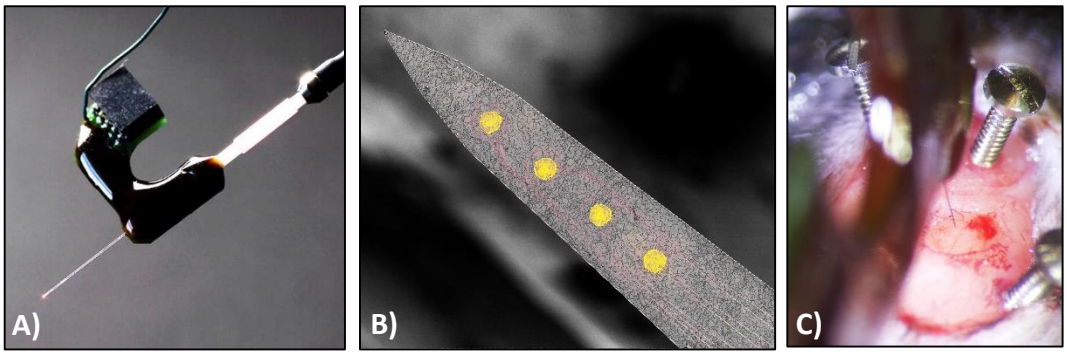

*Figure 106 - Neuronexus optrodes were successfully and entirely coated with a monolayer of graphene and implanted in 10 mice motorcortex 10 Optrodes **(A)** were purchased. 5 underwent graphene covering with the whole new process **B)** SEM picture of a Graphene coated probe with yellow colored 4 recording site emplacements and red colored electrode contacts pathways **C)** Implantation procedure shows craniotomy of a mouse with implant aligned in top of targeted area: motor cortex. Four titanium screws are used to provide the implant and its connector a stable anchoring to the skull.*

The previous experiments with six rats led us to the realization that animal sample population is of paramount importance for proper statistical results' interpretation. This time, mice were

preferred to rats because they are easier to manipulate and less fragile, but also because we had the possibility to use transgenic mice in order to perform optogenetics during our recording with commercial.

Optogenetic allows to control, with a stimulation monochromatic light, the activation of ion channels of neurons (see chapter I) and thus to control neuronal activity of the target zone. In order for our mice to have, within their motor cortex neurons, those light gated ions channels called channel rhodopsin, they must be transgenic. They thus undergo transfection with a gene that will trigger channel rhodopsin expression.

The implants were inserted in the motor cortex of **nine transgenic mice** using the same surgery procedure than the one described in the end of the chapter III: mice were anesthetized with Dorbene© and kept unconscious with Isofluorane gas while a stereotaxic frame helped maintaining the head still during insertion. The implantation was done under a binocular to ensure implant penetration and control any eventual bleeding.

The targeted area of the implant electrodes is **layer 5 of the primary motor cortex**, as it provides, in mice, the most important density of neurons projection to drive movement (pyramidal cells). Optogenetic stimulation of layer 5 has been a way for us to make sure we were recording motor signals by triggering massive amount of motor neurons activation around the sensors (Figure 107A), thus simplifying the experiments.

4.3.2 Motor neurons activity recording

Motor cortex activity was recorded once a week with mice moving in cage as illustrated on Figure 107B. Light stimulation allowed the good isolation of neurons signals and identification as motor neurons.

Figure 107C shows spikes sorted from the recording made on a mouse with a coated implant, 2 weeks after surgery. The very good distinction of 3 different neurons in function of their amplitude and spiking velocity testify of a very good quality of recording. This quality of recording was tracked for each of the 9 mice, on each of the 4 electrodes per mouse:

Some electrodes were **not efficient to record** any neuron and were given the score **0**, others were able to record apparent neuronal activity but **not strong enough** to distinguish if they were related to motor activity. They were given the score **0.5**. The electrodes able to record **one or more motor neurons spiking activity** like illustrated on Figure 107C were given the score **1**.

I then used these scores in order to track the **rate of operational sensors** along weeks after surgery and thus compare the signal evolution between coated implants population and control implants as illustrated on Figure 107D. We can see on this illustration that coated implants behave better than control 2 weeks after surgery. Whereas coated implants are able to record moto neuron activity with a mean operational rate stabilized at 50% until 5weeks, the control implants signals start decreasing strongly after 3 weeks to a mean operational rate of 10%.

4.3 Graphene bioacceptance In-vivo study - Motor neurons activity recording

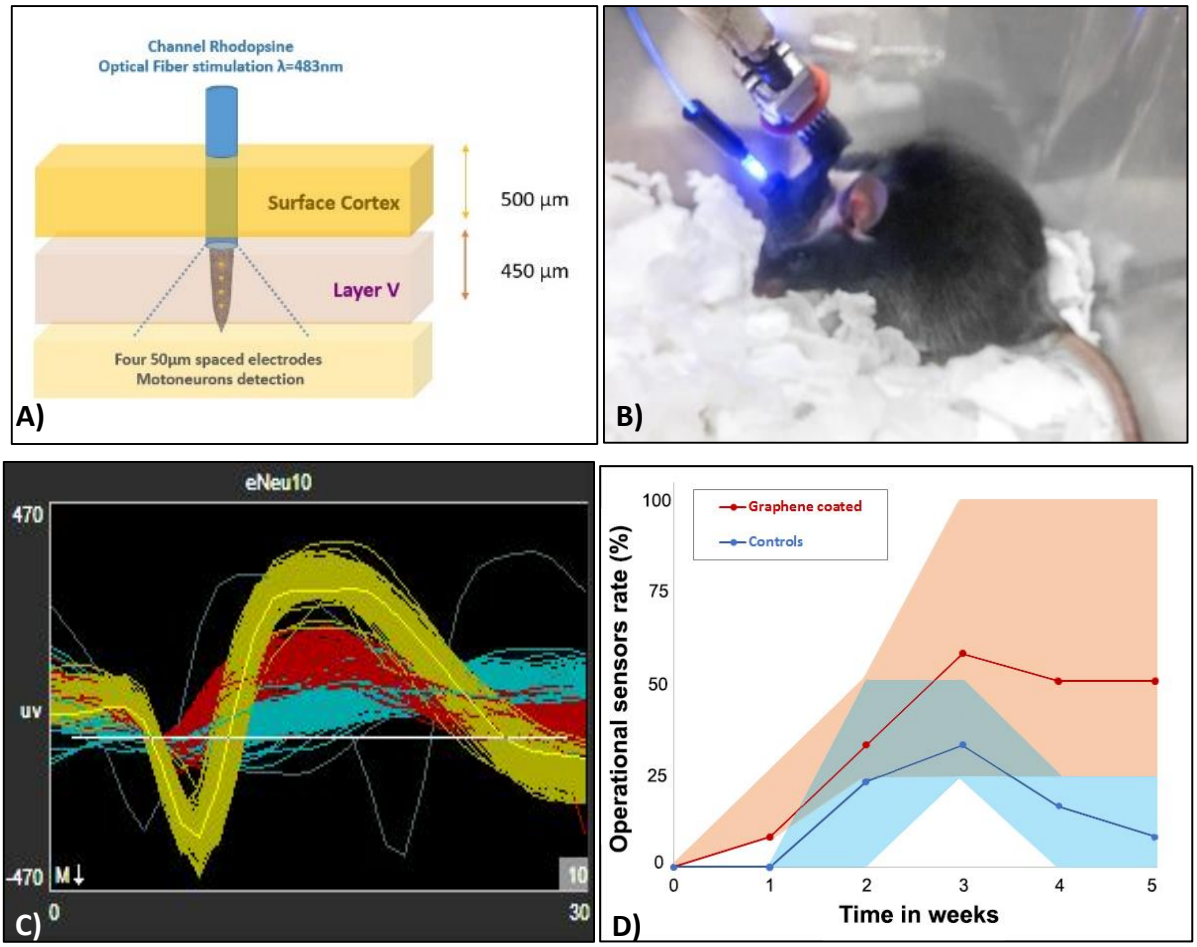

Figure 107 – Optogenetic helps to trigger moto neurons spikes and isolate them in line with spike sorting ***A)*** *Illustration of the optrodes implant motor cortex positioning in order to detect cortex layer 5 activity and stimulate it with blue light to activate channel rhodopsin and trigger action potentials.* ***B)*** *a mouse is shown during a short 1 min recording in cage with optical pulses of 1ms.* ***C)*** *Sorted spikes showing 3 distinct neurons detected by one of the graphene coated probes. The clear distinction between 3 neurons in function of their amplitude and spiking velocity testify of the very good quality of the recordings* ***D)*** *The number of operational sensors of each probe is tracked week after week. On this graphic, we show the mean number of operational sensor for each population of implants: graphene coated or not. Large colored areas show the variability in each population.*

These results suggest **a signal quality and durability improvement** with graphene coating of the implants. Graphene coating may have brought a surface bioacceptance improvement, a global inflammatory reaction reduction or a neuron-sensor coupling improvement.

4.3.3 Post-mortem analysis

a - SEM Abiotic characterization of implants

Graphene connection between electrodes had been measured after transfer to verify the continuity of our graphene (Figure 104). Just after the surgery, the measurement was done again and the values were the same, testifying of the **non-tearing off of our graphene during penetration** in the pia matter. Two weeks after the surgery, this connection was only found between few electrodes of 2 implants, and three weeks after surgery there was not any interconnection left, suggesting progressive **graphene layer degradation**.

Five weeks after surgery, animals were sacrificed and extraction of the implants was carried out. I processed to SEM observation and it confirmed the electrical measurement suggestion, revealing that the implants were nearly totally uncoated. Graphene has been found in a degraded state on top of electrodes sites (Figure 108C). This suggests a slow degradation process due to chemical or cellular activity around the implant.

I used the general views of the implant inside the skull scalp to verify the implant penetration depth and found out it was accurate at ±8.4%, implants tip being between 880µm and 1030µm depth (with a target of 950µm, see Figure 107A.)

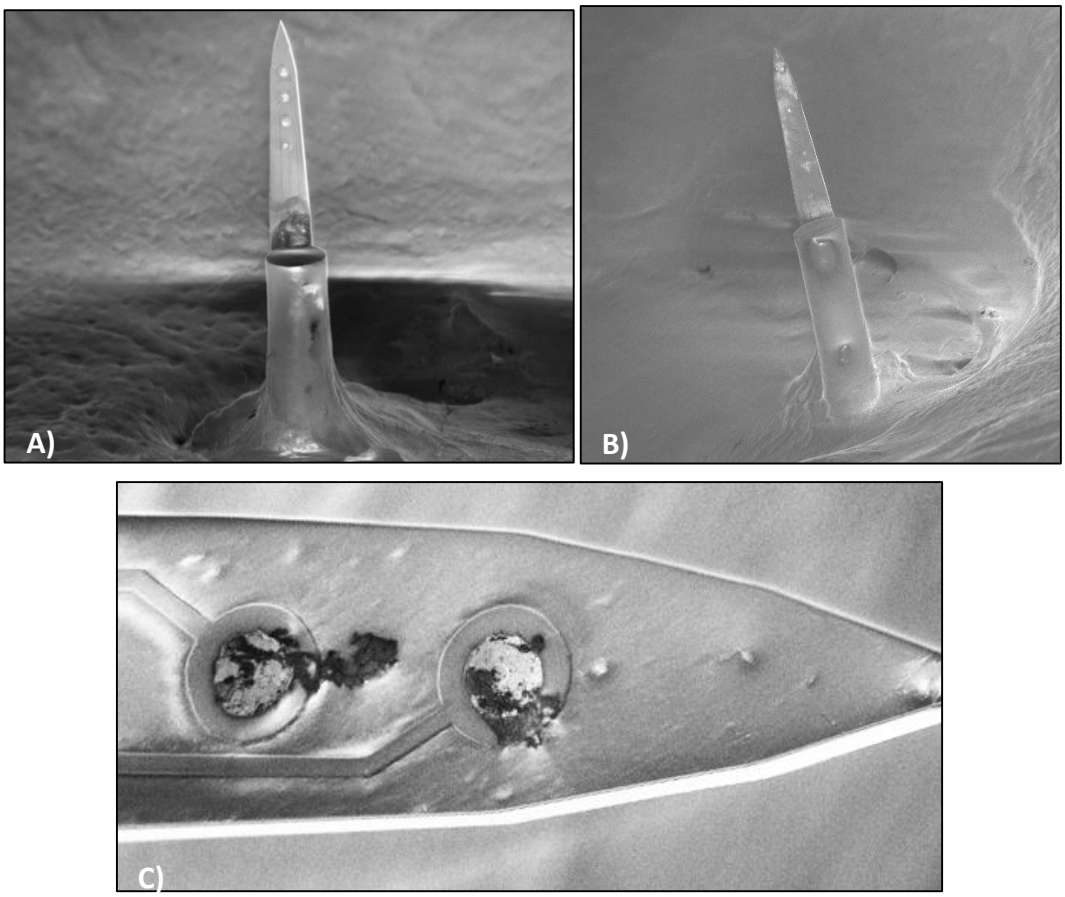

Figure 108 – SEM surface analysis of graphene coated implants five weeks after implantation in mice cortex: ***A) & B)*** *Implants are imaged directly inside the cut skull, making the SEM analysis challenging in term of angle and working distance. The pictures are used to check the depth of implantation and verify the precision of our surgery. Implants depth was found very accurate for all 5 coated implants.* ***C)*** *SEM close up picture of an optrode after extraction shows degraded graphene on top of the electrodes but nowhere else on the surface, 5 weeks after implantation, suggesting chemical or cellular activity degradation.*

This campaign showed an apparent **disputable naked graphene intracortical durability**. In order to further investigate the time graphene took to degrade, the same type of surgery campaign should be conducted with a weekly mouse immuno-histology during a five weeks minimum period. One might also verify that the loss of adhesion between graphene and implant surface is not responsible for a connection mismatch and a tearing of graphene during implant extraction.

However, this graphene fragility to in vivo tissue exposure confirms the **need to develop a protective coating** (Chapter III) to improve graphene durability in its future uses as intracortical bioelectronics.

b - Immunohistochemistry – Gliosis analysis

In order to investigate a possible relation between the apparent improvements offered by graphene coating in term of signal quality and the reduction of the inflammation around the coated implants, we have performed an immunohistochemistry analysis. This was undergone using the same protocol as we presented in chapter III. Two combinations of staining are performed in order to check both for the presence of astrocytes and microglia linked to the chronic inflammatory reaction, gliosis as described at the beginning of chapter III. The aim of such a process is the tracking of reactive cells concentration around the site of implantation.

After injection of animals and implants extractions, mice brains were isolated. 55 slices of thickness 30 micrometer are obtained. The resulting brain coronal sections were incubated overnight in a serum containing either:

- Ionized Calcium Binding Adapter molecule 1 (Iba1) with Nissl as control with a serum containing anti-Iba1 (1:1000, Abcam, USA) antibodies for **microglia** staining.

- Glial Fibrillary Acidic Protein (GFAP) with DAPI as control using a serum containing anti-GFAP (1:1000, Dako, USA) antibodies for **astrocytes** staining.

Iba1 and GFAP could not be performed simultaneously on a same slice because antibodies were labeled with the same dye. After staining, slices were analyzed in order to find the implantation site using the characteristic shape of the implant covered in astrocytes (red). Once found, **the most inflammatory slice** for each mouse **was isolated** and is displayed in the following analysis.

As the variations in shape of lateral ventricles section shape suggest (white arrows in Figure 109), the **implantation site strongly vary** in between specimen**.** This variability could have influenced signal quality variability displayed on Figure 107D. One control-implantation site (#220) was not analyzed because the implant appeared broken during extraction. One graphene-coated implant failed to perforate the pia-matter leading to a strong and large inflammatory reaction of the motor cortex and is therefore not related to graphene presence.

Over the 7 remaining mice (4 with graphene-coated implant and 3 control specimen), only 6 coronal slices picture are shown. Indeed one graphene-coated implanted mouse (#785) triggered such a low inflammation that it wasn't possible to find the implantation site.

We can see on Figure 109 that, by parallel comparison of coated mices and control, the graphene coated implants seem to have triggered a **lower astrocytic presence after 5 weeks**, either related to a lower inflammation or a better gliosis reduction along the five weeks.

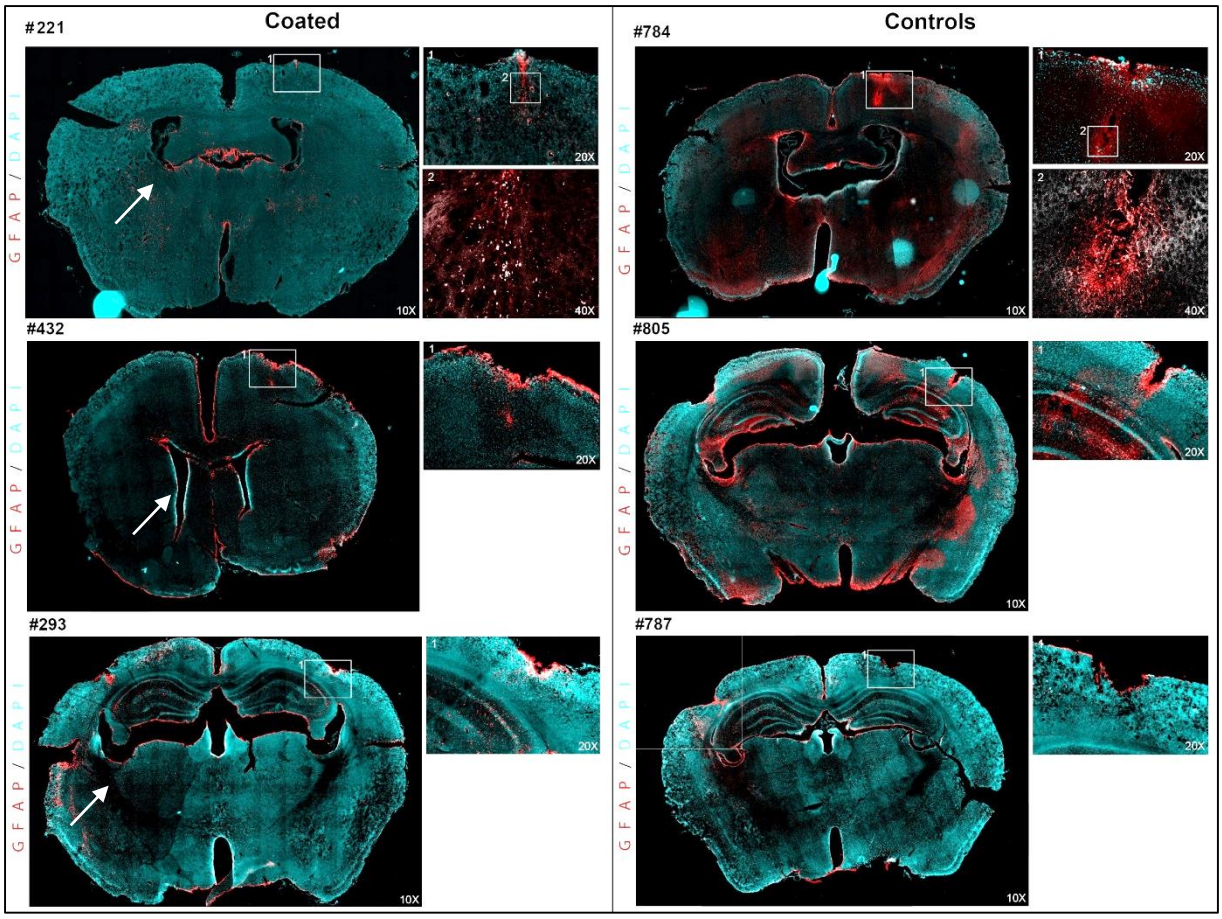

Figure 109 - Immunohistochemistry was performed on coronal brain slices at the location of the implant in our mice, in order to quantify the chronic inflammation. Chronic inflammation around the implant is revealed by astrocytes density, here tracked with GFAP in red and DAPI as a control to highlight neurons soma. We use these pictures to compare differences between graphene coated and control implants. Here #221 corresponds to a graphene coated implant whereas #784 is a control that triggered a more important inflammatory reaction at implantation site as highlighted in red. #432 and #805 shows the same tendency with a light tearing of the surface tissues during implant extraction. #293 and #787 have suffered important tissue damages during extraction and it's hard to compare inflammatory reaction between coated implant and control. White arrows show strong variation in lateral ventricles shape on the coronal slice of the implant, suggesting variation during implantation.

Although the population of animals analyzed is too low to **meet statistical significance,** these preliminary results suggest the **absence of intracortical cytotoxicity** of graphene and even a **better bioacceptance** after five weeks as astrocytes concentration is significantly lower on the graphene coated implanted mice brain with respect to the control. Whereas some implantation sites were hard to find and could be overlooked, some damages on the surface linked to extraction process or slicing procedure clearly indicate the implantation localization on #293 and #787 (Figure 109). **The inflammation status** shown on each of these slices **match the quality of the signal recorded** by the corresponding implants over 5 weeks. This correspondence gives strength to our graphene improvement hypothesis.

On the Figure 110, a close-up view of the most representative implants sites is displayed. Whereas graphene coated implants related glial scar (#221 and #432) show a low astrocyte density along the implant site, the control glial scar (#785) is surrounded by a thick layer of astrocytes and shows a weak density of neurons in the proximity of the implant. This implant (#785) has been silent during the whole 5 weeks, whereas coated implant #432 was still able to record moto neurons activity on 4 of its microelectrodes. A deep pack of astrocytes is nonetheless visible on implant 432. A proposed explanation is meningeal cells carried in triggered reactive gliosis as explained in 3.1.1b -.

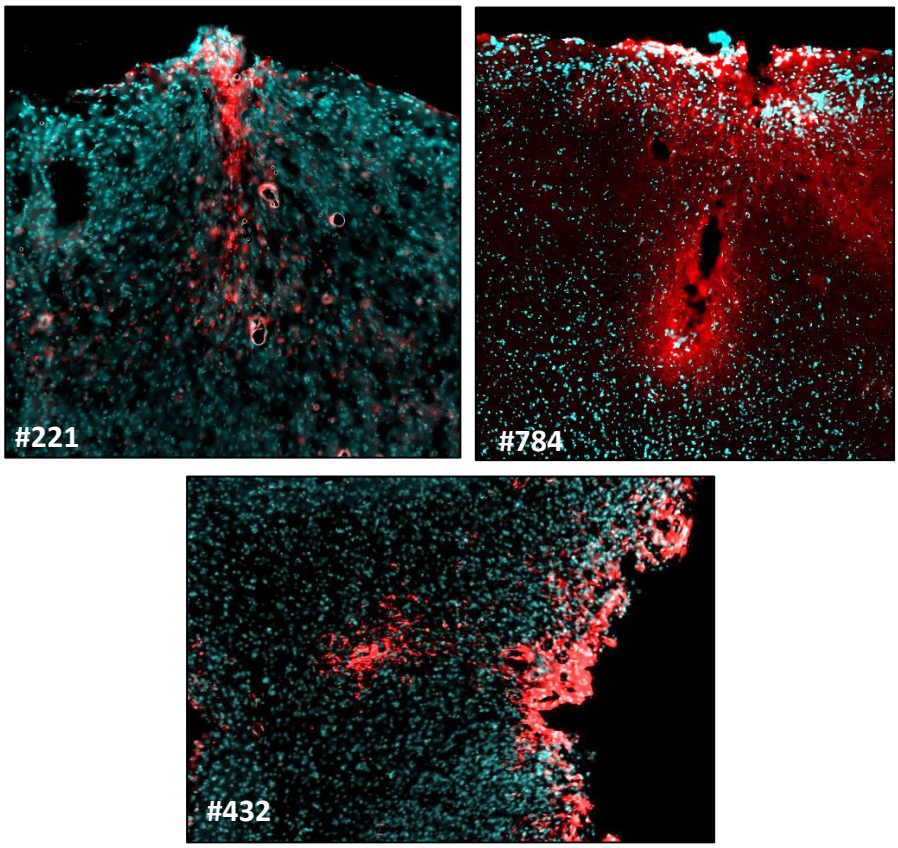

Figure 110 - Close up view of the implantation sites in our mice motor cortex shows variability in astrocytes (in red) mobilization and impact on neurons density (in blue): #221, graphene coated shows a low presence of astrocytes, mainly on the surface. #784, a control, shows strong damages to the tissues and thick astrocytes around the implant site. #432 coated shows a light deep inflammatory reaction, might be caused by meningeal tissue migration, whereas the surface seems to have been teared during extraction.

4.4 Chapter conclusion

Along this chapter, I have demonstrated the possibility to embed graphene sensors on flexible polyimide devices and on 15µm-thick 3D micro-machined silicon probes. Existing devices have been coated thanks to innovative post-processing methods that allowed standard graphene transfer on unconnected devices and direct graphene transfer on connected or on complex devices. This last transfer technique based on uncoated free-standing graphene avoids the use of the polymer capping layer during graphene transfer and thus allows transfer on complex objects such as plastic or biopolymer coatings sensitive to solvents (plastics, proteins etc…).

This direct transfer method have been used to coat commercial probes and to implant them in mice motorcortex. After 5 weeks in-vivo graphene monolayer was assessed for its bioacceptance. Two conclusions were made after this in vivo assessment campaign:

1. *The abiotic characterization using SEM analysis revealed that graphene underwent a slow degradation in tissue and was found in minute amounts on extracted implants after 5 weeks suggesting the almost complete release of graphene into the brain. A graphene protection layer might therefore be of some interest to perform long time intracranial implantation with graphene-based bioelectronics. The recipe developed in chapter III involving HA biopolymer coatings can provide such additional protection.*
2. *The bare graphene coating have, nevertheless, been responsible for an improvement in signals quality and durability, by increasing the number of operational sensors after 5 weeks compared to control implants. The reason for this improvement have been revealed by performing immunohistochemistry. We show that our coated implants allowed an important gliosis reduction after 5 weeks. Graphene involvement in this inflammation reduction might be a direct anti-inflammatory action or an improvement of the electrical coupling to neural cells that may have influenced the neuronal regeneration around the implant.*

Conclusion and perspectives

In this thesis, I have developed a multidisciplinary approach to build a new generation of intracortical implants: this work involved the synthesis, transfer and integration of graphene on soft materials and micro-machined devices. It was further shown that Graphene can be grafted with biopolymer useful to further improve the bioacceptance. Finally, graphene coated implants have been tested in the motorcortex for the first time in vivo.

Three issues have been specifically addressed:

1. Biopolymer adsorption makes graphene a multimodal platform to fight glial cells settlement in the brain area targeted by the implant.

The biopolymer we have developed and integrated exhibits uniform adhesion and neutrality with respect to the host graphene layer. We have demonstrated that assemblies of HA and PLL multilayers improve neurons affinity in vitro and show no toxicity in vivo when inserted in the deep motor cortex of rats.

This uniformly adsorbed layer will allow future graphene protection regarding shear forces during insertion as we first wanted to implement. Further covering such a functionalized graphene layers with thicker hydrogels could provide drug delivery functions, such as sustained release, together with preventing long-term aging of a future implant.

As a perspective, we note that HA polymers and its covering hydrogel will be degraded in vivo by hyaluronidase, leading to minimal invasiveness. Further in-vitro experiments performed in the presence of this enzyme and involving thickening and hardening of a drug encapsulation film, could allow controlled drug release. In-vivo studies would then request drug delivery tests using neurons growth factor or anti-inflammatory drugs encapsulated in hydrogels [199] that were shown to reduce gliosis [198]. In vivo assessment of graphene-HA multilayers assembly durability also remains to be investigated. That would involve a study on degradation speed of the assembly together with analysis of the graphene properties over time.

2. Graphene synthesis and optimized transfer methods provide a toolbox to integrate graphene into the next generation of biomedical devices either as a biosensor or as a conformal protection layer to encapsulate 3D systems.

High-quality graphene has been proved mandatory to improve cytocompatibility in–vivo. I have thus synthetized and integrated monolayer graphene with an improved reproducibility thanks to innovative methods of growth and transfer. Graphene devices fabrication on flexible and rigid materials have been described in this thesis and can be used to build flexible implants as much as to improve traditional silicon based probe electronics. The broad spectrum of tools developed to integrate graphene as a biosensing material on large and 3D surfaces might be of use for future thin film coating of biological devices. Graphene can thus be investigated as an efficient diffusion barrier stopping metal leaching, together with added antimicrobial properties. We have shown a process to use it as a coating membrane on complex devices. Indeed, this thesis process of graphene coating without polymer scaffold is of very high interest for conformal coating 3D micro-machined devices in which no post processing such as polymer removal is allowed. 3D in situ lithography has been explored to pattern this graphene according to underlying electronics.

Whereas graphene FETs are promising biosensors for ultra-sensitive neuronal activity recordings, their integration to record neuronal signals in vivo in motor cortex remains to be explored. In comparison to graphene MEAs, GFETs could improve the sensitivity of detection and then increase implants lifetime. GFETs integration as intracortical biosensors will benefit from this thesis work on multimodal bioacceptance improvements techniques, given the fact that a strong neuron-sensor couplings is paramount in order to record electrical activity at the single cell level.

3. The graphene bioacceptance in mice cortex has been investigated in vivo for the first time and have shown an improvement of long-term recorded signal quality together with a lowering of tissue inflammation.

Graphene biodegradability in the motor cortex have been highlighted by this thesis work. Whereas invasive MEA-based silicon probes encapsulation with monolayer graphene brought an improvement in term of signal quality recorded during five weeks, graphene have been degraded without any adverse effect on surrounding tissues.

Beyond the electronic sensors design and graphene integration on numerous flexible substrates or rigid devices, this work have demonstrated a bioacceptance improvement by graphene in neuronal tissues. The possibility to further coat graphene with biodegradable polymers to prevent or control its proven degradation thus opens the way to a next generation of soft, degradable and electronically reliable implants.

Bibliography

[1] K. S. Novoselov *et al.*, “Electric field effect in atomically thin carbon films.,” *Science (80-.).*, vol. 306, pp. 666–669, 2004.

[2] M. Pumera, “Graphene in biosensing,” *Materials Today*. 2011.

[3] Y. Wei, B. Wang, J. Wu, R. Yang, and M. L. Dunn, “Bending rigidity and Gaussian bending stiffness of single-layered graphene,” *Nano Lett.*, vol. 13, no. 1, pp. 26–30, 2013.

[4] V. C. Tung, M. J. Allen, Y. Yang, and R. B. Kaner, “High-throughput solution processing of large-scale graphene.,” *Nat. Nanotechnol.*, vol. 4, no. 1, pp. 25–29, 2009.

[5] S. Bae *et al.*, “Roll-to-roll production of 30-inch graphene films for transparent electrodes,” 2010.

[6] L. H. Hess *et al.*, “Graphene transistor arrays for recording action potentials from electrogenic cells,” *Adv. Mater.*, vol. 23, no. 43, pp. 5045–5049, 2011.

[7] B. M. Blaschke *et al.*, “Flexible graphene transistors for recording cell action potentials,” *2D Mater.*, vol. 3, no. 2, p. 25007, 2016.

[8] M. D. Angione *et al.*, “Carbon based materials for electronic bio-sensing,” *Mater. Today*, vol. 14, no. 9, pp. 424–433, 2011.

[9] R. R. van den Brand *et al.*, “Restoring voluntary control of locomotion after paralyzing spinal cord injury.,” *Science (80-.).*, vol. 336, no. 6085, pp. 1182–1185, 2012.

[10] D. Borton, S. Micera, J. D. R. Millán, and G. Courtine, “Personalized neuroprosthetics.,” *Sci. Transl. Med.*, vol. 5, no. 210, p. 210rv2, 2013.

[11] S. P. Wise and R. Shadmehr, “Motor Control,” *Encycl. Hum. Brain*, vol. 3, no. 1, pp. 1–21, 2002.

[12] C. S. Sherrington, “Flexion-reflex of the limb, crossed extension-reflex, and reflex stepping and standing,” *J. Physiol.*, vol. 40, no. 1–2, pp. 28–121, Apr. 1910.

[13] M. R. Dimitrijevic, Y. Gerasimenko, and M. M. Pinter, “Evidence for a spinal central pattern generator in humans,” *Ann. N. Y. Acad. Sci.*, vol. 860, pp. 360–376, 1998.

[14] A. Bignami, M. Hosley, and D. Dahl, “Hyaluronic acid and hyaluronic acid-binding proteins in brain extracellular matrix.,” *Anat. Embryol. (Berl).*, vol. 188, pp. 419–433, 1993.

[15] L. W. Lau, R. Cua, M. B. Keough, S. Haylock-Jacobs, and V. W. Yong, “Pathophysiology of the brain extracellular matrix: a new target for remyelination.,” *Nat. Rev. Neurosci.*, vol. 14, no. 10, pp. 722–9, 2013.

[16] F. W. Lodish H, Berk A, Zipursky SL., “Intracellular Ion Environment and Membrane Electric Potential.,” *Mol. Cell Biol.*, no. 4th edition., p. Section 15.4, 2000.

[17] F. G. Donnan, “Theorie der Membrangleichgewichte und Membranpotentiale bei Vorhandensein von nicht dialysierenden Elektrolyten. Ein Beitrag zur physikalisch-chemischen Physiologie.,” *Zeitschrift f{ü}r Elektrochemie und Angew. Phys. Chemie*, vol. 17, no. 14, pp. 572–581, 1911.

[18] D. Purves, “Neuroscience, 3rd Edition.”

[19] B. Y. D. E. Goldman, “IN MEMBRANES (From the Department of] Physiology , College of Physicians and Surgeons , Columbia University , New York) The Journal of General Physiology,” pp. 37–60, 1943.

[20] A. L. Hodgkin and B. Katz, “The effect of sodium ions on the electrical,” *J. Physiol. J. Physiol. Online UNIV UTAH*, vol. 108, pp. 37–77, 1949.

[21] O. P. Hamill, A. Marty, E. Neher, B. Sakmann, and F. J. Sigworth, “Improved patch-clamp techniques for high-resolution current recording from cells and cell-free membrane patches,” *Pfl??gers Arch. Eur. J. Physiol.*, vol. 391, no. 2, pp. 85–100, 1981.

[22] M. S. Lewicki, “A review of methods for spike sorting: the detection and classification of neural action potentials.,” *Network*, vol. 9, no. 4, pp. R53-78, 1998.

[23] K. P. Michmizos, D. Sakas, and K. S. Nikita, “Prediction of the timing and the rhythm of the parkinsonian subthalamic nucleus neural spikes using the local field potentials,” *IEEE Trans. Inf. Technol. Biomed.*, vol. 16, no. 2, pp. 190–197, 2012.

[24] C. Rossant *et al.*, “Spike sorting for large, dense electrode arrays,” *bioRxiv*, vol. 19, no. 4, p. 15198, 2015.

[25] E. Crivellato and D. Ribatti, “Soul, mind, brain: Greek philosophy and the birth of neuroscience,” *Brain Res. Bull.*, vol. 71, no. 4, pp. 327–336, 2007.

[26] B. Hans, “Uber das elektrenkephalogramm des menshen,” *Arch. für Psychiatr. Nervenkrankheiten*, vol. 278, no. 1875, p. 87: 527-570., 1929.

[27] T. O. W. a R. D. D. Brain-computer and J. J. Vidal, “Tow ard direct brain-computer 9027 communication,” *Annu. Rev. Biophys. Bioeng.*, vol. 2, pp. 157–80, 1973.

[28] A.-L. Benabid *et al.*, “Deep brain stimulation for Parkinson’s disease,” *Adv. Neurol.*, vol. 86, pp. 405–412, 2001.

[29] I. R. Minev *et al.*, “Electronic dura mater for long-term multimodal neural interfaces,” *Science (80-.).*, vol. 347, no. 6218, pp. 159–163, 2015.

[30] S. Raspopovic *et al.*, “Restoring natural sensory feedback in real-time bidirectional hand prostheses.,” *Sci. Transl. Med.*, vol. 6, no. 222, p. 222ra19, Feb. 2014.

[31] K. Masamune *et al.*, “Laboratory Investigation Development of an MRI-Compatible Needle Insertion Manipulator for Stereotactic Neurosurgery,” *J. Image Guiakd Surg.*, vol. 1, no. December 2016, pp. 242–248, 1995.

[32] S.-G. Kim, W. Richter, and K. U??urbil, “Limitations of temporal resolution in functional MRI,” *Magn. Reson. Med.*, vol. 37, no. 4, pp. 631–636, Apr. 1997.

[33] C. C. Gallen, E. C. Hirschkoff, and D. S. Buchanan, “Magnetoencephalography and magnetic source imaging. Capabilities and limitations.,” *Neuroimaging Clin. N. Am.*, vol. 5, no. 2, pp. 227–249, 1995.

[34] C. Del Gratta, V. Pizzella, F. Tecchio, and G. L. Romani, “Magnetoencephalography - a noninvasive brain imaging method with 1 ms time resolution,” *Reports Prog. Phys.*, vol. 64, no. 12, p. 1759, 2001.

[35] E. D. Kondylis *et al.*, “Detection of high-frequency oscillations by hybrid depth electrodes in standard clinical intracranial EEG recordings,” *Front. Neurol.*, vol. 5 AUG, no. August, pp. 1–11, 2014.

[36] R. Muller *et al.*, “24.1 A miniaturized 64-channel 225??W wireless electrocorticographic neural sensor,” *Dig. Tech. Pap. - IEEE Int. Solid-State Circuits Conf.*, vol. 57, pp. 412–413, 2014.

[37] E. Asano *et al.*, “Origin and propagation of epileptic spasms delineated on electrocorticography,” *Epilepsia*, vol. 46, no. 7, pp. 1086–1097, 2005.

[38] M. Gomez-Rodriguez *et al.*, “Epidural ECoG online decoding of arm movement intention in hemiparesis,” *Proc. - Work. Brain Decod. Pattern Recognit. Challenges Neuroimaging, WBD 2010 - Conjunction with theInternational Conf. Pattern Recognition, ICPR 2010*, pp. 36–39, 2010.

[39] D.-H. Kim *et al.*, “Dissolvable films of silk fibroin for ultrathin conformal bio-integrated electronics,” *Nat. Mater.*, vol. 9, no. 6, pp. 511–517, 2010.

[40] E. J. O. Hamel, B. F. Grewe, J. G. Parker, and M. J. Schnitzer, “Cellular Level Brain Imaging in Behaving Mammals: An Engineering Approach,” *Neuron*, vol. 86, no. 1, pp. 140–159, 2015.

[41] C. Grienberger and A. Konnerth, “Imaging Calcium in Neurons,” *Neuron*, vol. 73, no. 5, pp. 862–885, 2012.

[42] B. Heider, J. L. Nathanson, E. Y. Isacoff, E. M. Callaway, and R. M. Siegel, “Two-photon imaging of calcium in virally transfected striate cortical neurons of behaving monkey,” *PLoS One*, vol. 5, no. 11, pp. 1–13, 2010.

[43] B. F. Grewe, D. Langer, H. Kasper, B. M. Kampa, and F. Helmchen, “High-speed in vivo calcium imaging reveals neuronal network activity with near-millisecond precision.,” *Nat. Methods*, vol. 7, no. 5, pp. 399–405, 2010.

[44] Y. Ziv and K. K. Ghosh, “Miniature microscopes for large-scale imaging of neuronal activity in freely behaving rodents,” *Curr. Opin. Neurobiol.*, vol. 32, pp. 141–147, 2015.

[45] J. P. Seymour, N. B. Langhals, D. J. Anderson, and D. R. Kipke, “Novel multi-sided, microelectrode arrays for implantable neural applications,” *Biomed. Microdevices*, 2011.

[46] D. Pellinen, T. Moon, R. Vetter, R. Miriani, and D. Kipke, “Multifunctional flexible parylene-based intracortical microelectrodes.,” *Conf. Proc. IEEE Eng. Med. Biol. Soc.*, vol. 5, pp. 5272–5275, 2005.

[47] S. Kisban *et al.*, “Microprobe array with low impedance electrodes and highly flexible polyimide cables for acute neural recording,” in *Annual International Conference of the IEEE Engineering in Medicine and Biology - Proceedings*, 2007.

[48] J. K. Nguyen *et al.*, “Mechanically-compliant intracortical implants reduce the neuroinflammatory response.,” *J. Neural Eng.*, vol. 11, no. 5, p. 56014, 2014.

[49] P. R. Kennedy and R. a Bakay, “Restoration of neural output from a paralyzed patient by a direct brain connection.,” *Neuroreport*, vol. 9, no. 8, pp. 1707–11, 1998.

[50] D. M. Taylor *et al.*, “Direct cortical control of 3D neuroprosthetic devices.,” *Science*, vol. 296, no. 5574, pp. 1829–32, 2002.

[51] D. Borton *et al.*, “Corticospinal neuroprostheses to restore locomotion after spinal cord injury,” *Neuroscience Research*. 2014.

[52] L. C. Bachmann, A. Matis, N. T. Lindau, P. Felder, M. Gullo, and M. E. Schwab, “Deep Brain Stimulation of the Midbrain Locomotor Region Improves Paretic Hindlimb Function After Spinal Cord Injury in Rats,” *Sci. Transl. Med.*, vol. 5, no. 208, p. 208ra146-208ra146, 2013.

[53] G. Courtine *et al.*, “Transformation of nonfunctional spinal circuits into functional states after the loss of brain input.,” *Nat. Neurosci.*, vol. 12, no. 10, pp. 1333–1342, 2009.

[54] R. van den Brand *et al.*, “Neuroprosthetic technologies to augment the impact of neurorehabilitation after spinal cord injury,” *Ann. Phys. Rehabil. Med.*, vol. 58, no. 4, pp. 232–237, 2015.

[55] M. Hubli and V. Dietz, “The physiological basis of neurorehabilitation--locomotor training after spinal cord injury.,” *J. Neuroeng. Rehabil.*, vol. 10, p. 5, 2013.

[56] G. Berlucchi and H. A. Buchtel, “Neuronal plasticity: Historical roots and evolution of meaning,” in *Experimental Brain Research*, 2009, vol. 192, no. 3, pp. 307–319.

[57] S. Mary, E. Merriam, O. Srivannavit, M. N. Gulari, and K. D. Wise, “A Three-Dimensional 64-Site Folded Electrode Array Using Planar Fabrication,” *J. MICROELECTROMECHANICAL Syst.*, vol. 20, no. 3, 2011.

[58] K. D. Wise, J. B. Angell, and A. Starr, “An Integrated-Circuit Approach to Extracellular Microelectrodes,” *IEEE Trans. Biomed. Eng.*, vol. BME-17, no. 3, pp. 238–247, 1970.

[59] K. Najafi, K. D. Wise, and T. Mochizuki, “A High-Yield IC-Cfompatible Multichannel Array Reco rding,” *Electron Devices IEEE Trans.*, vol. 32, no. 7, pp. 1206–1211, 1985.

[60] K. L. Drake, K. D. Wise, J. Farraye, D. J. Anderson, and S. L. BeMent, “Performance of Planar Multisite Microprobes in Recording Extracellular Single-Unit Intracortical Activity,” *IEEE Trans. Biomed. Eng.*, 1988.

[61] P. K. Campbell, K. E. Jones, R. J. Huber, K. W. Horch, and R. A. Normann, “A silicon-based, three-dimensional neural interface: manufacturing processes for an intracortical electrode array,” *IEEE Trans. Biomed. Eng.*, vol. 38, no. 8, pp. 758–768, 1991.

[62] R. R. Harrison *et al.*, “A low-power integrated circuit for a wireless 100-electrode neural recording system,” *IEEE J. Solid-State Circuits*, vol. 42, no. 1, pp. 123–133, 2007.

[63] A. Prasad *et al.*, “Abiotic-biotic characterization of Pt/Ir microelectrode arrays in chronic implants.,” *Front. Neuroeng.*, vol. 7, p. 2, Jan. 2014.

[64] J. Silver and J. H. Miller, “Regeneration beyond the glial scar,” *Nat. Rev. Neurosci.*, vol. 5, no. 2, pp. 146–156, 2004.

[65] P. C. Georges, W. J. Miller, D. F. Meaney, E. S. Sawyer, and P. A. Janmey, “Matrices with compliance comparable to that of brain tissue select neuronal over glial growth in mixed cortical cultures.,” *Biophys. J.*, vol. 90, no. 8, pp. 3012–3018, Apr. 2006.

[66] Y. Sun *et al.*, “Hippo/YAP-mediated rigidity-dependent motor neuron differentiation of human pluripotent stem cells,” 2014.

[67] D. H. Szarowski *et al.*, “Brain responses to micro-machined silicon devices.,” *Brain Res.*, vol. 983, no. 1–2, pp. 23–35, Sep. 2003.

[68] J. N. Turner *et al.*, “Cerebral astrocyte response to micromachined silicon implants.,” *Exp. Neurol.*, vol. 156, no. 1, pp. 33–49, 1999.

[69] H. Lee, R. V Bellamkonda, W. Sun, and M. E. Levenston, “Biomechanical analysis of silicon microelectrode-induced strain in the brain,” *J. Neural Eng.*, vol. 2, no. 4, p. 81, 2005.

[70] P. J. Rousche, D. S. Pellinen, D. P. Pivin, J. C. Williams, R. J. Vetter, and D. R. Kipke, “Flexible polyimide-based intracortical electrode arrays with bioactive capability.,” *IEEE Trans. Biomed. Eng.*, vol. 48, no. 3, pp. 361–371, 2001.

[71] K. C. Cheung, P. Renaud, H. Tanila, and K. Djupsund, “Flexible polyimide microelectrode array for in vivo recordings and current source density analysis.,” *Biosens. Bioelectron.*, vol. 22, no. 8, pp. 1783–1790, 2007.

[72] T. Suzuki, K. Mabuchi, and S. Takeuchi, “A 3D flexible parylene probe array for multichannel neural recording,” in *International IEEE/EMBS Conference on Neural Engineering, NER*, 2003, vol. 2003–Janua, pp. 154–156.

[73] Sung Eun Lee *et al.*, “A Flexible Depth Probe Using Liquid Crystal Polymer,” *IEEE Trans. Biomed. Eng.*, vol. 59, no. 7, pp. 2085–2094, Jul. 2012.

[74] H. J. Lee, Y. Son, J. Kim, C. J. Lee, E.-S. Yoon, and I.-J. Cho, “A multichannel neural probe with embedded microfluidic channels for simultaneous in vivo neural recording and drug delivery,” *Lab Chip*, vol. 15, no. 6, pp. 1590–1597, 2015.

[75] K. B. Neeves, C. T. Lo, C. P. Foley, W. M. Saltzman, and W. L. Olbricht, “Fabrication and characterization of microfluidic probes for convection enhanced drug delivery,” *J. Control. Release*, vol. 111, no. 3, pp. 252–262, 2006.

[76] T. D. Y. Kozai *et al.*, “Ultrasmall implantable composite microelectrodes with bioactive surfaces for chronic neural interfaces.,” *Nat. Mater.*, vol. 11, no. 12, pp. 1065–73, 2012.

[77] C. H. Chen *et al.*, “A flexible hydrophilic-modified graphene microprobe for neural and cardiac recording,” *Nanomedicine Nanotechnology, Biol. Med.*, 2013.

[78] D.-W. Park *et al.*, “ARTICLE Graphene-based carbon-layered electrode array technology for neural imaging and optogenetic applications,” *Nat. Commun.*, vol. 5, 2014.

[79] A. K. Geim and K. S. Novoselov, “The rise of graphene,” *Nat. Mater.*, vol. 6, no. 3, pp. 183–191, 2007.

[80] P.R.Wallace, “The Band Theory of Graphite - PhysRev.71.622,” *Phys. Rev.*, vol. 329, no. 1909, pp. 622–634, 1946.

[81] K. S. Novoselov *et al.*, “Two-dimensional gas of massless Dirac fermions in graphene,” *Nature*, vol. 438, no. 7065, pp. 197–200, 2005.

[82] L. D. Landau, “Zur Theorie der phasenumwandlungen II,” *Phys. Z. Sowjetunion*, vol. 11, pp. 26–35, 1937.

[83] R. Peierls, “Quelques propriétés typiques des corps solides,” *Ann. l’I.H.P.*, vol. 5, no. 3, pp. 177–222, 1935.

[84] N. D. Mermin, “Crystalline order in two dimensions,” *Phys. Rev.*, vol. 176, no. 1, pp. 250–254, 1968.

[85] J. C. Meyer, A. K. Geim, M. I. Katsnelson, K. S. Novoselov, T. J. Booth, and S. Roth, “The structure of suspended graphene sheets,” *Nat*, vol. 446, no. March, pp. 60–63, 2007.

[86] X. Xiao, Y. Li, and Z. Liu, “Graphene Commercialization,” *Nat. Publ. Gr.*, vol. 15, no. 7, pp. 697–698, 2016.

[87] P. R. Wallace, “The band theory of graphite,” *Phys. Rev.*, vol. 71, no. 9, pp. 622–634, 1947.

[88] X. Du, I. Skachko, A. Barker, and E. Y. Andrei, “Approaching ballistic transport in suspended graphene,” *Nat. Nanotechnol.*, vol. 3, no. 8, pp. 491–495, 2008.

[89] K. I. Bolotin *et al.*, “Ultrahigh electron mobility in suspended graphene,” *Solid State Commun.*, vol. 146, no. 9–10, pp. 351–355, 2008.

[90] A. H. Castro-Neto, N. M. R. Peres, K. S. Novoselov, and A. K. Geim, “The electronic properties of graphene,” *Rev. Mod. Phys.*, vol. 81, no. 1, pp. 109–162, 2009.

[91] P. Avouris, “Graphene: Electronic and photonic properties and devices,” *Nano Lett.*, vol. 10, no. 11, pp. 4285–4294, 2010.

[92] F. Schwierz, “Graphene transistors,” *Nat. Nanotechnol.*, vol. 5, no. 7, pp. 487–496, Jul. 2010.

[93] I. S. Ionica, “Effet de champ et blocage de Coulomb dans des nanostructures de silicium élaborées par microscopie à force atomique,” p. 242, 2005.

[94] N. Arora, “MOSFET Models for VLSI Circuit Simulation Theory and Practice Springer,” *New York*, 1993.

[95] L. H. Hess *et al.*, “High-transconductance graphene solution-gated field effect transistors,” *Appl. Phys. Lett.*, vol. 99, no. 3, pp. 2011–2014, 2011.

[96] S. D. Sarma, S. Adam, E. H. Hwang, and E. Rossi, “Electronic transport in two dimensional graphene,” *arXiv Prepr. arXiv1003.4731*, pp. 1–85, 2010.

[97] S. Kim *et al.*, “Realization of a high mobility dual-gated graphene field-effect transistor with Al2O3 dielectric,” *Appl. Phys. Lett.*, vol. 94, no. 6, 2009.

[98] S. Adam, E. H. Hwang, V. M. Galitski, and S. Das Sarma, “A self-consistent theory for graphene transport.,” *Proc. Natl. Acad. Sci. U. S. A.*, vol. 104, no. 47, pp. 18392–7, 2007.

[99] I. Meric, M. Y. Han, A. F. Young, B. Ozyilmaz, P. Kim, and K. L. Shepard, “Current saturation in zero-bandgap, top-gated graphene field-effect transistors,” *Nat. Nanotechnol.*, vol. 3, no. 11, pp. 654–659, 2008.

[100] J. Martin *et al.*, “Observation of Electron-Hole Puddles in Graphene Using a Scanning Single Electron Transistor,” *Nat. Phys.*, vol. 4, no. February, p. 13, 2007.

[101] F. Veliev, “Interfacing neurons with nanoelectronics : from silicon nanowires to carbon devices,” 2016.

[102] Z. Han *et al.*, “Homogeneous optical and electronic properties of graphene due to the suppression of multilayer patches during CVD on copper foils,” *Adv. Funct. Mater.*, vol. 24, no. 7, pp. 964–970, 2014.

[103] K. Matsumoto, K. Maehashi, Y. Ohno, and K. Inoue, “Recent advances in functional graphene biosensors,” *J. Phys. D Appl. Phys. J. Phys. D Appl. Phys. J. Phys. D Appl. Phys*, vol. 47, no. 47, pp. 94005–6, 2014.

[104] A. A. Lebedev *et al.*, “Graphene-based biosensors,” *Tech. Phys. Lett.*, vol. 42, no. 7, pp. 729–732, 2016.

[105] B. M. Blaschke *et al.*, “Flexible graphene transistors for recording cell action potentials,” *2D Mater.*, vol. 3, no. 2, p. 25007, 2016.

[106] D. Kuzum *et al.*, “ARTICLE Transparent and flexible low noise graphene electrodes for simultaneous electrophysiology and neuroimaging,” *Nat. Commun.*, vol. 5, 2014.

[107] H. Ji *et al.*, “Capacitance of carbon-based electrical double-layer capacitors.,” *Nat. Commun.*, vol. 5, no. Cmcm, p. 3317, 2014.

[108] J. T. Ye *et al.*, “Liquid-gated interface superconductivity on an atomically flat film,” *Nat. Mater.*, vol. 9, no. 2, pp. 125–128, 2010.

[109] N. Li *et al.*, “The promotion of neurite sprouting and outgrowth of mouse hippocampal cells in culture by graphene substrates,” *Biomaterials*, 2011.

[110] F. Veliev, A. Briançon-Marjollet, V. Bouchiat, and C. Delacour, “Impact of crystalline quality on neuronal affinity of pristine graphene,” *Biomaterials*, vol. 86, pp. 33–41, Apr. 2016.

[111] P. Delmas, J. Hao, and L. Rodat-Despoix, “Molecular mechanisms of mechanotransduction in mammalian sensory neurons.,” *Nat. Rev. Neurosci.*, vol. 12, no. 3, pp. 139–153, 2011.

[112] L. E. Freed, G. C. Engelmayr, J. T. Borenstein, F. T. Moutos, and F. Guilak, “Advanced material strategies for tissue engineering scaffolds,” *Adv. Mater.*, vol. 21, no. 32–33, pp. 3410–3418, 2009.

[113] M. K. Blees *et al.*, “Graphene kirigami,” *Nature*, vol. 524, no. 7564, pp. 204–207, 2015.

[114] C. Lee, X. Wei, J. W. Kysar, and J. Hone, “Measurement of the elastic properties and intrinsic strength of monolayer graphene.,” *Science*, vol. 321, no. 5887, pp. 385–388, 2008.

[115] T. Someya, Z. Bao, and G. G. Malliaras, “The rise of plastic bioelectronics,” *Nature*, vol. 540, no. 7633, pp. 379–385, 2016.

[116] O. M. Nayfeh, “Graphene Transistors on Mechanically Flexible Polyimide Incorporating Atomic-Layer-Deposited Gate Dielectric,” *IEEE Electron Device Lett.*, vol. 32, no. 10, pp. 1349–1351, Oct. 2011.

[117] C. Sire *et al.*, “Flexible gigahertz transistors derived from solution-based single-layer graphene,” *Nano Lett.*, 2012.

[118] M. A. Worsley *et al.*, “Mechanically robust 3D graphene macroassembly with high surface area,” *Chem. Commun.*, vol. 48, no. 67, pp. 8428–8430, 2012.

[119] R. R. Nair *et al.*, “Fine Structure Constant Defines Visual Transperency of Graphene,” *Science (80-.).*, vol. 320, no. June, p. 2008, 2008.

[120] P. Blake *et al.*, “Making graphene visible,” *Appl. Phys. Lett.*, vol. 91, no. 6, pp. 13–15, 2007.

[121] A. N. Grigorenko, M. Polini, and K. S. Novoselov, “Optical properties of graphene,” *Nat. Photonics*, 2012.

[122] P. Anikeeva *et al.*, “Optetrode: a multichannel readout for optogenetic control in freely moving mice,” *Nat. Neurosci.*, vol. 15, no. 1, pp. 163–170, 2011.

[123] D. Park *et al.*, “Fabrication and utility of a transparent graphene neural electrode array for electrophysiology , in vivo imaging , and optogenetics,” *Nat. Protoc.*, vol. 11, no. 11, pp. 2201–2222, 2016.

[124] S. V. Morozov, K. S. Novoselov, F. Schedin, D. Jiang, A. A. Firsov, and A. K. Geim, “Two-dimensional electron and hole gases at the surface of graphite,” *Phys. Rev. B - Condens. Matter Mater. Phys.*, vol. 72, no. 20, pp. 2–5, 2005.

[125] B. Partoens and F. M. Peeters, “From graphene to graphite: Electronic structure around the K point,” *Phys. Rev. B - Condens. Matter Mater. Phys.*, vol. 74, no. 7, pp. 1–11, 2006.

[126] Zheng (Vitto) HAN, “Macroscopic CVD Graphene for Nano-electronics: from growth to proximity-induced 2D superconductivity,” *Univ. Grenoble Alpes, Fr.*, 2013.

[127] K. S. Novoselov *et al.*, “A roadmap for graphene,” *Nature*, vol. 490, no. 7419, pp. 192–200, 2013.

[128] V. Huc, N. Bendiab, N. Rosman, T. Ebbesen, C. Delacour, and V. Bouchiat, “Large and flat graphene flakes produced by epoxy bonding and reverse exfoliation of highly oriented pyrolytic graphite.,” *Nanotechnology*, vol. 19, no. 45, p. 455601, 2008.

[129] S. Stankovich *et al.*, “Synthesis of graphene-based nanosheets via chemical reduction of exfoliated graphite oxide,” *Carbon N. Y.*, vol. 45, no. 7, pp. 1558–1565, 2007.

[130] E. Pallecchi *et al.*, “High Electron Mobility in Epitaxial Graphene on 4H-SiC (0001) via post-growth annealing under hydrogen,” *Sci. Rep.*, vol. 4, no. 1, p. 4558, 2014.

[131] B. Lang, “A LEED study of the deposition of carbon on platinum crystal surfaces,” *Surf. Sci.*, vol. 53, no. 1, pp. 317–329, 1975.

[132] M. Yudasaka *et al.*, “Graphite thin film formation by chemical vapor deposition,” *Appl. Phys. Lett.*, vol. 64, no. 7, pp. 842–844, 1994.

[133] X. Li *et al.*, “Large-area synthesis of high-quality and uniform graphene films on copper foils.,” *Science*, vol. 324, no. 5932, pp. 1312–1314, 2009.

[134] R. E. X. B. Mclellan and P. Chraska, “A Vapor Transport Study of Nickel-Copper-Carbon Solid Solutions,” vol. 77001, pp. 9–13, 1970.

[135] X. Li, W. Cai, L. Colombo, and R. S. Ruoff, “Evolution of graphene growth on Cu and Ni studied by carbon isotope labeling,” *Mech. Eng.*, vol. 9, no. Cvd, p. 15, 2009.

[136] S. M. Kim *et al.*, “The effect of copper pre-cleaning on graphene synthesis,” *Nanotechnology*, vol. 24, no. 36, p. 365602, 2013.

[137] L. Zhao *et al.*, “Influence of copper crystal surface on the CVD growth of large area monolayer graphene,” *Solid State Commun.*, vol. 151, no. 7, pp. 509–513, 2011.

[138] M. Losurdo, M. M. Giangregorio, P. Capezzuto, and G. Bruno, “Graphene CVD growth on copper and nickel: role of hydrogen in kinetics and structure,” *Phys. Chem. Chem. Phys.*, vol. 13, no. 46, p. 20836, 2011.

[139] V. Bouchiat, J. Coraux, and Z. Han, “Process and device for forming a graphene layer,” US patent n° 9458020, 2014.

[140] Z. Han *et al.*, “Suppression of Multilayer Graphene Patches during CVD Graphene growth on Copper,” *Arxiv Prepr. arXiv*, p. 4, 2012.

[141] Z.-J. Wang *et al.*, “Direct Observation of Graphene Growth and Associated Copper Substrate Dynamics by in Situ Scanning Electron Microscopy,” *ACS Nano*, vol. 9, no. 2, pp. 1506–1519, Feb. 2015.

[142] H. . Richardson and J. Zhang, “Copper Compounds,” *Ullmann’s Encycl. Ind. Chem.*, 2006.

[143] K. L. Chavez and D. W. Hess, “A Novel Method of Etching Copper Oxide Using Acetic Acid,” *J. Electrochem. Soc.*, vol. 148, no. 11, p. G640, 2001.

[144] J. B. Menke, “Nitrieren mit Nitraten,” *Recl. des Trav. Chim. des Pays-Bas*, vol. 44, no. 2, pp. 141–149, 1925.

[145] C. L. Bauer and R. J. Farris, “Determination of poisson’s ratio for polyimide films,” *Polym. Eng. Sci.*, vol. 29, no. 16, pp. 1107–1110, 1989.

[146] N. W. Pu *et al.*, “Graphene grown on stainless steel as a high-performance and ecofriendly anti-corrosion coating for polymer electrolyte membrane fuel cell bipolar plates,” *J. Power Sources*, vol. 282, pp. 248–256, 2015.

[147] A. Krishnamurthy *et al.*, “Superiority of Graphene over Polymer Coatings for Prevention of Microbially Induced Corrosion,” *Sci. Rep.*, vol. 5, p. 13858, 2015.

[148] M. Schriver, W. Regan, W. J. Gannett, A. M. Zaniewski, and M. F. Crommie, “Graphene as a Long-Term Metal Oxidation Barrier : Worse Than Nothing,” no. 7, pp. 5763–5768, 2013.

[149] P. Y. Huang *et al.*, “Grains and grain boundaries in single-layer graphene atomic patchwork quilts,” *Nature*, vol. 469, 2011.

[150] A. C. Ferrari, “Raman spectroscopy of graphene and graphite: Disorder, electron-phonon coupling, doping and nonadiabatic effects,” *Solid State Commun.*, vol. 143, no. 1–2, pp. 47–57, 2007.

[151] D. Graf, F. Molitor, K. Ensslin, and C. Stampfer, “Spatially resolved Raman spectroscopy of single-and few-layer graphene,” *Nano Lett.*, vol. 7, pp. 238–42, 2007.

[152] L. M. Malard, M. A. Pimenta, G. Dresselhaus, and M. S. Dresselhaus, “Raman spectroscopy in graphene,” *Phys. Rep.*, vol. 473, no. 5–6, pp. 51–87, 2009.

[153] M. Baclayon, G. J. L. Wuite, and W. H. Roos, “Imaging and manipulation of single viruses by atomic force microscopy,” *Soft Matter*, vol. 6, no. 21, p. 5273, 2010.

[154] S. Metz, A. Bertsch, D. Bertrand, and P. Renaud, “Flexible polyimide probes with microelectrodes and embedded microfluidic channels for simultaneous drug delivery and multi-channel monitoring of bioelectric activity,” *Biosens. Bioelectron.*, vol. 19, no. 10, pp. 1309–1318, 2004.

[155] T. R. Hoare and D. S. Kohane, “Hydrogels in drug delivery: Progress and challenges,” *Polymer (Guildf).*, vol. 49, no. 8, pp. 1993–2007, Apr. 2008.

[156] D. P. Pelvig, H. Pakkenberg, A. K. Stark, and B. Pakkenberg, “Neocortical glial cell numbers in human brains,” *Neurobiol. Aging*, vol. 29, no. 11, pp. 1754–1762, 2008.

[157] F. A. C. Azevedo *et al.*, “Equal numbers of neuronal and nonneuronal cells make the human brain an isometrically scaled-up primate brain,” *J. Comp. Neurol.*, vol. 513, no. 5, pp. 532–541, 2009.

[158] C. C. Stichel and H. W. Müller, “The CNS lesion scar: New vistas on an old regeneration barrier,” *Cell Tissue Res.*, vol. 294, no. 1, pp. 1–9, 1998.

[159] N. J. Abbott, L. Rönnbäck, and E. Hansson, “Astrocyte–endothelial interactions at the blood–brain barrier,” *Nat. Rev. Neurosci.*, vol. 7, no. 1, pp. 41–53, 2006.

[160] J. S. Pachter, H. E. de Vries, and Z. Fabry, “The blood-brain barrier and its role in immune privilege in the central nervous system.,” *J. Neuropathol. Exp. Neurol.*, vol. 62, no. 6, pp. 593–604, 2003.

[161] A. M. Butt, H. C. Jones, and N. J. Abbott, “Electrical resistance across the blood-brain barrier in anaesthetized rats: a developmental study.,” *J. Physiol.*, vol. 429, pp. 47–62, 1990.

[162] K. Kacem, P. Lacombe, J. Seylaz, and G. Bonvento, “Structural organization of the perivascular astrocyte endfeet and their relationship with the endothelial glucose transporter: A confocal microscopy study,” *Glia*, vol. 23, no. 1, pp. 1–10, 1998.

[163] P. Brodal, *The central nervous system*. 2010.

[164] N. J. Abbott, L. Rönnbäck, and E. Hansson, “Astrocyte–endothelial interactions at the blood–brain barrier,” *Nat. Rev. Neurosci.*, vol. 7, no. 1, pp. 41–53, Jan. 2006.

[165] T. Takano, L. Bekar, and M. Nedergaard, “NIH Public Access,” vol. 5, no. 218, 2012.

[166] C. M. Lin *et al.*, “Hyaluronic acid inhibits the glial scar formation after brain damage with tissue loss in rats,” *Surg. Neurol.*, vol. 72, no. SUPPL. 2, pp. S50–S54, 2009.

[167] J. W. Fawcett and R. A. Asher, “The glial scar and central nervous system repair,” *Brain Res. Bull.*, vol. 49, no. 6, pp. 377–391, 1999.

[168] K. Abnet, J. W. Fawcett, and S. B. Dunnett, “Interactions between meningeal cells and astrocytes in vivo and in vitro,” *Dev. Brain Res.*, vol. 59, no. 2, pp. 187–196, 1991.

[169] K. R. Bulsara, B. J. Iskandar, A. T. Villavicencio, and J. H. P. Skene, “A new millenium for spinal cord regeneration: growth-associated genes.,” *Spine (Phila. Pa. 1976).*, vol. 27, no. 17, pp. 1946–1949, 2002.

[170] D. a Henze, Z. Borhegyi, J. Csicsvari, a Mamiya, K. D. Harris, and G. Buzsáki, “Intracellular features predicted by extracellular recordings in the hippocampus in vivo.,” *J. Neurophysiol.*, vol. 84, no. 1, pp. 390–400, 2000.

[171] T. Saxena *et al.*, “The impact of chronic blood-brain barrier breach on intracortical electrode function,” *Biomaterials*, vol. 34, no. 20, pp. 4703–4713, 2013.

[172] J. Thelin *et al.*, “Implant size and fixation mode strongly influence tissue reactions in the CNS,” *PLoS One*, vol. 6, no. 1, 2011.

[173] L. Karumbaiah *et al.*, “Relationship between intracortical electrode design and chronic recording function,” *Biomaterials*, 2013.

[174] T. Suzuki, K. Mabuchi, and S. Takeuchi, “A 3D flexible parylene probe array for multichannel neural recording,” *Int. IEEE/EMBS Conf. Neural Eng. NER*, vol. 2003–Janua, pp. 154–156, 2003.

[175] G. Lind, C. E. Linsmeier, J. Thelin, and J. Schouenborg, “Gelatine-embedded electrodes--a novel biocompatible vehicle allowing implantation of highly flexible microelectrodes.,” *J. Neural Eng.*, vol. 7, no. 4, p. 46005, 2010.

[176] D. H. Szarowski *et al.*, “Brain responses to micro-machined silicon devices.,” *Brain Res.*, vol. 983, no. 1–2, pp. 23–35, Sep. 2003.

[177] S. P. Massia, M. M. Holecko, and G. R. Ehteshami, “In vitro assessment of bioactive coatings for neural implant applications.,” *J. Biomed. Mater. Res. A*, vol. 68, no. 1, pp. 177–186, 2004.

[178] W. He, G. C. McConnell, T. M. Schneider, and R. V. Bellamkonda, “A novel anti-inflammatory surface for neural electrodes,” *Adv. Mater.*, 2007.

[179] W. He and R. V. Bellamkonda, “Nanoscale neuro-integrative coatings for neural implants,” *Biomaterials*, vol. 26, no. 16, pp. 2983–2990, 2005.

[180] A. Bendali *et al.*, “Purified Neurons can Survive on Peptide-Free Graphene Layers,” *Adv. Healthc. Mater.*, 2013.

[181] M. S. Mannoor *et al.*, “Graphene-based wireless bacteria detection on tooth enamel,” *Nat. Mater.*, vol. XXXIII, no. 2, pp. 81–87, 2014.

[182] D. R. Kipke, R. J. Vetter, J. C. Williams, and J. F. Hetke, “Silicon-substrate intracortical microelectrode arrays for long-term recording of neuronal spike activity in cerebral cortex.,” *IEEE Trans. Neural Syst. Rehabil. Eng.*, vol. 11, no. 2, pp. 151–155, 2003.

[183] K.-K. Lee *et al.*, *Polyimide-based intracortical neural implant with improved structural stiffness*, vol. 14, no. 1. 2003, pp. 32–37.

[184] A. Szarpak *et al.*, “Designing hyaluronic acid-based layer-by-layer capsules as a carrier for intracellular drug delivery,” *Biomacromolecules*, vol. 11, no. 3, pp. 713–720, 2010.

[185] J. C. F. Kwok, D. Carulli, and J. W. Fawcett, “In vitro modeling of perineuronal nets: Hyaluronan synthase and link protein are necessary for their formation and integrity,” *J. Neurochem.*, vol. 114, no. 5, pp. 1447–1459, 2010.

[186] A. Tona and A. Bignami, “Effect of hyaluronidase on brain extracellular matrix in vivo and optic nerve regeneration,” *J. Neurosci. Res.*, vol. 36, no. 2, pp. 191–199, 1993.

[187] M. Morra, “Engineering of biomaterials surfaces by hyaluronan,” *Biomacromolecules*, vol. 6, no. 3, pp. 1205–1223, 2005.

[188] D. D. Allison and K. J. Grande-Allen, “Review. Hyaluronan: a powerful tissue engineering tool.,” *Tissue Eng.*, vol. 12, no. 8, pp. 2131–2140, 2006.

[189] G. Kogan, L. Šoltés, R. Stern, and P. Gemeiner, “Hyaluronic acid: A natural biopolymer with a broad range of biomedical and industrial applications,” *Biotechnol. Lett.*, vol. 29, no. 1, pp. 17–25, 2007.

[190] W. Y. J. Chen and G. Abatangelo, “Functions of hyaluronan in wound repair,” *Wound Repair Regen.*, vol. 7, no. 2, pp. 79–89, 1999.

[191] A. A. Antipov, G. B. Sukhorukov, E. Donath, and H. Möhwald, “Sustained Release Properties of Polyelectrolyte Multilayer Capsules,” *J. Phys. Chem. B*, vol. 105, no. 12, pp. 2281–2284, 2001.

[192] P. A. Janeesh, H. Sami, C. R. Dhanya, S. Sivakumar, and A. Abraham, “Biocompatibility and genotoxicity studies of polyallylamine hydrochloride nanocapsules in rats,” *RSC Adv.*, vol. 4, no. 47, p. 24484, 2014.

[193] H. Chang, L. Tang, Y. Wang, J. Jiang, and J. Li, “Graphene fluorescence resonance energy transfer aptasensor for the thrombin detection,” *Anal. Chem.*, vol. 82, no. 6, pp. 2341–2346, 2010.

[194] D. Chen, L. Tang, and J. Li, “Graphene-based materials in electrochemistry.,” *Chem. Soc. Rev.*, vol. 39, no. 8, pp. 3157–80, 2010.

[195] R. Bansil, I. V. Yannas, and H. E. Stanley, “Raman Spectroscopy: A structural probe of glycosaminoglycans,” *BBA - Gen. Subj.*, vol. 541, no. 4, pp. 535–542, 1978.

[196] T. W. Barrett and W. L. Peticolas, “Laser Raman inelastic light scattering investigations of hyaluronic acid primary and secondary structure,” *J. Raman Spectrosc.*, vol. 8, no. 1, pp. 35–38, 1979.

[197] S. Kadi *et al.*, “Alkylamino hydrazide derivatives of hyaluronic acid: Synthesis, characterization in semidilute aqueous solutions, and assembly into thin multilayer films,” *Biomacromolecules*, vol. 10, no. 10, pp. 2875–2884, 2009.

[198] Z. Z. Khaing, B. D. Milman, J. E. Vanscoy, S. K. Seidlits, R. J. Grill, and C. E. Schmidt, “High molecular weight hyaluronic acid limits astrocyte activation and scar formation after spinal cord injury,” *J. Neural Eng*, vol. 8, pp. 46033–12, 2011.

[199] D. Tarus *et al.*, “Design of hyaluronic acid hydrogels to promote neurite outgrowth in three dimensions,” *ACS Appl. Mater. Interfaces*, p. acsami.6b06446, 2016.

[200] V. Brunetti *et al.*, “Neurons sense nanoscale roughness with nanometer sensitivity.,” *Proc. Natl. Acad. Sci. U. S. A.*, vol. 107, no. 14, pp. 6264–6269, 2010.

[201] J. Zhao, A. Buldum, J. Han, and J. P. Lu, “Gas molecule adsorption in carbon nanotubes and nanotube bundles,” *Nanotechnology*, vol. 13, no. 2, p. 195, 2002.

[202] M. Adrian-Scotto, K. Ben Abdallah, G. Mallet, and D. Vasilescu, “Quantum molecular modeling of free radical saccharides from hyaluronan,” *J. Mol. Struct. THEOCHEM*, vol. 636, pp. 89–113, 2003.

[203] S. Kim *et al.*, “PubChem substance and compound databases,” *Nucleic Acids Res.*, vol. 44, no. D1, pp. D1202–D1213, 2016.

[204] S. Kuddannaya, J. Bao, and Y. Zhang, “Enhanced in Vitro Biocompatibility of Chemically Modified Poly(dimethylsiloxane) Surfaces for Stable Adhesion and Long-term Investigation of Brain Cerebral Cortex Cells,” *ACS Appl. Mater. Interfaces*, vol. 7, no. 45, pp. 25529–25538, 2015.

[205] S. P. Murarka and D. B. Fraser, “Thin film interaction between titanium and polycrystalline silicon,” *J. Appl. Phys.*, vol. 51, no. 1, pp. 342–349, 1980.

[206] N. Stark, “Literature review: biological safety of parylene C,” *Med. Plast. Biomater.*, vol. 3, pp. 30–35, 1996.

[207] F. Laermer and A. Schilp, “Method of Anisotropic Etching Silicon.” p. 6, 1996.

[208] F. Laermer and A. Schilp, “Method of anisotropic etching of silicon,” no. 6531068. 2003.

[209] F. Laermer, A. Schilp, K. Funk, and M. Offenberg, “Bosch deep silicon etching: improving uniformity and etch rate for advanced MEMS applications,” in *Technical Digest. IEEE International MEMS 99 Conference. Twelfth IEEE International Conference on Micro Electro Mechanical Systems (Cat. No.99CH36291)*, 1999, pp. 211–216.

[210] C.-H. H. Chen *et al.*, “A flexible hydrophilic-modified graphene microprobe for neural and cardiac recording.,” *Nanomedicine*, vol. 9, no. 5, pp. 600–4, Jul. 2013.

[211] A. Prasad *et al.*, “Abiotic-biotic characterization of Pt/Ir microelectrode arrays in chronic implants.,” *Front. Neuroeng.*, vol. 7, p. 2, Jan. 2014.

[212] J. C. Gerbedoen, A. Aliane, A. Gigu??re, D. Drouin, R. Ares, and V. Aimez, “All evaporation submicron lift-off lithography process with negative e-beam QSR-5 resist,” *Microelectron. Eng.*, vol. 103, pp. 123–125, 2013.